

Tracing hydrological connectivity



Marta Antonelli

Propositions

1. DNA barcoding on diatom species is the only technique that will allow diatoms to be practically used as hydrological tracer.
(this thesis)
2. Temperature observations contain a wealth of information on hydrological processes that is unmatched by the current generation of hydrological models.
(this thesis)
3. The work of experimentalists must not solely be guided by modellers' needs for parameterization.
4. For perceptual models, expert knowledge and experience of the study site should be considered at par with the information provided by data.
5. In science, competition kills creativity.
6. The need for research branding among young scientists comes at the cost of research time.

Propositions belonging to the thesis, entitled

Tracing hydrological connectivity

Marta Antonelli
Wageningen, 25 May 2020

Tracing hydrological connectivity

Marta Antonelli

Thesis committee

Promotors

Dr A.J. Teuling
Associate Professor, Hydrology and Quantitative Water Management Group
Wageningen University & Research

Prof. Dr R. Uijlenhoet
Professor of Hydrology and Quantitative Water Management
Wageningen University & Research

Co-promotor

Dr L. Pfister
Head of Catchment and Eco-Hydrology research group
Luxembourg Institute of Science and Technology, Esch-sur-Alzette, Luxembourg
Affiliated Professor, Faculty of Science, Technology and Medicine
University of Luxembourg, Esch-sur-Alzette, Luxembourg

Other members

Prof. Dr G.B. de Deyn, Wageningen University & Research
Dr A.M.J. Coenders, Delft University of Technology
Dr H.J. van Meerveld, University of Zurich, Switzerland
Dr N.L.M.B. van Schaik, Technical University of Berlin, Germany

This research was conducted under the auspices of the Graduate School for Socio-Economic and Natural Sciences of the Environment (SENSE)

Tracing hydrological connectivity

Marta Antonelli

Thesis

submitted in fulfilment of the requirements for the degree of doctor
at Wageningen University
by the authority of the Rector Magnificus,
Prof. Dr A.P.J. Mol,
in the presence of the
Thesis Committee appointed by the Academic Board
to be defended in public
on Monday 25 May 2020
at 4 p.m. in the Aula.

Marta Antonelli
Tracing hydrological connectivity,
viii + 186 pages.

PhD thesis, Wageningen University, Wageningen, the Netherlands (2020)
With references, with summary in English

ISBN 978-94-6395-387-0
DOI <https://doi.org/10.18174/520386>

Contents

Chapter 1

Introduction	1
1.1 The concept of hydrological connectivity.....	1
1.2 Challenges in investigating hydrological connectivity.....	2
1.3 Advancing hydrological connectivity understanding through interdisciplinary approaches	3
1.3.1 Terrestrial diatoms.....	4
1.3.2 Thermal Infrared imagery	5
1.4 Thesis objectives and outline	7
1.5 Thesis outline.....	11

Chapter 2

On the potential for terrestrial diatom communities and diatom indices to identify anthropic disturbance in soils..... 13

2.1 Introduction	14
2.2 Materials and methods	15
2.2.1 Study area	15
2.2.2 Sampling and analysis of diatoms and soil	15
2.2.3 Statistical analyses.....	17
2.3 Results	18
2.3.1 Soil diatom communities	18
2.3.2 Partial RDA.....	22
2.3.3 Random forest model.....	24
2.4 Discussion	25
2.4.1 Environmental controls on terrestrial diatom communities and species sensitivity to disturbance	25
2.4.2 Anthropic disturbance inferred from terrestrial diatoms	25
2.5 Conclusions	26

Chapter 3

Exploring streamwater mixing dynamics via handheld thermal infrared imagery

29	
3.1 Introduction	30
3.2 Materials and Methods	31
3.2.1 Study sites.....	31

3.2.2 Field measurements.....	33
3.2.3 TIR image acquisition.....	33
3.3 Results and Discussion	38
3.3.1 Consistency between temperatures “sensed” with the TIR camera and a submerged probe	38
3.3.2. Inferring complete mixing from TIR stream observations	39
3.3.3. Comparison between stream EC and temperature inferred from submerged probe and TIR-inferred water surface temperature.....	40
3.3.4 Influence of discharge and streambed morphology on location of the mixing front and mixing width	45
3.4 Conclusions	46

Chapter 4

Technical note: Mapping surface saturation dynamics with thermal infrared imagery

4.1 Introduction	50
4.2 Mapping surface saturation with TIR imagery: state of the art and examples .	52
4.2.1 Fundamental principles	52
4.2.2 Image acquisition interferences	54
4.2.3 Generation of TIR panorama images.....	57
4.2.4 Application examples	60
4.3 Quantification of saturation through pixel classification.....	63
4.3.1 Methods for generating binary saturation maps.....	63
4.3.2 Comparison of methods for generating binary saturation maps for TIR images	64
4.4 Discussion	67
4.4.1 Mapping surface saturation with TIR imagery.....	67
4.4.2 Pixel classification methods	69
4.5 Summary and conclusions	70

Chapter 5

Saturated areas through the lens: 1. Spatio-temporal variability of surface saturation documented through Thermal Infrared imagery.....

5.1 Introduction	74
5.2 Study site – the Weierbach catchment.....	78
5.3 Materials and Methods	79
5.3.1 Hydro-meteorological measurements and catchment storage calculation	79
5.3.2 Monitoring of surface saturated areas in the riparian zone.....	80

5.3.3 Statistical data analysis.....	84
5.4 Results.....	86
5.4.1 Hydrological response and catchment storage.....	86
5.4.2 Characteristics of the investigated riparian areas and correspondent upslope catchments	90
5.4.3 Range of surface saturation estimations.....	90
5.4.4 Spatio-temporal dynamics of surface saturation and their relationship with meteorological conditions.....	91
5.5 Discussion	104
5.6 Conclusions	108
Chapter 6	
Saturated areas through the lens: 2. Spatio-temporal variability of streamflow generation and its relationship with surface saturation.....	111
6.1 Introduction.....	112
6.2 Study site - Weierbach catchment.....	114
6.3 Materials and Methods	115
6.3.1 Hydro-meteorological measurements and catchment storage calculation	115
6.3.2 Monitoring of saturated areas in the riparian zone and stream network dynamics	116
6.3.3 Salt dilution gauging.....	117
6.3.4 Data analysis.....	119
6.4 Results.....	120
6.4.1 Spatio-temporal variability of streamflow	120
6.4.2 Stream network dynamics and relationship between riparian surface saturation and reaches' streamflow contribution.....	124
6.4.3 Relationships between topography and streamflow contribution.....	128
6.5 Discussion	132
6.6 Conclusion	136
Chapter 7	
Synthesis.....	137
7.1 Main findings.....	137
7.2 Contribution of this work to hydrological sciences.....	139
7.2.1 Local hydrology research	139
7.2.2 International hydrology research.....	141
Scientific advancements	141

Technical advancements	141
7.3 Concluding remarks and future avenues.....	142
Appendix	145
Appendix to Chapter 2	145
Appendix to Chapter 5	150
Bibliography.....	155
Summary	177
Acknowledgments	179
List of publications.....	181

Chapter 1

Introduction

Understanding the general behaviour of hydrological systems (i.e. catchments, defined as the areas of land from which water flows into rivers, lakes or reservoirs) is a challenging task that has driven hydrological research over the past decades. By definition, a system is “*a set of things working together as parts of a mechanism or an interconnecting network; a complex whole*” (Oxford dictionary). Similarly, a catchment is a system consisting of a series of structural elements such as landforms, geology, soil types and structures, ecological elements and artificial structures, and by functional elements, that are the multitude of hydrological processes taking place within the catchment such as precipitation, evapotranspiration, infiltration, to mention but a few. Understanding how the different structural and functional elements of a catchment *connect* together to generate spatially and temporally variable fluxes of water, sediment and nutrients is fundamental for gaining a holistic comprehension of catchments' functions of water collection, storage and release.

The aim of this thesis is to investigate connectivity between different structural and functional elements of the hydrological system by looking at the spatial and temporal dynamics of surface water, through an innovative multidisciplinary approach. This will eventually lead to an improved understanding of how streamflow is generated and open new possibilities for a better management of hydrological systems (and their ecological integrity), increasingly put under pressure by climate change and anthropogenic activities.

1.1 The concept of hydrological connectivity

When investigating fundamental hydrological functions of catchments (i.e. collection, storage and release of water and matter), the spatial and temporal variability of hydrological connectivity is a key element (Black, 1997). Introduced in hydrology in the early 1980s by Burt & Gaidner (1982), the concept of hydrological connectivity has only recently attracted the attention of the scientific community. Over the past two decades, hydrological connectivity has become an important conceptual framework within which the spatial and temporal variability of streamflow generation and sediment transport can be conceptualised from a holistic perspective, considering the structural and functional connectivity between the

different elements of the hydrological system (Bracken and Croke, 2007; Parsons et al., 2015; Wainwright et al., 2011).

One of the first – and probably still the most referenced – definition of hydrological connectivity has been provided by Pringle in 2001, within an eco-hydrological context. Pringle defined hydrological connectivity as the “*water-mediated transfer of matter, energy and organisms within or between elements of the hydrological cycle*”. Here, hydrological connectivity is defined as an ecological property, fundamental for the maintenance of the biological integrity of hydro-ecosystems (Pringle, 2001). More recently, Bracken and Croke (2007), and subsequently Turnbull et al. (2008), proposed a distinction between structural and functional (or process-based) connectivity. Structural connectivity refers to the extent of the physical linkage between different landscape elements at different spatial scales, while functional connectivity defines the way the physical linkage between different landscape elements affects geological, ecological and hydrological processes.

Elements of structural and functional connectivity can present heterogeneities within the hydrological system. For example, in a single catchment different types of bedrock geology, soil types and structures with different water infiltration rates, vegetation with different transpiration rates, can coexist. These heterogeneities all influence the way water from precipitation travels within the catchment in terms of pathways and residence in different compartments (Turnbull et al., 2008). Moreover, structural and functional connectivity are interrelated and exert feedback effects on each other over different spatial and temporal scales (Keesstra et al., 2018; Wainwright et al., 2011). These mutual interactions result in dynamic connectivity and dis-connectivity of different streamflow-generating portions of the catchment (Bracken and Croke, 2007), which in turn may result in nonlinear catchment responses to precipitation (McDonnell, 2003; Turnbull et al., 2008). Heterogeneous system components and their interrelation, and catchment nonlinear responses represent important challenging aspects when investigating hydrological connectivity.

1.2 Challenges in investigating hydrological connectivity

Hydrological connectivity does not only delineate a concept but it is also an emergent property of hydrological systems. In fact, connectivity at larger scales (i.e. catchment-scale) is the result of the interaction between smaller-scale system's components (i.e. sub-catchment / hillslope-scale) (Ali and Roy, 2009). However, understanding how spatial patterns and processes at smaller scales influence water fluxes at larger scales over time is one of the main challenges in the investigation of hydrological connectivity, and scaling issues (i.e. issues related to transferring information across different scales) are still relevant (Cammerrat, 2002; Vereecken et al., 2019). Current approaches for upscaling observations include extrapolation (Rinderer et al., 2019), scaling theory based on “similar media concept” (Miller and Miller, 1956) and model upscaling (Zehe et al., 2006). These approaches are based on assumptions made *a priori*, as for example the assumption that sites with similar landscape characteristics would also have a similar hydrological behaviour. Often, these assumption are invalid due to the presence of heterogeneous landscape

structures and connectivity pathways (Gammeraat, 2002; Wohl et al., 2019). Failure in assessing these heterogeneities may lead to erroneous process conceptualisation and discrepancies between processes observed at smaller scales and responses that may occur at larger scales (Ward and Packman, 2019). Assessing system heterogeneities is also particularly important for restoration purposes (Ward and Packman, 2019; Wohl et al., 2019), since the management of systems' hydrological (and ecological) functions should account for this variability to be properly implemented.

Recently, Wohl et al. (2019) and Blöschl et al. (2019) have highlighted the need to consider hydrological systems as borderless, in a way that the transition zones (or interfaces) between different landscape elements should be characterised for their own processes and fluxes to have a better perception of where and when connectivity may take place. Similarly, Krause et al. (2017) stressed the importance of system interfaces as “hot spots of ecological, biogeochemical and hydrological processes” arguing that an improved understanding of large-scale landscape interactions will only be possible once interface processes would be incorporated in system conceptualisation.

1.3 Advancing hydrological connectivity understanding through interdisciplinary approaches

When investigating hydrological systems connectivity, it is fundamental to consider the ecological and geomorphic components of the landscape and the way they interact with the hydrological components. In this sense, research on hydrological connectivity intrinsically requires a certain level of interdisciplinarity (i.e. incorporating knowledge and techniques from different disciplines) (Paton et al., 2019; Turnbull et al., 2018). During the last decade, several authors have emphasised the importance of interdisciplinary approaches – and of improving the dialogue between hydrologists and specialists of different disciplines – in order to further advance our understanding of hydrological connectivity (Cooper, 2010; Smith et al., 2019; Wainwright et al., 2011). More specifically, Wainwright et al. (2011) suggested that we should focus on developing new interdisciplinary approaches able to obtain information about the system's structure (spatial variability) and functions (both spatial and temporal variability) simultaneously, in order to understand the dynamics of their connections.

Even though interdisciplinary approaches have been identified as the *way to go* for tackling the still relevant issues related to the investigation of hydrological connectivity, the collection of interdisciplinary datasets is not so easy to achieve in practice. To be suitable for tackling the aforementioned challenges, these datasets should indeed provide information at different spatio-temporal scales and resolutions and on possible system heterogeneities (Hannah et al., 2007). The development of innovative approaches and techniques for tracing hydrological connectivity is indispensable for generating new information on connectivity processes across multiple scales (Abbott et al., 2016; Hannah et al., 2007). In this thesis, two approaches, namely terrestrial diatoms and ground-based thermal infrared (TIR) imagery, are presented and employed in an innovative way to trace hydrological connectivity, with a focus on surface water dynamics. Although their application is

widespread in other research fields, the use of these techniques in hydrological studies is still relatively limited.

1.3.1 Terrestrial diatoms

Diatoms (Bacillariophyta) are unicellular, eukaryotic algae (10 – 200 microns) (Fig. 1.1). They constitute the largest group of microalgae (Guiry, 2012; Round et al., 1990), present in nearly every habitat where water is found (i.e. aquatic and terrestrial environments) as single cells or colonies, attached or unattached to the substratum. Diatoms show high morphological heterogeneity due to their species-specific cell wall impregnated of silica (called frustule) (Fig. 1.1), feature on which their taxonomy and systematics are based. Aquatic diatom species are largely employed in many different fields of research (Flower, 2005) and especially in the assessment of water quality and biomonitoring programmes thanks to their ubiquity and sensitivity to several environmental and anthropogenic factors such as light, moisture, temperature, pH, as well as organic and inorganic pollution (among others) (Lobo et al., 2016). For this reason, aquatic diatoms are widely studied and ecologically well characterised (Soininen, 2007). Compared to aquatic diatoms, terrestrial diatom (i.e. assemblages developing on terrestrial substratum such as soil surface, rocks, litter, vegetation etc ...) have been far less studied and rarely applied in research in general.

In 2009, Pfister et al. pioneered the possibility to employ terrestrial diatoms as a tracer in catchment hydrology. This study required the collaboration between several hydrologists and diatom taxonomists. Pfister and colleagues successfully tested the hypothesis that terrestrial diatoms could be used to trace connectivity and water sources along the hillslope-riparian-stream (HRS) continuum by showing that, during precipitation events, terrestrial diatoms were mobilised from the terrestrial environment to the stream through surface runoff (Fig. 1.1). Moreover, because of the specificity of diatom assemblages to particular habitats and moisture conditions (Van Dam et al., 1994), it was possible to understand that the source of surface runoff was mainly the riparian zone. This proof-of-concept study paved the way for several other studies, which further confirmed the potential for terrestrial diatoms to serve as a tracer at the HRS scale (Coles et al., 2016; Klaus et al., 2015; Martínez-Carreras et al., 2015a; Tauro et al., 2016).

Klaus et al. (2015) extended the use of terrestrial diatoms to trace connectivity at large scales. Within a set of nested catchments (0.45 – 247 km²), they showed that different species assemblages were to be attributed to sub-catchments with different physiographic characteristics. As a consequence, the occurrence of particular species at the 247 km²-catchment outlet during precipitation events provided information on both the occurrence of riparian-stream connectivity in different sub-catchments and the source of stream water to the outlet.

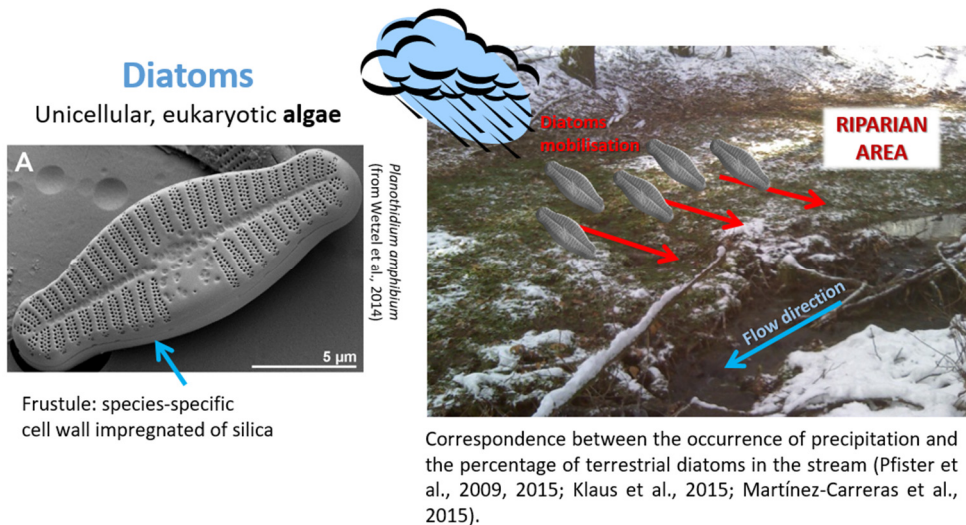


Figure 1.1: Example of a diatom cell as observed with the scanning electron microscope (SEM) (*Planothidium amphibium* from Wetzel et al. (2014) , SEM picture by Carlos Wetzel) (left). Simplified representation of diatom mobilisation from the riparian area to the stream in response to precipitation (right).

1.3.2 Thermal Infrared imagery

Thermal infrared (TIR) is the region of the electromagnetic spectrum at wavelengths comprised between 3-5 and 8-14 µm. Thermal infrared radiation is emitted by every object having a temperature above the absolute zero, and the amount of emitted radiation is a function of temperature. Thermographic techniques (thermal imaging or video – Fig 1.2) allow the detection and quantification of objects' radiation emission variations (i.e. temperature variation) by converting the information from invisible infrared radiation into visible images of that radiation (thermographs), based on the Stefan-Boltzmann's law for a blackbody (i.e. an object capable to absorb all incident electromagnetic radiation at any frequency and incidence angle):

$$T = \sqrt[4]{W/\sigma}$$

where T is the object's surface temperature (K), W is the intensity of infrared radiation (Wm^{-2}) and σ is the Stefan-Boltzmann constant ($5.57 \times 10^{-8} \text{ Wm}^{-2}\text{K}^{-4}$). The emissivity ϵ is an important object parameter that has to be introduced in the Stefan-Boltzmann equation for material-specific radiometric correction:

$$T = \sqrt[4]{W/\epsilon\sigma}$$

The emissivity ϵ is a measure of how much radiation an object emits compared to the emitted radiation from a blackbody at the same temperature.

When observing an object with an infrared camera, the measured radiation is not only the one from the object (W_{obj}) but also the radiation reflected from the surroundings (W_{refl}). Moreover, the sum of these radiations is attenuated by the atmosphere (W_{atm}) between the camera and the object. Considering all these components, the total radiation detected by the camera is defined as:

$$W_{tot} = \varepsilon\tau W_{obj} + (1 - \varepsilon)\tau W_{refl} + (1 - \tau)W_{atm}$$

where τ is the transmittance of the atmosphere, which depends on the distance between the camera and the object and on air humidity. In order to accurately measure an object's temperature, recent TIR camera models directly provide information on material-specific ε , atmospheric temperature, air humidity, distance between the camera and the object and the effective temperature of the surrounding objects.

TIR measurements started to be employed in hydrology from the second half of the 20th century (Estes, 1966). The first studies were mainly based on TIR images obtained via airborne acquisitions and used for the detection of groundwater discharge into marine bays (Banks et al., 1996; Pluhowski, 1972) and estimation of soil water content and evaporation (Reginato et al., 1976; Schmutge, 1978). Government agencies such as NASA and USGS were often the principal financial supporters of these studies and suppliers of costly aircrafts and thermal infrared scanners. With the technical advancements of the 21st century, TIR sensors became more reliable, portable and affordable. Both airborne and ground-based TIR devices with high resolution and thermal sensitivity started to be employed for the investigation of hydrological processes such as groundwater – surface water interaction (Briggs and Hare, 2018; Schuetz and Weiler, 2011), water flow-paths and velocities (Deitchman and Loheide, 2009; Schuetz et al., 2012) and for the detection of water inputs into stream channels and monitoring of stream water temperature (Loheide and Gorelick, 2006; Torgersen et al., 2001).

In 2010, Pfister and colleagues employed ground-based TIR imagery to investigate small-scale hydrological processes taking place along the HRS continuum. In this proof-of-concept study, they focused their attention on surface saturated areas (i.e. areas presenting water at the ground surface), important key areas for runoff generation, especially in humid-temperate environments (Ambrose, 2004; Birkel et al., 2010; Bracken and Croke, 2007; Hewlett, 1961; Tetzlaff et al., 2007). Employing a handheld TIR camera, they monitored the dynamics of surface saturation in a forested area of 3 x 5 meters – including a portion of hillslope, riparian zone and stream – during the wetting-up period of the catchment. Thanks to this approach, they were able to capture the dynamics of small-scale processes at the riparian-stream interface, such as groundwater exfiltration, expansion and contraction of riparian surface saturation, and to identify moments and locations of surface water connectivity to the stream (Fig. 1.2). As an outcome of this study, ground-based TIR imagery showed to be a valuable tool for observing and potentially quantifying the spatio-temporal variability of HRS connectivity.

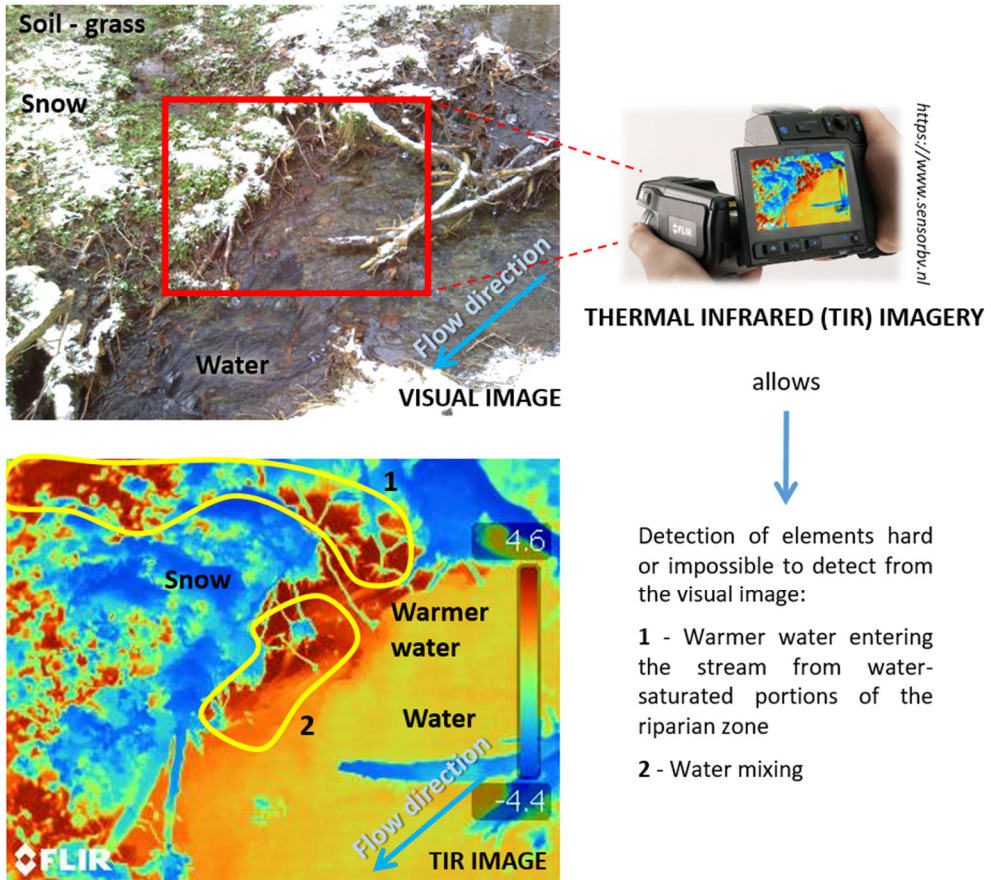


Figure 1.2: Riparian-stream portion (visual image) observed through a TIR camera. The TIR image reveals warm water from the riparian area connecting to the stream and mixing with the colder stream water (Pictures by Marta Antonelli; location: Weierbach catchment, Luxembourg; 6 of February 2015).

1.4 Thesis objectives and outline

This thesis is wired around two complementary objectives. First, the overarching scientific objective is to advance our understanding on hydrological connectivity at different spatial and temporal scales. Second, we aim to leverage pioneering work carried out in recent years to eventually improve the applicability of terrestrial diatoms and TIR imagery for tracing the on- and offset of surface water connectivity. For this reason, the different chapters of this thesis have their focus set on the development of the aforementioned techniques (Chapters 2 to 4), as well as their subsequent use for the exploration of specific hydrological processes (Chapters 5 and 6).

The work presented in this thesis is the follow-up of a set of precedent studies. Figure 1.3 outlines the thesis framework and shows how each chapter of this thesis can be assigned to a different broader research topic (Fig. 1.3, red

rectangles 1, 2, and 3). Within the three groups, each chapter focuses on specific objectives:

- 1- *Terrestrial diatoms as a tracer of hydrological connectivity at the catchment scale* (Chapter 2).

Objective: to investigate how gradients in landuse, soil type and geology control terrestrial diatom communities. Although Chapter 2 mainly focuses on testing the hypothesis that terrestrial diatoms could be used to assess the quality of terrestrial sites, understanding the physiographic controls on terrestrial diatom communities is fundamental for advancing their further use as tracers of hydrological connectivity at the catchment scale.

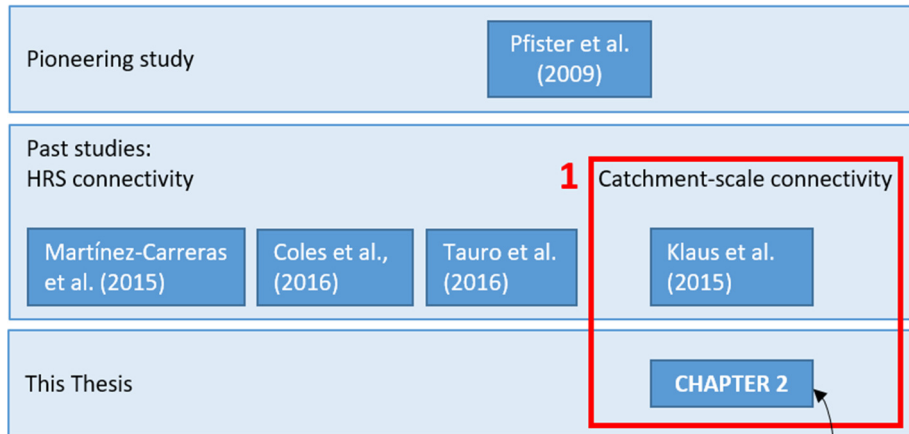
- 2- *New avenues for TIR imagery as a tracer of hydrological connectivity* (Chapters 3 and 4).

Objective: to investigate the potential for handheld TIR imagery to provide instantaneous mapping of stream water mixing patterns at or near the water surface (Chapter 3) and to provide an exhaustive reference guide for the application of TIR imagery for mapping surface saturation dynamics (Chapter 4).

- 3- *TIR imagery as a tracer of hydrological connectivity along the HRS continuum* (Chapters 5 and 6).

Objective: to explore possible internal heterogeneity of the catchment by characterising the spatio-temporal dynamics of expansion and contraction of surface saturation in different riparian areas (Chapter 5) and to understand how these dynamics relate to the spatio-temporal variability of streamflow generation in the catchment (Chapter 6).

Terrestrial diatom studies



TIR studies

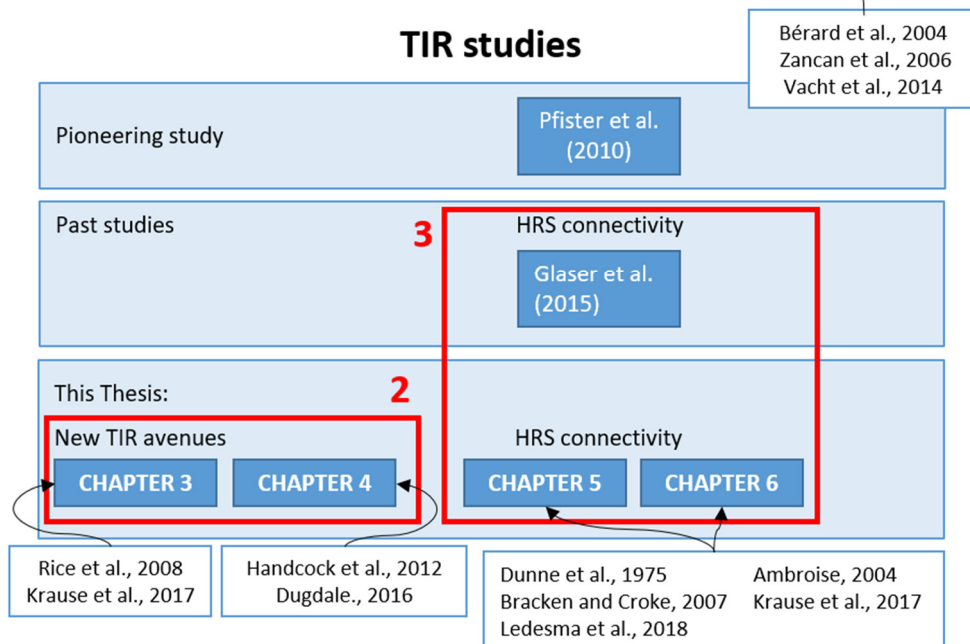


Figure 1.3: Thesis framework. Blue filled rectangles indicate studies carried out in Luxembourg. Outside the blue filled rectangles are indicated some of the studies from different research groups which have influenced the research presented in this thesis. Each chapter is assigned to a different broad research topic (indicated by the red boxes): 1) Terrestrial diatoms as a tracer of hydrological connectivity at the catchment scale (Chapter 2); 2) New avenues for TIR imagery as a tracer of hydrological connectivity (Chapters 3 and 4); 3) TIR imagery as a tracer of hydrological connectivity along the HRS continuum (Chapters 5 and 6).

All the data used in this thesis have been obtained from fieldwork carried out in the nested-catchment set-up of the Attert River basin in the Grand Duchy of Luxembourg (Fig. 1.4). The Attert River basin has been selected for the investigation of the physiographic controls on terrestrial diatom communities (Chapter 2) because its sub-catchments exhibit a wide range of contrasted geological settings, land use and soil types (cf. Fig. 2.1), while sharing the same average climatological conditions (Pfister et al., 2000). In this way, the influence of climate on terrestrial diatom samples collected in different sub-catchments could be considered homogeneous. The Weierbach catchment (a sub-catchment of the Attert catchment) was employed for the studies on the dynamics of expansion and contraction of riparian surface saturation (Chapters 4, 5 and 6). This catchment is a long-term studied headwater catchment (0.42 km²), representative of the Luxembourgish Ardennes (Sougnéz and Vanacker, 2011) and considered as a reference site for rainfall-dominated mountainous catchments (Zuecco et al., 2018).

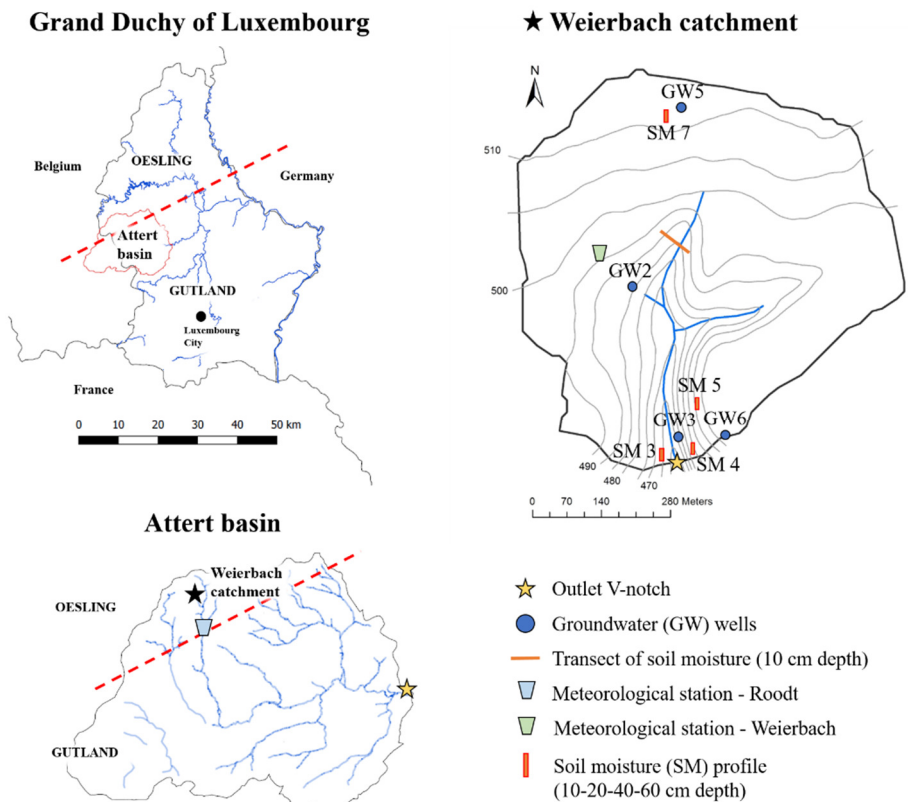


Figure 1.4: Location of the Attert River basin within the Grand Duchy of Luxembourg, and of the Weierbach catchment within the Attert River basin. The red dashed line indicates the contact zone between two geological regions: the schistose Ardennes massif (Oesling region) and the sedimentary Paris Basin (Gutland region).

1.5 Thesis outline

The following five chapters (from 2 to 6) address the specific objectives described in the previous section. Being based on manuscripts that have been published or are under review in peer-reviewed journals, each chapter includes its own detailed introduction and conclusions. Chapter 7 presents a synthesis of the results of the individual chapters. In this chapter, the relevance of this work with regard to advancing our understanding of hydrological connectivity and suggestions for future research avenues are also presented.

Chapter 2

On the potential for terrestrial diatom communities and diatom indices to identify anthropic disturbance in soils

Abstract

A large amount of studies focuses on aquatic diatoms' ecology and their use in the assessment of water quality. Little is known about terrestrial diatoms' ecological behaviour and sensitivity to environmental factors. We hypothesise that terrestrial diatom communities can serve as a proxy of anthropic disturbance levels in terrestrial sites. To test our hypothesis, we apply an aquatic index to soil communities that is to deliver new information on the physiographic controls on soil diatoms. Diatom and soil samples were collected in the Attert River basin in Luxembourg during three seasons, in sites characterised by different combinations of geological, soil (schist, marl and sandstone) and land use (forest, grassland and agriculture) features. We found an effect of seasonality on soil diatom communities, reflected by different species dominance and abundances in samples during the three seasons. Soil pH and land use (which translates in a different amount of total carbon and nitrogen in soil) were identified as the variables having the largest impact in structuring the communities and as among the features with the highest importance in defining the ecological status of the sites (i.e. disturbed farmlands having higher pH and lower carbon and nitrogen content). However, the lack of information about the sensitivity of some of the most abundant terrestrial species in our study area caused some discrepancies between the expected (i.e. forested areas with low anthropic disturbance) and the obtained results, with several forested sites classified as having high anthropic disturbance. These results suggest that soil communities are likely to contain information about soil ecological status and highlight the importance of a better characterisation of terrestrial diatom species for developing a quality index based on soil communities.

This chapter is based on: Antonelli M, Wetzel CE, Ector L, Teuling AJ, Pfister L. On the potential for terrestrial diatom communities and diatom indices to identify anthropogenic disturbance in soils. 2017. Ecol. Indic., 75:73 – 81. <https://doi.org/10.1016/j.ecolind.2016.12.003>.

2.1 Introduction

Aquatic diatoms are a biological indicator commonly used for assessing the ecological status of water bodies. Their sensitivity to multiple factors, among which organic and inorganic pollution, pH and salinity, is well documented (Gibson et al., 2006; Kelly et al., 1995; Kwadrans et al., 1998; Lobo et al., 2016; Prygiel and Coste, 1993). In order to estimate degradation levels of waterbodies, several diatom-based indices such as the IPS (Specific Pollution Sensitivity Index; Coste in Cemagref, (1982)), the TDI (Trophic diatom index; Kelly and Whitton, (1995)) and the BDI (Biological diatom index; Lenoir and Coste, (1996)) have been developed. These indices are systematically used in biomonitoring programmes related to the European Water Framework Directive (The European Parliament and the Council of the European Union, (2000)).

While aquatic diatoms are commonly studied and well ecologically characterised, also because of their use in the calculation of water quality indices (Soininen, 2007), studies on terrestrial diatoms communities (i.e. diatom assemblages which can be found on soil surface) are rather scarce. Studies considering soil algae communities in general, have shown that they are quite responsive to disturbance factors (Bérard et al., 2004; Vacht et al., 2014; Zancan et al., 2006). Similarly, studies focusing on terrestrial diatoms assemblages were conducted in agricultural ecosystems with the aim to test the effect of different factors such as land use, farming and tillage practices on the communities. As a result, Heger et al. (2012) reported a difference in the community structure of terrestrial diatoms in response to different agricultural practices (i.e. organic and conventional farming systems). Stanek-Tarkowska and Noga (2012) found a possible correlation between cultivation and fertilisation systems and variation in organic matter content, pH and moisture content of soils. These factors are likely to influence the species composition of soil diatom communities (Van Dam et al., 1994; “Van de Vijver & Beyens 1998 Eur. J. Soil Biol. 34 (3) 133-141 soil diatom assemblages Crozet Subantarctica.pdf,” n.d.).

Despite the documented sensitivity of terrestrial diatoms to farming practices, to the best of our knowledge, no diatom index has ever been developed for qualitatively assessing terrestrial sites. The main obstacle to progress is due to the scarce information on terrestrial diatom ecology and to the difficult identification of environmental factors that can directly influence soil diatom communities' composition and species distribution (Stanek-Tarkowska et al., 2015). Here we propose to investigate how gradients in land use, soil type and geology control soil diatom communities. Our hypothesis is that terrestrial diatom communities can be used to define the quality of terrestrial sites. Soil diatom communities are characterised by species living exclusively or almost exclusively in terrestrial environments and by species that can be widely found also in aquatic environment. For this reason, to test our hypothesis we apply a quality index developed for aquatic diatoms (i.e. IPS) to soil diatom communities. Our purpose is to adopt the IPS index as an investigation tool to assess the potential for terrestrial diatoms to provide information on the degree of anthropic influence on the communities prevailing at different terrestrial sites.

We tested our hypothesis in the Attert River basin in Luxembourg (Europe). Our study area is characterised by a large diversity in physiographic settings. In the

first section we develop on the study area, sampling protocol and analytical protocols, while the following sections are dedicated to the presentation and discussion of results. The final section of our manuscript provides an outlook on future research lines based on findings from our seminal work.

2.2 Materials and methods

2.2.1 Study area

The Attert River basin (245 km²) is located in the North-West of the Grand Duchy of Luxembourg (49°46'13.0" N, 5°59'9.2" E) (Fig. 2.1). The basin exhibits a wide range of contrasted geological settings, land use and soil types. Schists are the dominating bedrock in the north-western part of the basin, while the 'Buntsandstein' (red sandstone) is characteristic of the north-eastern part. Marls and Luxembourg sandstone dominate in the central and southern parts of the basin, respectively. The soil types mostly map onto bedrock geology, with silty-clay soils having developed on marls, silty-stony soils on schists and red sandstone and sandy-loamy soils on Luxembourg sandstone. Recently formed soils from alluvial deposition are located in the vicinity of streams. Land use in the basin is comprised of forested areas, grasslands and farmland. Specifically, forested areas are dominated by a combination of European beech (*Fagus sylvatica*) and Norway spruce (*Picea abies*). Grasslands are mainly used for cattle grazing, while predominantly rapeseed, corn and wheat are grown on farmland.

The climate regime of the basin is semi-oceanic. The sampling period extended from July 2014 to March 2015, July 2014 and August 2014 were the warmest months in this period (average temperature of 19.7°C and 16.3°C, respectively). The coldest temperatures were observed in January and February 2015 (average temperature of 0.9°C and 1.0°C, respectively). Average monthly precipitation was 71.5 ± 39.7 mm. The maximum aggregated monthly precipitation was observed in July 2014 (140.9 mm). Monthly precipitation reached a minimum in September 2014 (23.8 mm) (ASTA, Ministry of Agriculture).

2.2.2 Sampling and analysis of diatoms and soil

Soil diatom samples were collected at the soil surface in 34 locations during three sampling campaigns (August 2014, November 2014 and March 2015) (Fig. 2.1). Sampling points were chosen in order to optimize the relative representation of geology, soil type and land use. We used metal rings (Ø 5.6 cm) to obtain soil samples with equal size. Diatom cells were extracted washing the soil surface with sparkling water and then fixed with formaldehyde (each final sample was composed of three sub-samples). Diatoms were prepared for microscopic counts following the CEN 13946 procedure (European Committee for Standardization, (2003)). A minimum of 200 valves were counted and identified in each sample (Bate and Newall, 2002). Soil samples were collected during all three campaigns at the same locations and analysed for electrical conductivity (EC) and pH_{CaCl2} (pH) (following the

ISO 11265 (1994) and ISO 10390 (2005) directives, respectively). CHN analyses (Truespec CHN, LECO) were performed on dried soil samples in order to determine the total percentages of carbon (C) and nitrogen (N) contents (for raw data see Table A2.1 a in Appendix 2). Precipitation, air and soil temperature and air humidity were obtained from local meteorological stations (ASTA, Ministry of Agriculture; for raw data see Table A2.1-b in Appendix 2).

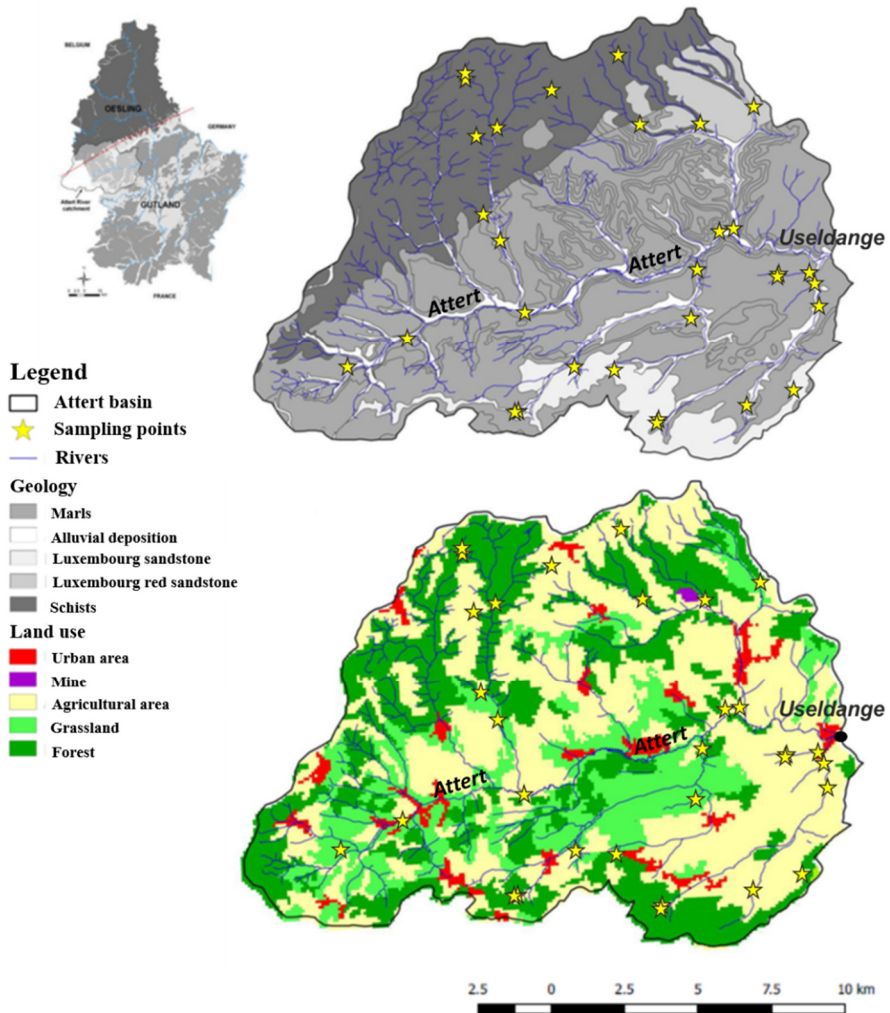


Figure 2.1: Physiographic characteristics of the Attert River basin in Luxembourg.

2.2.3 Statistical analyses

Before carrying out statistical analyses, the species dataset was reduced by eliminating species with less than 2% of relative abundance in all the samples. Samples with a low number of valves (<200 valves) were also removed from the dataset (3 out of the 92 total samples collected were excluded).

In order to identify clusters in soil diatom species assemblages, we used self-organising maps (SOM) (Kohonen, 1982). We applied the SOM algorithm optimised for diatom community data developed by Bottin et al. (2014) in the diatSOM package for R (R Core Team, 2015). To investigate the influence of environmental variables on soil diatom communities we used the partial Redundancy Analysis (RDA) (Ecology and Jun, 2016; Legendre and Legendre, 1998). Since our purpose was to test the relationship between a set of geographical (i.e. land use, soil type and geology) and chemical (EC, pH, C, N) variables and the variability in the soil diatom communities species assemblage, we carried out the partial RDA analysis constraining the variability related to the seasonality (i.e. month, temperatures, precipitation, air humidity). Prior to the partial RDA analysis, Hellinger transformation was applied to the dataset of species abundances (Rao, 1995). We also performed correlation analyses between geographical and chemical environmental parameters to test the independency of the variables. To test how well the applied 2D ordination predicts the explanatory variables and to test the significance of the partial RDA axes, we used Monte Carlo permutation tests (perm = 999).

IPS indices were calculated for each site taking into account the whole dataset of terrestrial diatom species. The IPS index (as also the TDI) is based on the formula of Zelinka and Marvan (1961). This formula takes into account the abundance of each species in the sample, the “indicator value” of each species (i.e. a value of relative probability of each taxon to occur in one of five saprobic categories) and their sensitivity value (i.e. sensitivity to pollution). Classes from 1 to 5 were associated to ranges of IPS values (1 = IPS > 17 “excellent”; 2 = IPS 15–17 “good”; 3 = IPS 12–15 “moderate”; 4 = IPS 8–12 “tolerable”; 5 = IPS < 8 “bad”) (Noga et al., 2013; Rakowska and Szczepocka, 2011) and were related in this study to increasing degrees of anthropic disturbance. The IPS was selected as the reference quality index for this study, since it is the index with the higher number of taxa included and the most updated.

In order to understand which environmental variables can be considered as the best predictors of anthropic disturbance levels of our sampling sites, we used an ensemble model (random forest of regression trees (Breiman, 2001; Breiman et al., 1984)) considering the calculated IPS values as output (dependent variable). The model was structured along the same environmental variables taken into account for the partial RDA. An estimation of the R^2 has been calculated in order to test the efficiency of the predictive model.

Correlation analyses for the environmental variables and the partial RDA analysis were carried out in R 3.2.2 (the package ‘vegan’ (Oksanen et al., 2015) was used for the partial RDA analysis). The IPS indices were calculated using the software OMNIDIA version 6.0.1 (2016) (Lecoointe et al., 1993). OMNIDIA was also used to calculate other ecological indices like Shannon’s diversity, species richness

and sensitivity values (S) of the species. The random forest model was run using Scikit-learn: Machine Learning in Python (Pedregosa et al., 2011).

2.3 Results

2.3.1 Soil diatom communities

An overall number of 251 species (before dataset reduction) were identified in the samples. Communities sampled in August showed the highest species richness with a maximum value of 46 and a minimum of 7 (average 21.5 ± 8.8), while we observed slightly lower values in November and March with a maximum richness of 41 and a minimum of 5 for both months (November average = 20.4 ± 7.2 ; March average = 18.2 ± 10.4). Shannon's diversity index was similar between the three months (average 3.3 ± 0.8). About 55% of the identified species were present in at least one sample from all three months. The dominant species (>5% averaged relative abundance within the months) for the samples collected in August were *Hantzschia amphioxys* (Ehrenberg) Grunow, *Pinnularia obscura* Krasske, and *Hantzschia abundans* Lange-Bertalot. In November we found *Hantzschia amphioxys* to be again the most frequent, followed by *Stauroneis thermicola* (J.B. Petersen) J.W.G. Lund, *Hantzschia abundans* and *Sellaphora atomoides* (Grunow) C.E. Wetzel & Van de Vijver. In March the most abundant species were *Caloneis lancettula* (P. Schultz) Lange-Bertalot & Witkowski and *Stauroneis parathermicola* Lange-Bertalot (Table 2.1-a). We found the aforementioned species to be particularly abundant in farmland and grassland areas. In forested areas we documented high relative abundances of species *Navicula tenelloides* Brébisson in Kützing, *Pinnularia schoenfelderii* Krammer, *Sellaphora atomoides* and *Stauroneis parathermicola*.

The SOM cluster analysis identified eight different groups (UPGMA clustering using Bray-Curtis distance; dendrogram cut: 0.5). The 9.6% of the species were present in all clusters. Table 2.1-b shows the most abundant species (>5% average relative abundance) in each cluster.

A selection of the most representative diatom species is shown in Fig. 2.2.

Table 2.1: List of the most abundant diatom species (> 5% relative abundance) found in the samples collected during each of the three months (a) and in each SOM cluster (b – next page) ordered by decreasing abundance. In brackets, the values of relative abundance for each species expressed in percentages. In the lower part of the SOM clusters table: the dominant land use in each cluster (red: agriculture; yellow: grassland; green: forest). The codes assigned to each species follow the OMNIDIA code system (ABRY: *Adlafia bryophila* (J.B.Petersen) Gerd Moser, Lange-Bertalot & Metzeltin; CLCT: *Caloneis lancettula* (P.Schultz) Lange-Bertalot & Witkowski in Lange-Bertalot & Metzeltin; CMOL: *Caloneis molaris* (Grunow) Krammer in Krammer & Lange-Bertalot; FFVI: *Fragilariforma virescens* (Ralfs) D.M.Williams & Round; GVRD: *Gomphonema varioeduncum* Jüttner, Ector, E.Reichardt, Van de Vijver & E.J.Cox in Jüttner et al.; HABU: *Hantzschia abundans* Lange-Bertalot; HAMP: *Hantzschia amphioxys* (Ehrenberg) Grunow in Cleve & Grunow; HLMO: *Halamphora montana* (Krasske) Levkov; HUCO: *Humidiphila contenta* (Grunow) R.L.Lowe et al.; LFRQ: *Luticola frequentissima* Levkov, Metzeltin & A.Pavlov; MAAT: *Mayamaea atomus* (Kützing) Lange-Bertalot; MPMI: *Mayamaea permitis* (Hustedt) Bruder & Medlin; NACD: *Nitzschia acidoclinata* Lange-Bertalot; NCIN: *Navicula cincta* (Ehrenberg) Ralfs in Pritchard; NIPU: *Nitzschia pusilla* (Kützing) Grunow emend. Lange-Bertalot; NPAL: *Nitzschia palea* (Kützing) W.Smith; NTEN: *Navicula tenelloides* Hustedt; PISS: *Pinnularia isselana* Krammer; POBS: *Pinnularia obscura* Krasske; PPRI: *Pinnularia perirrorata* Krammer; PSHO: *Pinnularia schoenfelderi* Krammer; PTLA: *Planothidium lanceolatum* (Brébisson ex Kützing) Lange-Bertalot; SEAT: *Sellaphora atomoides* (Grunow) C.E.Wetzel & Van de Vijver in Wetzel et al.; SPTH: *Stauroneis parathermicola* Lange-Bertalot in Hofmann et al.; STER: *Surirella terricola* Lange-Bertalot & Alles in Lange-Bertalot & Metzeltin; STHE: *Stauroneis thermicola* (J.B.Petersen) J.W.G.Lund).

a. Months

	August	November	March
Abundant species	HAMP (12.2 %)	HAMP (7.6 %)	CLCT (8.8 %)
	HABU (5.4 %)	STHE (6.2 %)	SPTH (5.8 %)
	POBS (5.2 %)	HABU (5.4 %)	
		SEAT (5.1 %)	

b. SOM clusters

	I	II	III	IV	V	VI	VII	VIII
Abundant species	HAMP (23.3%)	NIPU (11.2%)	NCIN (11.4%)	HABU (12.5%)	CLCT (30.7%)	PTLA (14.2%)	NACD (11.5%)	PPRI (22.7%)
	POBS (7.2%)	CLCT (11.1%)	HLMO (6.5%)	NPAL (7.8%)	SPTH (6.5%)	FFVI (12.7%)	STHE (7.4%)	SPTH (14.5%)
	MAAT (6.9%)	HUCO (10.7%)	STER (6.3%)	HAMP (7.0%)	STHE (6.0%)		SPTH (6.6%)	PSHO (7.4%)
	MPMI (6.8%)	LFRQ (6.5%)	NTEN (5.5%)	LFRQ (5.8%)	CMOL (5.4%)		SEAT (6.3%)	
	HABU (6.6%)	CMOL (6.4%)	ABRY (5.4%)	HLMO (5.7%)			POBS (6.3%)	
	STHE (5.3%)	GVRD (5.8%)	SEAT (5.3%)	POBS (5.4%)				
		PISS (5.1%)						



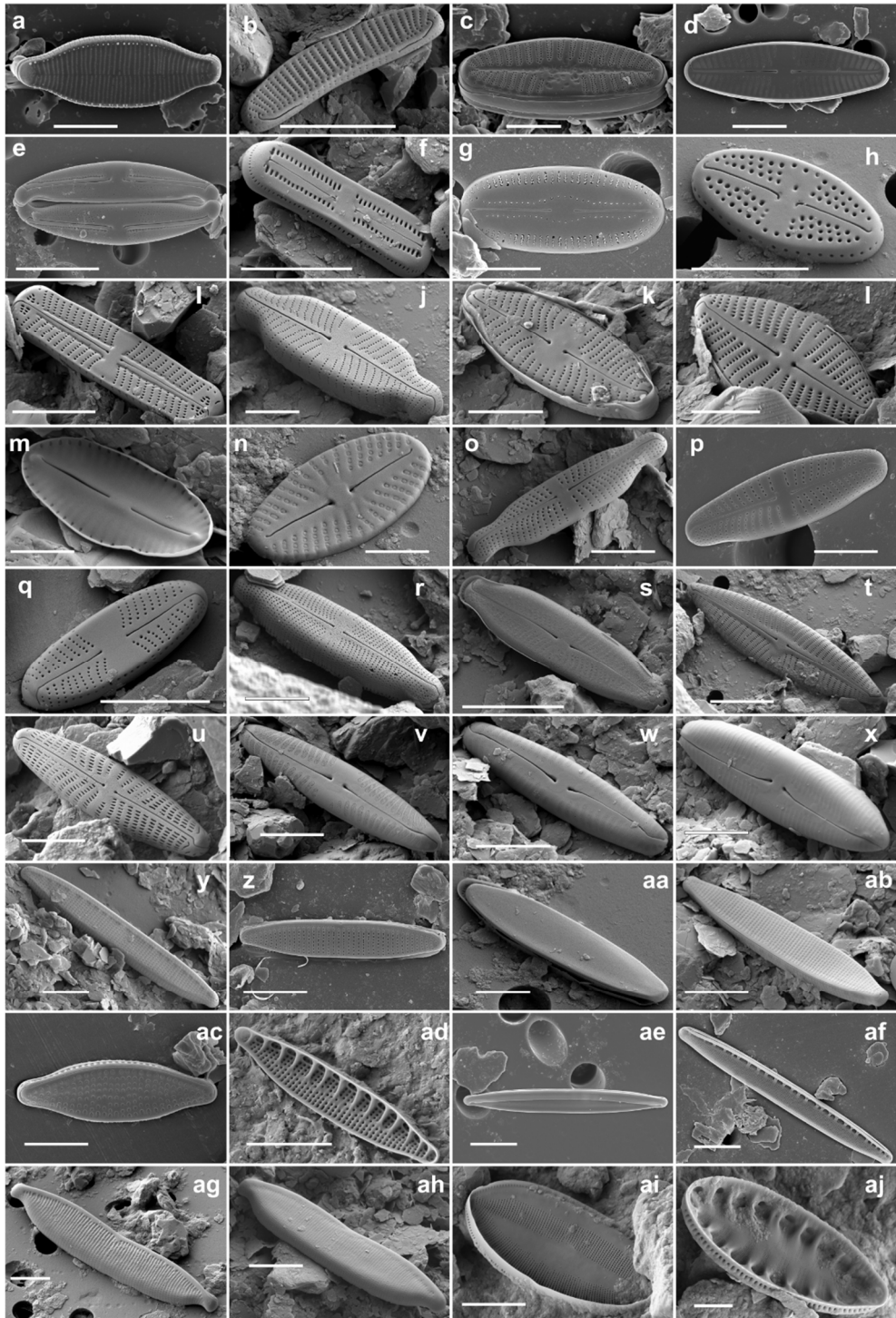


Figure 2.2 – see figure caption on next page.

Figure 2.2 (previous page): Selected scanning electron microscope (SEM) pictures of some of the most abundant soil diatom species found in the Attert catchment. (a) *Fragilariforma virescens* (Ralfs) D.M.Williams & Round; (b) *Eunotia botuliformis* Wild, Nörpel & Lange-Bertalot in Lange-Bertalot; (c-d) *Planothidium lanceolatum* (Brébisson ex Kützing) Lange-Bertalot; (e) *Halamphora montana* (Krasske) Levkov; (f) *Humidophila contenta* (Grunow) R.L.Lowe et al.; (g) *Diploneis* cf. *oculata* (Brébisson in Desmazières) Cleve; (h) *Luticola* cf. *micra* Levkov, Metzeltin & A.Pavlov; (i) *Geissleria paludosa* (Hustedt) Lange-Bertalot & Metzeltin; (j) *Placoneis paraelginensis* Lange-Bertalot in Rumrich et al.; (k) *Placoneis ignorata* (Schimanski) Lange-Bertalot in Rumrich et al.; (l) *Placoneis hambergii* (Hustedt) Bruder & Medlin; (m) *Mayamaea arida* (W.Bock) Lange-Bertalot; (n) *Mayamaea excelsa* (Krasske) Lange-Bertalot; (o) *Stauroneis thermicola* (J.B.Petersen) J.W.G.Lund; (p) *Stauroneis parathermicola* Lange-Bertalot in Hofmann et al.; (q) *Sellaphora atomoides* (Grunow) C.E.Wetzel & Van de Vijver in Wetzel et al.; (r) *Adlafia brockmannii* (Hustedt) Bruder in Bruder & Medlin; (s) *Adlafia bryophila* (J.B.Petersen) Gerd Moser, Lange-Bertalot & Metzeltin; (t) *Navicula cryptotenella* Lange-Bertalot in Krammer & Lange-Bertalot; (u) *Navicula cincta* (Ehrenberg) Ralfs in Pritchard; (v) *Pinnularia perirrorata* Krammer; (w) *Pinnularia sinistra* Krammer; (x) *Caloneis lancettula* (P.Schulz) Lange-Bertalot & Witkowski in Lange-Bertalot & Metzeltin; (y) *Nitzschia* cf. *hantzschiana* Rabenhorst; (z) *Nitzschia acidoclinata* Lange-Bertalot; (aa) *Nitzschia pusilla* (Kützing) Grunow emend. Lange-Bertalot; (ab) *Nitzschia palea* (Kützing) W.Smith; (ac-ad) *Nitzschia solgensis* Cleve-Euler; (ae-af) *Nitzschia harderi* Hustedt in Brendemühl; (ag) *Hantzschia abundans* Lange-Bertalot; (ah) *Hantzschia amphioxys* (Ehrenberg) Grunow in Cleve & Grunow; (ai) *Tryblionella debilis* Arnott ex O'Meara; (aj) *Surirella terricola* Lange-Bertalot & Alles in Lange-Bertalot & Metzeltin. Scale bars = 5 µm. SEM pictures by Carlos Wetzel.

2.3.2 Partial RDA

The results of the correlation analyses showed that the geographical and chemical environmental variables were not correlated between each other (R^2 not higher than 0.5 for all the variables) except for carbon and nitrogen soil content which resulted correlated ($R^2 = 0.9$). Both carbon and nitrogen soil content variables were retained in the partial RDA analysis since they did not show strong collinearity with other variables (variables' variance inflation factors (VIF) analysis; carbon soil content VIF = 9.5, nitrogen soil content VIF = 10.2).

The partial RDA ordination shows the samples collected during the three campaigns divided according to the cluster categories obtained from the SOM analysis (Fig. 2.3-a). The total variation explained by the partial RDA was 26.4%. The 6.5% of the variation was conditioned by the seasonal variability (for the partial RDA model output see Table A2.2 in Appendix 2). The 2D ordination was significant in predicting all the variables ($P < 0.001$). The first two RDA axes covered together 51.6% of the total explained variation and they both resulted as significant ($P < 0.001$) after the permutation test. The analysis revealed how different SOM clusters are distributed on the bi-plot environment (Fig. 2.3-a). The first four clusters plotted on the right side of the bi-plot. Clusters I, II and IV were associated with samples collected mainly in farmland and grassland areas, having higher averaged pH values (6.2 ± 0.8) and overall lower C and N soil content (C: $3.2 \pm 2.8\%$; N: $0.3 \pm 0.2\%$). Cluster III correlated most with the high values of soil pH (7.1 ± 0.4) and included most of the samples from forested areas within this group of clusters. On the opposite side of the bi-plot we found the clusters VI, VII and VIII. In particular, these clusters were associated to samples from forested areas (clusters VI and VIII) and grass-land (cluster VII) – these areas having lower averaged pH values (respectively 5.3 ± 0.8 and 5.7 ± 0.6) and higher C and N soil content (C: $6.0 \pm 4.7\%$; N: $0.5 \pm 0.3\%$). The cluster VIII also showed a good association with schistose bedrock and schist derived soils. Samples belonging to cluster V did not show well defined

characteristics. Of all the analysed variables only soil pH and N were significantly different between the clusters (ANOVA $P < 0.001$). Contrarily to what has been commonly observed for river (Soininen, 2007; Soininen et al., 2016) and lake (Blanco, 2014) diatom communities, the effect of electrical conductivity on soil assemblages is difficult to interpret, since the samples inside each cluster showed a very heterogeneous range of EC values. Bedrock geology and soil type were identified as having a minor effect on terrestrial diatom communities.

Fig. 2.3-b shows the most abundant species found in the eight clusters. The distribution of the species reflects that of the correspondent cluster, followed by the effect of land use, soil pH and C and N soil content on species abundance. The two subgroups were obtained considering the IPS related sensitivity value of each species, with species having $S \geq 4$ (more sensitive) plotting on the left side of the graph and species having $S \leq 2$ (less sensitive) plotting on the right.

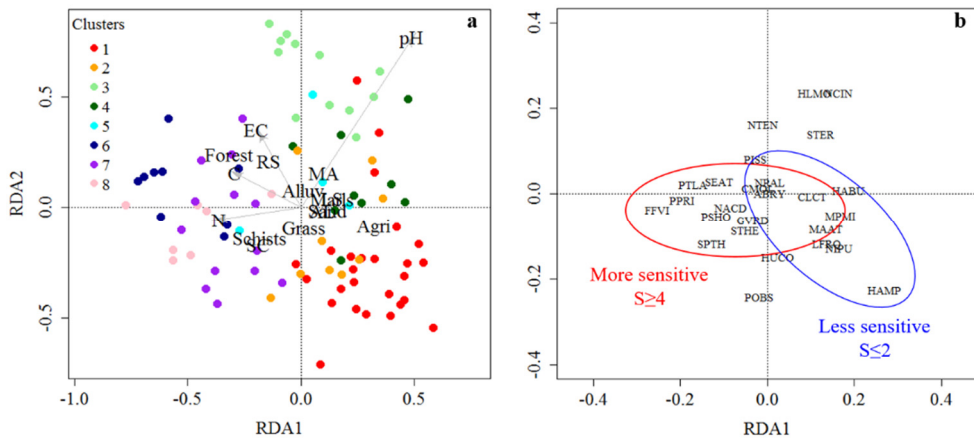
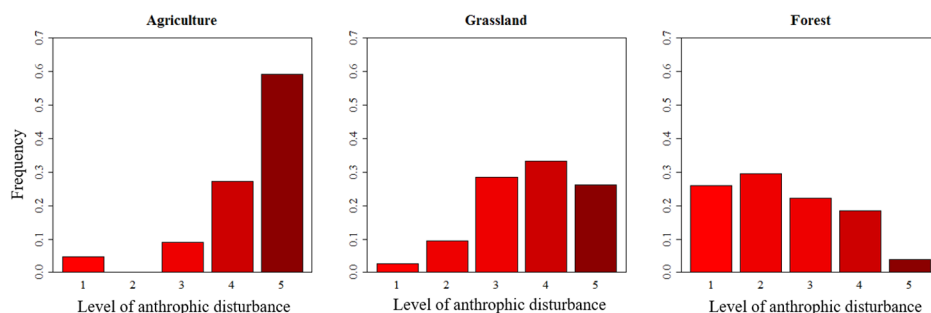


Figure 2.3: Redundancy Analyses (RDAs) bi-plots showing the relationship between terrestrial diatom communities (grouped based on SOM clusters) and environmental parameters (pH: pHCaCl₂; EC: electrical conductivity; N: total soil nitrogen; C: total soil carbon; Forest: forested land; Grass: grassland; Agri: farmland; Schists: schistose geology; Sand: sandstone geology; Alluv: alluvial deposit; Marls: marly geology; MA: silty-clay soils from marls; SC: Silty-Stony soils from schists; RS: Silty-stony soils from red sandstone; AL: Recent soils from alluvial valleys; LS: Sandy and loamy soils derived from sandstone) (a). In (b): the abundant species in the clusters (> 5% relative abundance). The two ellipses include the species with higher (red ellipse) or lower (blue ellipse) sensitivity values. See Table 2.1 for the diatom codes – species relationship.

2.3.3 Random forest model

The random forest model we used was based on 100 trees and had a R^2 of 0.9 for the learning dataset and 0.8 for the test dataset. The features importance (as defined in Breiman (Breiman, 2001)) in predicting the soil quality status was calculated for the different environmental variables. The highest score was attributed to pH (0.3) followed by land use, N and EC (all around 0.2). The other variables had lower scores (C and seasonality scored around 0.1, while pedological and geological features scored 0).

The relative frequency of the five anthropic disturbance categories (obtained from the calculated IPS values) in each type of land use is shown in Fig. 2.4. Passing from farmland to forested areas an increase in the frequency of categories 1 and 2 and a decrease of category 5 was noticed. The average pH value was generally lower in samples from areas exposed to less anthropic influence. However, significant differences in pH values between the five categories were only documented for forested areas ($P < 0.01$).



	Anthropic disturbance classes				
	1	2	3	4	5
Agriculture	5	/	5.8 ± 0.8	6.4 ± 0.8	5.9 ± 0.7
Grassland	7	6.0 ± 0.7	5.9 ± 0.7	6.3 ± 0.7	6.6 ± 0.7
Forest	5.1 ± 0.7	5.7 ± 0.9	6.9 ± 1.1	6.7 ± 0.8	7.5

Figure 2.4: Relative frequency of the five anthropic disturbance classes (1 to 5, low to high disturbance) for each type of land use. In the table are reported the average values of soil pH for the samples in each class.

2.4 Discussion

2.4.1 Environmental controls on terrestrial diatom communities and species sensitivity to disturbance

The RDA analysis showed that the environmental variables which mainly influenced the terrestrial diatom species distribution in our study area were soil pH and land use (the latter is also likely to influence the values of total C and N soil content, where lower percentages were found on farmland (Compton and Boone, 2000; Davidson and Ackerman, 1993)). Our findings are in agreement with other studies that recognised agricultural practices and soil tillage to influence soil nutrient content and pH and, consequently, diatom community structure (Hahn and Neuhaus, 1997; Heger et al., 2012; Stanek-Tarkowska et al., 2015; Stanek-Tarkowska and Noga, 2012; van Kerckvoorde et al., 2000; Zancan et al., 2006). Moreover, the influence of pH and human activities on diatom communities is well known and highly documented also in studies on fresh water diatoms (Hlúbiková et al., 2014; Lavoie et al., 2004; Liu et al., 2016; Rimet et al., 2004).

We found a clear distinction between clusters I, II and IV (agriculture and grassland, higher pH) and clusters VI and VIII (forested, lower pH) (Fig. 2.3-a). Those two groups of clusters were dominated by very different species, showing sensitivity to disturbance that was lower in the first group and higher in the second (Fig. 2.3-b). For example, a dominance of *Hantzschia amphioxys*, *Nitzschia pusilla* (Kützing) Grunow and *Hantzschia abundans* was found mainly in samples collected on farmland and grassland (clusters I, II and IV). Those species are classified as mainly occurring at pH values near 7 (Van Dam et al., 1994) and having high tolerance to disturbance (indicator value 'S' value between 1.2. and 2). The same species were found on soil treated under traditional tillage by Stanek-Tarkowska and Noga (2012). Similarly, species like *Pinnularia irrorata* Krammer and *Planothidium lanceolatum* (Brébisson ex Kützing) Lange-Bertalot were found to be frequent in forested areas of the catchment (Coles et al., 2016; Wetzel et al., 2013) (clusters VI and VII) and having a low tolerance to disturbance (S respectively 5 and 4.6). In samples from cluster III (forested areas with higher soil pH) and cluster VII (grasslands with lower soil pH), almost all dominant species showed a sensitivity value of 3, among which *Navicula cinta* (Ehrenberg) Ralfs in Pritchard and *Nitzschia acidoclinata* Lange-Bertalot were abundant. A similar result was found by Kelly et al. (2009) in fresh water environment, where species of the genera *Nitzschia* and *Navicula* were found abundant in areas with an intermediary disturbance (in their study, exemplified by the transition good/moderate status of the river).

2.4.2 Anthropogenic disturbance inferred from terrestrial diatoms

The results obtained from the random forest model indicated soil pH and land use as the most important factors in predicting sites with higher or lower anthropic impact in our study area. However, even if the pH was determined as the factor with the highest predictive importance, we found that there was a significant difference of pH values between the five quality categories only in forested areas

(Fig. 2.4). Indeed, the samples with higher human impact in forested areas (category 4 and 5) showed a higher pH and were mainly collected close to unpaved roads or in transition areas between forest and grassland. We obtained a good correspondence between the areas we expected to be more or less disturbed by anthropic activities (due to the abundance of very tolerant or very sensitive species) and the frequency of the different categories. Category 5 (high human impact) was the most frequent on farmland and categories 1 and 2 were the most frequent in forested areas (low human impact). Nevertheless, we also found an opposite trend in this case where one farmland site was classified as having a very good status (Fig. 2.4).

These results suggested that, while pH and land use have a proven influence in structuring diatom communities (in terrestrial, as well as in freshwater systems), it is not always the case when we attempted to predict the anthropic influence on a terrestrial site. These discrepancies are mainly due to our lack of knowledge of the ecological behaviour of terrestrial diatom species. For example, *Caloneis lancettula* was found to be abundant in samples from farmland and grassland despite being classified as a very sensitive species. This could suggest an adaptation of this species to grow on a disturbed soil, showing a lower sensitivity compared to that documented in fresh water. *Stauroneis parathermicola* was particularly abundant in a sample from farmland classified under quality category 1. However, *Stauroneis parathermicola* could not be included in the calculation of the IPS index (and thus of the anthropic disturbance categories), since it has no indicator value attributed and there is only little information about its ecology (Stanek-tarkowska et al., 2013). Another source of uncertainty is represented by the nomenclature and classification of the species, since different name attributions lead to different results in quality indices calculations (Dreßler et al., 2015; Kahlert et al., 2016, 2012).

2.5 Conclusions

In recent years, several pioneering studies exploring the potential for terrestrial diatoms to serve as hydrological tracers have been carried out in the Attert basin (Coles et al., 2016; Klaus et al., 2015; Martínez-Carreras et al., 2015b; Pfister et al., 2009).

As an extension to this exploratory work, we have tested the hypothesis that terrestrial diatom communities can be used as indicators of soil quality. As of today, the ecological status of soils is mainly inferred taking into account soil biological and chemical parameters (Bastida et al., 2008). The results of this study suggested that some of these parameters (i.e. soil pH, land use, total C and N soil content) have an influence in shaping the terrestrial diatom communities and that the species assemblages we found in our study area were able to provide information about different anthropic disturbance levels.

The results we obtained applying the IPS to soil diatom communities generally matched with our expectations (i.e. farmland sites classified as more impacted than forested sites). However, some of the species we found to be abundant in our study area could not be taken into account because of missing information on their ecological behaviour and sensitivity to disturbance.

In order to develop a soil quality index based on terrestrial diatom species we need to continue our research on the soil communities to better characterise the abundant species and improving our understanding of their interaction with the environment and reaction to anthropic disturbance (i.e. focusing on differences and variability of the communities in response to distinct farming practices).

Chapter 3

Exploring streamwater mixing dynamics via handheld thermal infrared imagery

Abstract

Stream confluences are important hotspots of aquatic ecological processes. Water mixing dynamics at stream confluences influence physio-chemical characteristics of the stream as well as sediment mobilisation and pollutant dispersal. In this study, we investigated the potential for handheld thermal infrared (TIR) imagery to provide rapid information on stream water mixing dynamics at small scales. In-situ visualisation of water mixing patterns can help reduce analytical errors related to stream water sampling locations and improve our understanding of how confluences and tributaries influence aquatic ecological communities. We compared TIR-inferred stream temperature distributions with water electrical conductivity and temperature (measured with a submerged probe) data from cross-channel transects. We show that the use of a portable TIR camera can enhance the visualisation of mixing dynamics taking place at stream confluences, identify the location of the mixing front between two different water sources and the degree of mixing. Interpretation of handheld TIR observations also provided information on how stream morphology and discharge can influence mixing dynamics in small streams. Overall, this study shows that TIR imagery is a valuable support technique for eco-hydrological investigation at small stream confluences.

This chapter is based on: Antonelli M, Klaus J, Smettem K, Teuling AJ, Pfister L. 2017. Exploring Streamwater Mixing Dynamics via Handheld Thermal Infrared Imagery. Water, 9, 358. <https://doi.org/10.3390/w9050358>.

3.1 Introduction

Water flow fields in rivers control the dispersal of solutes and pollutants, as well as the mobilisation of sediments – eventually influencing habitat variability and stream biodiversity (Kiffney et al., 2006; Power and Dietrich, 2002; Rice, 2017; Rice et al., 2008). Furthermore, proper consideration of water mixing dynamics near the surface is key for reducing errors in water sampling protocols and tracer experiments in small catchments and/or near stream confluences (Sanders, 1982; Sanders et al., 1977). Complete mixing of different water end-members stands as a fundamental assumption in classic hydrograph separation (Klaus and McDonnell, 2013). Likewise, it is a prerequisite for hydrometric measurements such as salt dilution gauging (Hongve, 1987). Streamwater samples can be strongly influenced by lateral inflows from soil or groundwater (Kemp and Dodds, 2001; Rademacher et al., 2005; Soulsby et al., 2005).

In experimental hydrology, stream temperature is widely recognised as an effective indicator of hydrological connectivity, water flow paths and hyporheic exchanges (Abbott et al., 2016; Birkinshaw and Webb, 2010; Hannah et al., 2008). In rivers, temperature exerts an important control on physiochemical characteristics of water (Webb et al., 2008) and it is a driver of numerous biological processes, controlling the structure of ecological communities and habitat complexity (Logez et al., 2013; Pletterbauer et al., 2015). Approaches for measuring stream water temperature cover a wide range of methods including temperature loggers and thermometers (Lewkowicz, 2008; Story et al., 2003; Sutton et al., 2007), fiber-optic distributed temperature sensing (FO-DTS) (J. S. Selker et al., 2006; Westhoff et al., 2011) and thermal infrared (TIR) cameras (Cardenas et al., 2011, 2008; Torgersen et al., 2001).

Among these measurement tools, TIR cameras are particularly suitable for the collection of temperature data at multiple spatial and temporal scales with high resolution (Dugdale, 2016; Handcock et al., 2012), overcoming the limitations of discrete measurements. To date, airborne and ground-based TIR imagery have been successfully used to describe longitudinal profiles of river temperature (Cherkauer et al., 2005; Dugdale, 2016; Dugdale et al., 2015; Fullerton et al., 2015), to provide information on soil moisture and surface saturation patterns (Glaser et al., 2016; Luscombe et al., 2015), to detect ground water exfiltration along the hillslope-riparian-stream continuum and inferring connectivity dynamics of water exfiltrating to the stream (Deitchman and Loheide, 2009; Eschbach et al., 2017; Pfister et al., 2010; Röper et al., 2013; Schuetz and Weiler, 2011). Furthermore, information obtained through TIR imagery has been used as a data source for hydrological model validation (Ala-aho et al., 2015; Glaser et al., 2016). Thus far, the potential for handheld TIR imagery to assess water mixing dynamics in small streams has not been fully assessed (Cardenas et al., 2011; Cristea and Burges, 2009; Schuetz and Weiler, 2011; Torgersen et al., 2001), with the vast majority of the studies relying on airborne TIR observations or reporting only some marginal observations specifically on water mixing. Most studies on water mixing at small scales rely on measurements of water temperature, electrical conductivity and flow velocities with probes placed at different depths in the water column (Gaudet and Roy, 1995; Lewis and Rhoads, 2015; Rhoads and Kenworthy, 1998; Rhoads and Sukhodolov, 2001). Ground-based TIR imagery could be a potentially useful method for supporting in-situ selections of

representative sampling locations – thereby reducing uncertainties inherent to fundamental mixing assumptions or water quality monitoring campaigns (Do et al., 2012; Sanders et al., 1977).

In this paper we investigate the potential for handheld TIR imagery to provide instantaneous mapping of stream water mixing patterns at or near the water surface. We test if thermal patterns observed at the stream surface adequately represent water mixing dynamics. More specifically, we investigate if mixing length, location and width of the mixing front and gradients of solute concentrations between different sources can be inferred from ground-based TIR images under low flow conditions in small streams.

First, we compare information extracted from the TIR observations with data of water electrical conductivity and temperature obtained with a submerged multi-probe from cross-channel transects, located downstream of two confluences in a natural and an urban setting. Next, we analyse and discuss the results to provide an overview of the possible advantages and disadvantages of the hand-held TIR technology.

3.2 Materials and Methods

3.2.1 Study sites

We selected two stream confluences in the Attert River basin (247.03 km² – located in the North-West of the Grand Duchy of Luxembourg) for our investigations (Fig. 3.1).

The confluence of the Koulbich and the Rennbach (natural stream confluence [NAT] – 49°48'42.4" N, 5°48'49.8" E) creeks corresponds to a symmetrical headwater junction located in a natural area – mostly dominated by forests further upstream. At the confluence, the two creeks flow through meadows directly on the schistose bedrock, characteristic of the northern part of the Attert River basin. Together with the coarse bedload sediment, this bedrock confers a highly irregular bed profile to the creeks.

The confluence of the Schwebich and the Wollefsbach (urban stream confluence [URB] – 49°45'51.3"N, 5°58'36.9" E) creeks corresponds to a channelized asymmetrical junction flowing through a small village. No accumulated material is present in the proximity of the junction and the stream bed has a regular trapezoidal cross section.

In both sites we observed a difference in water depth of the two streams before the junction. The Rennbach (mid-point depth: ~5-8 cm) and the Schwebich (mid-point depth: ~20-22 cm) were deeper than the Koulbich (mid-point depth: ~2-5 cm) and the Wollefsbach (mid-point depth: ~5 cm), respectively.

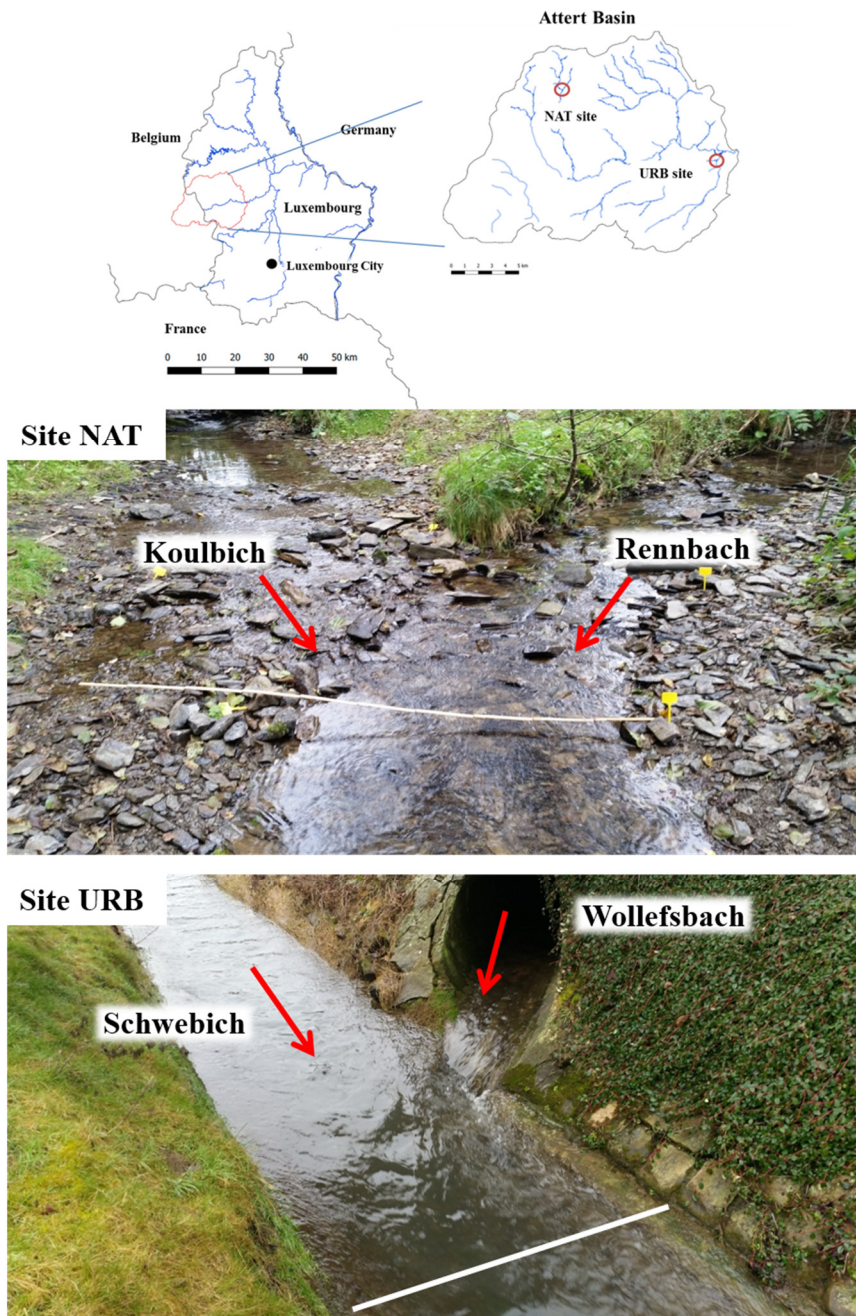


Figure 3.1: Location (map) and overview (pictures) of the study sites. Top: location within Luxembourg and the Atttert basin. Middle: overview of the natural stream confluence (NAT site). Bottom: overview of the urban stream confluence (URB site). Location of crossing transect A is displayed on both pictures (NAT site: folding meter ruler; URB site: bold white line). The pictures were collected on the 28 September 2016 at the NAT site and on the 2 of February 2017 at the URB site (pictures: M. Antonelli).

3.2.2 Field measurements

During storm events, surface roughness, deeper water columns as well as stream temperature homogenisation due to precipitation tend to influence the applicability of remotely sensed data (Dugdale, 2016; Dugdale et al., 2013). Consequently, because we are making these measurements for the first time we concentrated on winter low flows, when these disturbances were small and temperature contrasts more pronounced. In the investigated catchments, these particular flow conditions are equivalent to summer low flow.

We measured discharge, water electrical conductivity (EC) and water temperature on four days (21 and 28 September, 17 November and 1 December 2016) at the NAT site and on two days (2 and 9 February 2017) at the URB site. Although we had carried out a significantly larger number of TIR observations at the two sites (on the 21 and 27 October 2016 and 10 and 24 November 2016 at the NAT site and on the 17 and 27 January 2017 at the URB site), on the aforementioned six dates the temperature contrast between the tributaries was found to be particularly suitable for our TIR observations.

Water EC and temperature were measured using a conductivity meter WTW Multi 3420 equipped with a TetraCon 925 probe (Xylem Analytics, Weilheim, Germany), providing a conductivity resolution of 0.1 $\mu\text{S}/\text{cm}$ from 0 to 199 $\mu\text{S}/\text{cm}$ and 1 $\mu\text{S}/\text{cm}$ from 200 to 1999 $\mu\text{S}/\text{cm}$; and a temperature resolution of 0.1 from -5 to 100 °C. Measurements were taken every 5 or 10 cm along three cross-channel transects, at 1.5 m (transect A), 3 m (transect B) and 9 m (transect C) downstream of the junctions. Measurements were made at the stream bottom and, when the water was deep enough (i.e., ≥ 8 cm due to the probe's sensor length), also near the surface. Streambed cross-sectional depth profiles were obtained for the transect locations at both sites.

We measured stream discharge up- and downstream of the junction using the salt dilution method at the NAT site and from stream gauges at the URB site (estimated from water level data via a rating curve). Air temperature was obtained from meteorological stations operated by the Ministry of Agriculture and located in the vicinity of our experimental sites (~2 km between the meteorological station and the NAT site and ~1 km between the meteorological station and the URB site).

3.2.3 TIR image acquisition

We collected TIR images from both study sites using a handheld FLIR TIR camera (FLIR T640, FLIR Systems, Wilsonville, OR, USA). With this technology, the radiation emitted by an object's surface (i.e., the first 0.1 mm of the water surface in this study) can be quantified and converted into visible temperature patterns in thermal images. The camera used produces thermal images of 640 x 480 pixels over a spectral range of 7.5 to 14 μm . Its temperature range is -40 °C to 2000 °C, with a thermal sensitivity of <0.035 °C at 30 °C.

Before acquiring the images it is necessary to provide the camera with information about object emissivity " ϵ " (usually set between 0.95 and 0.97 for freshwater), atmospheric temperature, air humidity, object's distance from the camera and reflected ambient temperature (FLIR Systems, 2010). The employed

camera automatically corrects the detected temperature for the aforementioned parameters. TIR images were taken in each transect simultaneously to the other measurements (Figure 3.2 A).

The images were taken by positioning the handheld camera perpendicular to the stream section under study and trying to cover the widest possible width with a single image. Since our purpose was to extract temperature cross-sectional distributions from the thermal images, we avoided using the panoramic picture mode, where shifts in absolute temperature can occur between contiguous images as a product of the camera's non-uniformity correction (Dugdale, 2016). Moreover, both confluences were chosen in cleared areas in order to avoid tree shading effects which can influence the temperature detection.

In order to understand if distance to complete mixing (i.e., the distance downstream from the confluence where no differences in water EC could be detected along a stream cross-section and in the water column) can be assessed from TIR in-situ observations, we walked downstream from the confluences during the different sampling dates, monitoring the streams with the TIR camera until no difference in temperature could be detected between the stream banks. Ground measurements of water EC and water temperature were then carried out at the same distance downstream from the confluence where no temperature difference was detectable between the stream banks using the TIR camera.

A summary of air temperature values (daily average), stream discharge, relative difference in temperature and EC between the tributaries, distance to complete mixing for the different sampling days and the stream temperature at that location are listed in Table 3.1. Information on the sub-basin area at the two confluences, cross-section geometry at the transects, stream bed roughness and tracer velocities are also reported. Examples of stream depth cross-sectional profiles are shown in Figure 3.2 B (the two examples are representative of the depth profiles along the transects in the NAT site and the URB site).

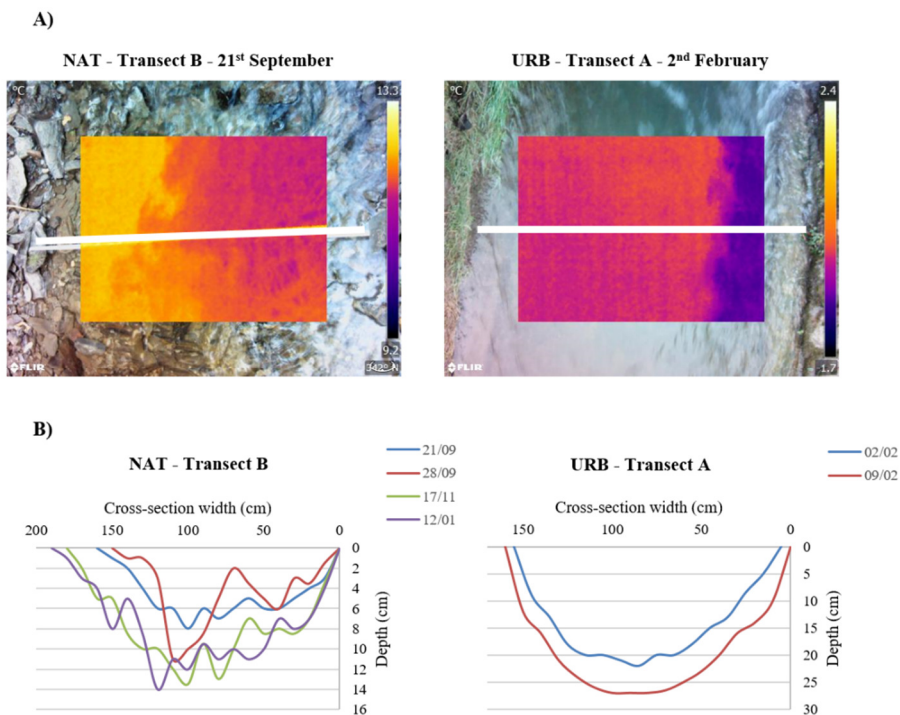


Figure 3.2: Cross-sectional characteristics. A) Examples of TIR images collected at two cross-sectional transects. Note that the TIR images cover a smaller domain for illustrative purposes; when possible, we covered the widest transect width with a single TIR image (pictures: M. Antonelli). B) Stream depth profiles at the two cross-sectional transects. In the NAT site, the width of the stream at the transects increased with increasing discharge, expanding exclusively on the left side of the stream. The presence of coarse sediment in the stream makes the depth profiles at the same location highly variable. In the URB site, the stream width increased with increasing discharge expanding uniformly on the left and right bank.

Table 3.1: Summary of environmental parameters and stream characteristics relative to the two study sites. Manning's n for channels (Chow, 1959) is reported for Mountain streams, no vegetation in channel, banks usually steep, trees and brush along banks submerged at high stages (a. bottom: gravels, cobbles, and few boulders) (*) and Lined or Constructed Channels (h. Dressed ashlar/stone paving) (**). Tracer velocity has been measured in the streams at locations directly upstream the junctions. Velocity values are reported for days of lower discharge (21/09/2016 for the NAT site and 02/02/2017 for the URB site) and higher discharge (17/11/2016 for the NAT site and 09/02/2017 for the URB site).

		NAT Site				URB Site	
		21 Sep '16	28 Sep '16	17 Nov '16	01 Dec '16	02 Feb '17	09 Feb '17
	Air temp (°C)	13.9	13.7	7.9	-0.4	5.2	0.6
Discharge (L/s)	Rennbach	4.7	2.8	19.0	17.7	Schwebich 131	203
	Koulbich	3.6	2.6	13.2	15.9	Wollefsbach 30	42
	Downstream	8.5	5.0	31.0	29.4	Downstream 161	245
	Distance to complete mixing (m)	9.0	12.0	29.5	19.5	82	47
	Stream temperature (°C) at complete mixing	13.1	11.5	7.6	2.1	4.9	4.5
	Δ Temperature tributaries (°C)	0.8	1.3	0.3	0.3	1.0	0.5
	Δ EC tributaries (μS/s)	35	32	65	55	97	65
Sub-basin area (Km ²)	Rennbach	4.8				Schwebich 22.2	
	Koulbich	4.9				Wollefsbach 4.4	
	Cross-section geometry	Semi-circular/highly irregular				Trapezoidal/ semi-circular	
	Bed roughness	0.03-0.05 *				0.013-0.017 **	
Tracer velocity (m/s)	Rennbach	0.07	/	0.14	/	Schwebich 0.22	0.34
	Koulbich	0.19	/	0.08	/	Wollefsbach 0.24	0.46

3.2.4 Data processing and analyses

Temperature cross-sectional distributions were extracted from the thermal images using the FLIR ResearchIR software (Fig.3.3). We applied cubic spline smoothing (Green and Silverman, 1994) on EC, temperature and TIR-inferred temperature data collected along the different transects. We tested the correlation between the original data and the smoothed distributions through correlation analysis and analysis of the residuals. This approach allowed us to highlight curve trends and simplify the comparison between the information from the EC and temperature measurements and the TIR-inferred temperature.

The inflection point on the smoothed curves indicates the point along the transects where the main shift between two different water sources occurs (mixing front). Analogously, we use the width of the slope surrounding the inflection point as an indicator of the portion of the transect where the mixing preferentially occurs (mixing width). This portion is where stream water EC and temperature start to show differences from the EC and temperature of the two original sources.

We defined the main slope of the curve as the section with a gradient of at least 50% of the curve's maximum gradient. We choose this threshold to account for the inherent variability of the curves' profiles. The main slope and the inflection point were estimated from the first and second derivative, respectively, which were calculated using a finite difference approximation of the smoothed curves.

To test if gradients of solute concentration between different sources can be inferred from ground-based TIR images, we quantified the relation between the curves of EC, temperature and TIR temperature using correlation analyses. Then we compared the location of the mixing front and the mixing width inferred from all the curves (along all the cross-sectional transects for each sampling date at both study sites).

The data smoothing and the correlation analyses were carried out in R 3.2.2 (R Core Team, 2015).

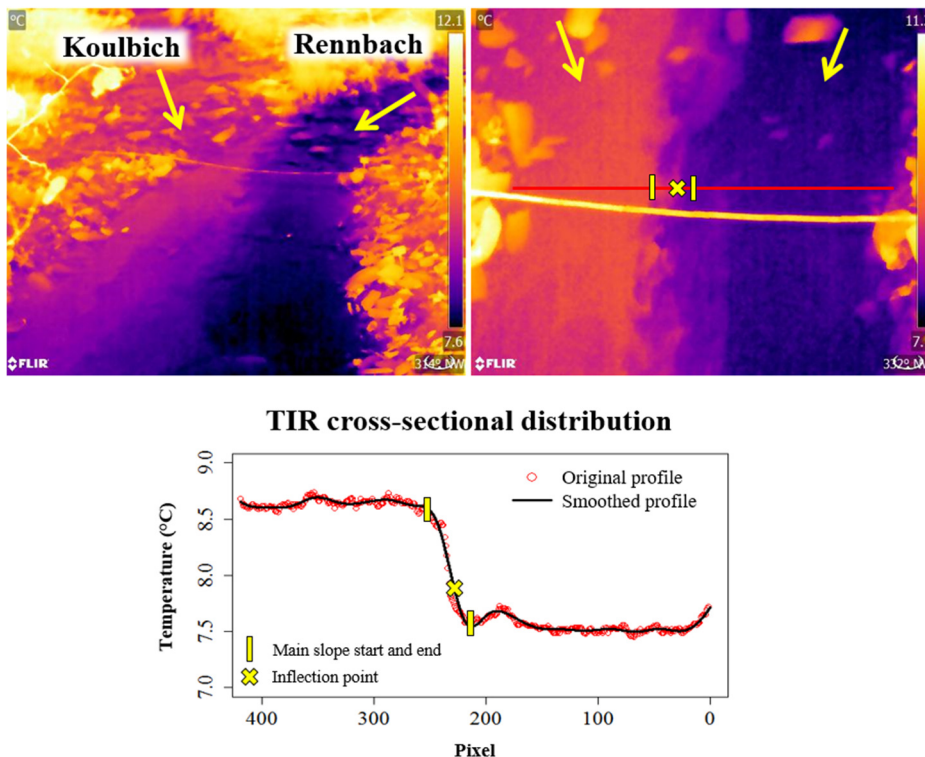


Figure 3.3: Illustration of the analysis procedure. TIR images (top panel) and cross-sectional temperature distribution as collected in the individual transects. The shown temperature distribution was extracted from the image collected on the 28th September at the NAT site (transect A) (pictures: M. Antonelli).

3.3 Results and Discussion

3.3.1 Consistency between temperatures “sensed” with the TIR camera and a submerged probe

Stream water temperatures detected by the TIR camera did not exactly match the temperature probe measurements. The temperature difference ranged between 1 and 2.8 °C on days of higher air temperature (21 and 28 September) and between 3.8 and 5.4 °C on days with lower air temperature (17 November, 1 December and 2 and 9 February). We identified several potential reasons that might cause these discrepancies in temperature measurements: (1) while the camera is only ‘sensing’ long-wave radiation emitted by the surface of the water column (0.1 mm depth), the probes need to be totally submerged and therefore represent temperature over a depth of 4 cm; (2) the camera hardware appeared to be sensitive

to external temperatures – the difference in temperatures ‘sensed’ by the TIR imagery and measured with the submerged probe was significantly enhanced during days with low air temperature.

Despite the aforementioned differences between temperatures measured with the TIR camera and the probe, the relative temperature difference determined between the tributaries was identical for both devices, with a maximum difference of 0.8 °C (again, occurring on the day with colder air temperature – 1 December).

3.3.2. Inferring complete mixing from TIR stream observations

The environmental parameters measured during the different sampling days at the two sites (summarised in Table 3.1) helped us to partition our observations into two different hydrological conditions. During the first two sampling dates for the NAT site (the 21 and 28 September 2016) and the first sampling date for the URB site (the 2 February 2017) we observed higher air and stream temperature, together with higher temperature contrasts between the tributaries and lower stream discharge than during the other sampling dates (17 November and the 1 December 2016 for the NAT site and the 9 February for the URB site). At the NAT site the length to complete mixing increased with increasing stream discharge, while it decreased with increased stream discharge at URB. Nevertheless, the distance to complete mixing can be influenced by a number of factors, such as stream discharge, stream bed morphology and particular features as riffles and pools and water density (Best, 1987; Lewis and Rhoads, 2015).

Information on complete mixing inferred from monitoring the stream with the TIR camera was found to be discordant with the information from the water EC values measured in the stream. In most cases, homogeneities in temperature were detected by the TIR camera and the temperature probe before EC complete mixing was reached. This discordance can be due to the different magnitude of in stream EC and temperature differences between the two tributaries (EC relative difference between the streams was always higher than the difference in temperature) combined with the measurement resolution of the probe and the TIR camera. In our case, we could obtain finer measurements of stream water EC than of temperature both from TIR observations and measured with the probe. Ultimately, this may jeopardize the detection of temperature differences at downstream locations where differences in EC would still be measurable. Indeed, the best match in the measurements of TIR-inferred temperature and water EC was observed in two cases: the 28 of September in the NAT site and the 2 of February for the URB site. During those dates we recorded the highest temperature contrast between the tributaries at both sites and a nearly total absence of waves on the water surface. The lower emissivity that characterizes rippled water surfaces influences the temperature measurements made with a TIR camera (Cardenas et al., 2011; Torgersen et al., 2001). Even when there are strong temperature contrasts between two water sources, surface roughness may complicate the in-situ interpretation of TIR images and ultimately the inference of reliable distances to complete mixing.

3.3.3. Comparison between stream EC and temperature inferred from submerged probe and TIR-inferred water surface temperature

The correlation between the original measured data and the curves obtained via smoothing techniques was generally good (Pearson's $R^2 > 0.83$). Surface water TIR distributions showed a good correlation with the measurements of water EC and temperature (Pearson's $R^2 > 0.85$) in particular at the NAT site along the transect A (Figure 3.4) and B, located closer to the junction. At the URB site, the best correlation was found during the first sampling day, especially for transect C, located furthest from the junction. When poor correlation occurred, it was often associated with a combination between poor temperature contrast and surface roughness (mainly related to the presence of surface waves). Nevertheless, in the NAT site, transect C was the one placed in the cross-section presenting the highest superficial roughness (mainly due to the streambed morphology at that location), while in the URB site, the majority of the roughness was located closer to the junction, caused by the presence of the junction itself (Figure 3.4). Moreover, at transect A (URB) we observed during both sampling days the highest vertical differences in EC and temperature measurements between the bottom and the surface of the water column. The water from the shallowest tributary (Wollefsbach) tended to flow on top of the deepest tributary (Schwebich), especially during the day of lower discharge (2 February) (Cristea and Burges, 2009). Despite flow pattern complexities at this location, the TIR cross-sectional distribution showed modest correlation with the distribution of EC and temperature measured at the surface ($R^2 = 0.70$ and $R^2 = 0.59$, respectively).

Other sources of poor correlation were to attribute to the presence of an "aura" in some TIR images surrounding the digital image (probably due to sensor noise), which noticeably influenced the extraction of the TIR data for the images collected on the 17 November in the NAT site (Figure 3.5) and to reflection from the river banks (which occurred in particular on the 9 February at the URB site). In this case, cross-sectional distributions affected by these sources of error have been corrected by excluding the area influenced by the error (usually places at the extremities of the distribution).

Table 3.2 shows the absolute distance (in cm) between the location of the mixing front calculated from the TIR cross-sectional distributions and the other parameters (water EC and temperature measured at the streambed and surface) for both dates along all transects at each site. Overall, 71% of the times the TIR observations placed the mixing front at less than or equal to 30 cm from the location inferred through water EC or temperature. In 43% of these cases the distance was less than 10 cm. Differences higher than 30 cm have been detected especially during days when the two tributaries had the lower relative difference in temperature and the higher relative difference in EC (i.e., 17 November at the NAT site and the 9 February at the URB site). As mentioned earlier, the resolution of the different instruments could affect inter-comparison of the different measurements. For example, we expected the information provided by the camera to have a higher similarity (in terms of correlation and mixing front location) to water temperature (measured with the probe) than to EC. Nevertheless, in some cases the smoothing technique (and the consequent calculation of inflection point and main slope of the curve) did not work properly on the temperature probe data. This may be due to the fact that, when the temperature difference between the tributaries is small, the

resolution of the probe (0.1 °C) is too low causing the smoothing to fail (regardless of the number of original data points considered in the analysis).

Figure 3.4 (next page): Example of stream conductivity and temperature. Upper and middle panels: stream EC and temperature (measured at the stream bottom – “bottom” – and near the surface – “top”). Lower panel: TIR–inferred temperature distributions. At the NAT site (21st September) we found a good correlation between the TIR distribution and stream EC ($R^2 = -0.96$) and temperature data ($R^2 = 0.96$) (on this date, collected only on the bottom because of low water depth). At the URB site (2nd February) we found a poor correlation between the TIR distribution and stream EC (bottom: $R^2 = 0.49$; top: $R^2 = 0.70$) and temperature data (bottom: $R^2 = 0.47$; top: $R^2 = 0.59$). For the temperature data measured near the stream surface (URB site) it was not possible to determine a univocal inflection point.

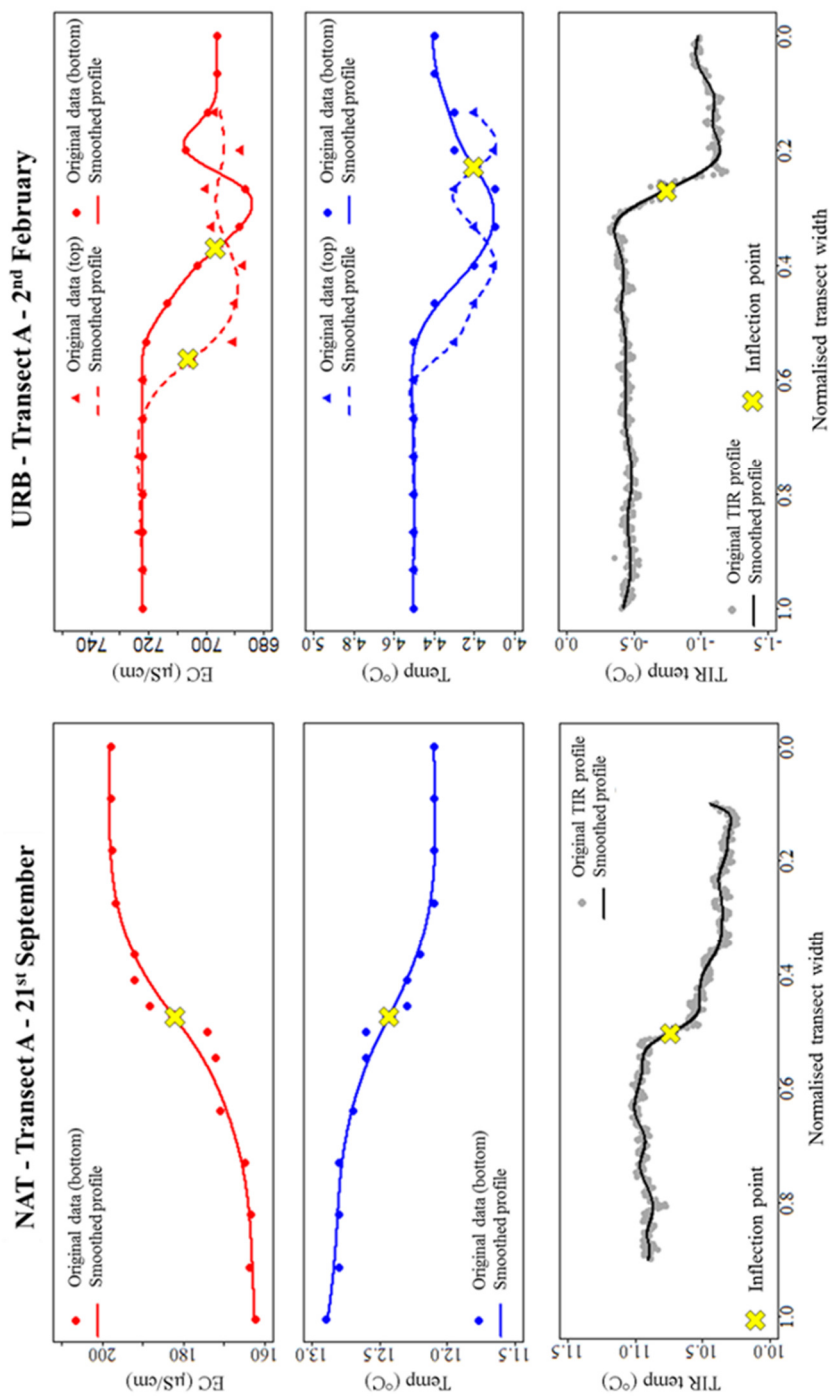


Figure 3.4 – see figure caption on previous page.

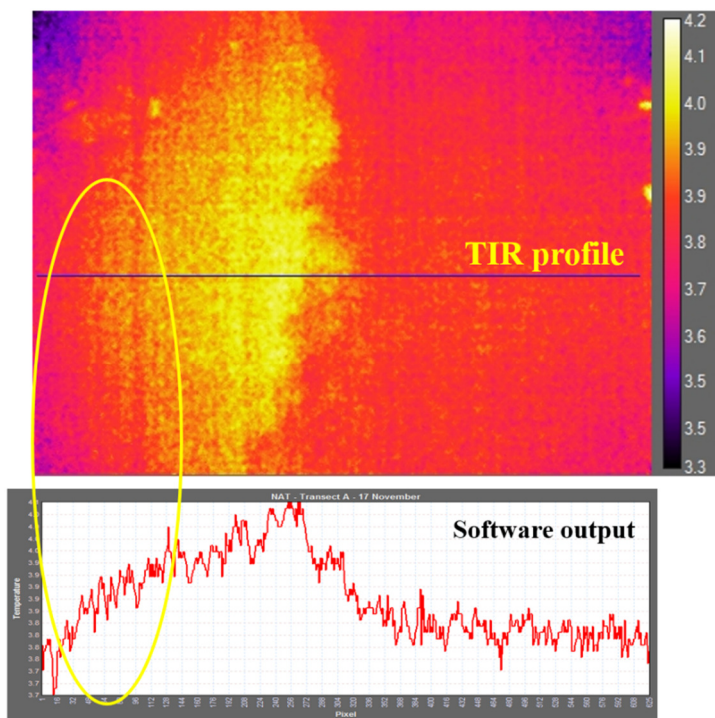


Figure 3.5: Illustration of circular “aura” effect. The “aura” is visible at the edges of the TIR image (NAT – Transect A – 17th November) and directly affects the extraction of TIR temperature cross-sectional distributions (as can be seen in the software output).

Table 3.2: Absolute distance (in cm) between the location of the mixing front calculated through the TIR-inferred temperature distributions and the other parameters (water EC and temperature measured at the stream bottom and surface). No value fields in the NAT and URB tables indicate that water depth was too low for obtaining measurements near the water surface or cases where it was not possible to determine a univocal inflection point from the smoothed curve. Color code: white: distance ≤ 10 cm; blue: distance ≤ 20 cm; green: distance ≤ 30 cm; red: distance > 30 cm.

NAT site					URB site				
A					A				
	EC		Temp			EC		Temp	
	Bottom	Top	Bottom	Top		Bottom	Top	Bottom	Top
21/09/16	3.0		3.2						
28/09/16	0.7	4.0	1.0	0.1					
17/11/16	0.7	18.0	35.9	17.0					
01/12/16	3.3	17.9	17.9	17.8					
B					B				
	EC		Temp			EC		Temp	
	Bottom	Top	Bottom	Top		Bottom	Top	Bottom	Top
21/09/16	6.8		4.9						
28/09/16	21.8	30.4	24.5	33.0					
17/11/16	32.0	33.4	30.0	28.9					
01/12/16	7.0	6.3	4.0						
C					C				
	EC		Temp			EC		Temp	
	Bottom	Top	Bottom	Top		Bottom	Top	Bottom	Top
21/09/16	43.0		29.3						
28/09/16	8.8		12.8						
17/11/16	49.3	64.1	64.1	36.5					
01/12/16	8.8	1.6	22.5	15.8					
					A				
					EC		Temp		
					Bottom	Top	Bottom	Top	
02/02/17					15.0	44.7	5.9		
09/02/17					59.9	63.0	99.2	24.5	
					B				
					EC		Temp		
					Bottom	Top	Bottom	Top	
02/02/17					8.6	27.8	29.2	23.3	
09/02/17					13.6	36.1	7.7	11.9	
					C				
					EC		Temp		
					Bottom	Top	Bottom	Top	
02/02/17					34.9	27.7	52.2	32.3	
09/02/17					18.5	25.8	62.1	22.9	

3.3.4 Influence of discharge and streambed morphology on location of the mixing front and mixing width

For both study sites, we did not detect a clear relationship between the mixing width (i.e. the portion along the transects where mixing preferentially occurs, expressed here as a percentage of the total transect width) and stream discharge (Fig. 3.6). For this analysis, we accounted only for cases where a good correlation between the TIR–inferred temperature distribution and water EC and temperature had been observed. In the NAT site, the mixing width generally increased with increasing distance from the stream junctions, while in the URB site this trend was less evident (Fig. 3.6). For both sites, the mixing width retrieved from the TIR distributions was usually shorter than the one inferred from water EC and temperature, especially when measured at the stream bottom. Mixing dynamics taking place in the water column could not unequivocally be translated into clear thermal patterns near the water surface. Indeed, the TIR–inferred mixing widths turned out to be more similar to those calculated from water EC and temperature distributions measured near the stream surface.

Transect length and stream water depth increased with rising discharge at both sites. However, regardless of discharge values, the mixing front was located mainly on the right side of the stream (looking upstream) in both study sites. At the NAT site, stream bed morphology may control the location of mixing fronts. For example, the right tributary (Rennbach) and the right side of the stream after the junction were found to be deeper than the left side. In this case, water from the shallower tributary could tend to flow on top of water flowing from the deeper one (Gaudet and Roy, 1995). Eventually this may result in a shift of mixing areas towards the right side of the stream, although the confluence has a symmetrical shape. In the URB site, characterised by a paved stream bed, the predominant right–side location of the mixing front may reflect the hydrological conditions of the stream together with the considerable depth difference between the two tributaries and their junction angle.

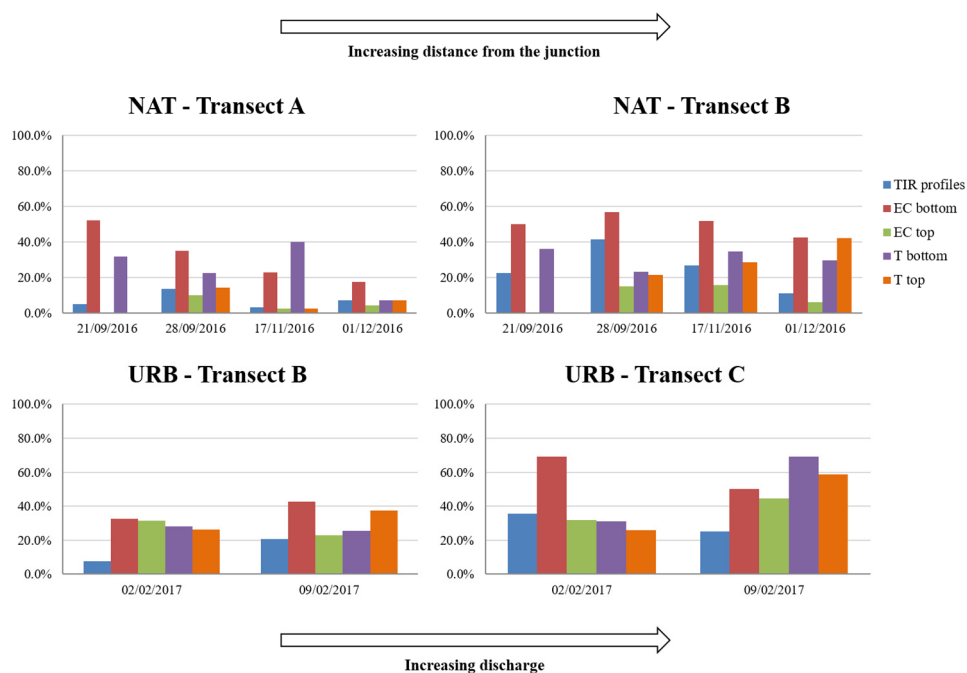


Figure 3.6: Mixing widths for different stream cross-channel transects. The mixing widths were calculated from the curves obtained via data smoothing of TIR-inferred stream temperature and water EC and temperature measured at the bottom and near the surface, and are expressed as percentage of the total transect width. No value fields in the NAT graphs indicate that water depth was too low for obtaining measurements near the water surface.

3.4 Conclusions

In two contrasting experimental sites, we have documented how water surface temperature data obtained from handheld TIR cameras compares to in-stream EC and temperature data. A common feature to all our TIR observations is that cross-sectional variability in surface temperature reflects in-stream temperature and chemistry variability. This relationship is even stronger when temperature contrasts are high between two tributaries and superficial roughness is low at the observed cross-section.

We have shown that ground-based TIR imagery provides valuable information for rapid *in-situ* visualisation of water mixing and mixing dynamics at the scales represented in this study. In particular, we were able to identify the position of the mixing front along the stream cross-sections and the distance to complete mixing, especially when the TIR images were acquired under favourable conditions.

More research is needed before one can unequivocally determine distance to complete mixing through TIR imagery. Future work should focus on the effects of low temperature contrasts and water surface roughness, which can directly influence temperature measured by TIR cameras. Additional investigations may also explore

further the potential for TIR observations to characterise streambed morphology and discharge controls on water mixing dynamics.

Stream confluences represent important eco-hydrological hotspots, where water with potentially different physio-chemical characteristics mixes along an interface (Krause et al., 2017). Our methodology using ground-based TIR imagery could be a valuable support tool for eco-hydrological studies interested in identification of changing environmental conditions around confluences (Rice et al., 2008). The use of a handheld TIR camera allows visualisation of this mixing process as it evolves from clear separation of tributary sources at the confluence to complete mixing further downstream.

Handheld TIR approach as presented in this study could aid optimization of water sampling procedures for qualitative and quantitative hydrological analyses at the proximity of confluences, by assisting in the determination of in-stream representative sampling locations (Do et al., 2012; Sanders et al., 1977). Handheld TIR observations of water mixing could also provide insights on the dispersal dynamics of suspended sediments and dissolved substances at confluences (Best, 1987; Boyer et al., 2006).

In order to improve validation of the method, we are now undertaking additional work with *in-situ* TIR cameras to improve the handheld TIR imagery approach under changing hydrological conditions.

Chapter 4

Technical note: Mapping surface saturation dynamics with thermal infrared imagery

Abstract

Surface saturation can have a critical impact on runoff generation and water quality. Saturation patterns are dynamic, thus their potential control on discharge and water quality is also variable in time. In this study, we assess the practicability of applying thermal infrared (TIR) imagery for mapping surface-saturation dynamics. The advantages of TIR imagery compared to other surface saturation mapping methods are its large spatial and temporal flexibility, its non-invasive character, and the fact that it allows for a rapid and intuitive visualization of surface saturated areas. Based on an 18-month field campaign, we review and discuss the methodological principles, the conditions in which the method works best, and the problems that may occur. These considerations enable potential users to plan efficient TIR imagery-mapping campaigns and benefit from the full potential offered by TIR imagery, which we demonstrate with several application examples. In addition, we elaborate on image post-processing and test different methods for the generation of binary saturation maps from the TIR images. We test the methods on various images with different image characteristics. Results show that the best method, in addition to a manual image classification, is a statistical approach that combines the fitting of two pixel class distributions, adaptive thresholding, and region growing.

This chapter is based on: Glaser B, Antonelli M, Chini M, Pfister L, Klaus J. Technical note: Mapping surface-saturation dynamics with thermal infrared imagery. 2018. Hydrology and Earth System Sciences, 22(11), 5987–6003. <https://doi.org/10.5194/hess-22-5987-2018>.

4.1 Introduction

The patterns and dynamics of surface saturation areas have been on hydrological research agendas ever since the formulation of the variable source area (VSA) concept by Hewlett and Hibbert (1967). Surface saturation is relevant for runoff generation and for water quality, due to variable active and contributing areas (Ambrose, 2004) as well as critical source areas (e.g. Doppler et al., 2014; Frey et al., 2009; Heathwaite et al., 2005). Likewise, surface saturation patterns and their dynamics are closely linked to groundwater–surfacewater interactions (e.g. Frei et al., 2010; Latron and Gallart, 2007) and catchment storage characteristics and dynamics (e.g. Soulsby et al., 2016b; Whiting and Godsey, 2016).

Despite the prominent role of saturated areas in hydrological processes research, mapping them remains a challenging exercise. The most straightforward mapping method consists of locating saturated areas by walking through the catchment. However, this simple but labour-intensive “squishy boot” method (e.g. Blazkova et al., 2002; Creed et al., 2003; Latron and Gallart, 2007; Rinderer et al., 2012) is neither suitable for large areas nor for fine-scale spatial resolutions. Dunne et al. (1975) introduced topography, soil morphology, hydrometric measurements (soil moisture, water table level, base flow), and vegetation as useful indicators for delineating saturated areas. Today, it is still a valid research question of how to best make use of these catchment characteristics to delineate saturated areas (e.g. Ali et al., 2013b; Doppler et al., 2014; Grabs et al., 2009; Kulasova et al., 2014a, 2014b). Hydrometric measurements offer the potential for monitoring the local temporal evolution (in increments ranging from minutes to months) of dynamic surface saturation. The analysis of topography, soil morphology, or vegetation allows lasting saturation patterns to be identified for large contiguous areas.

Remote sensing has proven to be well-suited for mapping temporal dynamic patterns of surface saturation over large areas. It is possible to extract flooded areas in the order of metres to kilometres from data acquired with satellite and airborne platforms, such as synthetic aperture radar (SAR) images (e.g. Matgen et al., 2006; Verhoest et al., 1998), or the normalized difference water index (NDWI) and the normalized difference vegetation index (NDVI; De Alwis et al., 2007; Mengistu and Spence, 2016). Observations at higher spatial resolutions (order of centimetres) require unmanned aerial vehicles (UAVs) or ground-based instruments. Due to various technical constraints, to date, SAR image acquisitions are rarely used for UAV-based applications or for ground-based applications that are not restricted to a fixed location (e.g. Li and Ling, 2015; Luzzi, 2010). NDWI and NDVI are applicable at these scales (e.g. Orillo et al., 2017; Wahab et al., 2018), however, to the best of our knowledge, the necessary simultaneous acquisition of short-wave infrared and visible light (VIS) images has not yet been performed by UAVs or on the ground for mapping surface saturation.

Ishaq and Huff (1974) and Dunne et al. (1975) suggested the use of VIS or infrared photographs for mapping surface saturation. However, this suggestion has rarely been followed in the last 40 years (with Portmann, 1997, being a notable exception), despite VIS cameras having been deployed on the ground and mounted on UAVs, airborne platforms, or satellite platforms for a long time. Recently, Chabot and Bird (2014) and Spence and Mengistu (2016) successfully used VIS cameras mounted on UAVs for mapping surface water (a wetland of 128 ha and an

intermittent stream surveyed via three transects of 2 km each). Silasari et al. (2017) mapped surface-saturated areas on an agricultural field (100m x 15 m) using a VIS camera mounted on a weather station for high-frequency image acquisition.

Since the advent of affordable, handheld thermal infrared (TIR) cameras, TIR imagery features the same temporal and spatial flexibility as VIS imagery. In the context of this technical advancement, TIR imagery started to be used for analysing hydrological processes such as groundwater surface-water interactions (e.g. Alahho et al., 2015; Briggs et al., 2016; Pfister et al., 2010; Schuetz and Weiler, 2011) or water flow paths, velocities, and mixing (e.g. Antonelli et al., 2017; Deitchman and Loheide, 2009; Schuetz et al., 2012). However, applications of TIR imagery for mapping surface saturation are rare. Two examples are from Pfister et al. (2010) and Glaser et al. (2016), who demonstrated the potential for TIR imagery to map surface saturation by carrying out repeated TIR image acquisitions at small spatial scales (centimetres to metres) with handheld cameras.

One reason for the scarce number of studies that use TIR imagery for mapping surface saturation is certainly that few descriptions of the methodological advantages and challenges exist. However, there are several general guidelines and methodological descriptions for TIR imagery applications. These studies focus on one specific aspect of TIR imagery, such as co-registration (Turner et al., 2014; Weber et al., 2015) or on how to acquire correct surface water temperatures, which is the most common application of TIR imagery in hydrology (e.g. Dugdale, 2016; Handcock et al., 2012, 2006; Torgersen et al., 2001). Many of these recommendations can be directly applied for mapping surface saturation via TIR imagery (e.g. choice of sensor type). However, some recommendations are redundant (e.g. temperature corrections) or different (e.g. optimal time scheduling) for the application of TIR imagery for surface saturation mapping.

Here, we go beyond the mere demonstration of the potential for TIR imagery to map saturated surface areas and address the related application-specific technical and methodological challenges. The novelty of this work is that we assimilate, within one study, fundamental principles, technical aspects, and methodological possibilities and challenges with an exclusive focus on the mapping of surface saturation. This includes all steps, from image acquisition to the generation of binary saturation maps. To do this, we (1) review relevant technical and methodological aspects from existing TIR imagery literature and (2) complement them with our expertise and results from an 18-month field campaign.

The field campaign focused on the recurrent acquisition of panoramic images with a portable TIR camera in seven distinct riparian areas. The precautions and considerations that we describe in this technical note are also valid for surface saturation mapping campaigns with permanently installed ground-based TIR cameras and TIR cameras mounted on UAVs and airborne or satellite platforms.

The paper is structured in two main parts. The first part (Sect. 2) focusses on the mapping approach itself and combines a literature review with examples of our own experience. The second part (Sect. 3) demonstrates the application of different pixel classification techniques for generating binary saturation maps from TIR images by applying and comparing them for different example images. A discussion and a conclusion section evaluate the key features of the paper and outline perspectives for future research and applications for TIR imagery in hydrological sciences.

4.2 Mapping surface saturation with TIR imagery: state of the art and examples

4.2.1 Fundamental principles

TIR cameras are used for measuring surface temperatures remotely (e.g. 100 μm penetration depth for water columns) within an area of interest. The cameras sense the intensity of thermal infrared radiation emitted by the objects the camera is pointed at. The surface temperature T (K) of the objects is then calculated from the sensed radiant intensity W (Wm^{-2}), based on Stefan-Boltzmann's law with the Stefan-Boltzmann constant $\sigma = 5.67 \cdot 10^{-8} \text{ Wm}^{-2}\text{K}^{-4}$. This law can be formulated as

$$T = \sqrt[4]{(W/\sigma)} \quad (1)$$

Considering radiometric corrections for material-specific emissivity ϵ , for reflections of radiation from the surroundings, and for atmospheric induced and attenuated radiation, the radiant intensity W is split into the emissions from the object (W_{obj}), from the ambient sources (W_{refl}), and from the atmosphere (W_{atm}).

$$W = \epsilon\tau W_{obj} + (1 - \epsilon)\tau W_{refl} + (1 - \tau)W_{atm} \quad (2)$$

with τ being the transmittance of the atmosphere, which depends on the distance between the object and the camera sensor, as well as on relative air humidity. Ultimately, values for the temperature of the ambient sources and the atmosphere, the targeted object's emissivity, the distance between object and camera, and the relative humidity are required for accurately estimating an object's surface temperature T .

Details on the principles of TIR imagery, TIR sensor types (i.e. wave length, sensitivity), and considerations for choosing the most appropriate camera and remote sensing platform for the desired acquisition (i.e. accuracy, resolution) are provided in the literature (Dugdale, 2016; Handcock et al., 2012). For this study, we relied on two different handheld TIR camera models: a FLIR B425 with a resolution of 320 x 240 pixels and an angle of view of 25° and a FLIR T640 with a resolution of 640 x 480 pixels and an angle of view of 45° (FLIR Systems, Wilsonville. USA). The wider angle of view of the FLIR T640 clearly facilitated the image acquisition in this study, while a pixel resolution lower than the resolutions of the two cameras would still have been sufficient for the identification of surface saturation patterns.

We define surface saturation as water ponding or flowing on the ground surface (even if only present as a very thin layer). Mapping surface saturation with TIR imagery requires (1) a sufficient temperature contrast between surface water and the surrounding environment (e.g. dry soil, rock, vegetation) and (2) at least one pixel of the TIR image being known to correspond to surface water. When these two requirements are met, it is possible to visually identify the surface saturation patterns in a TIR image. This is exemplified with a TIR image of a riparian-stream zone (Fig. 4.1). The substantial temperature contrast (requirement 1) allows us to differentiate between two TIR pixel groups, i.e. surface water pixels and surrounding environment

pixels. With ground truth data at hand (here, VIS image – alternatives include stream water temperature or knowing the location of the creek) for point 1 of Fig. 4.1 (requirement 2), the group of pixels with higher temperatures can be identified as surface water. The group of pixels with lower temperatures can be regarded as the non-saturated surrounding environment (cf. Fig. 4.1, point 2). With this classification in mind, the TIR image significantly amplifies the appearance of surface-saturated areas relative to a VIS image. Moreover, the TIR image reveals additional surface-saturated areas that are not clearly identifiable (cf. point 3, Fig. 4.1) or not visible (cf. area above point 6, Fig. 4.1) within a VIS image.

The example shows that the identification of surface saturation relies on temperature contrasts between surface water and the surrounding environment. Radiometric corrections of TIR images for obtaining correct temperature values are thus not necessary. However, interferences that affect temperature, such as shadow casts or reflections (Dugdale, 2016; Handcock et al., 2012), cannot be disregarded as they can influence the temperature contrast (see Section 4.2.2). In cases where the water temperature is too similar to the surrounding materials, saturated areas might be falsely identified as dry, whereas surrounding materials might be falsely identified as wet. In cases where non-uniform water temperatures occur, different water sources may be distinguished (cf. Fig. 4.1, where point 4 likely represents stream water, points 5 and 7 likely represent the exfiltration of warmer groundwater). However, a bimodal distribution of water temperatures (e.g. cold stream and warm exfiltrating groundwater or warm ponding water) can also lead to a misinterpretation of temperature contrasts to the surrounding environment (e.g. a surrounding material with a temperature that is in between the water temperatures might be identified as water).

For the above-mentioned reasons, it is important to evaluate the applicability of the TIR images for identifying the surface-saturated areas with some ground truth and validation data. For the validation, we relied on immediate visual verification during image acquisition as well as on VIS images. Another option is to install sensors that can verify the presence or absence of water on the ground surface locally, yet this is an experimental effort and only results in validation data for selective points. Validating the TIR images with other saturation mapping techniques is difficult, since most of these techniques implicitly include saturation in the upper soil layer, while the current use of TIR imagery excludes the soil. For example, saturated areas inferred via the squishy boot method account for areas where water is squeezed out of the soil when stepping on it, whereas such areas are not detected as saturated areas by the non-invasive TIR imagery.

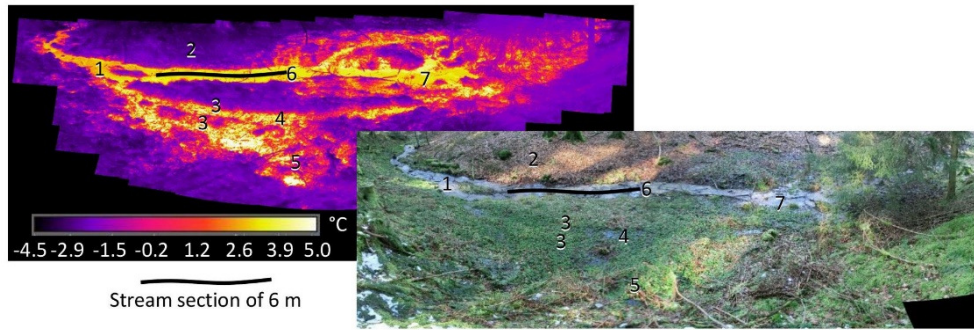


Figure 4.1: TIR image and VIS image of a riparian-stream zone (pictures: B. Glaser, M. Antonelli). The temperature contrast between the water and the surrounding environment allows us to clearly differentiate between surface-saturated and dry areas in the TIR image. The numbers indicate identical locations in the TIR and VIS images and relate to dry areas (2), stream water (1, 4, 6), points of supposed groundwater exfiltration (5, 7: warmer water temperatures), and locations in which surface saturation is clearly visible in the TIR image but not in the VIS image (3, area above 6).

4.2.2 Image acquisition interferences

Impact of weather conditions

Weather conditions can interfere with TIR image acquisition (Dugdale, 2016; Handcock et al., 2012). The main problem stems from the similar temperatures of water and the surrounding environment, compromising an identification of surface saturation with TIR images (Fig. 4.2 a). Water has a higher thermal capacity than most environmental materials, and the water surface temperature therefore generally aligns more slowly with the air temperature than the surface temperatures of surrounding materials. During our field campaign, it became clear that, particularly during day-night-day or seasonal transitions, this difference in thermal capacities induced a convergence of the surrounding environment's temperatures (which align to the air temperature) to the water temperature. Furthermore, the direct exposure of the study site to sunlight, combined with shadow casts, commonly distorted the temperature contrasts. Surrounding materials in the shade with temperatures different to the same surrounding materials in sunlight led to reduced temperature contrasts between these materials and the surface water (Fig. 4.2 b). Once the direct sun exposure ceased, the different thermal capacities of different materials heated by the sun could still cause patches of warmer and colder temperatures. Rain and fog may also influence image quality due to water droplets falling between the TIR sensor and the ground, eventually blurring the images and causing uniform temperature signatures (Fig. 4.2 c).

To avoid the acquisition of unuseable TIR images, we advise for the planning of field campaigns adapted to the weather forecasts. The ideal situation is to work during dry weather with warm or cold air temperatures in order to ensure a clear difference between the temperature of the surrounding materials and the more temperate surface water temperatures. Dugdale (2016) reported the time period

from mid-afternoon to night-time as an optimal TIR image acquisition period for monitoring water surface temperatures. Based on our 18-month field campaign, we suggest that the optimal TIR image acquisition time for identifying surface saturation patterns is early morning. At this time, there are no undesirable effects due to sunlight (shadows, warming-up), and there are generally high temperature contrasts between water surfaces and the surrounding environment. Cloudy conditions can also help to avoid the effect of direct sunlight. A site-specific analysis of the sun exposure throughout the day can help pinpoint the other times at which images can be taken in favourable conditions for a specific study site.

Camera position

Obstructions in the TIR camera's field of view are obviously problematic. Yet, permanent view obstructions on the ground (e.g. tree trunks, Fig. 4.2 d, point 6) proved to be useful ground reference points during our field campaign. Temporary view obstructions, such as growing vegetation (Fig. 4.2 d), recent litter, and snow cover are a problem for repeated imaging campaigns. Cutting the vegetation during the growing season is an option for small study sites. Our experience is that the coverage of grasses and herbaceous plants with small leaves is normally low enough to permit the recording of the ground surface temperature, while the coverage of ferns or tree leaves is normally completely opaque. Snow cover usually hides surface saturation. Yet, periods where the amount of snow is low are commonly unproblematic, since the saturated areas mainly stay uncovered due to a warmer water temperature and thus the fast melting of the snow.

Ideally, images are taken from above and at nadir to the study site. Oblique angles of view ($>30^\circ$ of nadir) reduce the object's emissivity and thus distort the detected temperatures in the TIR images (Dugdale, 2016). The incorrect temperature values are not critical as such for mapping surface saturation patterns, but we observed that wide ranges of angles can result in distinct temperature distortions and thus reduced temperature contrasts within the images. In a similar way, varying distances between camera and ground surface for different positions within one image (e.g. top and bottom, left and right) do not only provoke pixels with varying area equivalents, but can also distort the temperature detection and thus temperature contrasts. Therefore, ground-based cameras should be positioned at locations that minimize the range of angles of view and the distances between camera and ground surface. In the event of the repeated image acquisitions of a given area of interest, we took the pictures from the same position each time in order to facilitate subsequent image comparisons. For repeated image campaigns, it could be useful to install a structure that allows several images to be acquired by moving the camera to specific positions with fixed heights above the ground and fixed angles of view. This could simplify the post-processing and assemblage of the images into panoramic images (cf. Section 4.2.3).

Measurement artefacts during image acquisition

For determining surface saturation, the TIR images should cover an area known to be surface-saturated (e.g. stream, visually obvious wet spots) in order to have a reference for water temperature (cf. Section 4.2.1). In addition, a VIS image

should be acquired simultaneously to the TIR image for comparison. The TIR imagery parameters necessary for correcting and converting the radiation signal to temperature values (e.g. air temperature, humidity) do not need to correspond to the actual conditions, since only the temperature contrast, and not the correct temperature value, is required for defining saturated areas. Certainly, 'wrong' temperatures influence the temperature contrast between the surroundings and the water, but this effect on the contrast can be negative or positive. If correct temperatures are targeted, radiometric corrections need to be applied during the image post-processing procedure. This allows, for example, for the consideration of different emissivities for different surface materials by using appropriate values for each individual image pixel (Aubry-Wake et al., 2015). However, in our experience, setting realistic parameter values during the image acquisition helped the auto-focus process of the camera and prevented the observation of unrealistic surface temperatures. Nonetheless, in the event of clear skies or on cold winter days, we occasionally observed negative temperatures for flowing water. The explanations for these observations remain speculative. Potentially, a particularly strong reflection of the radiation from the surroundings and the sky in the water influenced the temperature detection. However, for the identification of surface saturation patterns, such unrealistic negative temperatures do not pose a problem since the temperature range stays correct (Antonelli et al., 2017).

Reflections of surrounding objects on the water surface (Fig. 4.2 e) and image vignetting can occur during image acquisition and can compromise a further use of the TIR images. Vignetting is the falloff of radiation intensity towards the edges of the image, which is mainly generated by the geometry of the sensor optics (especially wide angle lenses) (cf. Kelcey and Lucieer, 2012). As a consequence, the monitored temperature can change towards the edges of the picture (Antonelli et al., 2017). In this study, the image vignetting was unproblematic, especially where a panorama was built from several images (cf. Section 4.2.3). This is due to the fact that the effect of image vignetting only occurs at the edges of the pictures and it is of minor relevance in images with high temperature contrasts. Reflections of surrounding objects on the water surface limit the value of the images for saturation identifications in a similar way to shadows (cf. Fig. 4.2 d and e). The difference with shadows is that reflections also occur with diffuse light, which makes it difficult to predict their occurrence and thus to avoid them.

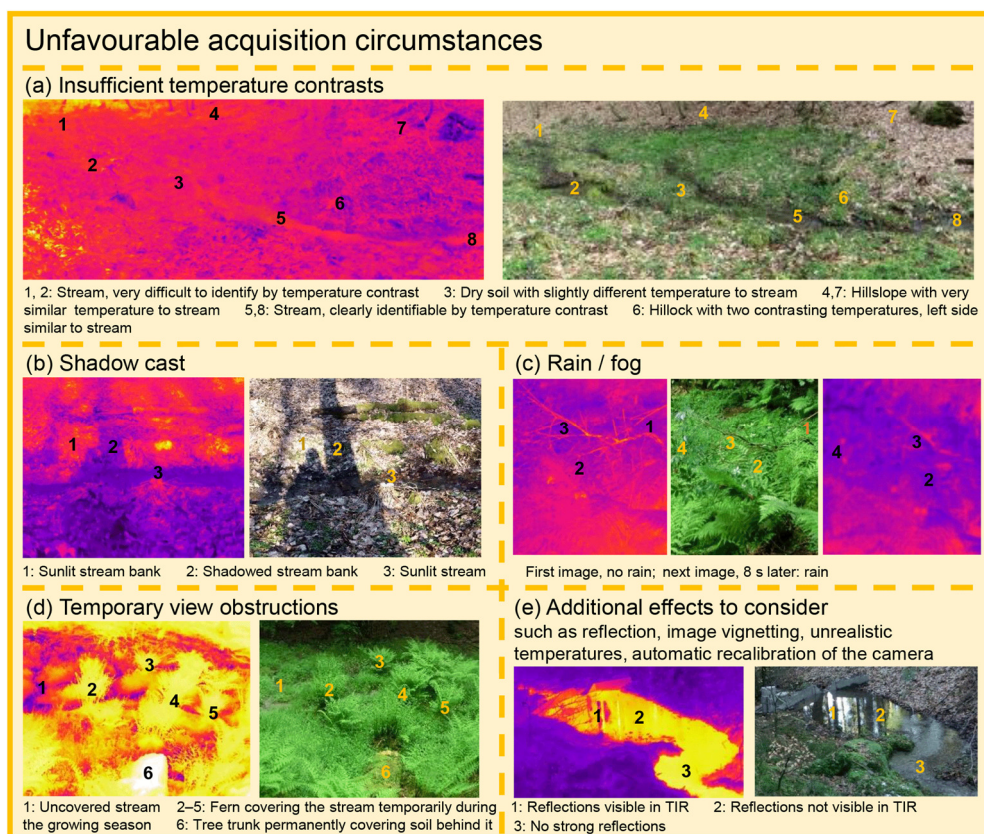


Figure 4.2: Example images showing how unfavourable image acquisition circumstances influence the usability of TIR imagery for the identification of surface saturation (pictures: B. Glaser, M. Antonelli). The numbers indicate identical locations in the TIR and VIS images.

4.2.3 Generation of TIR panorama images

We acquired the images used for the assemblage of a panoramic view in two different ways: (1) by taking single, overlapping images and (2) by taking a video of the area of interest. While both approaches deliver similar final results, videos are recorded faster than sequences of individual images. Independently from the chosen data format, we ensured that the saving format retained the temperature information as radiometric data for further image processing (see below and Fig. 4.3). Sun disappearance and appearance and automatic noise corrections by the camera (Dugdale, 2016) can lead to considerable shifts in recorded temperatures from one image and video frame to another. Since correcting such temperature shifts is difficult (Dugdale, 2016), we opted to control them by fixing the temperature-colour scale and restarting image acquisition if the colour (and thus temperature) of overlapping image parts changed.

We acquired the images and video frames in such a way that the area of interest formed the central part of a panorama. This allowed us to avoid image gaps and distortion effects at the borders of the area of interest. When possible, we ensured that the single pictures and video frames included overlapping parts with identifiable structures, such as the stream bank, tree stems, or stones, as natural reference points. For videos, it was essential to move the camera slowly enough to obtain sharp images and to use a low frame rate (e.g. 2 Hz) to keep the number of video frames reasonable (enough frames for obtaining area overlaps, but not too many frames showing the same area).

The generation of a panorama from overlapping TIR images or video frames acquired with a ground-based camera involves some challenges that specifically relate to TIR and/or ground-based images. This needs to be addressed in TIR-specific panorama generation and image processing steps, as presented briefly by Cardenas et al. (2014). Our approach consisted of transforming the acquired images and video frames containing the radiometric information (see above) into grey-scaled, standard format images / videos (Fig. 4.3, step 1) in order to allow the use of ordinary panorama assemblage software. We relied on grey-colour-scale images, linearly splitting the colour shades over the global temperature range of the acquired images and video frames, since this prevents the creation of artefacts by colour-mixing effects and allowed us to embed the temperature information in the generated panoramas. When the extreme temperature values of an image were not relevant for the identification of saturated areas, we truncated the global temperature range in favour of a better colour contrast and a finer temperature class width retained in the grey values (e.g. the retained temperature class width is 0.1 °C in case of a temperature range of 25.5 °C and an image with 255 grey values).

We employed Microsoft's Image Composite Editor (ICE) and the PTGui panorama software (New House Internet Services) to create panorama images (Fig. 4.3, step 2). ICE and PTGui allow for the creation of panoramas from single images (and from video frames for ICE) with an automatic mosaicking function (i.e. a function that geometrically transforms, aligns, and overlaps the single images). TIR images generally show less identifiable features and lower contrasts than VIS images (Weber et al., 2015). Therefore, a (partial) failure of automatic mosaicking is not uncommon and manual interactions with image alignment (i.e. defining control points for matching distinct points in overlapping images in PTGui) were frequently necessary for the TIR images taken during our 18-month field campaign.

In order to compare several panorama images of the same area, one needs to co-register the panoramas (Fig. 4.3, step 3). In principle, it is possible to georectify the TIR images by allocating geographical coordinates to the images, which are derived from ground control points (Keys et al., 2016; Silasari et al., 2017) or from a virtually projected elevation model (Cardenas et al., 2014; Corripio, 2004; Härer et al., 2013). However, this can result in large gaps or strong interpolations and distortions in the images, due to view obstructions in the picture. Instead of this, therefore, we co-registered TIR panoramas of the same area against each other (Cardenas et al., 2014; Glaser et al., 2016). More specifically, we registered and cropped them to the dimensions of a reference TIR panorama of the area of interest (Fig. 4.3, step 3).

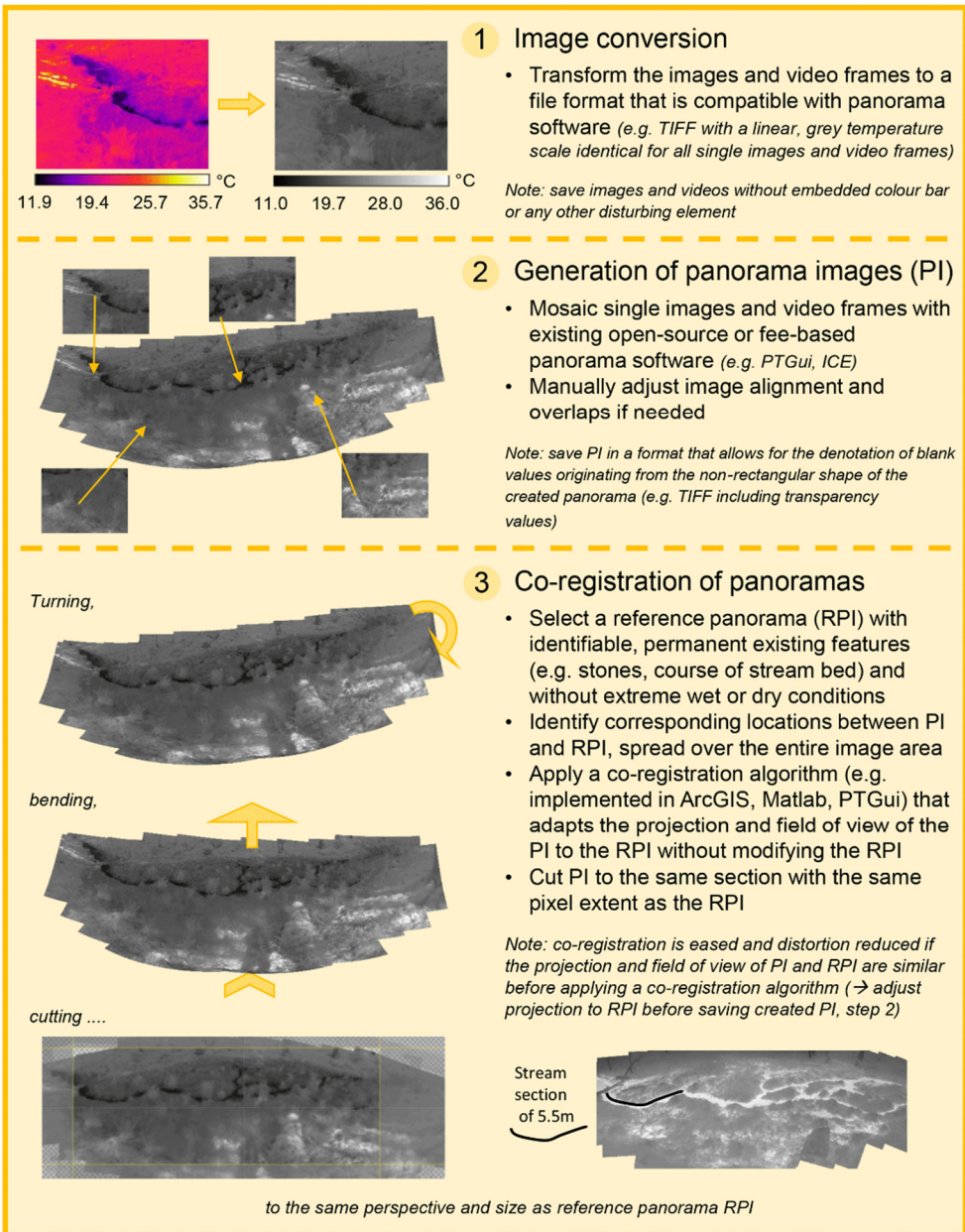


Figure 4.3: Workflow for processing single TIR images and video frames to co-registered panoramic images.

4.2.4 Application examples

In this section, we present three examples from our 18-month field campaign that demonstrate the potential for TIR imagery to analyse surface saturation patterns and their dynamics. All images were taken in the Weierbach catchment - a forested, 0.42 km² headwater research catchment in western Luxembourg (Glaser et al., 2016; Klaus et al., 2015; Martínez-Carreras et al., 2016; Schwab et al., 2018). We avoided unfavourable environmental conditions for the image acquisitions (cf. section 4.2.2, Fig. 4.2) by allowing a few days of tolerance around the targeted biweekly or weekly recurrence frequency. Additionally, we cut ferns that obstructed the camera view during the summer months. The 364 acquired panorama images were divided into three groups classified as usable without restrictions (32.4 %), usable with some restrictions (small negative effects of low temperature contrasts or covering vegetation visible, 31.1 %), and unusable (36.5 %).

The usable panoramas captured the temporal evolution of surface saturation over the 18-month field campaign. This demonstrates the robustness of TIR imagery through the complete range of seasonal conditions (Fig. 4.4), including snow and growing vegetation, as well as warm and cold water. The full extent of the added value provided by TIR imagery compared to VIS imagery was documented for cases with different seasonal conditions (Fig. 4.4), particularly for situations with less pronounced differences in discharge levels (Fig. 4.4 a-c). For example, the comparison of the VIS images of December 2015 and June 2016 (Fig. 4.4 a vs. Fig. 4.4 c) suggests wetter conditions for December 2015, while the two TIR images show similar saturation patterns for the two dates.

In addition to surface saturation dynamics, the TIR images can also reveal distinct types of saturation patterns. For example, the orientation of saturated areas may change over a few metres from perpendicular (Fig. 4.5 a, b) to parallel (Fig. 4.5 c, d) to the adjacent stream. The extension of saturated areas along the left bank (Fig. 4.5 c, d) appears to be created by a parallel extension of the stream in a flat riparian zone that becomes an extended stream bed. The surface saturation oriented perpendicularly to the stream at the right bank (Fig. 4.5) appears to be generated from exfiltrating groundwater that flows downhill to the stream at the soil surface. Thus, the different directional extents of the saturated areas can indicate different processes underlying the surface saturation formation.

Finally, the images allow us to identify the spatial heterogeneity of temporal saturation dynamics across different study sites. Figure 4.6 shows TIR images of the riparian zone of two different source areas with different degrees and dynamics of surface saturation. In area 1 (Fig. 4.6, panels a, c, and e), the pattern of saturation areas barely changed from February to April, while in area 2 (Fig. 4.6, panels b, d, and f) some locations had dried out (red circles). In December 2016, the riparian zones of both source areas were completely dry and the stream started further downstream in comparison to the other observation dates (red arrows). This suggests that both source areas evolve from very wet to very dry conditions (during which surface saturation is mainly represented by spots with stable groundwater exfiltration) with distinctly different transition dynamics.

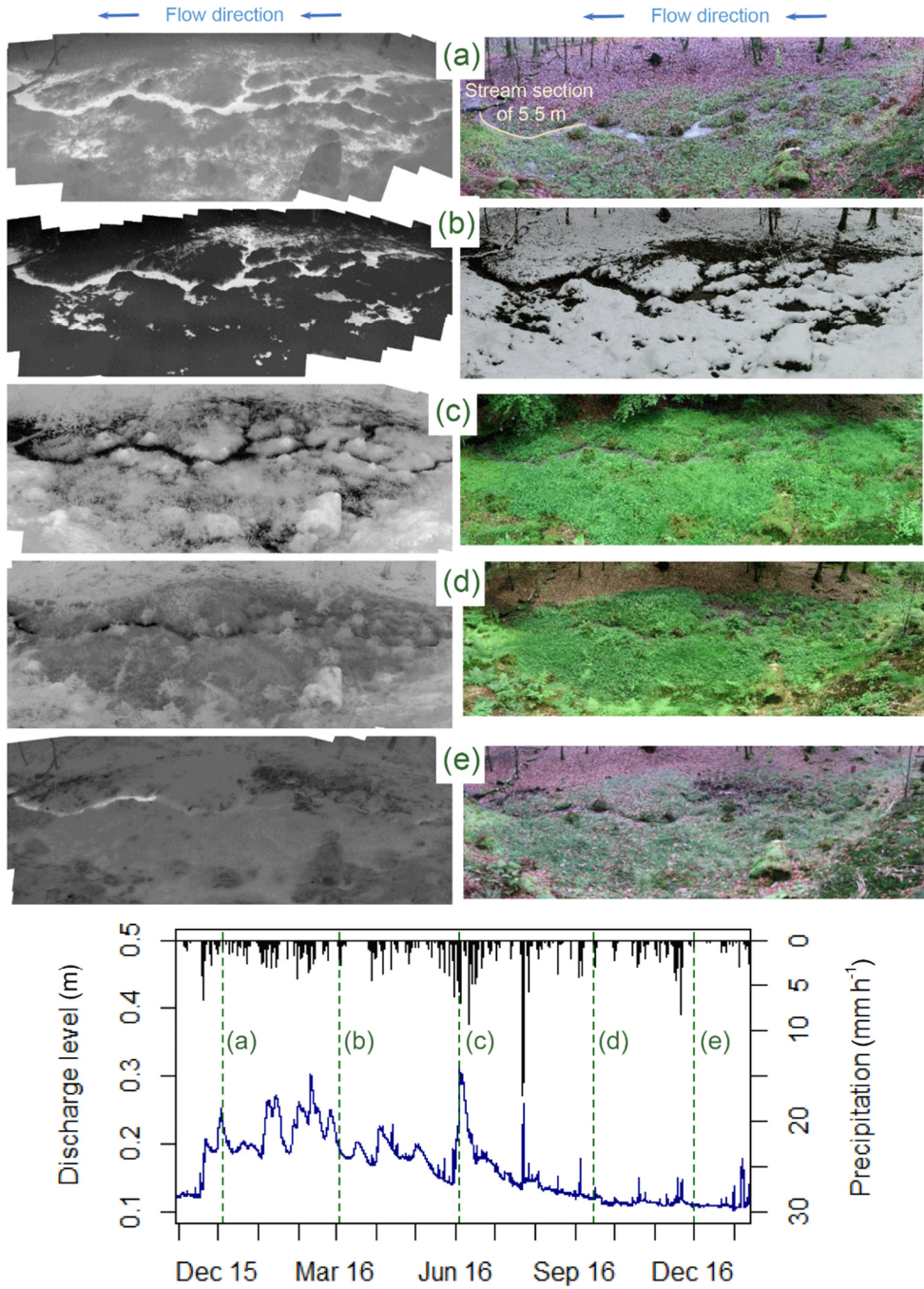


Figure 4.4: Time-lapse TIR and VIS panoramas, showing the variation of surface-saturation patterns with varying discharge levels under diverse seasonal conditions (pictures: B. Glaser, M. Antonelli).

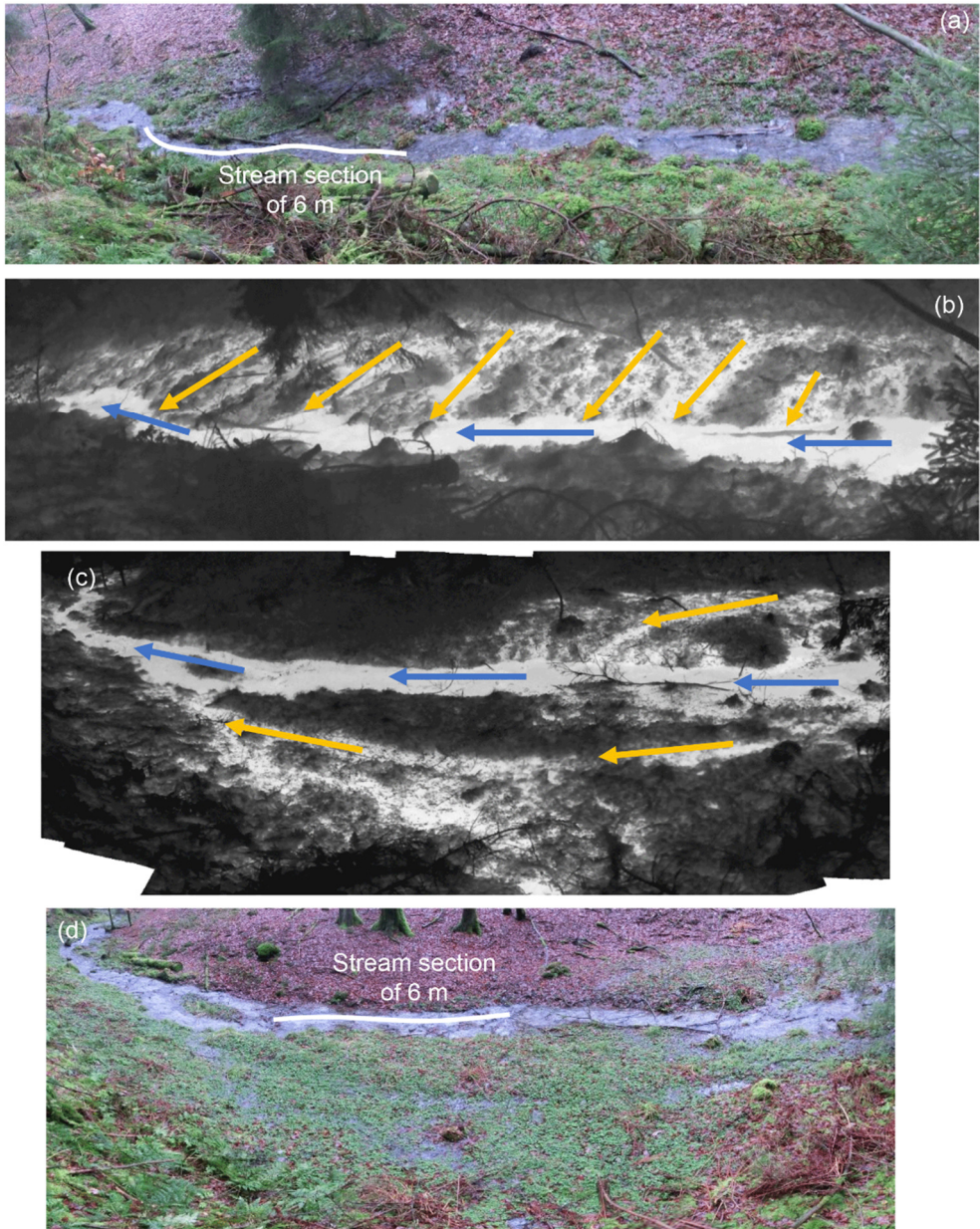


Figure 4.5: Comparison of different types of surface-saturation patterns. The yellow arrows indicate the orientation of the saturated areas towards the stream (blue arrows represent flow direction). The perpendicular direction (a, b) is likely caused by exfiltrating groundwater connecting to the stream, and the parallel direction (c, d) is likely caused by a parallel flow of the stream expanding into the riparian zone. The red ovals indicate where the two panorama images connect. Pictures: B. Glaser, M. Antonelli.

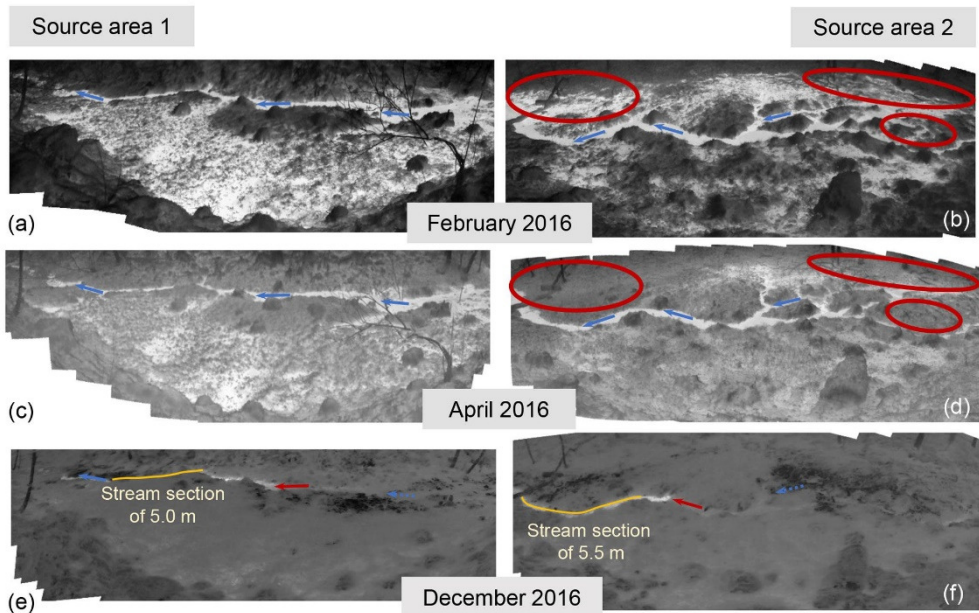


Figure 4.6: Transition of two source areas (a, c, e vs. b, d, f) from very wet (a, b) to very dry conditions (e, f). Surface saturation in source area 1 (a, c, e) barely changed between February and April 2016, whereas source area 2 is clearly drier at some locations (red ovals) in April 2016. In December 2016, both source areas were completely dry on each side of the stream (blue arrows represent flow direction), and the stream started further downstream (red arrows).

4.3 Quantification of saturation through pixel classification

4.3.1 Methods for generating binary saturation maps

The application examples described in Section 4.2.4 demonstrate the potential for TIR images to rapidly and intuitively visualize surface-saturated areas. However, the ‘raw data’ images need to be transformed into binary saturation maps for further analyses based on quantitative values (as e.g. saturation percentages). A common approach to making an image binary is histogram thresholding (e.g. Rosin, 2002). This allows a TIR image to be transformed into a binary saturation map by taking the temperature range of pixels that are known to be saturated (i.e. stream pixels) and defining all pixels in that image that fall into that temperature range as saturated (Glaser et al., 2016; Pfister et al., 2010). Several thresholding algorithms can be found in the literature, each of which has its characteristic assumptions with respect to image content (Patra et al., 2011). Unsupervised approaches other than thresholding are also used for making an image binary, e.g. clustering (Li et al., 2015). Yet thresholding is the most rapid technique for achieving a binary classification of an image, even though the selection of an adequate threshold value

represents a critical step and its choice strongly influences the classification outcome.

One possibility for selecting a threshold value for classifying surface saturation is to manually adapt the temperature range until the resulting saturation map matches best the visual assessment of the original TIR and – if possible – VIS image. A more objective and, for time-lapsed images, faster method consists of relying on the temperature of preselected pixels or a predefined mask for saturated and unsaturated parts in all images. Such pixels and masks can be selected based on a visual interpretation of the images or on information obtained from reference sensors in the field, indicating whether a location was wet or dry at the surface at the time of image acquisition.

Silasari et al. (2017) applied an automatic image classification for unimodal distributions based on a threshold parameter that needs to be calibrated to specific image conditions (in this case, the brightness of VIS images). This is only straightforward in cases where the temperature distribution between water and the surrounding environment is clearly bimodal. Chini et al. (2017) presented a parametric adaptive thresholding algorithm especially suited for images that do not show a clear bimodal distribution. The algorithm makes use of an automatic selection of image subsections with clear bimodal distributions, a hierarchical split-based approach (HSBA), and a subsequent parameterization of the distributions of the two pixel classes. Since the two decomposed distributions might still overlap to a certain extent, Chini et al. (2017) advise complementing the decomposed distribution information with contextual information of the image for the final generation of a binary image, instead of selecting a single threshold value between the two decomposed distributions. Several approaches are available in the literature for including contextual information in the classification of a single spectral image, such as mathematical morphology (Chini et al., 2009) or second-order textural parameters (Pacifici et al., 2009). Chini et al. (2017) suggested a region-growing algorithm where the seeds and the stopping criteria are constrained by the identified distribution of the class of interest (here, saturation).

4.3.2 Comparison of methods for generating binary saturation maps for TIR images

We applied three of the approaches described above to generate the binary saturation maps of our TIR image data set. Here, we present the results for four example images with differing conditions during image acquisition (e.g. very wet or dry conditions, water being the warmest or coldest material, Fig. 4.7). We evaluated the results of the three different approaches based on our observations from the field and the corresponding VIS image as ground truth.

First, we manually chose a temperature range of saturation for each image. By nature, this pixel classification approach creates results that are very close to ground truth. However, finding an unequivocal temperature range was not feasible and the selection of the most plausible temperature range (Fig. 4.7, dark-green asterisk) remained somewhat subjective. Furthermore, artefacts (such as pixels corresponding to vegetation covering the stream) induced some uncertainty in the pixel classification, eventually leading to discrepancies compared to visually

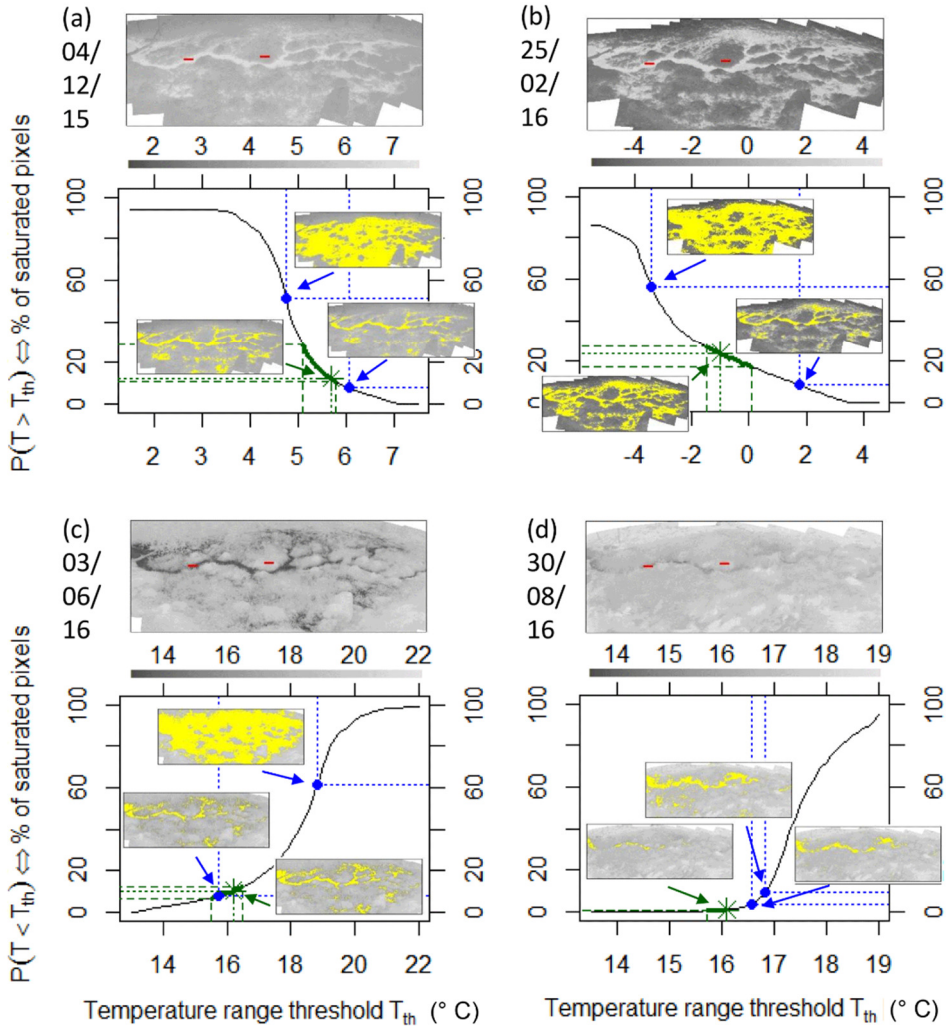
identified saturation patterns. Consequently, a pixel classification based on this manual procedure remained tarnished by some uncertainties. The definition of an uncertainty range within which the temperature range can be considered plausible (Fig. 4.7, dark-green, dashed lines) was also subjective. Generally, the uncertainty range was small for images with low saturation and gradually increased with higher saturation (compare Fig. 4.7 d with Fig. 4.7 b). Accordingly, images with a large difference in percentages of saturated pixels (e.g. Fig. 4.7 b vs. Fig. 4.7 d) did not encounter an overlap of the uncertainty ranges. For some images, the uncertainty range was rather high (Fig. 4.7 a) and a comparison with other images with percentages of saturated pixels in the same range was thus problematic. In such cases, it is preferable that only one person defines the optimal temperature ranges and thus saturation patterns for all images that are intended to be compared in order to ensure consistency in the image interpretation.

Secondly, we performed an objective selection of the temperature range of saturation based on masks with known pixel classes. For this, we used two masks, one with 2000 pixels falling into an area that always stayed dry and one with 2000 pixels falling into an area where the stream was flowing all year (red rectangles, Fig. 4.7). Based on the mask, we selected the threshold for the temperature range as the 90th percentile and 10th percentile of the temperature of the stream mask pixels and dry mask pixels, respectively (i.e. 90% of the pixels falling below the mask were defined as saturated and dry, respectively). By using the two different masks, we obtained two temperature ranges, resulting in two different saturation percentages for each image (Fig. 4.7, blue points). The identification of saturated areas based on the dry mask was clearly not constrained enough. The identification of saturated areas based on the stream mask sometimes approached the manual identification of saturation (Fig. 4.7 a, c) but, in other cases, even exceeded it (Fig. 4.7 d). The uncertainty range of saturation obtained with the two masks could be reduced by selecting a more extreme percentile for the temperature threshold definition. However, this increased the risk of obtaining a clearly incorrect value (cf. Fig. 4.7 d), since the stream and dry mask can cover pixels of the wrong category (due to artefacts like vegetation covering the stream or due to distorted co-registered images, resulting in a shifted mask). A reduced mask size prevents such wrong pixels, but also reduces the captured variability in temperature (in an extreme case down to one temperature value), which in turn increases the risk of missing the warmest or coldest temperature of the wet or dry areas.

Finally, we tested the usability of the approach proposed by Chini et al. (2017), constraining a region growing algorithm to (a) a bimodal distribution derived from the HSBA applied to the entire image, (b) a bimodal distribution derived from the HSBA where the selection of bimodal image subsections was constrained to image-specific manual predefinitions of temperature ranges of saturation, and (c) a bimodal distribution derived from pre-selected parts of the image that include clearly wet and dry areas. While in some cases the fully automatic image classification (point a) worked very well in comparison to the manual selection of a temperature range (cf. Fig. 4.8 4 December 2015, 30 August 2016), for the other cases, saturation was mostly underestimated (cf. Fig. 4.8 25 February 2016, 03 June 2016). The additional constraint with image-specific temperature ranges (point b) improved the matches with the manually defined saturation patterns, but the result was strongly influenced by the match of the given constraint range to the range that was defined as the optimum for the image. A constraint with a rough estimated temperature for

saturation worked less well than a constraint with the temperature range as selected in the detailed manual assessment described earlier in the Section (cf. Fig. 4.7 green asterisks and lines). The classification based on preselected parts of the image (c) tended to result in higher saturation amounts. This improved the match for the cases that were underestimated with the fully automatic classification (a) (cf. Fig. 4.8 25 February 2015, 3 June 2016), but this overestimated saturation for the cases where the fully automatic classification (point a) showed good results (cf. Fig. 4.8 4 December 2015, 30 August 2016).

Figure 4.7 (next page): Example TIR images, with their cumulative saturation curves showing the percentage of pixels that have a higher (a, b) or lower (c, d) temperature than the temperature range threshold T_{th} and are thus defined as saturated (marked as yellow pixels in the inset TIR images). The green asterisks mark the temperature ranges that were manually chosen as optimum following a visual assessment of the images. Green dashed lines define the uncertainty of the optimum temperature ranges. The red rectangles in the TIR images depict the masks used for the identification of temperature ranges from a constantly wet (a, c) and constantly dry (b, d) area. The respective temperature ranges and saturation percentages are marked in blue. As a reference for the spatial dimension of the images, we refer the reader to the indicated stream section in Figs. 3 or 4.



4.4 Discussion

4.4.1 Mapping surface saturation with TIR imagery

The main advantages of TIR imagery in comparison to other surface saturation mapping methods are its non-invasive character and its large temporal and spatial flexibility (centimetres to kilometres, minutes to months). Another advantage is that TIR images allow a rapid and intuitive identification and analysis of the dynamics of surface saturation patterns. The raw data images can be used without any additional processing to study surface-saturated areas, their evolution over time, and how and where they occur – ultimately contributing to a better

mechanistic understanding of the hydrological processes prevailing in the studied area. The pure visual information provided by the images per se is also usable as soft data, e.g. for model validation (e.g. different types of extent compared to stream, Fig. 4.5, more and less stable saturation patterns, Fig. 4.6). VIS imagery offers similar advantages (Silasari et al., 2017), but commonly the saturated areas are not as clearly visible as with TIR imagery (cf. Fig. 4.1 and Fig. 4.4). Moreover, VIS imagery is not usable during the night and cannot provide additional information about water sources and processes underlying the surface saturation formation (cf. Fig. 4.1 and Fig. 4.5, groundwater inflow vs. stream water). Nevertheless, VIS imagery provides good complementary information to the TIR imagery and should always be considered as a ground truth information source.

In our study, unfavourable image acquisition conditions (cf. Section 4.2.2) caused 36.5 % of the acquired images to be unusable for further processing. High amounts of unusable images are a common problem in environmental imagery (cf. e.g. cloud cover for satellite images, night-time for VIS images (De Alwis et al., 2007; Silasari et al., 2017)). Flexibility in the scheduling of a field campaign is thus necessary for reducing the number of acquisitions during unfavourable conditions. A concern for the use of TIR imagery for mapping saturation patterns is that some saturated areas (e.g. warmed-up ponding water) might not be identified as saturated due to a temperature that is very different from the stream temperature. This relates to the fact that temperature is only used as an indicator for saturation. Compared to other saturation indicators, such as vegetation mapping or hydrometric measurements (Dunne et al., 1975), we consider TIR imagery with the above-mentioned advantages as the better indirect mapping method. However, the only way to directly map surface saturation consists of walking through the area of interest (e.g. squishy boot method), which remains restricted to small areas and / or low mapping frequencies.

The amount of fieldwork for imagery mapping is generally reduced compared to other methods for mapping surface saturation (e.g. vegetation or soil mapping), allowing more frequent campaigns with higher spatial precision. Yet, consistent with other imagery-mapping studies (Spence and Mengistu, 2016), the image post-processing in this study was time-consuming. Mosaicking and the co-registering of images is often considered particularly difficult for TIR images, since ground control points with a thermal signature are needed (Dugdale, 2016; Weber et al., 2015). Our experience showed that the images normally offered enough natural thermal ground control points (e.g. the stream bank) in cases where the temperature contrast between water and ambient materials was good enough for image usability. In combination with the post-processing workflow presented, the post-processing effort was reasonable. More automatized workflows like the one proposed by Turner et al. (Turner et al., 2014) for mosaicking UAV-acquired TIR images could also be adapted and applied.

The image acquisition considerations, post-processing steps, and application examples described, focused on biweekly or weekly panoramic images of small areas, acquired with a portable TIR camera. A transfer of the TIR imagery technique to different temporal or spatial scales does not change the principles and possibilities of the technique, but it will require some additional scale- and platform-dependent considerations. For example, using permanently installed ground-based cameras for image acquisitions with high temporal frequencies might challenge technical aspects such as protection of the camera against environmental

influences, an automatic triggering of image acquisition, and power supply. These aspects might also be relevant for TIR imagery acquisition at larger spatial scales, especially when using UAVs. Besides this, image acquisitions based on UAV or aeroplane overflights might, for example, require considerations of overflight regulations. Users of UAVs or aeroplanes should also be aware that saturation patterns within a forest might only – if at all – be mapped during the dormant season and ground control points and ground truth data might be more difficult to obtain. Such challenges are partly addressed in existing literature (Vivoni et al., 2014; Weber et al., 2015), but others will need to be figured out by applying the TIR technique at such different scales.

4.4.2 Pixel classification methods

More challenging than TIR image mosaicking and co-registering was the generation of saturation maps from the TIR images. The different pixel classification methods tested all yielded somewhat different results compared to pixel classification based on manual visual assessment. Nevertheless, realizing an objective, automatic classification of saturated areas is not more challenging than for other surface saturation mapping methods. Saturation maps created based on the squishy boot method or vegetation or soil mapping are subjective due to decisions made during the fieldwork. The supervised and unsupervised classification methods that are commonly used for creating saturation maps from remote sensing data (e.g. VIS images, NDVI or NDWI) also contain some uncertainty (Chabot and Bird, 2014; De Alwis et al., 2007; Mengistu and Spence, 2016; Spence and Mengistu, 2016).

Moreover, the main problem for all of the tested saturation map generation methods (cf. Section 4.4) is that they are not applicable without being adapted to individual image conditions (very wet, very dry, water being the warmest or coldest material, slightly different field of views). Other image processing methods for deriving saturation maps also do not fulfil this requirement; it is necessary to adapt the parameters (Silasari et al., 2017) or to perform a new supervision (with new classification pixels or masks) for the classification of images with different conditions (Chabot and Bird, 2014; Keys et al., 2016). At this stage, we consider a manual choice of temperature range for saturated pixels as the best approach for time-lapsed images with very variable conditions and slight perspective shifts, even though it is labour-intensive and somewhat subjective. For time-lapsed images with a fixed vantage point and for time spans with similar conditions (e.g. storm events), the automatable methods presented represent valuable options. In particular, the combination of an automatic decomposition of two pixel class distributions with a region-growing algorithm yielded objective saturation maps close to the manual saturation classification and visual assessment of the TIR images (Fig. 4.8). Small adaptations of the constraint for the decomposition of two pixel class distributions were sufficient for obtaining good results for the different image conditions (cf. Fig. 4.8 a – c), and further developments of the method might even allow such adaptations to be performed in a semi-automatic and automatic ways. More work on pixel classification might also include the application of machine-learning techniques or, especially for time-lapsed images, the analysis of the temperature signals of individual pixels over time. Another interesting option may consist of combining the

TIR images with additional data (e.g. VIS images or NIR images), which will allow multi-spectral classification methods to be applied (Chini et al., 2008) and contextual information to be integrated at the same time (Chini et al., 2014).

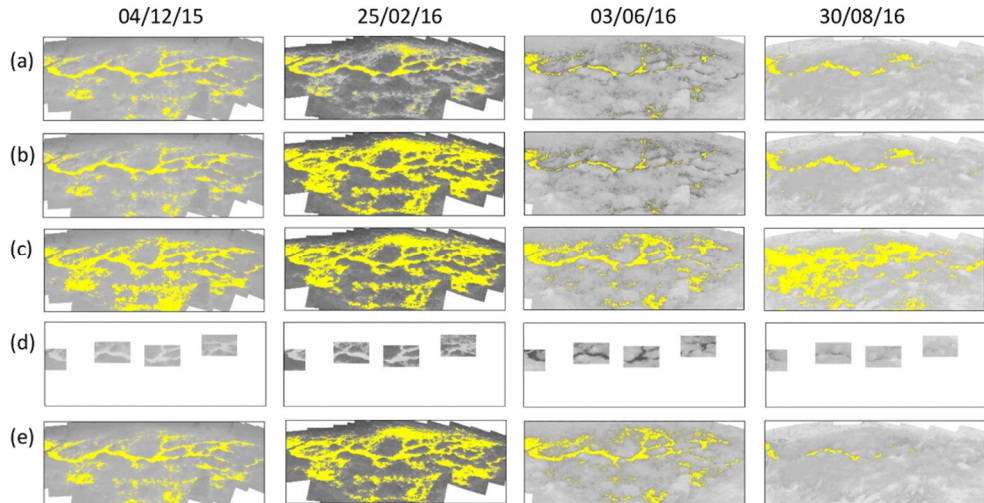


Figure 4.8: Comparison of saturation maps (yellow represents saturation), generated with a region-growing process whose seeds and stopping criteria were automatically constrained to (a) bimodal distributions derived from the HBSA applied to the entire image, (b) bimodal distributions derived from the HBSA where the selection of bimodal image subsections was constrained to image-specific manual predefinitions of temperature ranges of saturation, and (c) bimodal distributions derived from preselected parts of the image (which include clearly wet and dry areas and are shown in d). The saturation maps generated with manually selected temperature ranges based on visual assessment (cf. Fig. 4.7; green asterisk) are shown for comparison (e). As a reference for the spatial dimension of the images, we refer the reader to the indicated stream section in Fig. 4.3 or 4.4.

4.5 Summary and conclusions

This technical note presents recent work carried out in the Weierbach catchment, where we tested the potential for TIR imagery to map surface saturation dynamics. To the best of our knowledge, this is the first comprehensive review and summary of the TIR imagery-related methodological principles and the required precautions and considerations for a successful application of TIR imagery for mapping surface saturation. We give advice for all steps, from image acquisition to processed saturation maps. The main requirement is a clear temperature contrast between water and the surrounding environments. Image acquisition during an 18-month campaign showed that the method works best during dry nights or dry early mornings and that images should be taken from well-chosen positions without obstructions in view towards the ground. The workflow presented for acquiring panoramic images is particularly suitable for small areas of interest (centimetres to metres) that are monitored with intermediate to low mapping frequencies (days to months). Moreover, the information contained in this technical note is also beneficial

for applications at different temporal and spatial scales (fixed cameras for high-frequency images, drone and satellite images for larger spatial scales), considering that some adaptation and further developments of the methodology might be necessary.

We demonstrated with three examples that TIR imagery is applicable throughout the year and can reveal spatially heterogeneous surface saturation dynamics and distinct types of saturation patterns. The saturation patterns can also be used to identify different processes underlying the surface saturation formation, such as groundwater exfiltration or stream expansion. The surface saturation information visualized in the images can be used directly as soft data for characterizing field conditions, for analysing ongoing hydrologic processes and for model validation.

The methods presented for obtaining binary, objective saturation maps from TIR images contain some uncertainties and are not automatable for data sets containing many images with varying characteristics (e.g. very wet or dry, water warmest or coldest material, slightly different fields of view). In such cases, a manual choice of the temperature range for saturated pixels is the most reliable approach. Yet for image subsets with similar conditions, the pixel classifications tested work well, and we think that the combination of an automatic decomposition of the image distribution in two pixel classes and a region-growing algorithm is a very promising option for obtaining objective, comparable saturation maps. In conclusion, we consider the TIR imagery a very powerful method for mapping surface saturation in terms of practicability and spatial and temporal flexibility and we believe it can provide new insights into the role of saturated areas and subsequent spatial and temporal dynamics in rainfall-runoff transformation.

Chapter 5

Saturated areas through the lens: 1. Spatio-temporal variability of surface saturation documented through Thermal Infrared imagery

Abstract

Surface saturated areas are key features in generating runoff. A detailed characterisation of the expansion and contraction of surface saturation in riparian zones and its connectivity to the stream is fundamental to improve our understanding of the spatial and temporal variability of streamflow generation processes. In this first contribution of a series of two papers, we used ground-based thermal infrared (TIR) imagery for characterising riparian surface saturation seasonal dynamics of seven different riparian areas in the Weierbach catchment (0.42 km²), a small forested catchment in Luxembourg. We collected bi-weekly panoramic images of the seven areas over a period of two years. We identified the extension of saturation in each collected panoramic image (i.e. percentage of pixels corresponding to saturated surfaces in each riparian area) to generate time series of surface saturation. Riparian surface saturation in all areas was seasonally variable and its dynamics were in accordance with lower hillslope groundwater level fluctuations. Surface saturation in the different areas related to catchment outlet discharge through power law relationships. Differences in these relationships for different areas could be associated with the location of the areas along the stream network and to a possible influence of local riparian morphology on the development of surface saturation, suggesting a certain degree of intra-catchment heterogeneity. This study paves the way for a subsequent investigation of the spatio-temporal variability of streamflow generation in the catchment, presented in our second contribution.

This chapter is based on: Antonelli, M., Glaser, B., Teuling, A.J., Klaus, J., Pfister, L. 2020. Saturated areas through the lens: 1. Spatio-temporal variability of surface saturation documented through thermal infrared imagery. Hydrological Processes, 34: 1310– 1332. <https://doi.org/10.1002/hyp.13698>.

5.1 Introduction

Saturation-excess overland flow and its connection to saturated areas was first documented in the seminal work by Dunne and Black (1970a). Surface saturated areas (i.e. areas presenting water at the ground surface) have been recognised as key areas for mediating the on- and offset of hydrological connectivity between hillslopes and streams in humid temperate environments (Ambrose, 2004; Birkel et al., 2010; Bracken and Croke, 2007; Hewlett, 1961; Tetzlaff et al., 2007). Saturation dynamics and the associated hydrological connectivity have been on the agenda of both modelling and experimental studies. Many monitoring studies of surface saturation focused on the near-stream area (i.e. riparian area), which is particularly relevant for runoff generation due to its intrinsic proximity to the stream. Several studies have shown that the spatial extent of near-stream surface saturated areas is a valuable indicator of the general hydrological state of the catchment and, in particular, of groundwater storage during baseflow conditions (i.e. Ambrose, 2016; Gburek and Sharples, 1998; Myrabø, 1997). During precipitation events, riparian surface saturated areas can quickly extend and convey event water to the stream and act as mixing areas for hillslope water contributions (Soulsby et al., 2016a; Tetzlaff et al., 2014; Weill et al., 2013). This is often observed in catchments characterised by confined valley bottoms, where persistent saturation can develop in riparian locations with low relief and a shallow water table (Dunne et al., 1975; Niedda and Pirastru, 2014). Thus, an accurate characterisation of expansion and contraction dynamics of riparian surface saturation is needed to fully interpret the hydrological behaviour of catchments exhibiting these features and to accurately predict runoff dynamics and associated water and nutrient flowpaths.

Varying riparian morphological traits and upland topographic characteristics have been associated to the variability in hydrological and biogeochemical functions of riparian zones. Several studies have accounted for the spatial variability of riparian zones when exploring riparian functions such as water table fluctuation (Grabs et al., 2012), vertical and lateral connectivity (Leach et al., 2017; Ploum et al., 2018), or water travel distance and retention of chemicals (Grabs et al., 2012; Ledesma et al., 2018; Roulet, 1990; Vidon and Hill, 2004). On the other hand, riparian surface saturation dynamics have been mainly investigated by taking into account single riparian sections (Zillgens et al., 2007) or the dynamics of the riparian system as a whole (Ocampo et al., 2006). Due to the spatial variability of riparian characteristics (i.e. riparian width, slope and soil depth), monitoring of surface saturation that is restricted to a single riparian section can be far from being representative of the whole catchment's riparian zone. Similarly, mapping the dynamics of surface saturation of the riparian zone as a whole may conceal important small-scale variability. Therefore, it is fundamental to characterise riparian surface saturation by accounting for riparian zones' spatial heterogeneity.

As early as in 1975, Dunne et al. made a call for the development of a routine method for the "recognition and quantification of the seasonal and in-storm [and inter-storm] variation of the saturated runoff-producing zones". Progress toward a routine method for mapping the spatio-temporal variability of saturated areas in humid environments remains hampered by technological limitations, especially when it comes to mapping surface saturation dynamics with high spatial and temporal resolution. In order to get a better understanding of the spatial and temporal scales

at which previous studies have addressed surface saturation, we reviewed a total of 64 studies on surface saturation. In 25 of the reviewed studies, surface saturation dynamics were estimated through the use of proxies for surface saturation such as riparian water table level variations (e.g. Waddington et al., 1993; Vidon and Hill, 2004; Ocampo et al., 2006; Tetzlaff et al., 2014), modelling approaches (e.g. Appels et al., 2016; Beven and Kirkby, 1979; Blumstock et al., 2016; Dick et al., 2015; O'Loughlin, 1987; Weill et al., 2013), or a combination of the two (e.g. Baker et al., 2001; Frei et al., 2010; Myrabø, 1997; Stieglitz, 2003; von Freyberg et al., 2014). Proxies for surface saturation such as water table dynamics can be collected at high temporal resolution but are limited to punctual spatial observations. Modelling approaches for estimating surface saturation dynamics commonly rely on the estimation of topography-based wetness such as the topographic wetness index (TWI) employed in TOPMODEL (Beven and Kirkby, 1979), multiple existing TWI-variants, or geomorphic indices (Ali et al., 2013a). These models allow for an estimation of surface saturation over large spatial extents (up to hundreds of km²). However, some of the models' underlying assumptions may not always be valid (e.g. the local slope may not be a valid proxy of the downslope hydraulic gradient), especially in catchments of flat terrain (Grabs et al., 2009; Rodhe and Seibert, 1999). Other modelling studies relied on spatially-distributed, physically-based simulations of surface saturation dynamics (e.g. Frei et al., 2010; Weill et al., 2013), yet these studies lacked a detailed assessment of the validity of the model results against field observations.

Direct mapping of surface saturation (rather than relying on the use of proxies or modelling) was performed within 30 of the 64 reviewed studies for varying spatial extents and with varying monitoring frequencies (Figure 5.1 provides a graphical representation of the space-time sampling characteristics of surface saturation mapping from these 30 studies, plus this contribution). Except for a few exceptions (i.e. Birkel et al., 2010; Coles and McDonnell, 2018; Tanaka et al., 1988), field surveys (e.g. squishy boot method) have been applied for mapping areas below 5 km² and at low temporal resolution (i.e. mainly monthly and punctual observations). Saturation mapping via remote sensing tools has been mainly relying on satellite and airborne platforms. These techniques are less labour-intensive compared to field surveys and can deliver a higher amount of observations in a certain time frame and for larger areas (i.e. > 5 km²) (De Alwis et al., 2007; Mengistu and Spence, 2016; Phillips et al., 2011). However, similar to field surveys, remote sensing observations from satellite platforms do not provide the necessary spatial and temporal resolution for detecting heterogeneous riparian surface saturation dynamics within a catchment. Ground-based remote sensing techniques (i.e. thermal infrared – TIR – or visible light imagery) can provide observations at higher temporal (i.e. minutes to weeks) and spatial (i.e. centimetres to meters) resolution (Glaser et al., 2016; Pfister et al., 2010; Silasari et al., 2017). These techniques will likely become pivotal in generating new, more detailed insights into the functioning of surface saturated area variability and dynamics. Similarly to ground-based TIR, other techniques based on temperature detection (such as thermal imagery from unmanned aerial vehicles (UAVs) and fiber optic distributed temperature sensing (DTS)) can also provide observation at high spatial (i.e. centimetres to kilometres) and temporal (i.e. minutes to weeks) resolution, although until today they have been primarily employed for the characterisation of longitudinal stream temperatures and detection of GW exfiltration (Briggs et al., 2019; J. Selker et al., 2006). Within the 64 reviewed studies, 11 did

not report clear information on the spatial and temporal scales at which surface saturation was addressed.

Here, we analyse the temporal variability of different riparian surface saturated areas under a new resolution and perspective – namely “through the lens” of a TIR camera. We employed ground-based TIR imagery in an analogous approach to Pfister et al. (2010) and Glaser et al. (2018, 2016) (i.e. to detect temperature differences between the water at the ground surface – saturated areas – and the surrounding environment – unsaturated areas), to obtain a unique dataset of two years of bi-weekly observations of different riparian surface saturated areas within the Weierbach catchment in Luxembourg. This long-term studied headwater catchment (0.42 km²) is a reference site for rainfall-dominated mountainous catchments (Zuecco et al., 2018). The Weierbach is characterised by homogeneous pedology and geology, and exhibits a hydrological response that is highly influenced by the wetness state of the system. This leads to a single peak response during dry conditions and a double-peak response during wet conditions – after a threshold in catchment storage is exceeded (Martínez-Carreras et al., 2016). The Weierbach catchment has a well-developed riparian zone, characterised by variable morphology (e.g. riparian width, elevation) and the presence of perennial and/or temporary groundwater exfiltration points. Although there is a reasonable understanding of how the overall hydrological response of the catchment is generated (Fenicia et al., 2014; Glaser et al., 2016; Klaus et al., 2015; Martínez-Carreras et al., 2016; Schwab et al., 2018; Wrede et al., 2015), there is still a lack of understanding of the dynamics of small-scale riparian processes, like the spatial and temporal variability of riparian surface saturation, and of how these dynamics are related to the hydrological response (Scaini et al., 2017).

In this first contribution of a series of two papers, we apply ground-based TIR imagery as a routine method for mapping surface saturation dynamics across multiple seasonal and hydrological conditions and across multiple sites in the riparian zone of the Weierbach catchment. We analyse the spatio-temporal dynamics of surface saturation by applying statistical analyses on an extensive surface saturation dataset produced by direct field observation. In particular, through this novel approach we investigate the following questions on saturated area dynamics:

- 1- Are the overall surface saturation dynamics (i.e. seasonal and yearly dynamics) of the seven investigated areas similar?
- 2- How do hydrological conditions (i.e. precipitation, stream discharge, evapotranspiration, groundwater level, soil moisture and catchment storage) relate to the temporal (seasonal and yearly) variability of surface saturation in different riparian locations in a catchment?

We leverage the outcomes of this study in the accompanying manuscript (Chapter 6) for investigating how hillslope-riparian-stream (HRS) connectivity is established in the Weierbach catchment. This will eventually improve our understanding of how the spatial variability of streamflow generation is linked to surface saturation dynamics.

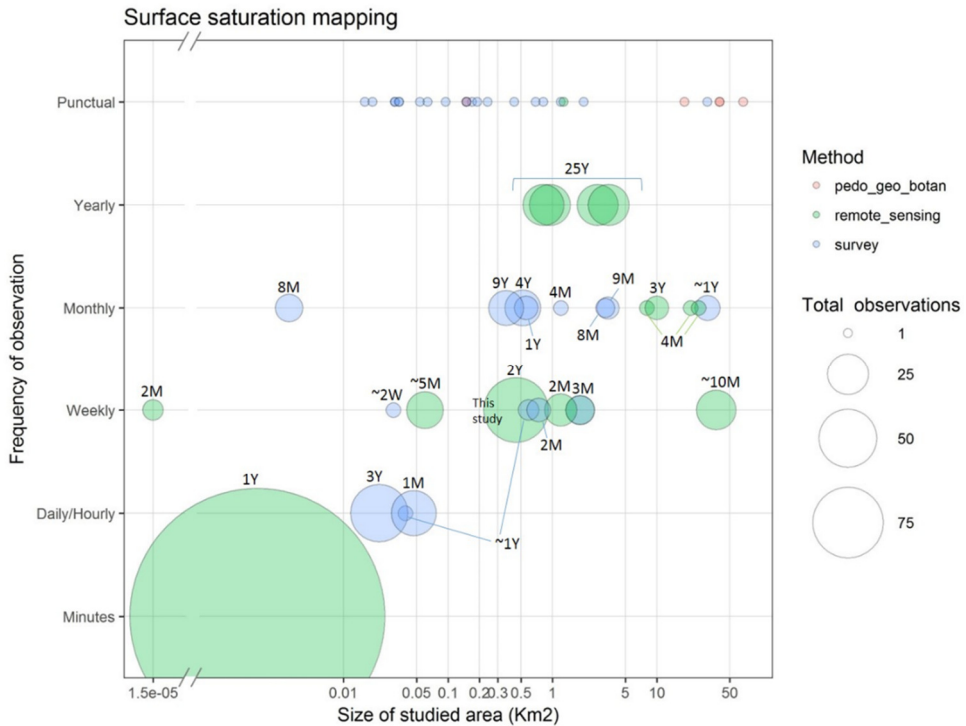


Figure 5.1: Space-time sampling characteristics of surface saturation mapping from 30 different studies which employed direct mapping of surface saturation, plus this contribution. The size of the studied area refers to the overall area of the investigated catchment or hillslope and the quantity value refers to the total number of times the area has been mapped (information acquired but not directly used in the publication has been included). Studies where different surface saturation mapping methods have been employed or where the same method was employed for different areas have been considered as multiple examples. Methods are indicated with “survey” (e.g. squishy boots method), “remote sensing” (e.g. ground-based and satellite) and “pedo-geo-botan” (i.e. pedological, geological and botanical aspects used to delineate permanently-surface saturated areas of the catchment). The total duration of the mapping period is indicated close to the circles for non-point observations (Y=years, M=months, W=weeks). In order to make the studies comparable in terms of surface saturation frequency of observation, we considered only the most recurrent time interval between two observations for each study. Studies which reported a seasonal mapping were included under the monthly frequency. Note that the big circle (which corresponds to a year of digital images acquired every minute during day time by Silasari et al. 2017) is not in scale for display purposes. References for the 30 studies considered for the review figure: Ali et al., 2013; Ambroise, 2016; Bari, Smettem, & Sivapalan, 2005; Birkel et al., 2010; Blazkova, Beven, & Kulasova, 2002; Brun et al., 1990; Buttle & Sami, 1992; Chabot & Bird, 2014; Coles & McDonnell, 2018; Creed, Sanford, Beall, Molot, & Dillon, 2003; D. A. De Alwis, Easton, Dahlke, Philpot, & Steenhuis, 2007; Devito, Creed, & Fraser, 2005; Dunne et al., 1975; Franks, Gineste, Beven, & Merot, 1998; Gineste, Puech, & Mérot, 1998; Glaser et al., 2016; Grabs, Seibert, Bishop, & Laudon, 2009; A. Güntner, Uhlenbrook, Seibert, & Leibundgut, 1999; Andreas Güntner et al., 2004; Inamdar & Mitchell, 2007; Kulasova, Beven, Blazkova, Rezacova, & Cajthaml, 2014; Latron & Gallart, 2007; McDonnell & Taylor, 1987; Mengistu & Spence, 2016; Pfister et al., 2010; Phillips et al., 2011; Rinderer, Kollegger, Fischer, Stähli, & Seibert, 2012; Roulet, 1990; Silasari et al., 2017; Tanaka et al., 1988. The bibliography for the 30 studies considered for the review figure can be found in Appendix 5.

5.2 Study site – the Weierbach catchment

The Weierbach experimental catchment (0.42 km²) is located in North-West Luxembourg (49°49' N, 5°47' E) (Fig. 5.2). The climate is semi-oceanic, with an annual average precipitation of 918 mm (2011-2017). Precipitation is rather evenly distributed throughout the year, whereas streamflow is lowest from May to September, mainly due to evapotranspiration losses. Pedology and geology are quite homogeneous throughout the catchment. Slate-dominated bedrock is fractured from 1.4 meters to 5 meters depth. Soil consists of a thin organic topsoil (~ first 5 cm) above a sandy-loamy *solum* (up to 50 cm depth) and *subsolum* (from 50 to 140 cm depth) characterised by rock fragments, , which volumetric portion increases with depth from 25% in the *solum* to more than 80% in the deeper fraction of the *subsolum* (Gourdol et al., 2018; Juilleret et al., 2011). Drainage porosity decreases from the *solum* (30% drainage porosity) to the *subsolum* (10% drainage porosity) (Gourdol et al., 2018).

Elevation ranges from 458 to 513 m. a.s.l. Topography is characterised by a quasi-horizontal plateau, covering 54% of the catchment and cut by steep ($\geq 5^\circ$) V-shaped valleys.

Vegetation is composed of Oak and Beech trees on the western side of the catchment and Spruce on the eastern side. Ferns and herbaceous plants dominate in the riparian zone. In this study, we identify the riparian zone considering a combination of different criteria. The change in dominant vegetation and the presence of shallow clay-loam, organic soil (i.e. Leptosol), peculiar of the low relief near-stream area of the catchment, set a visual basis for differentiating riparian from other landscape elements (i.e. hillslopes, plateau). The riparian zone is gently sloped ($<5^\circ$) and covers 1.2% of total catchment area.

The catchment's runoff response to precipitation is influenced by a storage threshold (Martínez-Carreras et al., 2016) and changes between the dry and the wet season. In case of dry antecedent conditions the catchment produces a single spiky peak of short duration (i.e. hours), while the response is bimodal during wet antecedent conditions - with a first peak followed by a broader second peak of longer duration (extending up to several days). Martínez-Carreras et al. (2016) showed that the first peak is mainly composed of water from precipitation, throughfall and rapid hillslope-riparian-stream connectivity through saturation excess overland flow and preferential flowpaths (such as macropores and/or fractures along the hillslopes), while the second peak mainly consists of infiltrated soil water and groundwater flowing through the fractured bedrock, once the storage threshold is exceeded.

5.3 Materials and Methods

5.3.1 Hydro-meteorological measurements and catchment storage calculation

Hydro-meteorological measurements are carried out in the Weierbach catchment since 2002 as part of a long-term monitoring programme. Water levels were measured and recorded every 15 minutes by a pressure transducer (ISCO 4120 Flow Logger) installed at a V-notch weir at the catchment outlet (Fig. 5.2) and translated into discharge via a rating curve (based on salt dilution measurements). Precipitation data were measured at a canopy-free location in the Weierbach catchment (see Fig. 5.2) and recorded every 5 minutes with a tipping bucket (Young, model 52203, connected to a Campbell logger CR200X). At the same location, air temperature and relative air humidity were monitored. These data were combined with readings from a meteorological station in Roodt (about 3.5 km from the catchment) to calculate the reference evapotranspiration (ET₀) following the FAO Penman-Monteith equation (Allen et al., 1998).

Ground water (GW) levels were measured every 15 minutes in four piezometers: GW2 (2.00 m depth, screened for the last lower 1.36 m) and GW3 (2.35 m depth, screened for the last lower 1.60 m) placed along a hillslope, and GW5 (7.57 m depth, screened for the last lower 3.82 m) and GW6 (4.85 m depth, screened for the last lower 3.50 m) located on the plateau (Fig. 5.2).

Volumetric soil water content (VWC) was measured in the shallow soil every 15 minutes using a Campbell CS616 sensor installed at 10 cm depth along a transect through the HRS continuum (Fig. 5.2, soil moisture transect), covering the west upslope (Beech-covered), mid-hillslope, foot of the hillslope, riparian zone and east upslope (Spruce-covered). Additionally, soil VWC was measured every 30 minutes using Campbell CS650 sensors installed at 10, 20, 40 and 60 cm depth in four sites (Fig. 5.2, soil moisture sites 3, 4, 5 and 7). Sites 3 and 4 are placed at low hillslope positions (Beech-covered and Spruce-covered, respectively), site 5 is placed at mid-hillslope position (Pines-covered) and site 7 is placed on the plateau (Beech-covered).

Catchment storage estimates were calculated following the methodology developed by Martínez-Carreras et al. (2016). In their study, the total amount of water stored in the catchment at a given time was calculated as the sum of storage in three separate zones:

$$S_{\text{TOTAL}} = S_{\text{UNSAT}} + S_{\text{SAT}} + S_{\text{RES}}$$

Where S_{UNSAT} is the water stored in the variably unsaturated zone (estimated from the VWC of the soil above the water content at field capacity – measured at the different soil depths in sites 3, 4, 5 and 7), S_{SAT} is the water stored in the variably saturated zone (within the range of water table fluctuations – estimated from GW levels in the hillslope and in the plateau: GW3 and GW5 respectively, in this study) and S_{RES} is the water stored in the residual saturated zone (i.e. estimated drainage porosity of the basal layer, fractured bedrock and fresh bedrock). S_{TOTAL} is obtained for the different landscape elements by multiplying the value of total storage by the

area of each element. For more specific information on the calculation of catchment storage the reader is referred to Martínez-Carreras et al. (2016).

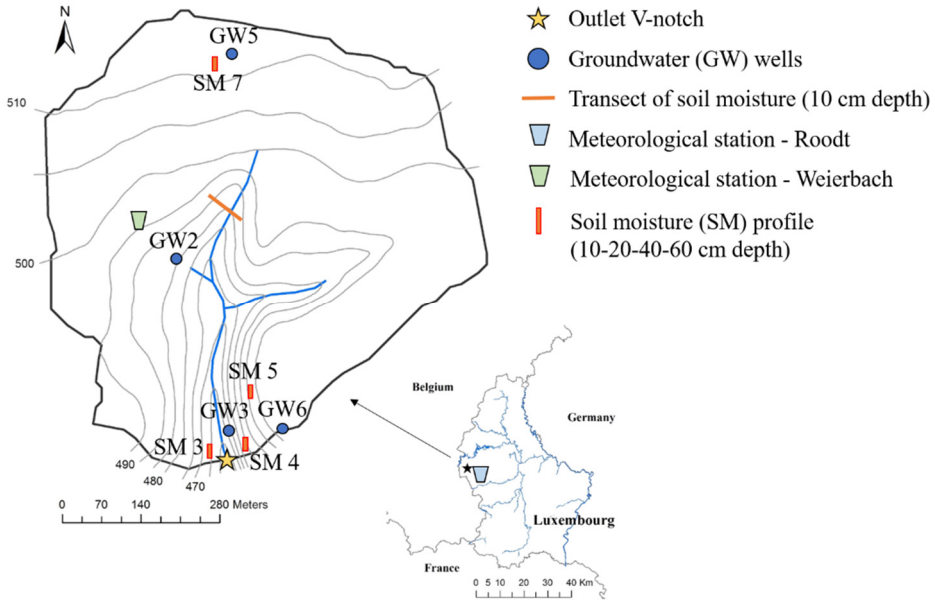


Figure 5.2: Location and instrumentation map of the Weierbach catchment.

5.3.2 Monitoring of surface saturated areas in the riparian zone

We focused on seven distinct riparian areas in the Weierbach catchment (Fig. 5.3). Each area was labelled with an abbreviation (cf. areas' name in Fig. 5.3) indicating the stream branch where it is located (i.e. L = riparian areas on the Left stream branch; M = riparian areas on the Middle branch; R = riparian areas on the Right branch and S = riparian areas on the main Stream) and its position along the branch (i.e. numbered from downstream to upstream). Descriptive topographic characteristics of the different riparian areas, such as average elevation, area extension (i.e. area covered by the monitoring) and maximum riparian width, were extracted from a high resolution LIDAR DEM (~ 5 cm resolution). TIR observations (i.e. sequential images and videos) and visible light photographs of the different riparian areas were acquired for a total of 63 mapping campaigns with a weekly to fortnightly recurrence interval from November 2015 to December 2017. The used handheld TIR camera (FLIR T640, FLIR Systems, Wilsonville, OR, USA) is sensitive to the radiation emitted from an observed surface (or the first 0.1 mm of a water column) over a spectral range of 7.5 to 14 μm , produces images of 640x480 pixels and covers a temperature range of -40°C to 2000 °C, with a thermal sensitivity of < 0.035°C at 30°C. Information about object emissivity "ε" (usually set between 0.95 and 0.97 for freshwater), atmospheric temperature, air humidity, object's distance

from the device and reflected ambient temperature were provided to the camera in order to correct the detected temperature for these parameters (the correction is automatically done by the camera's software).

The final product of the TIR camera is an image (or video) reporting surface temperatures for each image pixel. This temperature information can be used to classify the pixels into pixels corresponding to water ponding or flowing at the ground surface (saturated pixels, i.e. stream & riparian ponds) and pixels representing surrounding material (unsaturated pixels, i.e. soil, rock & vegetation) (Fig. 5.4 a, b). In order to be able to discern these two pixel classes, a clear temperature contrast between surface water (saturated pixels) and surrounding material (unsaturated pixels) is required. Moreover, the camera view on the saturated surfaces has to be free from obstructions (e.g. vegetation, snow, fog, heavy rain). Below, we shortly explain how we transformed the information from the acquired TIR images into information on the extent of surface saturation. A detailed description of the post-processing workflow and the TIR imagery technique applied for surface saturation mapping in general can be found in Glaser et al. (2018).

In order to prepare the TIR images (or videos) for the extraction of the extent of surface saturation in the investigated riparian areas, we followed a sequence of post-processing steps. The sequence consisted of i) creating panoramic images by overlapping single images (or video frames) (Fig. 5.4 a, d), ii) transforming all panoramas from the same area into the same perspective by co-referencing them to a selected reference panorama, and iii) cropping all images to the same area of interest. For more details on the post-processing steps, we refer to figure 3 in Glaser et al. (2018), where the methodology for the TIR approach was developed. We then calculated the percentage of saturated pixels in each panorama as proxy for the extent of surface saturation in the investigated areas following the manual approach for the generation of saturation maps described in Glaser et al. (2018). This approach consists in (I) manually selecting the temperature range corresponding to surface saturation, (II) adapting the selected range to create a saturation map with a pattern of saturated pixels matching best the saturation pattern identified via visual inspection of the TIR panoramas and visible light images (here defined as optimal solution) and (III) calculating the number of pixels falling into that temperature range over the total number of pixels of each image (Fig. 5.4 e). The three steps were repeated for each location and observation date, meaning that an individual temperature range was selected for each TIR panorama. TIR panoramas that showed poor temperature contrast and/or high influence from obstructing elements were excluded from the analyses (34% of the 441 acquired panoramas).

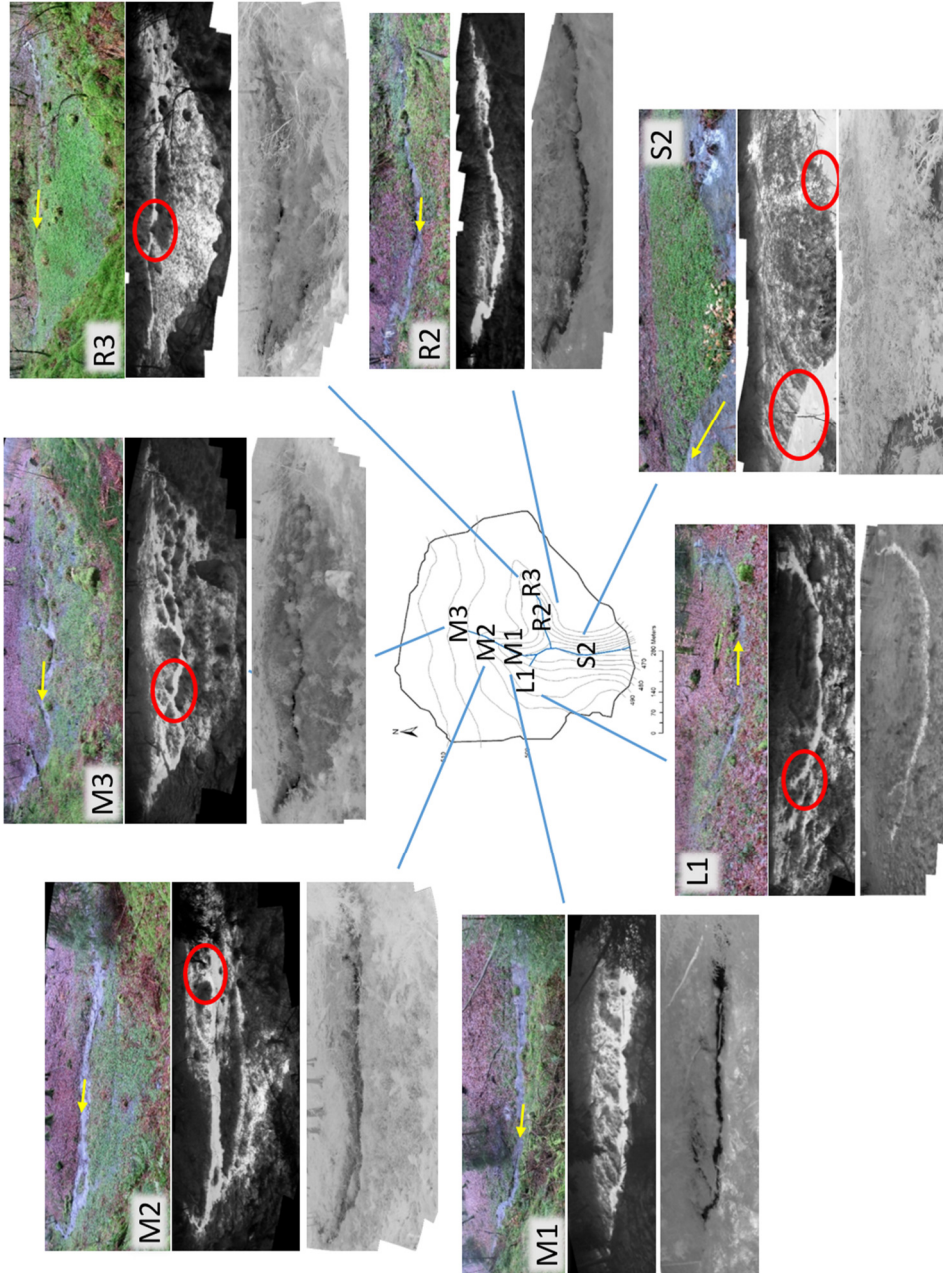
As shown by Glaser et al. (2018), the manual selection of temperature ranges is to date the best approach for generating reliable saturation maps from TIR datasets where images show very variable conditions (e.g. in terms of wetness, overall temperature range) and present slight perspective shifts. However, since the manual selection of an optimal solution for the saturation estimation is a subjective process, different operators may tend to select different optimal temperature ranges, including more or less pixels into the group of saturated pixels based on their individual perception.

To investigate the range of possible surface saturation outcomes, we varied for some panoramas the width of the saturated pixels temperature range (i.e. changing the higher and the lower values in small temperature steps) until the saturation pattern clearly mismatched the saturation pattern selected as the optimal

solution (cf. Glaser et al., 2018). The saturation pattern including the higher number of pixels, and still reflecting the realistic saturation pattern, was used to determine the maximum estimate of surface saturation. The saturation pattern including the lower number of pixels, and still reflecting the realistic saturation pattern, was used to determine the minimum estimate of surface saturation. We estimated different saturation outcomes for the investigated riparian areas taking into account images collected during different saturation levels (i.e. 5 to 7 images for each investigated area). We then plotted the minimum and maximum estimates of saturated pixels against the optimal estimation (within each area) and determined a regression equation from which we retrieved the minimum and maximum estimates of saturation for the whole time series of saturation of each of the areas.

The overall amount of surface saturation estimated from the TIR images in each area represents both riparian surface saturation and water in the stream channel. The stream channel receives water contributions from the riparian zone (i.e. lateral contribution) (cf. Fig. 5.3 red circles) and water supply from upstream along the stream channel itself (i.e. longitudinal/upstream contribution). The relative amount of water provided by these two different contributions is difficult to disentangle. However, between the investigated riparian areas, we expect upstream contributions to be higher in downstream areas compared to headwater areas. In order to strengthen the comparison of the relationships between riparian surface saturation in different areas (i.e. headwater areas vs. downstream areas) and stream discharge (cf. Fig. 5.11 in results section), we provide an example of an estimation of downstream areas' surface saturation with a reduced influence of the upstream contribution (i.e. excluding the stream from the calculation of surface saturation). However, this exercise leads to a considerable loss of information on the overall level of surface saturation since, by doing so, a substantial part of surface water represented by the lateral inflows is also excluded. For this reason, the estimation of surface saturation with a reduced influence of the upstream contribution is only provided as an example, and it is not employed in all the analyses.

Figure 5.3 (next page): Location and example of visible light and TIR panoramic photo of each investigated riparian area for a wet and dry condition. Visible light images are shown for wet conditions only. In the TIR panoramas collected during wet conditions, saturated pixels correspond to the lighter colours. In the TIR panoramas collected during dry conditions, saturated pixels correspond to the darker colours (except for area L1) (pictures: M. Antonelli and B. Glaser). Yellow arrow: flow direction. Red circles: location of permanent springs.



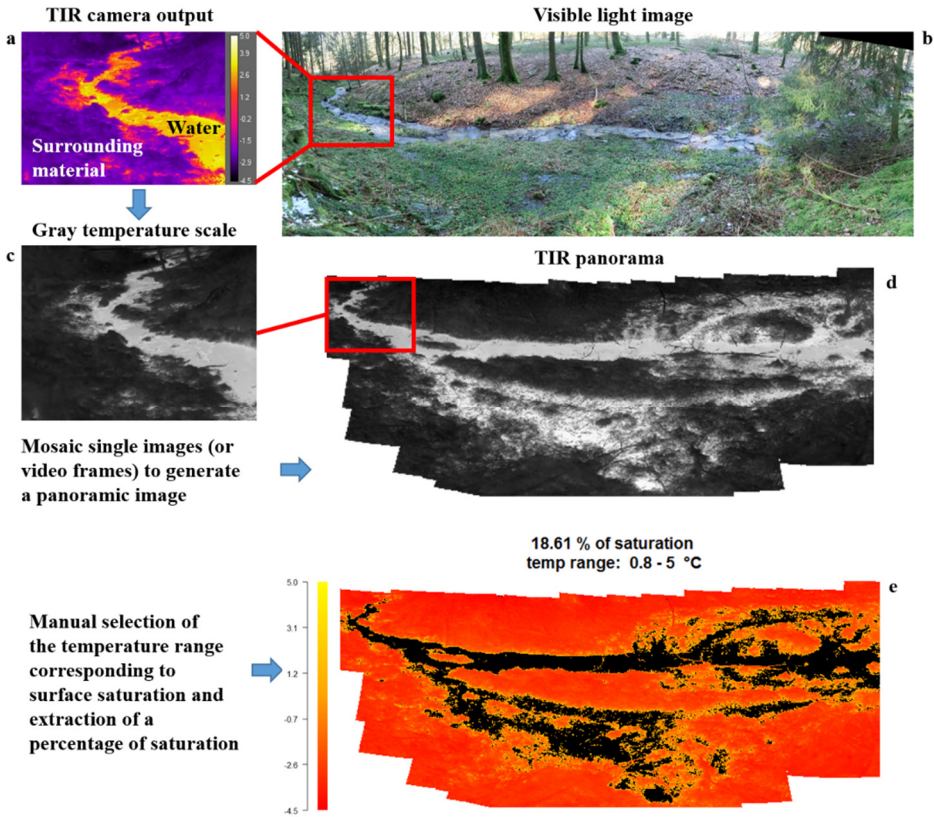


Figure 5.4: Workflow of the TIR image post-processing for the example of the TIR panorama of area M2 of 25/02/2016. For more details the reader is referred to Glaser et al. (2018).

5.3.3 Statistical data analysis

We analysed the time series of saturation of the seven riparian areas, in order to investigate the temporal dynamics of surface saturation. We applied a min-max normalisation to the percentage of saturated pixels for each area. We expressed the normalised values as a percentage in order to compare areas of different extension (cf. section 5.4.1). We will refer to these values as “normalised saturation”. For the normalisation we accounted for the percentage of saturated pixels from images acquired during periods where surface saturation was not affected by particular meteorological conditions such as frozen soils (which will be represented by normalised percentages below 0%) or rain-on-snow events (which will be represented by normalised percentages above 100%). By quantifying the observations obtained during the occurrence of frozen soils and rain-on-snow events in this way, they can be easily identified in the figures and provide information on the field conditions. These observations were retained in the statistical analysis of the

dataset because they are not statistical outliers. Nevertheless, we tested the statistics excluding these observations and the results remained consistent. Descriptive statistics and the non-parametric Mann-Whitney-Wilcoxon Test ($\alpha = 0.05$) were used to compare the temporal distribution of the normalised saturation in different areas.

In order to explore a possible influence of precipitation and evapotranspiration on the seasonal dynamics of surface saturation in the different areas, we compared the double mass curves (DMCs) of rainfall and runoff of the catchment for the two investigated hydrological years (HY) with the double mass curves of rainfall and surface saturation in the different areas (i.e. we cumulated the estimated values of normalised surface saturation from one date of observation to the other and highlighted moments of vegetation growth and high evapotranspiration). Classical rainfall-runoff DMCs can provide direct information on seasonal runoff formation (Pfister et al., 2002; Seibert et al., 2017). Similarly, by evaluating how cumulated surface saturation evolves in response to cumulated rainfall, we aimed to obtain information on the influence of seasonal variables (i.e. precipitation and evapotranspiration) on the development of surface saturation. Note that by cumulating normalised surface saturation we do not intend to give an estimation of a total amount of surface saturation of each HY. Instead, we consider the cumulated surface saturation as a way to identify periods of general increase or decrease of saturation.

As a measure of how fast the saturation changed in each area, we calculated the difference between the normalised saturation estimated on two consecutive dates and divided this value by the number of days in each period to obtain daily normalised rates of change. We tested similarities between the daily rates of change between different areas with the Mann-Whitney-Wilcoxon Test ($\alpha = 0.05$). The test was applied by taking into account each surface saturated area against every other area for the dates when an estimation of a change rate of saturation was available for both areas. Additionally, we tested if the difference in normalised saturation estimated between two consecutive dates was related to differences in GW levels, soil VWC along the HRS transect and soil VWC profiles at sites 3, 4, 5 and 7, catchment storage or to the amount of precipitation (expressed via the antecedent precipitation index - API - as per McDonnell, Owens, & Stewart, (1991)) observed between the same dates. We applied Spearman's rank correlation to test these relationships ($\alpha = 0.01$). As before, we only took into account the dates for which an estimation of saturation was available for the analysed area.

We applied Spearman's rank correlation test rho (ρ ; $\alpha = 0.01$) in order to test monotonic relationships between (I) the time series of normalised saturation estimated in the different investigated riparian areas and (II) between these values and the time series of hydrometric measurements (i.e. daily-averaged values of outlet discharge, estimated catchment storage, GW levels, soil VWC along the HRS transect and soil VWC profiles at sites 3, 4, 5 and 7). These relationships were tested for the whole study period.

In order to analyse the shape of the relationship between the surface saturation in the different areas and baseflow discharge at the catchment outlet, we relied on the observations of surface saturation that were not impacted by the occurrence of precipitation (i.e. images taken while rainfall occurred, during rising limbs or peaks of discharge and at the early stage of discharge recession) or by the occurrence of particular meteorological conditions such as frozen soils or rain-on-

snow events. This set of data describes the evolution of surface saturation along the gradual change in wetness state of the catchment and can be related to the surface saturation versus baseflow discharge relationship described by Ambroise (2016). We fitted various types of equations on the observations not impacted by the occurrence of precipitation and we found that power law equations ($Sat = a \cdot Q^b$) adequately approximate the observed trends (fitting carried out on non-transformed data; goodness-of-fit was tested with Kolmogorov-Smirnov test – p-value > 0.1).

5.4 Results

5.4.1 Hydrological response and catchment storage

We monitored the hydrological response of the Weierbach catchment from November 2015 to December 2017 (Fig. 5.5). Annual precipitation remained similar (921 mm/year and 913 mm/year) during the two monitored hydrological years (HY - extending from October to September of the following year). Annual runoff was ~752 mm/year and ~177 mm/year for the hydrological year 2015/2016 and 2016/2017, respectively. The particularly low runoff registered for the HY 2016/2017 may be explained by exceptionally low amounts of precipitation during the beginning of the HY, the low temperatures registered in January 2017, which caused the stream to freeze and the relatively higher evapotranspiration during the summer period compared to the HY 2016/2017 (Fig. 5.5). Accordingly, discharge was high for eight months (from November 2015 to June 2016) during the HY 2015/2016 and only for three months (from February to April 2017) during the HY 2016/2017. In December 2017 a rain-on-snow event produced a high peak discharge. Note that in January 2017 the stream was partially frozen (as a result no discharge data is available for that period).

Shallow soil VWC (10 cm depth) gradually decreased from the riparian zone toward the hillslopes. Riparian soil VWC was oscillating between a maximum of ~ 70% during wet conditions and a minimum of ~ 65 % during dry conditions. Shallow soil VWC at the other monitored locations was more variable (Fig. 5.5), showing marked reaction to precipitation. Soil VWC of the shallow soil measured in the Spruce-covered hillslope revealed a tendency of the soil to dry more rapidly than in other locations. Soil VWC measured in sites 3 and 4 was generally more responsive to precipitation compared to soil VWC measured at sites 5 and 7, at all depths (Fig. 5.6). Soil VWC measured at site 3 decreased from the 10 cm depth to the 60 cm depth, while the opposite was observed at site 7. Soil VWC measured at sites 4 and 5 was more similar along the depth profile (Fig. 5.6). As previously observed, Soil VWC profiles measured in the Spruce-covered and Pine covered hillslopes at all depths revealed a tendency of the soil to dry more rapidly than in other locations. GW levels responded to precipitation in all four wells. Water levels in GW2 (close to a source area) and GW3 (hillslope foot) were always shallower than 2.00 m. GW5 and GW6 (both located on plateaus) behaved differently - mostly during dry periods, when the water level in GW5 would recede at a constant rate, while GW6 would dry quickly and show a reaction to new water inputs more similar to the response in soil moisture (also in comparison to the shallower GW2 and GW3).

During the wet periods, catchment storage and discharge showed very similar trends. During the dry periods – when catchment storage mainly corresponded to the ground water reservoir – precipitation triggered more pronounced changes in discharge (as a single peak) in comparison to storage (cf. Fig. 5.5 b red arrows).

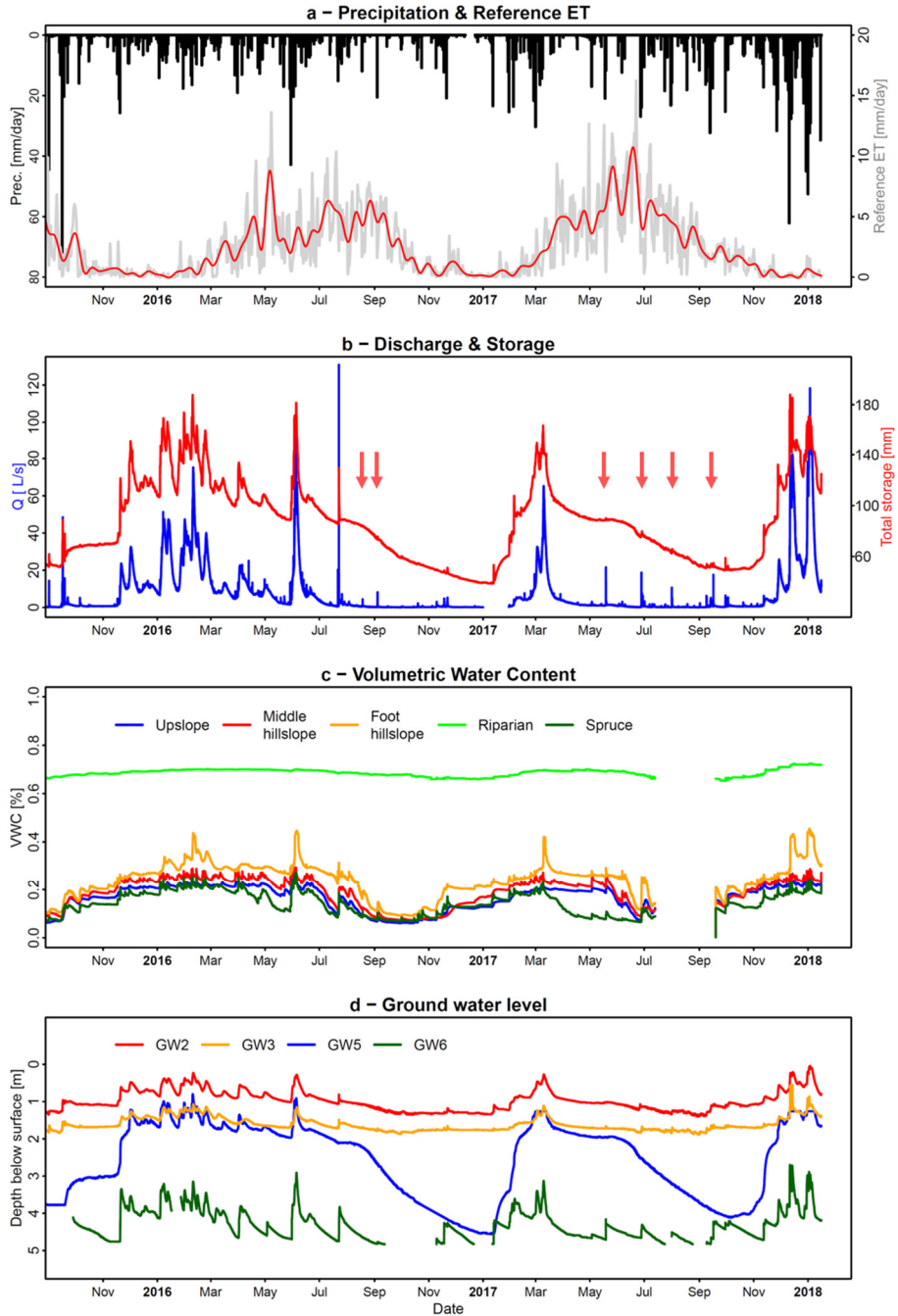


Figure 5.5: Time series of a) precipitation (black) and reference evapotranspiration (grey – smoothed trend of reference ET showed in red), b) discharge and catchment storage (red arrows show moments when discharge response was more pronounced than catchment storage), c) soil volumetric water content along the hillslope-riparian-stream transect (10 cm depth), and d) ground water levels from October 2015 to January 2018

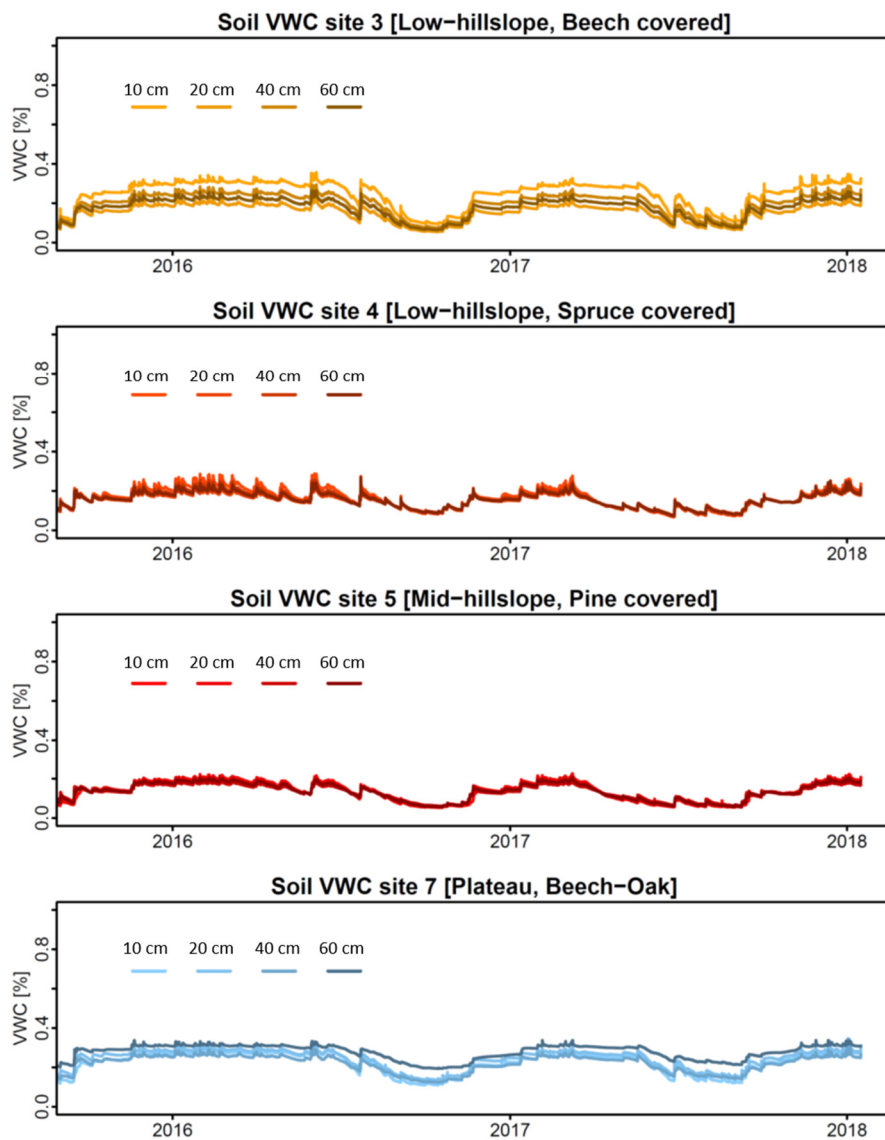


Figure 5.6: Time series of soil volumetric water content measured at 10, 20, 40 and 60 cm depth at sites 3, 4, 5 and 7, from October 2015 to January 2018.

5.4.2 Characteristics of the investigated riparian areas and correspondent upslope catchments

We assigned the investigated riparian areas in the Weierbach catchment to three main groups, based on intrinsic area characteristics (Table 5.1). Areas L1, M3 and R3 correspond to the most upstream locations (i.e. source areas) of the stream. They are wide (8.3 m in average) and fed by perennial groundwater exfiltration (e.g. stable exfiltration points observed via TIR imagery throughout the year, cf. Fig. 5.3). Areas M2 and S2 display similar characteristics, but are located further downstream (Fig. 5.3). In areas M1 and R2, the riparian zones are narrower (4.9 m in average) and without clearly identified points of perennial groundwater exfiltration. Based on these differences, we qualify the first group as “Stream Source Areas with Perennial springs (PSA)”, the second group as “Areas along the stream with Perennial Springs (PSpA)” and the third group as “Areas along the stream with Non-Perennial Springs (N-PSpA)”.

Table 5.1: Characteristics of the investigated riparian areas.

Rip. area	Area monitored with TIR imagery (m ²)	Headwater reach	Riparian max width (m)	Perennial GW exfiltration observed	Area elevation (Average – m.a.s.l.)	Group
L1	153.22	Yes	8.80	Yes	477	PSA
M1	83.80	No	5.86	No	479	N-PSpA
M2	168.95	No	10.37	Yes	480	PSpA
M3	231.69	Yes	9.53	Yes	483	PSA
R2	115.54	No	3.97	No	476	N-PSpA
R3	155.19	Yes	6.57	Yes	480	PSA
S2	169.66	No	8.87	Yes	464	PSpA

5.4.3 Range of surface saturation estimations

The estimated time series of surface saturation is shown with the range of maximum and minimum estimates of saturation for area S2 as an example in Fig. 5.7 (see Appendix 5 for the other areas). For all areas, the range between the calculated maximum and minimum estimates of saturation was larger (i.e. wider bounds around the optimal solution) for the panoramas presenting higher saturation,

and smaller (i.e. narrower bounds around the optimal solution) for the panoramas presenting lower saturation. Indeed, in TIR panoramas showing higher saturation, the threshold between the saturated and the unsaturated pixels often appeared less defined than in the TIR panorama showing lower saturation. The range between the maximum and minimum estimated saturation was narrow enough to preserve the general trend of the time series of estimated saturation as observed when considering the optimal solution. Thus, the temporal variability of surface saturation exceeded the variability that may derive from uncertain estimations of saturation (reflected in the range between the maximum and minimum estimates of saturation) and it is very likely that the overall estimated trend of saturation would remain similar, also if a different person would carry out the image processing procedure.

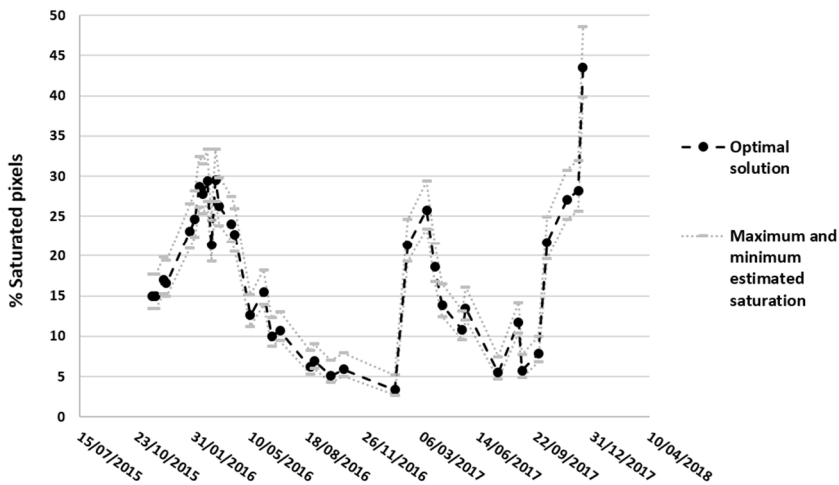


Figure 5.7: Range of possible outcomes for the estimation of the percentage of saturated pixels for area S2. Linear interpolations between the different observation dates are displayed as dotted and dashed lines and are meant to show the overall time series trend and might not reflect the actual saturation. The estimation for the other six investigated areas is reported in Figure A5.1 in Appendix 5.

5.4.4 Spatio-temporal dynamics of surface saturation and their relationship with meteorological conditions

The values of the estimated normalised surface saturation were highly monotonically related between the different areas over the whole study period (Spearman's rank test ρ not lower than 0.68 for all the correlations, p -value < 0.01). However, the seven areas reached their respective minima and maxima of saturation at different times (Fig. 5.8). In January 2017, the occurrence of frozen water in the riparian area corresponded to very low surface saturation in all areas (i.e. normalised saturation below 0%), except for areas M1 and M3, which reached their minimum

saturation in December and November 2016, respectively. Maximum saturation in areas M1, R2 and S2 resulted from a significant rain-on-snow event in December 2017 (i.e. normalised saturation above 100%). For the other four areas, the maximum level of saturation (i.e. normalised saturation = 100%) was reached in February 2016, under no particular meteorological conditions.

The distribution of normalised saturation from the time series was similar for areas L1, M2, M3, R2 and R3 (Mann-Whitney-Wilcoxon test p-value always higher than 0.05), whereas the distribution of areas M1 and S2 were statistically different from all other areas (Mann-Whitney-Wilcoxon test p-value always lower than 0.05 for M1 and S2) (Fig. 5.9). Areas M1, R2 and S2 had particularly high median values (Fig. 5.9; Table 5.2). The variability of the observations around the mean values (i.e. standard deviation) was similar for all areas (Table 5.2), although slightly higher in area S2 (~38%). A summary of the descriptive statistics for the normalised saturation distribution of the seven riparian areas is reported in Table 5.2 and Figure 5.9. All areas presented a similar distribution of the daily rates of change in saturation (Mann-Whitney-Wilcoxon test p-value always higher than 0.5, data not shown).

The comparison of the DMCs of rainfall-runoff and rainfall-surface saturation revealed a similar behaviour of runoff and surface saturation in all areas in response to precipitation and vegetative periods with high ET (Fig. 5.10). From October to May of the HY 2015/2016, cumulated runoff and cumulated surface saturation consistently increased with increasing cumulated precipitation, whereas, with the beginning of the vegetative period in May (Fig. 5.10 – green shade), additional precipitation did not provoke an increase in cumulative runoff and surface saturation. Two events occurring in June and July provoked cumulated runoff to sharply increase again while cumulated surface saturation appeared to be affected by these events only in areas M1 and M2. During the HY 2016/2017, both cumulative runoff and surface saturation remained low during a period of low precipitation amounts and low air temperatures with frost and started to accumulate with considerably higher amounts of precipitation from February on. Cumulative runoff abruptly flattened with the beginning of the vegetative period while surface saturation flattened more gradually, especially in PSpA and area R2. At the beginning of the HY 2017/2018, high precipitation and a rain-on-snow event caused both high cumulative amounts of runoff and surface saturation within a short period (especially in areas S2).

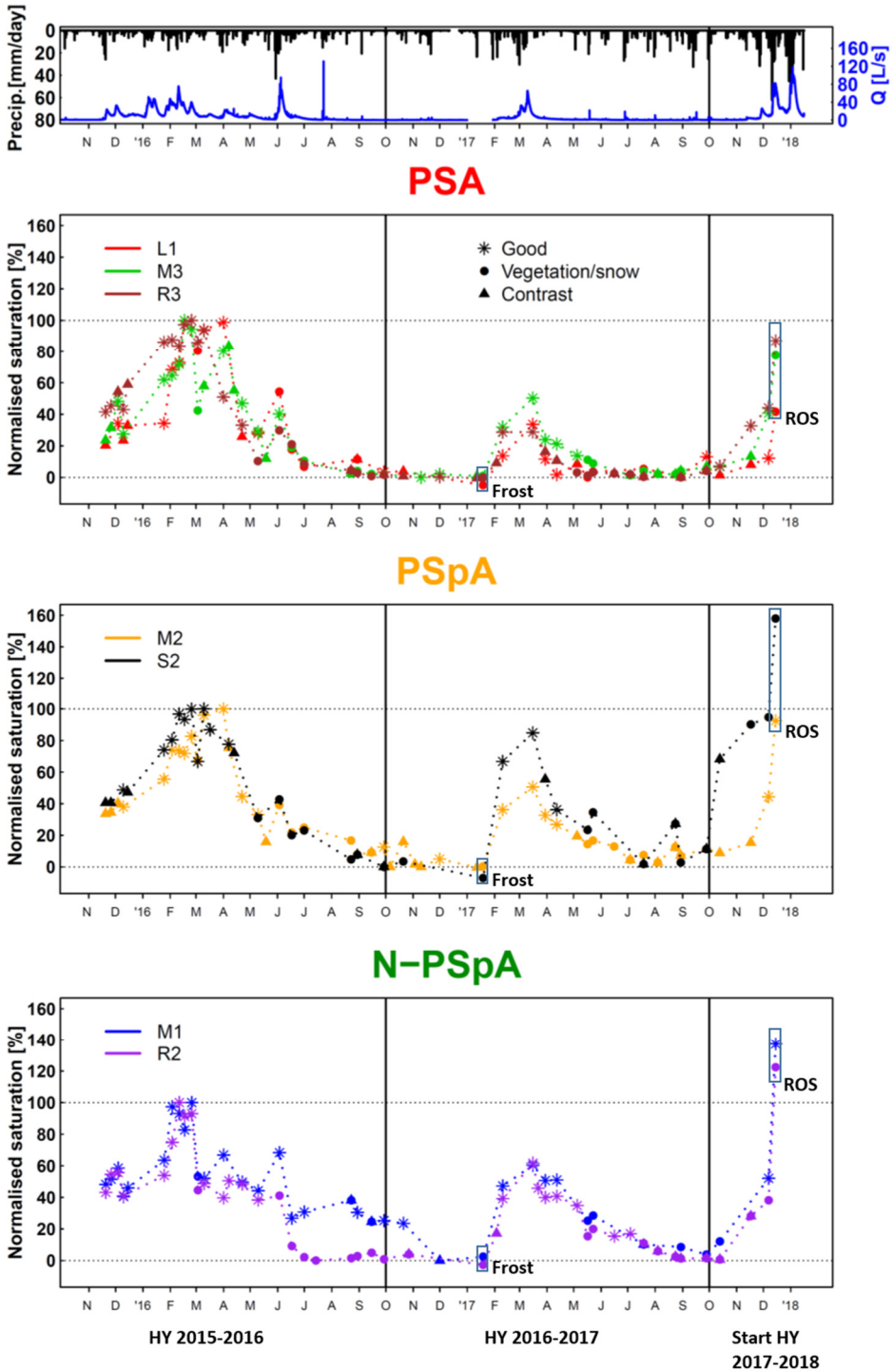


Figure 5.8 – see figure caption on next page.

Figure 5.8 (previous page): Time series of precipitation and discharge (upper panel) and temporal evolution of normalised saturation obtained from TIR observations in the seven different riparian areas grouped according to the PSA, PSpA and N-PSpA classification (PSA = Stream Source Areas with Perennial springs; PSpA = Areas along the stream with Perennial Springs; N-PSpA = Areas along the stream with Non-Perennial Springs). Out of the total number of 441 acquired TIR panoramas, 291 panoramas were used for the estimation of a value of surface saturation. Data represented with an asterisk refer to estimated values of surface saturation from TIR panoramas with optimal temperature contrast and no obstructive elements between the camera and the object ($n = 101$). Data represented with a circle and a triangle refer to TIR observations that were slightly influenced by the presence of vegetation or snow ($n = 110$) and where the temperature contrast was not optimal ($n = 80$), respectively, but that were still usable for the estimation of a value of surface saturation. Normalisation was done according to the highest and lowest observed percentage of saturation within each area individually, conditions with frost and rain-on-snow excluded. Frost = condition with frozen stream and riparian soil. ROS = rain-on-snow event.

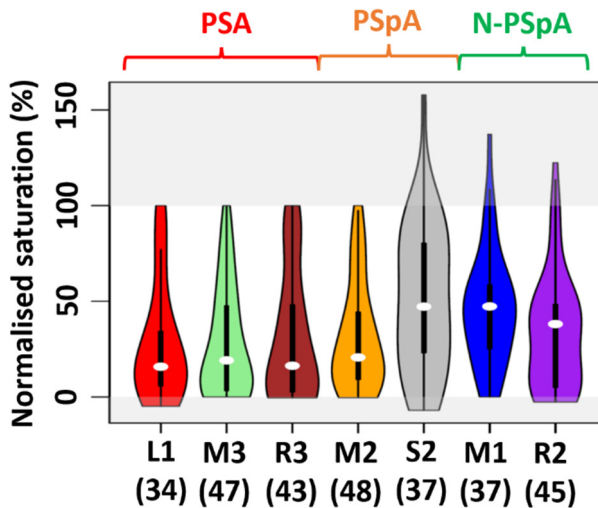


Figure 5.9: Violin plots of the distribution of normalised surface saturation from the time series of the seven studied areas (grouped according to the PSA, PSpA and N-PSpA classification: PSA = Stream Source Areas with Perennial springs; PSpA = Areas along the stream with Perennial Springs; N-PSpA = Areas along the stream with Non-Perennial Springs). Shaded areas highlight values of saturation acquired during particular boundary conditions such as frozen riparian soils (normalised saturation below 0%) and rain-on-snow events (normalised saturation above 100%). The number of samples used for each violin plot is indicated in brackets.

Table 5.2: Summary of the descriptive statistics for the distribution of normalised surface saturation from the time series of the seven studied areas. StDev = standard deviation. L1 n = 34; M1 n = 37; M2 n = 48; M3 n = 47; R2 n = 45; R3 n = 43; S2 n = 37.

	L1	M1	M2	M3	R2	R3	S2
Min	-4.90	0.00	-0.36	0.00	-2.74	-0.52	-6.98
Max	100.00	137.32	100.00	100.00	122.46	100.00	157.88
Mean	28.29	46.07	31.43	28.48	33.34	30.75	51.52
StDev	30.60	29.80	28.51	28.93	30.15	33.49	38.06
Median	15.70	47.25	20.63	19.07	38.11	16.31	47.21

Figure 5.10 (next page): Comparison between the rainfall-runoff DMCs (black line) and the surface saturation-runoff DMCs (coloured points) for the different investigated areas and hydrological years. Areas are grouped considering the PSA, PSpA and N-PSpA classification (PSA = Stream Source Areas with Perennial springs; PSpA = Areas along the stream with Perennial Springs; N-PSpA = Areas along the stream with Non-Perennial Springs). Frost = condition with frozen stream and riparian soil. ROS = rain-on-snow event. Green shading = occurrence of vegetation, high estimated reference ET.5.4.5 Relationship between surface saturation dynamics and hydrometric measurements.

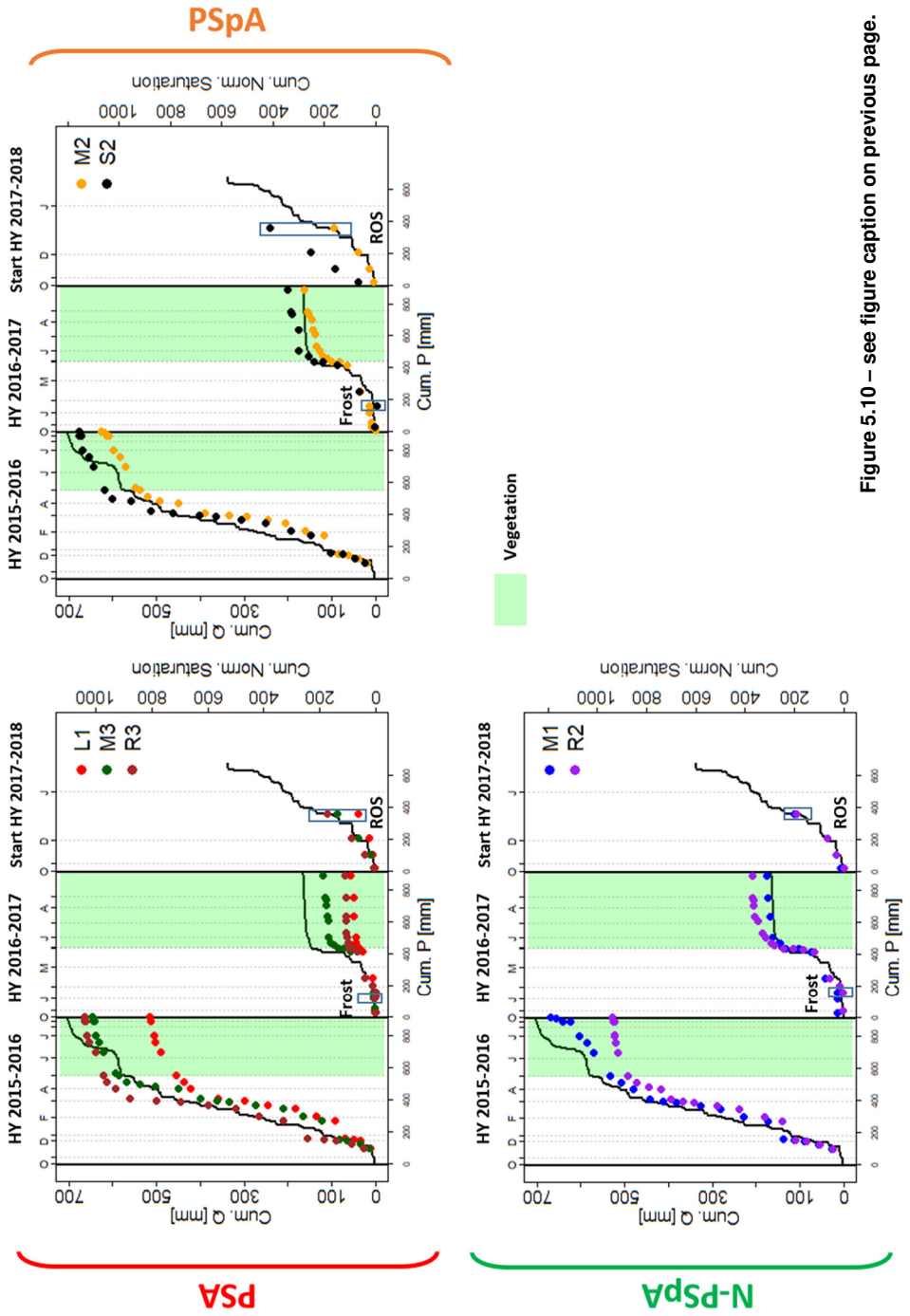


Figure 5.10 – see figure caption on previous page.

For all riparian areas, we identified a strong monotonic relationship between normalised saturation and catchment discharge (Spearman's rank test ρ not lower than 0.78 for all areas, p -value < 0.01) (Table 5.3). We found overall positive and significant monotonic relationships between the normalised saturation in the different areas and GW levels, VWC and the estimated storage of the catchment (Table 5.3). In particular, estimated catchment storage showed higher correlation with normalised saturation in areas M1, M2 and M3 ($\rho \sim 0.92$). GW levels measured in locations 2, 3 and 5 had in general higher correlation with normalised saturation ($0.73 \leq \rho \leq 0.94$) compared to GW6 ($0.59 \leq \rho \leq 0.75$) for all the areas. Soil VWC along the HRS transect had in general high correlation with normalised saturation in all areas ($0.64 \leq \rho \leq 0.88$), with the lower correlation being between saturation in area S2 and VWC measured at middle and foot hillslope positions and between saturation in area L1 and VWC measured at riparian position. Soil VWC measured in sites 3, 4, 5 and 7 at 10, 20, 40 and 60 cm depth also was highly correlated with normalised surface saturation in all areas ($0.67 \leq \rho \leq 0.88$), with the lower correlation being between saturation in area S2 and VWC in all sites and depths. Also, VWC measured at site 4 (low hillslope Spruce-covered) was generally less correlated with normalised surface saturation in all investigated riparian areas.

Changes in the extent of surface saturation between two observation dates were significantly related to the changes of GW level in location GW3 ($0.60 < \rho < 0.77$). All the areas except areas M2 and R2 showed also significant correlation with changes of GW level in GW2 ($0.58 < \rho < 0.67$) (Table 5.4). Area M1 was particularly correlated also with the GW levels measured in location GW5 ($\rho = 0.72$). Changes in the extent of surface saturation between two observation dates were also significantly related to the changes in catchment storage ($0.65 < \rho < 0.84$) in all areas. A low but significant correlation of the changes of surface saturation with the API was observed for the areas L1, M1, R2 and S2 ($\rho = 0.50$). Changes in soil VWC along the HRS transect (10 cm depth) were not significantly correlated to changes in surface saturation between two observation dates for any of the investigated riparian areas (Table 5.4). Changes in soil VWC measured at sites 3, 4, 5 and 7 at 10, 20, 40 and 60 cm depth were significantly correlated to changes in surface saturation (except for area L1 and soil VWC at site 3 at 10 cm depth) (Table 5.4). However, only surface saturation changes in areas R3 and S2 showed a good correlation with changes in soil VWC measured at different sites and depths. In particular, surface saturation changes in area R3 and S2 were particularly related to changes in soil VWC measured at site 4 and 5 (at low and mid slope positions, respectively) with $\rho \geq 0.56$ for area R3 and $\rho \geq 0.60$ for area S2.

The surface saturation vs. outlet baseflow discharge relationship has been investigated for the seven riparian areas (Fig. 5.11). At low baseflow discharge, the relationship between normalised saturation and discharge was more linearly shaped. Yet at higher baseflow discharge, a light hysteretic effect could be observed in particular for areas L1, M2, M3 and R3. In areas S2, M1 and R2, the observations obtained during low flow appeared more scattered than for the other areas, probably due to stream water contribution from upstream. In order to give an example of a reduced influence of upstream water contribution in areas M1, R2 and S2, we re-estimated the extent of surface saturation after having excluded stream pixels from the TIR images. One can notice a general shift toward lower saturation for areas M1 and R2 (see Fig. 5.11 M1, R2 and S2 "no upstream contr."). This is less pronounced for area S2, probably as a result of the presence of permanent springs within this

area, which maintain the riparian zone generally wetter. In general, scattering in the observations at low flow appears reduced in areas S2, M1 and R2 after having reduced the influence of upstream water contribution. Note that we did not apply the exercise of reducing upstream contribution to area M2, because we frequently inferred from the TIR images that the portion of stream before the perennial riparian inflow in area M2 was dry. Analysing the fitted curves for the surface saturation vs. baseflow discharge relationship for PSpA and N-PSpA (see Fig. 5.11), saturation in PSpA had an overall similar relationship with baseflow discharge: saturation in the two areas increased with higher discharge following a similar power law, especially when considering the saturation in areas S2 after the effect of the upstream contribution has been attenuated. The N-PSpA saturation vs. baseflow discharge relationship seemed to differ between each other and from the other areas, both before and after reducing the effect of upstream contributions. Finally, surface saturation in PSA presented similar relationships with baseflow discharge during low discharge rates. However, as baseflow discharge increased, saturation in areas M3 and R3 increased faster compared to area L1 and the other areas in general. When considering the observations affected by precipitation (Fig. 5.11, grey dots), a slight hysteretic effect could be observed for the surface saturation vs. discharge relationship, in particular for areas L1, M2, M3 and R3 at higher discharge.

Table 5.3: Spearman's rank correlation between the normalised saturation in the seven areas and hydrometric variables. All shown correlations are significant with $\alpha=0.01$. Q = catchment discharge (l/s) at catchment outlet; Stor. tot = total catchment storage; GW = ground water; VWC_U = volumetric water content (VWC) in upslope position (beech-covered); VWC_M = VWC in middle slope position; VWC_F = VWC in foot of the slope position; VWC_R = VWC in riparian zone; VWC_S = VWC in upslope position (spruce-covered). Site 3 10 cm = VWC measured at site 3 at 10 cm depth (similar naming for the other VWC sites and depths).

	L1	M1	M2	M3	R2	R3	S2
Q	0.86	0.92	0.89	0.91	0.88	0.91	0.78
Stor. tot	0.84	0.93	0.92	0.91	0.87	0.89	0.74
GW2	0.83	0.90	0.89	0.91	0.87	0.91	0.79
GW3	0.86	0.89	0.88	0.90	0.85	0.94	0.84
GW5	0.82	0.92	0.91	0.91	0.84	0.85	0.73
GW6	0.59	0.66	0.71	0.74	0.69	0.75	0.69
VWC_U	0.80	0.83	0.87	0.88	0.78	0.86	0.71
VWC_M	0.79	0.80	0.85	0.86	0.76	0.82	0.64
VWC_F	0.79	0.83	0.85	0.87	0.76	0.78	0.69
VWC_R	0.65	0.83	0.86	0.85	0.70	0.77	0.75
VWC_S	0.83	0.76	0.78	0.79	0.70	0.82	0.67
Site 3 10cm	0.84	0.82	0.86	0.88	0.79	0.86	0.71
Site 3 20cm	0.80	0.81	0.82	0.83	0.79	0.83	0.70
Site 3 40cm	0.84	0.84	0.85	0.87	0.81	0.87	0.73
Site 3 60cm	0.82	0.82	0.84	0.85	0.8	0.85	0.71
Site 4 10cm	0.82	0.78	0.76	0.77	0.72	0.81	0.67
Site 4 20cm	0.79	0.79	0.75	0.75	0.72	0.79	0.70
Site 4 40cm	0.82	0.79	0.76	0.76	0.72	0.80	0.69
Site 4 60cm	0.81	0.79	0.76	0.76	0.72	0.80	0.69
Site 5 10cm	0.84	0.81	0.81	0.84	0.75	0.84	0.78

Saturated areas through the lens: 1

Site 5 20cm	0.84	0.82	0.80	0.83	0.75	0.84	0.75
Site 5 40cm	0.83	0.84	0.81	0.84	0.76	0.86	0.76
Site 5 60cm	0.83	0.83	0.81	0.83	0.75	0.84	0.76
Site 7 10cm	0.83	0.80	0.84	0.86	0.79	0.84	0.68
Site 7 20cm	0.83	0.81	0.83	0.86	0.80	0.85	0.70
Site 7 40cm	0.80	0.79	0.82	0.84	0.77	0.82	0.67
Site 7 60cm	0.79	0.82	0.85	0.88	0.81	0.86	0.71

Table 5.4: Spearman's rank correlation between the changes in the amount of surface saturation between two consecutive observation dates and changes of hydrometric variables (GW = ground water; Stor. tot = total catchment storage; Site 3 10 cm = soil volumetric water content measured at site 3 at 10 cm depth – similar naming for the other sites and depths) and antecedent precipitation index (API) calculated between the same observation dates. All shown correlations are significant with $\alpha=0.01$. Changes in soil volumetric water content measured at 10 cm depth along the hillslope-riparian-stream transect did not show significant correlation with changes in surface saturation.

	L1	M1	M2	M3	R2	R3	S2
GW2	0.58	0.67	0.50	0.62	0.65	0.55	0.60
GW3	0.60	0.62	0.59	0.65	0.77	0.71	0.76
GW5	0.50	0.72	0.45	0.54	0.57	0.47	0.54
GW6	0.36	0.42	0.42	0.47	0.63	0.57	0.61
API	0.51	0.53	0.48	0.42	0.50	0.35	0.50
Stor. tot	0.66	0.84	0.65	0.71	0.66	0.67	0.68
Site 3 10cm	/	0.46	0.38	0.38	0.34	0.49	0.57
Site 3 20cm	/	0.42	0.41	0.36	0.33	0.48	0.54
Site 3 40cm	/	0.45	0.40	0.37	0.34	0.48	0.55
Site 3 60cm	/	0.43	0.40	0.36	0.34	0.48	0.54
Site 4 10cm	0.37	0.45	0.47	0.46	0.35	0.59	0.62
Site 4 20cm	0.38	0.50	0.45	0.43	0.39	0.56	0.66
Site 4 40cm	0.40	0.47	0.46	0.46	0.38	0.59	0.64
Site 4 60cm	0.39	0.50	0.45	0.44	0.38	0.57	0.64
Site 5 10cm	0.38	0.47	0.52	0.53	0.42	0.70	0.60
Site 5 20cm	0.39	0.47	0.51	0.51	0.42	0.67	0.60
Site 5 40cm	0.39	0.46	0.41	0.51	0.45	0.66	0.61

Saturated areas through the lens: 1

Site 5 60cm	0.38	0.46	0.46	0.50	0.43	0.66	0.61
Site 7 10cm	0.28	0.44	0.36	0.36	0.32	0.45	0.56
Site 7 20cm	0.25	0.40	0.37	0.35	0.31	0.46	0.53
Site 7 40cm	0.27	0.40	0.36	0.34	0.29	0.46	0.51
Site 7 60cm	0.27	0.44	0.42	0.37	0.29	0.51	0.55

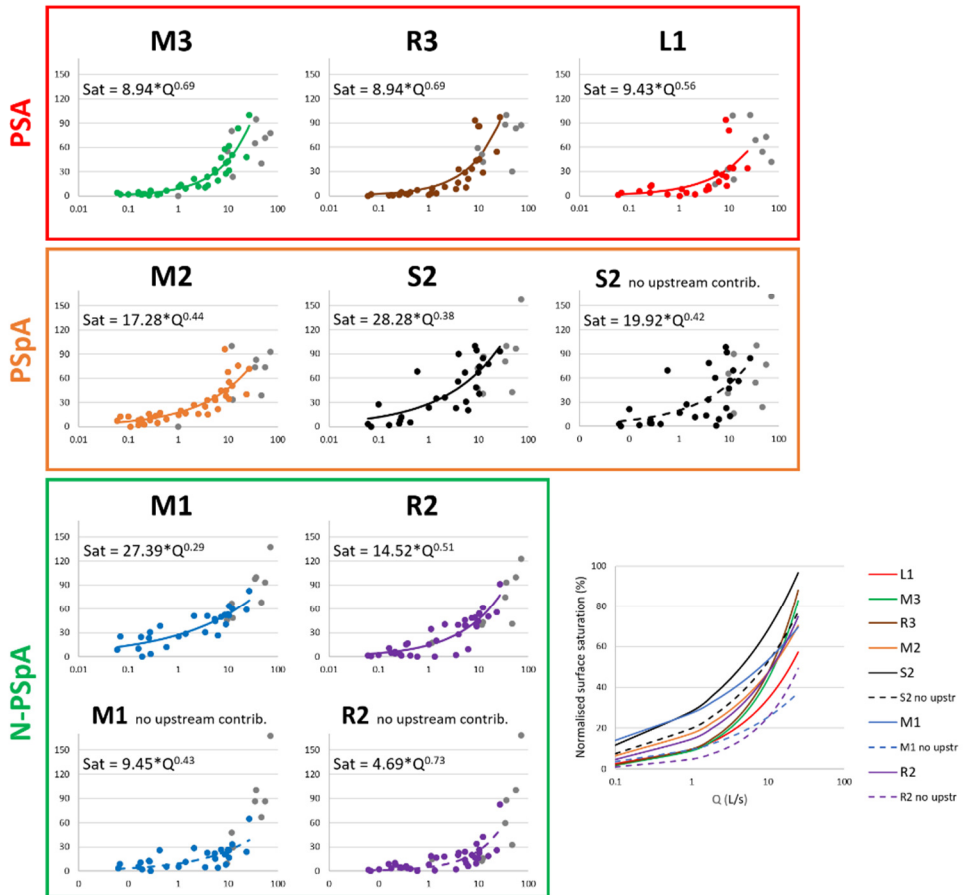


Figure 5.11: Relationships between normalised saturation (Sat) and catchment baseflow discharge (Q) at the outlet (daily-averaged values) for the seven investigated riparian areas. Abscissa = normalised surface saturation (%); ordinate = discharge (L/s). The data are plotted with a logarithmic ordinate to visualise the relationships for low and high discharge values in details. Coloured dots represent the observations not impacted by the occurrence of precipitation (cf. section 3.3). Grey dots represent observations influenced by precipitation during TIR image acquisition. Continuous and dashed lines represent the power-law relationships $Sat = a * Q^b$ fitted to the observations not impacted by the occurrence of precipitation (coloured dots only, non-transformed data). Plots marked with the wording “no upstream contribution” and dashed lines refer to the surface saturation data as estimated after having excluded the stream pixels from the images (cf. section 3.2). Areas are grouped considering the PSA, PSpA and N-PSpA classification (PSA = Stream Source Areas with Perennial springs; PSpA = Areas along the stream with Perennial Springs; N-PSpA = Areas along the stream with Non-Perennial Springs).

5.5 Discussion

We have used ground-based TIR imagery for mapping the spatio-temporal dynamics of riparian surface saturation expansion and contraction in the Weierbach catchment. For the first time, the dynamics of surface saturation in different riparian locations within the same catchment have been monitored at a temporal resolution high enough to characterise their seasonal variability. To the best of our knowledge, prior to this study extensive time-series of surface saturation dynamics have been displayed only as model outputs, often considering the overall amount of saturation in the catchment and rarely being validated (Birkel et al., 2010; Weill et al., 2013). We observed strong similarity in the expansion / contraction dynamics between the seven riparian surface saturated areas over the whole study period, although there were some differences in the timing of maximum or minimum levels of saturation in the seven areas. N-PSpA and area S2 showed generally higher normalised surface saturation values (i.e. high median value). The maximum of surface saturation in these areas occurred during a rain-on-snow event in December 2017. This is likely due to the fact that these areas receive the highest contributions of stream water from upstream than other areas (i.e. area M2 and PSA; cf. areas' locations in Fig. 5.3). We observed the lowest surface saturation extensions between November 2016 and January 2017 in all areas. For most of them, the lowest saturation values corresponded to the occurrence of frozen water in the riparian zone. On these occasions, the low values of surface saturation are likely to be the result of the combination of a dry period (i.e. lower amount of GW exfiltration and less water in the stream channel) and the fact that surface water in the riparian zone was frozen. We did not consider frozen surface water in the riparian zone as being surface saturation, since frozen (solid) water exhibits different characteristics than free (liquid) water, e.g. in terms of reaction to incident precipitation or movement dynamics.

The yearly and seasonal variability in the dynamics of surface saturation in the seven areas was found to reflect the yearly and seasonal variability of catchment runoff (cf. Fig 5.8 and 5.10). Increasing cumulated amounts of precipitation caused cumulated runoff and surface saturation to increase in a similar way during the wet periods. Increasing ET losses during the vegetative period led to moments of low runoff and low surface saturation (i.e. flatter cumulated runoff and surface saturation) despite that the amount of precipitation did not change considerably. Occurrence of breaks along the DMCs when passing from wet to dry conditions – and vice versa – were very similar between the rainfall-runoff and the rainfall-surface saturation DMCs. However, breaks and slope changes in the rainfall-surface saturation DMCs were generally less sharp than the slope changes observed in the rainfall-runoff DMCs. Martínez-Carreras et al. (2016) showed that the Weierbach catchment's runoff response is influenced by a storage threshold that, once exceeded, allows high discharge volumes to be generated by the catchment even in response to relatively small precipitation events. The similarity between the break points in the runoff and surface saturation DMCs may indicate that the same storage threshold influences the seasonal transition between low and high extents of surface saturation in the riparian areas. However, other aspects may play a role in regulating the seasonal expansion and contraction of surface saturation as well. For example, the smoother slope changes in the surface saturation DMCs than runoff DMCs may reflect that riparian soil hydraulic characteristics influence the expansion and

contraction of surface saturation by defining the degree of resilience of surface saturation to develop in response to increasing and decreasing catchment's wetness conditions. In this sense, the seasonal transition of riparian surface saturation may be subjected to a second, different threshold, which is defined by the riparian soil capacity to store and release water (Zehe et al., 2006). In order to further investigate the presence of thresholds for the development of surface saturation, a more frequent mapping during the seasonal transitions (i.e. by installing TIR fixed cameras) would have been required and might be targeted for the future.

Overall, the dynamics of saturation in the seven areas reflected the hydrological response of the catchment observed in terms of discharge, GW, soil VWC and estimated catchment storage (high Spearman's rank correlation between normalised surface saturation and discharge, GW, soil VWC and estimated catchment storage). Moreover, the daily-normalised rates at which surface saturation changed (i.e. increasing or decreasing) between the different observation dates were similar for all areas. These results indicate that the different areas in the riparian zone reacted to changes in the wetness state of the catchment in a similar way. Similarities between the different riparian areas emerged also from the comparison of the changes in surface saturation between two consecutive dates with the changes of the other hydrometric measurements between the same two consecutive dates (Table 5.4). Changes in surface saturation were particularly related to changes in catchment storage for all the investigated areas. Moreover, changes in surface saturation in the riparian areas were well related to changes in GW levels recorded at the hillslope foot position (GW3) and close to the riparian zone (GW2) for all investigated areas, except for area M1. The good relationship between both changes in catchment storage and GW levels recorded in GW3 and changes in surface saturation may suggest that the saturated compartment of the catchment storage (S_{SAT}) and specifically, the hillslope GW storage (estimated from GW3), may be the storage compartment relating the most with the riparian surface saturation dynamics observed in the different areas.

Water table variations observed in GW3 and GW2 are indicative for GW fluctuations within the *solum* and *subsolum* layers in the Weierbach catchment (*solum* and *subsolum* layers profile observed from soil pits and cores – Moragues-Quiroga et al. (2017)). These layers have been shown to play a significant role in the establishment of lateral GW connectivity between the hillslopes and the stream in the Weierbach catchment, especially during wet conditions (Martínez-Carreras et al., 2016; Rodríguez & Klaus, Accepted; Wrede et al., 2014). Similarly, our findings suggest that fluxes of GW from these layers may substantially contribute to sustaining riparian surface saturation during wet conditions in all investigated areas. Additionally, observed perennial GW exfiltration points (cf. Fig. 5.3 red circles) supported surface saturation in PSA and PSpA during both wet and dry conditions. Our observations are consistent with studies from other catchments that have assessed the role of GW level fluctuations occurring at mid and low hillslope locations in controlling the connectivity between the hillslopes and the riparian zone. In example, McGlynn and McDonnell (2003) found that the expansion of the saturated area was consistent with GW level dynamics in the lower hillslope and hollow zones in the Maimai catchment. Van Meerveld, Seibert & Peters (2015) noted in the Panola catchment that the hillslope and the riparian zone only became connected when GW levels rose in the lower part of the hillslope.

We did not observe a consistent relationship between changes in surface saturation and changes in soil VWC measured at different soil profiles. However, changes in surface saturation in areas R3 and S2 showed good correlation with changes in soil VWC measured in sites 4 (low-hillslope) and 5 (mid-hillslope) at all depths (Table 5.4). Although this result may suggest that variability in the unsaturated compartment of the catchment storage (S_{UNSAT} - estimated from the VWC of the soil profiles) could be related with the dynamics of riparian surface saturation in some areas, this particular relationship remains of difficult interpretation and further investigation on the water sources of riparian surface saturation is currently ongoing.

Considering the observed seasonal dynamics of surface saturation and the possible influence of lower hillslope GW fluctuations on surface saturation, we provide a perceptual model of how riparian surface saturation may evolve in the different monitored areas in Weierbach catchment during dry and wet periods, in absence of precipitation (Fig. 5.12). Note that our perceptual model is based on a combination of the visual inspection of the TIR observations (i.e. presence of perennial GW exfiltration, surface saturation patterns), estimated surface saturation time series and statistical correlations. Future investigations employing tracers, additional GW level measurements, or modelling might be useful to further refine and corroborate our perceptual model. Based on our current knowledge, we assume that the observed dynamics of surface saturation are the result of an interplay between the wetness state of the catchment and the morphological features of the observed areas (i.e. area width and elevation, existence of GW exfiltration points). During the dry season, perennial groundwater exfiltration supports the saturation in PSA and area M2 (Fig. 5.12 a). In N-PSpA, saturation (when present) is mainly represented by water in the stream channel. We assume this water to be mainly the result of upstream contributions (cf. Fig. 5.12 d, discussion of longitudinal/upstream contribution in section 5.3.2) since no perennial groundwater exfiltration points were detected in these areas during dry conditions. Moreover, some groundwater may exfiltrate directly into the stream channel from the hyporheic zone. Especially in area M1, saturation during the dry season was observed to be quite high, likely because this area receives contributions from two upstream areas with perennial groundwater exfiltration, i.e. area M2 and M3. Similarly, area S2 could exhibit high saturation because both perennial groundwater exfiltration and upstream contributions are present. During the wet season, as groundwater levels increase, saturation in PSA and PSpA develops extensively as riparian saturation and in the previously dry stream bed upstream (Fig. 5.12 b). Saturation in N-PSpA is assumed to increase during the wet season mainly due to higher contribution from upstream and from temporary springs that activate in the riparian zone (especially in area M1) (Fig. 5.12 e). In addition, the extension of surface saturation in the different areas may be influenced by stream expansion into the riparian zone (cf. Glaser et al., 2018) (Fig. 5.12 b and e). When passing again from wet to dry conditions, PSA and PSpA showed more persistent surface saturation in the riparian zone compared to N-PSpA (observed from TIR observations). This may be related to the fact that PSA and PSpA are generally wider than N-PSpA and can produce more extensive surface saturation which seems to dry slower (Glaser et al., 2019) (Fig. 5.12 c and f). We hypothesise that the presence of perennial springs in PSA and PSpA may contribute to keep the area generally wetter during the drying down period. At the occurrence of precipitation and events like rain-on-snow, surface saturation development can be

the result of the processes illustrated in Fig. 5.12 combined with the occurrence of infiltration excess.

The saturation – baseflow discharge relationships observed in the different riparian areas can be related to the dynamics illustrated in the perceptual model in Fig. 5.12. At low flow, the differences observed in the saturation – baseflow discharge relationships (i.e. amount of surface saturation and scattering in the observations, cf. Fig. 5.11) can be explained by the presence of perennial springs and the location of the riparian area (i.e. area elevation - which determines the variable amount of water reaching the area from upstream locations). At higher flow, the possibility for saturation to develop upstream in PSA (cf. Fig. 5.12 b) could explain the fast change in saturation with increasing discharge in these areas compared to the others (cf. Fig. 5.11). Indeed, it also has been observed by others that saturation that develops in previously dry channels is more reactive than saturation in riparian areas, which is rather influenced by the speed at which the soil drains (Dunne et al., 1975). The development of more persistent saturation in the riparian soils than the stream channel (Fig. 5.12 c) may explain the slight hysteretic effect that was observed in the saturation – discharge relationship of PSA and area M2 (cf. Fig 5.11 – grey dots). The hysteretic relationships between saturation and discharge that we observed in some areas provide a first actual feedback to the possible hysteretic relationship between surface saturation and outlet discharge that has been usually observed through modelling approach (Glaser et al., 2016; Weill et al., 2013). However, the hysteretic relationships between saturation and discharge observed in this study were never as clearly defined as those observed in modelling studies (Frei et al., 2010; Weill et al., 2013), despite the relative high number of observations at high flow stages. In this sense, TIR observations at a higher temporal resolution during precipitation events would help to clarify the hysteretic patterns that may occur in the different areas and could be used to validate hysteretic behaviour observed through simulations. Overall, the small but noticeable differences observed in the saturation – baseflow discharge relationships provided information on the different potential for lateral and longitudinal hydrological connectivity to be established through the different riparian areas during different flow stages.

To date, surface saturation – baseflow discharge relationships have been inferred considering only the total surface saturation extent in a catchment (Ambroise, 2016; Latron and Gallart, 2007). The surface saturation – baseflow discharge relationship has been defined by Ambroise (2016) as a characteristic curve of the catchment, fundamental for understanding and modelling the interaction of water from different sources on the saturated areas and its influence on streamflow during baseflow conditions. By repeatedly monitoring the dynamics of surface saturation in different areas, we found indication of possible intra-catchment variability of this relationship. Moreover, the frequency at which we observed surface saturation in this study allowed us to explore the dynamics of surface saturation during baseflow conditions under different flow stages. It also allowed us to consider how seasonality may affect the observed dynamics. Considering the fact that the broadly-used topography-driven indices and geomorphic indices for estimating surface saturation are known to perform relatively poorly during low flow stages (Ali et al., 2013b; Güntner et al., 2004; Western et al., 1999), our observation of surface saturation dynamics during low baseflow conditions is particularly valuable for obtaining new insights into riparian processes and potentially improve these indices. In example, from the analysis of the rainfall-surface saturation DMCs, we observed

that increasing ET losses during the vegetative period lead to moments of low surface saturation despite the amount of precipitation did not change considerably. The neglect of this shift in dominant processes in the indices calculation might be the reason for the poor performance during dry periods.

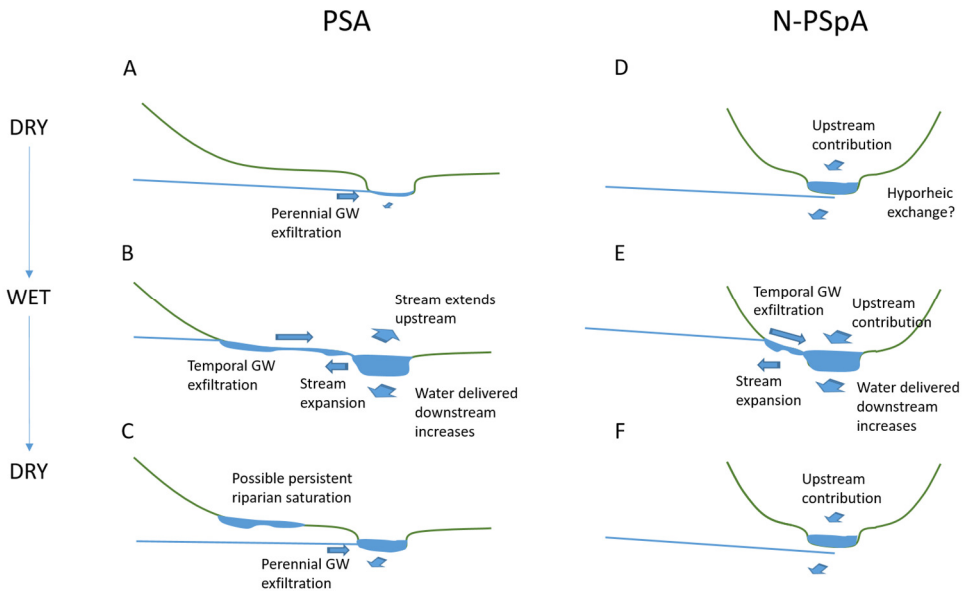


Figure 5.12: Proposed perceptual model for the development of surface saturation in PSA (Stream Source Areas with Perennial springs) and N-PSpA (Areas along the stream with Non-Perennial Springs) riparian areas.

5.6 Conclusions

This study is a contribution to the call for the development of a routine method for mapping surface saturated areas (Dunne et al., 1975) and to the need to start characterising the spatial and temporal variability of riparian processes for a better understanding of catchments hydrological and biochemical functioning (Grabs et al., 2012; Ledesma et al., 2018; Tetzlaff et al., 2008; Vidon and Hill, 2004). We applied TIR technology as a valid routine method for repeated mapping of surface saturation (in our case, at weekly or bi-weekly frequency) in the Weierbach catchment. The frequency at which we monitored surface saturation was critical to characterise the similarities and differences in both the temporal dynamics of surface saturation in different areas and their relationship with stream baseflow discharge.

The observed yearly and seasonal dynamics of surface saturation in the different riparian areas of the catchment were found to be similar. Based on the analysis of DMCs for the surface saturation in comparison to the DMC of discharge we hypothesised that storage thresholds control the transition between low extents of surface saturation and high extents of surface saturation in the Weierbach

catchment. Another similarity between the dynamics of surface saturation observed in different investigated areas has been found in their relationship with the variability in catchment's storage and GW levels measured in lower hillslope locations. This supports the role of riparian surface saturation as a valuable indicator of groundwater storage during baseflow conditions previously assessed in different studies (i.e. Ambroise, 2016; Gburek & Sharpley, 1998; Myrabø, 1997).

The shape of the relationship between surface saturation and baseflow discharge could be approximated with a power law in all cases. However, small differences in the relationships for the different areas could be associated with the location of the areas along the stream network (i.e. area elevation) and with the local riparian morphology (i.e. area width, presence of GW exfiltration points). These characteristics represent a source of intra-catchment variability that may have implications on the potential of different riparian surface saturated areas in mediating hydrological connectivity along the HRS continuum.

Based on our findings and conclusions, we may now ask "Are all riparian zones in our catchment the same, or would the small differences in their dynamics of surface saturation mirror the degree of hydrological connectivity of the different areas with the hillslopes?". With this question in mind, we will present our investigation on the spatial heterogeneity of streamflow generation in our second contribution (Chapter 6). The data and information obtained in this study will prove essential for investigating the spatial variability of streamflow generation in the Weierbach catchment and its relationship with surface saturation. The same approach used in this study can be potentially employed in other catchments as well, especially in those where the riparian zone represents an important interface between the hillslopes and the stream.

Saturated areas through the lens: 1

Chapter 6

Saturated areas through the lens: 2. Spatio-temporal variability of streamflow generation and its relationship with surface saturation

Abstract

Investigating the spatio-temporal variability of streamflow generation is fundamental to interpret the hydrological and bio-chemical functioning of catchments. In humid temperate environments, streamflow generation is often linked to the occurrence of near stream surface saturated areas, which mediate hydrological connectivity between hillslope and streams. In this second contribution of a series of two papers, we used salt dilution gauging to investigate the spatio-temporal variability of streamflow in different sub-catchments and for different reaches in the Weierbach catchment (0.42 km²), and explored the topographical controls on streamflow variability. Moreover, we mapped stream network expansion and contraction dynamics. Finally, we combined the information on the spatio-temporal variability of streamflow with the characterisation of riparian surface saturation dynamics of seven different areas within the catchment (mapped with TIR imagery, as presented in our first manuscript). We found heterogeneities in the streamflow contribution from different portions of the catchment. While the size of the contributing area could explain differences in sub-catchments' and reaches' net discharge, no clear topographic controls could be found when considering the area-normalised discharge. This suggests that some local conditions exert control on the variability of specific discharge (e.g. local bedrock characteristics and occurrence of perennial springs). Stream network dynamics were found not to be very responsive to changes in catchment's discharge (i.e. total active stream length vs. stream outlet discharge relationship could be described through a power law function with exponent = 0.0195). On the contrary, surface saturation dynamics were found to be in agreement with the level of streamflow contribution from the correspondent reach in some of the investigated riparian areas. This study represents an example of how the combination of different techniques can be used to characterise the internal heterogeneity of the catchment and thus, improve our understanding of how hydrological connectivity is established and streamflow is generated.

This chapter is based on: Antonelli, M., Glaser, B., Teuling, A.J., Klaus, J., Pfister, L. 2020. Saturated areas through the lens: 2. Spatio-temporal variability of streamflow generation and its relationship with surface saturation. Hydrological Processes, 34: 1333– 1349. <https://doi.org/10.1002/hyp.13607>.

6.1 Introduction

The spatio-temporal variability of surface saturated areas and its impact on the hydrological behaviour of catchments have been on top of research agendas for several decades. Surface saturated areas are recognised as key areas in generating runoff in humid temperate-regions (Ambrose, 2004; Hewlett, 1961) – mediating the on- and offset of hydrological connectivity between hillslopes and streams (Birkel et al., 2010; Bracken and Croke, 2007; Tetzlaff et al., 2007). In these environments, the development of surface saturated areas is primarily due to the occurrence of saturation-excess (Dunne and Black, 1970a) in near-stream areas with low relief and shallow water table (i.e. riparian zone) and up to the previously dry low-order channels (Bracken and Croke, 2007; Dunne et al., 1975; Montgomery and Dietrich, 1989). Both riparian surface saturated areas and stream networks are known to be highly dynamic (Dunne et al., 1975; Godsey and Kirchner, 2014; Shaw, 2016; Whiting and Godsey, 2016), quickly extending in response to precipitation and fostering the establishment of hydrological connectivity between the riparian zone and the stream – eventually triggering runoff generation (Bracken and Croke, 2007). Moreover, riparian surface saturated areas and stream network expansion and contraction dynamics reflect local groundwater dynamics. The spatial extent of riparian surface saturated areas can be considered as a valuable indicator of the hydrological state of the catchment and, in particular, of groundwater storage during baseflow conditions (Ambrose, 2016; Gburek and Sharpley, 1998; Myrabø, 1997). Similarly, stream network dynamics have been defined as a visible expression of subsurface processes otherwise hidden (Godsey and Kirchner, 2014). For these reasons, an accurate characterisation of surface saturation and stream network dynamics is required to fully interpret the hydrological behaviour of catchments in humid temperate environments and to accurately predict runoff dynamics and associated flowpaths.

Understanding how runoff is generated within a catchment and which features, namely catchment topography, geology, vegetation and climate, control its variability is crucial to interpret catchment responses and stream-water biogeochemical signatures and fluxes (Bergstrom et al., 2016a; Pinay, 2005). Some experimental studies on this subject have adopted catchment discretisation into defined landscape units such as hillslopes, riparian areas and stream (Jencso et al., 2009; McGlynn, 2003; McGlynn et al., 2004; McGlynn and McDonnell, 2003), providing fundamental information on runoff source area dynamics in terms of hillslope-riparian-stream (HRS) connectivity (defined as water table continuity across hillslope, riparian zone and stream). These studies helped to clarify the relative role of different landscape units as spatial sources of runoff and the importance of riparian zones in regulating the portion of “new” and “old” water in stormflow (McGlynn et al., 2004; McGlynn and McDonnell, 2003). Other studies have focused on characterising spatial and temporal variability of runoff by measuring discharge along continuous stream reaches (Anderson and Burt, 1978; Bergstrom et al., 2016a; Floriancic et al., 2018; Genereux et al., 1993; Huff et al., 1982; Kuraś et al., 2008; Payn et al., 2012; Shaw et al., 2017). Unlike the studies employing catchment discretisation, these studies take into account the dynamics of surface water (cf. Blume and van Meerveld, 2015), specifically the increase or decrease of streamflow between two measurement points. When applied over a whole stream network, this approach has

the advantage of providing a general indication of heterogeneities in streamflow generation within the catchment. This heterogeneity can be directly linked to hydrologic dynamics, structure and vegetation to understand how different processes are integrated along the stream to produce the total discharge volume at the outlet.

In humid-temperate regions, spatio-temporal variability of streamflow is very often linked to the location and temporal variability of surface saturated areas (Bracken and Croke, 2007). However, studies combining variability in streamflow generation with surface saturation dynamics are extremely rare (Shaw et al., 2017; Ward et al., 2018). Moreover, these studies tend to focus only on stream network dynamics. To the best of our knowledge, riparian surface saturation dynamics have only been investigated in relation to measurements of discharge at the catchment outlet or in relation to groundwater level fluctuations (Birkel et al., 2010; Dunne and Black, 1970b; Lana-Renault et al., 2014; Latron and Gallart, 2007; Martínez Fernández et al., 2015; Tanaka et al., 1988). The study of Kirnbauer and Haas (1998) in an Alpine catchment is a unique exception in this respect. They used stream gauges downstream of surface saturated areas to quantify their contribution to runoff. Combining a detailed description of surface saturation dynamics with the investigation of streamflow variability along the stream network could provide new insights on the spatial and temporal variability of HRS connectivity in humid temperate environments and, in particular, on the role of valley bottoms in regulating this connectivity. Additional experimental investigation along this line of work is needed across catchments with a range of geological and climate conditions to advance our understanding of surface saturation dynamics and its link to runoff generation.

The main obstacle to comparing surface saturation dynamics with streamflow dynamics along the stream network stems from the need to map surface saturation at the same temporal resolution to which streamflow is measured and for different locations within a restricted timeframe. Even though time consuming, mapping the active portion of the stream network can be achieved by walking along the stream and recording the active/inactive portions using a GPS receiver (Godsey and Kirchner, 2014; Shaw, 2016). More challenging is the mapping of riparian surface saturation, where classic approaches such as field surveys based on the “squishy boot” method may not provide an adequate spatio-temporal resolution (Pfister et al., 2010). In this regard, recent technological development is represented by ground-based remote sensing techniques (i.e. thermal infrared – TIR – or digital imagery) with which surface saturation can be mapped at a higher temporal (i.e. minutes to weeks) and spatial (i.e. centimetres to meters) resolution (Glaser et al., 2018, 2016; Pfister et al., 2010; Silasari et al., 2017).

Here, we investigate the link between surface saturation dynamics (read as both riparian surface saturation and dynamics of expansion and contraction of the active portion of the stream network) and streamflow generation in the Weierbach catchment in Luxembourg. The Weierbach catchment is a long-term studied catchment, nowadays considered as a reference-catchment for rainfall-dominated mountainous catchments (Zuecco et al., 2018). The catchment’s hydrological response is influenced by a storage threshold (Martínez-Carreras et al., 2016) and it is characterised by a single spiky peak in case of dry antecedent conditions and by a first spiky peak followed by a broader peak of longer duration in case of wet antecedent conditions (Martínez-Carreras et al., 2016; Wrede et al., 2014). The

riparian zone in this catchment presents seasonally dynamic surface saturated areas whose possible influence on the connectivity and hydrological response of the system has never been clarified.

This contribution is the second in a series of two papers. Here, we leverage (i) information obtained by monitoring the spatio-temporal dynamics of riparian surface saturation via TIR imagery (as presented in our first manuscript – Chapter 5) and (ii) manual mapping of the dynamic stream network and incremental flow gauging at different flow stages (this manuscript). We employ these datasets to:

1. Investigate the spatial distribution of streamflow generation in the Weierbach catchment during different flow conditions and compare the streamflow contributions from different sub-catchments and individual reaches between consecutive streamflow gauging points;
2. Explore the relationship between surface saturation and streamflow contributions from different reaches;
3. Understand how streamflow contributions from different stream reaches are controlled by riparian and upslope topographic characteristics (i.e. terrain indices extracted from a DEM).

Our findings will be discussed in light of the current perceptual model of the Weierbach catchment (Martínez-Carreras et al., 2016; Scaini et al., 2018; Wrede et al., 2014) and compared with previous research in a broader context.

6.2 Study site - Weierbach catchment

The Weierbach catchment (0.42 km²) is an experimental catchment located in the North-West of the Grand Duchy of Luxembourg (49°49' N, 5°47' E, see Fig. 6.1). The catchment is fully forested, with vegetation dominated by Oak and Beech trees, and Spruce mainly on the eastern side of the catchment. The climate is semi-oceanic, with an annual average precipitation of 918 mm (2011-2017). Detailed information about the soil and bedrock characteristics and seasonal hydrological response is reported in the companion paper by Antonelli et al. (2019) (Chapter 5) as well as in several other studies (Gourdol et al., 2018; Martínez-Carreras et al., 2016; Wrede et al., 2014). Here, we briefly summarise the information from the first manuscript about the riparian zone and the seven distinct areas within the catchment where we monitored riparian surface saturation (Fig. 6.1). The riparian zone has been identified by taking into account shifts in dominant vegetation, occurrence of shallow clay-loam, organic soil (i.e. Leptosol) and a gentle slope (< 5°). The riparian zone covers roughly 1.2 % of the total catchment area (0.42 km²). The seven riparian areas have been divided into three groups: areas L1, M3 and R3 as “Stream Source Areas with Perennial springs (PSA)”, areas M2 and S2 as “Areas along the stream with Perennial Springs (PSPA)” and areas M1 and R2 as “Areas along the stream with Non-Perennial Springs (N-PSPA)”. These groups have been defined based on some intrinsic characteristics of the areas, such as location within the catchment, riparian width and presence of perennial springs (see section 5.4.2 and Table 5.1 in Chapter 5).

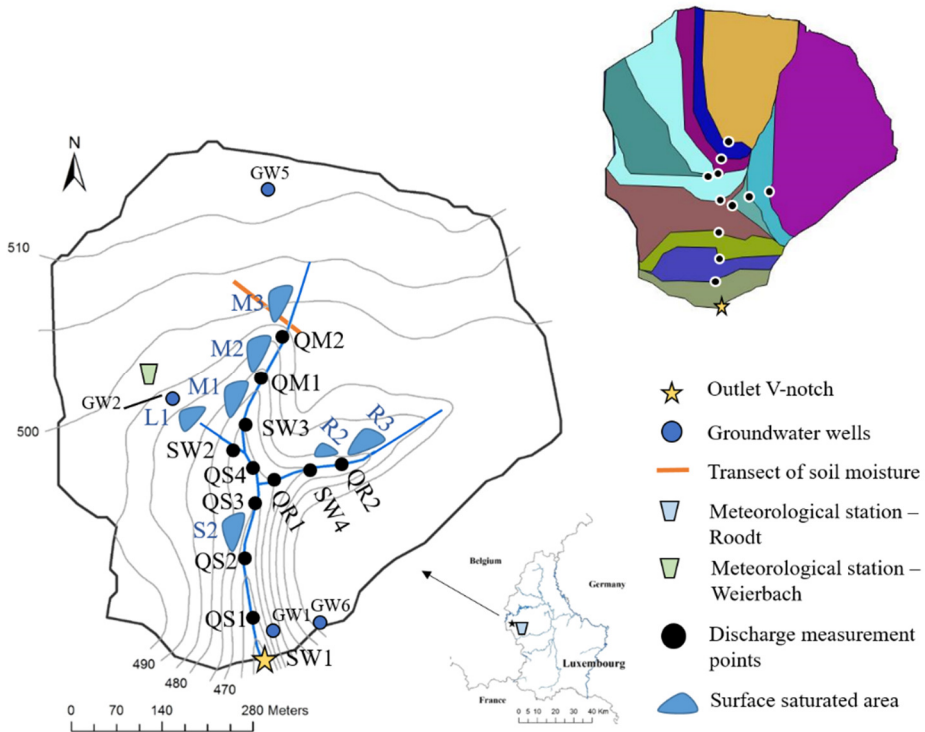


Figure 6.1: Map of location and instrumentation of the Weierbach catchment and location of the points along the stream where dilution gauging discharge measurements have been carried out. Upper right panel: contributing area to the different dilution gauging discharge measurement points.

6.3 Materials and Methods

6.3.1 Hydro-meteorological measurements and catchment storage calculation

Hydro-meteorological measurements of stream discharge at the outlet, ground water (GW) levels and soil volumetric water content (VWC) are carried out in the Weierbach catchment since 2002. The reader is referred to Chapter 5 for a complete description of the used instrumentation and data recording frequency, as well as for details on the hydro-meteorological measurements and estimations (i.e. reference evapotranspiration and catchment storage) employed in this study. Time series describing the hydrological response of the catchment for the study period from November 2015 to December 2017 are reported in the results section 5.4.1 in Chapter 5.

6.3.2 Monitoring of saturated areas in the riparian zone and stream network dynamics

Riparian surface saturation and stream network dynamics have been surveyed simultaneously, weekly or fortnightly from November 2015 to December 2017. Riparian surface saturation has been monitored in seven different locations via ground-based TIR imagery and its dynamic has been characterised through post processing of the TIR camera outputs (i.e. sequential images or videos) following the methodology outlined in Glaser et al. (2018). The riparian surface saturated areas were seasonally variable and were found to be particularly responsive to groundwater fluctuations. The development of surface saturation in the seven different areas is influenced by local riparian morphology which leads to small differences in the relationship between surface saturation and outlet discharge observed for the different areas. For a thorough characterisation of the dynamics of riparian surface saturation, the reader is referred to the accompanying manuscript (cf. results section 5.4.4 in Chapter 5).

We mapped stream network dynamics manually by walking along the stream channel (within a few hours) and tagging the locations where stream flow initiated or ceased (Fig. 6.2). We considered as locations of starting stream flow only those where water was flowing downstream, excluding locations where the water was just ponding without flowing. Tag positions along the stream were translated into coordinates on a high resolution LIDAR digital elevation model (DEM, ~ 5 cm) by manually measuring the distance between the tags and between the tags and ground control points that could be identified both in the field and in the DEM (i.e. trees, logs). Tag positions were recorded manually because of very poor GPS reception in the forested study site. For each tagged location we calculated its distance from the outlet and elevation. For each date of survey, we calculated the total active stream length (as per Whiting and Godsey, 2016).



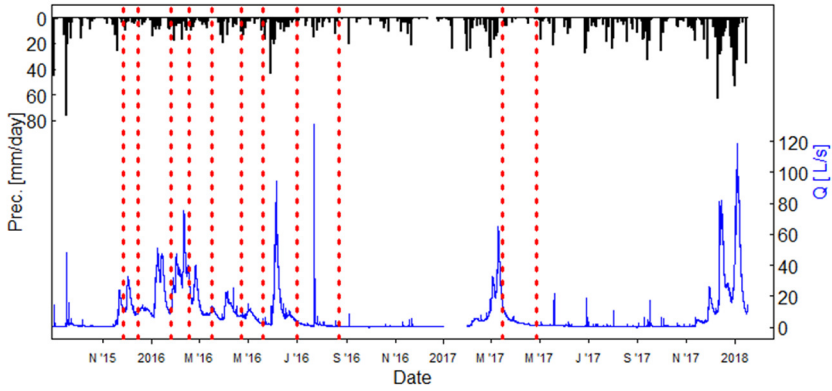
Figure 6.2: Illustration of tagging used to indicate initiation of stream flow in one of the headwater reaches. Tags were added during field visits under different wetness conditions. White arrows are added to indicate flow direction (photo: M. Antonelli).

6.3.3 Salt dilution gauging

Stream discharge was measured via salt dilution gauging at 12 locations along the stream network (Fig. 6.1). The measurements were carried out within a few hours on 11 dates with no rain and contrasting hydrological states (Fig. 6.3). Salt dilution gauging (Day, 1976) is a common method for measuring discharge in small streams with irregular streambed morphology (Moore, 2004). Measurement locations were selected based on two criteria: (i) include a surface saturated area between the upstream and downstream measurement locations and (ii) maximise the possibility for complete mixing of the injected salt solution and stream water between the injection point and the measurement location (i.e. by injecting just upstream of a riffle or a narrowing of the stream section), which is an important requisite for salt dilution gauging (Day, 1977; Moore, 2004). We injected a solution of a known amount of NaCl. Electrical conductivity (EC) was recorded at the discharge measurement locations using a WTW Multi 3420 device, equipped with a TetraCon 925 probe (Xylem Analytics, Weilheim, Germany).

Replicates of the salt dilution gauging were carried out for 15 of the measurements, covering different flow states and measurement locations. In these cases, a second injection was carried out after the stream EC returned to its background value. We found an average error between the two replicates of $\sim 3\%$,

with a minimum of 0% and a maximum of 10%, which was sufficient for our application.



FDC
October 2015 - January 2018

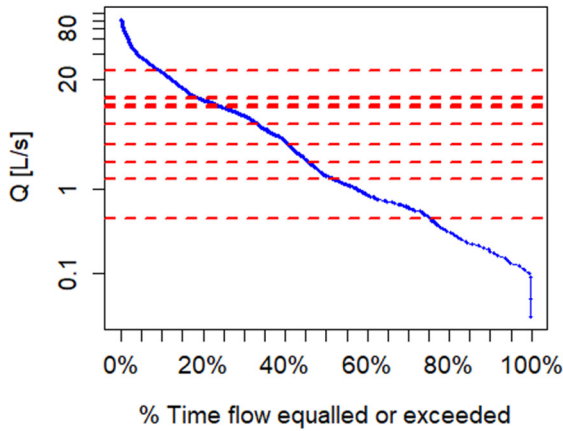


Figure 6.3: Streamflow dynamics at the catchment outlet and days of salt dilution gauging (dashed red lines). The same days are reported along the flow duration curve (2-year study period) for the catchment outlet.

6.3.4 Data analysis

The discharge values (L/s) retrieved via salt dilution gauging at the different locations along the stream were used to characterise the spatial and temporal variability of streamflow generation in the catchment. We compared the streamflow at the outlets of the different sub-catchments (i.e. catchment area above each discharge measurement location – Fig. 6.1 upper right panel) in terms of area-normalised discharge (specific discharge – mm/day). We calculated the net discharge between two measurement locations (i.e. for a reach – Fig. 1 upper right panel) as their difference in discharge (L/s). In order to compare reaches of different length, we expressed the net discharge as specific discharge (mm/day) and normalised it by the reach stream length (m). Similarities between specific discharge produced by each sub-catchment and similarities between normalised specific discharge contributions from the different reaches were tested with the Mann-Whitney-Wilcoxon Test ($\alpha = 0.05$). The test was applied by taking into account the sub-catchments against each other for the dates where a measure of discharge (or net discharge) was available for the considered pair. The same procedure was followed for the reaches. Spearman's rank correlation test rho (ρ ; $\alpha = 0.01$) was applied in order to test monotonic relationships between the sub-catchments' specific discharge and the other hydrometric measurements (i.e. stream discharge at the outlet, estimated catchment storage, ground water levels and soil volumetric water content – daily-averaged values) and between the normalised specific discharge contribution of the different reaches and the hydrometric measurements (i.e. daily-averaged values).

We used multiple linear regression analysis to investigate which topographic characteristics influenced discharge (L/s) and specific discharge (mm/d) contributions of the different sub-catchments and reaches (non-normalised values). We extracted several topographic features from a DEM (5 m resolution) and from a high resolution LIDAR DEM (~ 5 cm resolution). We extracted topographic features for the different sub-catchments and for the portion of the catchment draining between the two measurement locations defining a reach (i.e. upslope catchment area). Specifically, we considered catchment area, riparian area, percentage of riparian area, riparian buffer (riparian area/hillslope area), median slope (only for the reaches because too homogeneous between the sub-catchments), percentage of steep slope (i.e. $> 15^\circ$), median elevation, median flow length (only for the sub-catchments) and reach length (only for the reaches). The models were ran for each discharge measurement date and averaged through time. Variance inflation factor (VIF) analysis and backward selection were carried out to select the significant variables to retain in the models.

To investigate the relationship between stream network dynamics and stream outlet discharge, we related outlet discharge and stream length dynamics of the three headwater areas and tested the occurrence of monotonic relationships with Spearman's rank correlation ($\alpha = 0.01$). We also related outlet discharge and the total active stream length (i.e. total stream length considering the entire catchment) and fitted a power law equation (stream length = $a \cdot Q^\beta$) to this relationship following the approach of Godsey and Kirchner (2014). The total active stream length vs discharge relationship can provide an estimation of how much the total active stream length changes (in percentage) with changes in discharge. This estimation is

represented by the β power-law scaling exponent. Following a similar approach, we related the total active stream length and estimated catchment storage and GW level (measured in well GW5 on the plateau – the closest well to two out of three monitored headwater areas). We fitted equations that approximated the trend of these relationships. The goodness-of-fit of all the fittings was tested with Kolmogorov-Smirnov test (p -value > 0.1). All the hydrometric variables are daily averages.

Finally, we explored the relationship between riparian surface saturation dynamics in the seven investigated areas and (i) normalised specific discharge contributions and (ii) net discharge (expressed as percentage of the outlet discharge) of the correspondent reach. Note that the number of observations that could be used to explore these relationships was consistently lower than for the other investigated relationships. This was due to the low quality of the TIR images collected during some of the stream gauging dates. Therefore, and due to its low statistical significance, we avoided any quantification of the strength of this relationship. However, we believe that a description of the trends that could be observed from the scatterplots (cf. Fig. 6.8 and 6.9 in results section) would provide us with valuable information.

6.4 Results

6.4.1 Spatio-temporal variability of streamflow

Streamflow within the catchment was found to be highly variable in both space and time. The normalised specific discharge contributions of the different reaches and sub-catchments' specific discharge is shown for three days of stream gauging (Fig. 6.4). The selected dates can be considered as representative of the system during dry (Fig. 6.4 a), intermediate (Fig. 6.4 b) and wet (Fig. 6.4 c) conditions. In general, the relative difference between normalised specific discharge contributions from the different reaches was smaller during drier conditions compared to wetter conditions. For example, the percentage relative difference between the reach with the smallest contribution and the one with the largest contribution was 5.5 % on 01/07/2016 (Fig. 6.4 a) and 14.3 % on 17/02/2016 (Fig. 6.4 c). During dry conditions, some reaches exhibited a negative contribution (i.e. R-S1 and R-R1 in Fig. 6.4 a). The same reaches shifted to a positive contribution during intermediate wetness conditions and R-L1 and R-M2 started to contribute considerably more than others (Fig. 6.4 b). During wet conditions, the contribution of these reaches increased further and R-M1 and R-M3, R-R1, R-R2 and R-R3, R-S2 and R-S1 became more active as well (Fig. 6.4 c).

Considering all the measurement dates, some reaches were found to contribute positively to streamflow more frequently than others (i.e. R-L1, R-S2 in Fig. 6.4 d). Similarly, some reaches showed overall higher variability in contribution (i.e. R-S2, R-L1, R-M2 and R-R1) compared to others (Fig. 6.5 a). Between the reaches with most variable contribution, R-L1 and R-M2 were found to be particularly similar (Mann-Whitney-Wilcoxon test p -value = 0.7). Specific discharge contributions of the different sub-catchments appeared to be quite homogeneous within the same stream gauging dates (Fig. 6.4). Only the sub-catchment with outlet in point SW2

produced systematically higher specific discharge than the other sub-catchments, even though this difference was not statistically significant (Mann-Whitney-Wilcoxon test p -value always higher than 0.05) (Fig. 6.5 b). Overall, sub-catchments' contribution was generally less variable in space and in time than observed for the different reaches.

The values of specific discharge of the different sub-catchments showed generally a higher positive monotonic relationship with the other hydrometric measurements than the normalised specific discharge contributions of the different reaches as seen from the correlations described hereafter. In particular, all sub-catchments' discharge were well correlated between each other (Spearman's rank test ρ not lower than 0.83) and, with exception of the sub-catchment with outlet in point QR2, they were all well correlated with discharge at the catchment outlet and estimated catchment storage (ρ not lower than 0.8). GW levels measured in locations 2 and 3 were correlated with all the sub-catchments' discharge (ρ not lower than 0.82 except for QR2 sub-catchment) while GW levels in location 5 and 6 were mainly correlated with the sub-catchments with outlet to the central stream (i.e. from SW1 to SW3) and in SW4 ($0.74 \leq \rho \leq 0.93$). Soil VWC was less correlated with sub-catchments' specific discharge in general, with VWC measured in the spruce-covered hillslope showing the better correlation with most of the sub-catchments ($0.8 \leq \rho \leq 0.88$) and VWC measured in riparian location being correlated with none (non-significant correlations). When considering monotonic relationships between normalised specific discharge contributions of the different reaches, we observed that reaches R-S0, R-S1, R-L1, R-M1, R-R2 and R-R3 were not correlated to other reaches and, except R-L1 and R-R3, never correlated with catchment outlet discharge, estimated catchment storage or GW levels ($\rho \leq 0.75$ or non-significant correlations). VWC never correlated with normalised specific discharge contributions of any reach, except for R-S2 (ρ not lower than 0.81). Also in this case, VWC measured in riparian location did not correlate with any reach (non-significant correlations).

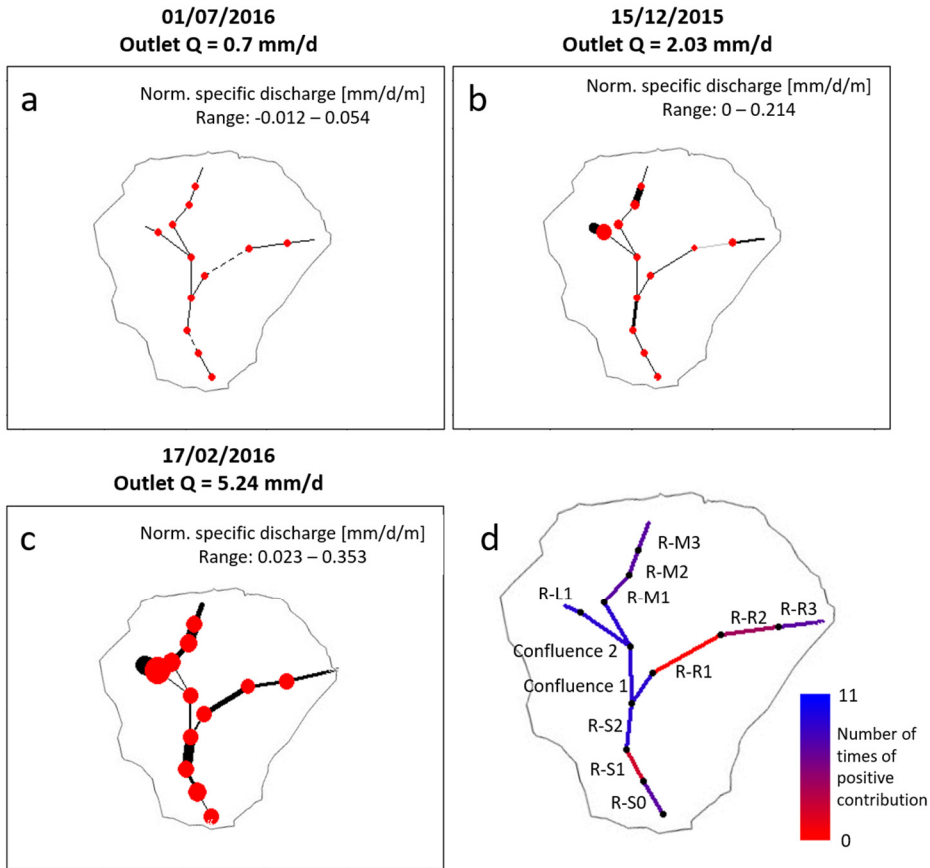


Figure 6.4: Distribution of specific discharge contributions across the Weierbach catchment. a) 1st July 2016, b) 15th December 2015 and c) 17th February 2016. Line width is proportional to the magnitude of reaches' specific discharge normalised to unit reach length, considering the range of contributions for each measurement date (in mm/d/m; reported in the graphs). The variable length of the headwater segments reflects the stream dynamics in these sections. Dashed lines represent sections with losing conditions and grey lines represent absence of contributions. Diameters of red points are proportional to sub-catchment specific discharge. The map on the bottom-right corner (d) provides an indication of the number of time the reaches contributed positively to streamflow considering all stream gauging dates (11). The map also reports the names for reaches. For the discharge measurement point names we refer to Figure 6.1.

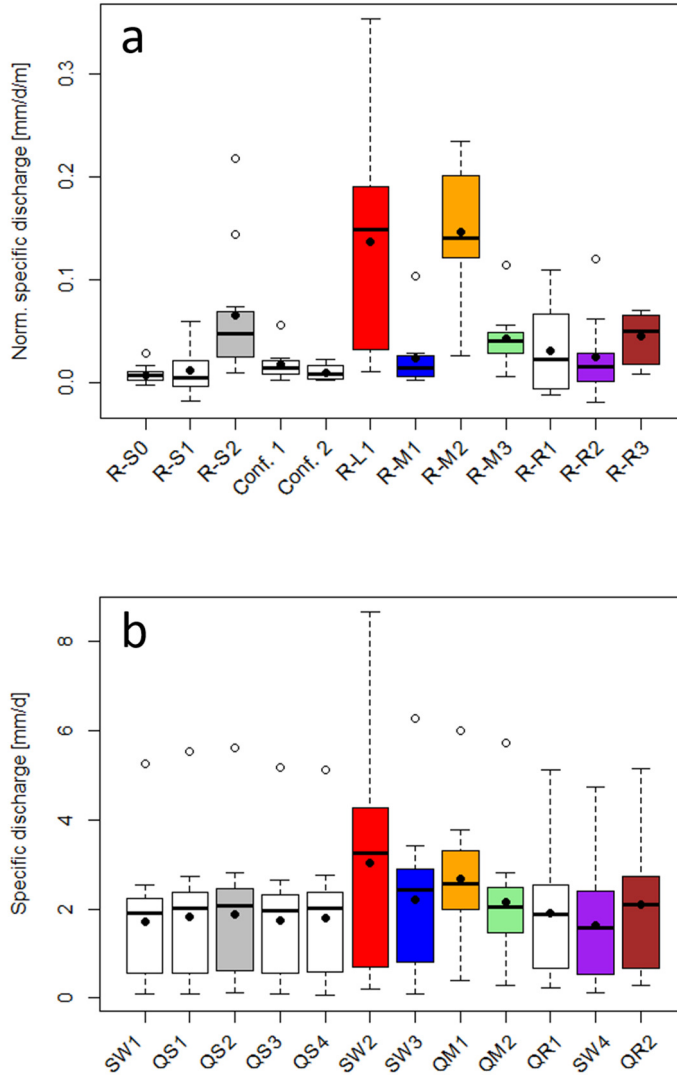


Figure 5.5: Distribution of specific discharge contributions. a) Distribution of normalized specific discharge contributions across the different reaches. b) Distribution of specific discharge of the different sub-catchments. The colour of the boxplots in both panels refer to the colours assigned to the different riparian surface saturated areas in Antonelli et al. (Chapter 5). For the reaches: a colour is assigned if the reach includes the correspondent riparian surface saturated area; for the sub-catchments: a colour is assigned if the sub-catchment outlet is right downstream the correspondent riparian surface saturated area.

6.4.2 Stream network dynamics and relationship between riparian surface saturation and reaches' streamflow contribution

During the study period, the stream network never dried out completely. We observed only occasionally lack of flow at the outlet (e.g. in January 2017, when the stream was partially frozen) or moments in which appreciably downstream sections of the stream became ephemeral (e.g. in September 2016, the stream stopped flowing in proximity of the discharge measurement point "QS3" and started flowing again close to the surface saturated area S2). In general, we could always detect flow starting points at the three headwater locations, even though sometimes the water re-infiltrated after few meters.

Stream network expansion and contraction dynamics in the three headwater stream reaches (R-L1, R-M3, R-R3) were all positively monotonically related to catchment's outlet discharge (Spearman's rank test ρ not lower than 0.81 – Fig. 6.6). R-L1 was the reach that expanded the least, with a difference between its maximum and minimum observed starting point of about 8 meters. In contrast, R-R3 extended about up to 60 meters above its minimum observed starting point. R-M3 extended upward along both the main reach direction (i.e. "R-M3 centre" in Fig. 6.6) and on the right (i.e. "R-M3 right" in Fig. 6.6). In both cases, the reach extended about 30 meters above its minimum observed starting point. We could observe one or more particularly stable flow starting points for all three headwater reaches (Fig. 6.6). In R-L1, this point was located at about 383 m upward from the outlet. In R-M3, stable points were found at about 480 m upward from the outlet (common part of the reach), 503 m (central direction) and 502 m (right direction). In R-R3, stable points were at about 409 m and 425 m upward from the outlet.

The relationship between the total active stream length and outlet discharge could be adequately described with a power law equation – linear in a log-log space (Fig. 6.7 a, $\beta = 0.0195$) (goodness-of-fit was tested with Kolmogorov-Smirnov test – p-value > 0.1). This shows that the total active stream length did not respond linearly to unit changes of outlet discharge. For the relationship between the total active stream length and both estimated catchment storage and GW level, a linear equation better fitted the data (Figure 6.7 b and c, $R^2 = 0.94$ and 0.9 respectively).

The relationships between surface saturation in the seven investigated riparian areas and streamflow contributions of the corresponding reaches showed some heterogeneities, especially when considering the normalised specific discharge contributions. For the areas L1, M2 and S2 we found a clear positive trend between extent of riparian surface saturation and normalised specific discharge contributions (Fig. 6.8). Areas M3, R3 and M1, showed a slight positive trend, but normalised specific discharge contribution varied less compared to L1, M2 and S2, with the observations almost plotting on a vertical line. No particular trend was observed for area R2. When considering the relationship between extent of riparian surface saturation and net discharge of the reaches (percentage of outlet discharge) we found that areas M3, M2, M1 and L1 contributed to a quite constant percentage of the total catchment discharge, regardless the dynamic riparian surface saturation (Fig. 6.9). Areas R3, R2 and S2 showed more variability in their percentage contributions to total discharge with changes in riparian surface saturation. For all the areas, no clear trends are apparent from the relationships considering percentage of outlet discharge.

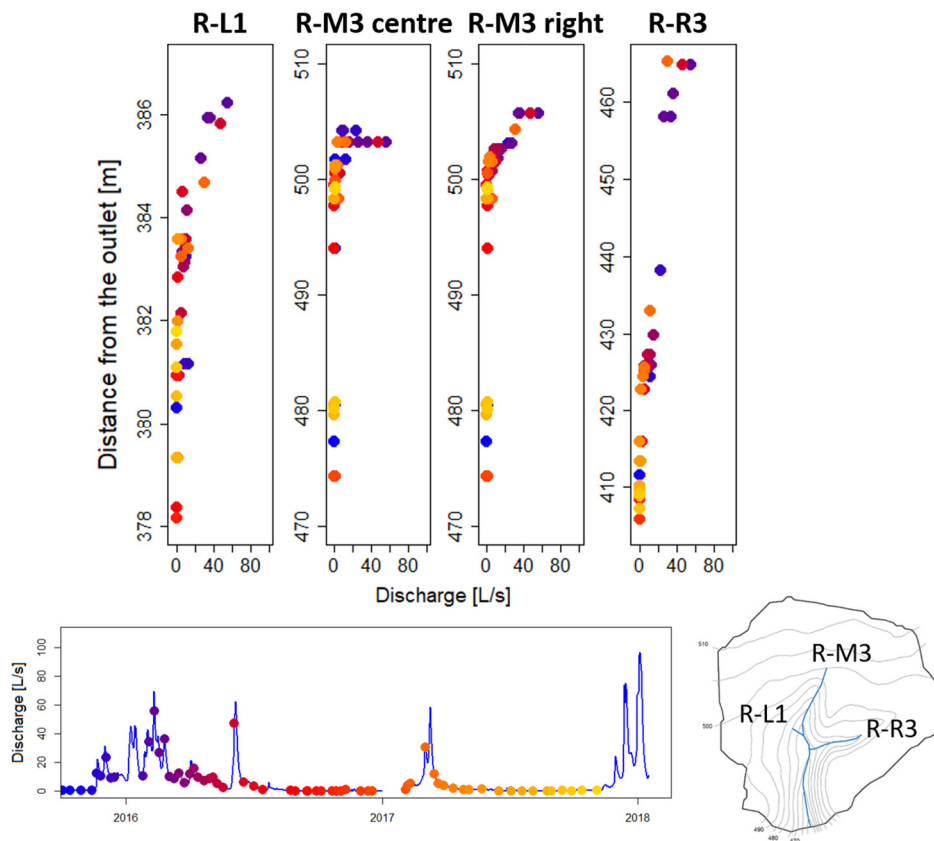


Figure 6.6: Dynamics of stream length expansion and contraction of the three headwater reaches in relation to catchment discharge at the outlet. The bottom panel shows the outlet discharge at the moments the flow starting locations have been mapped.

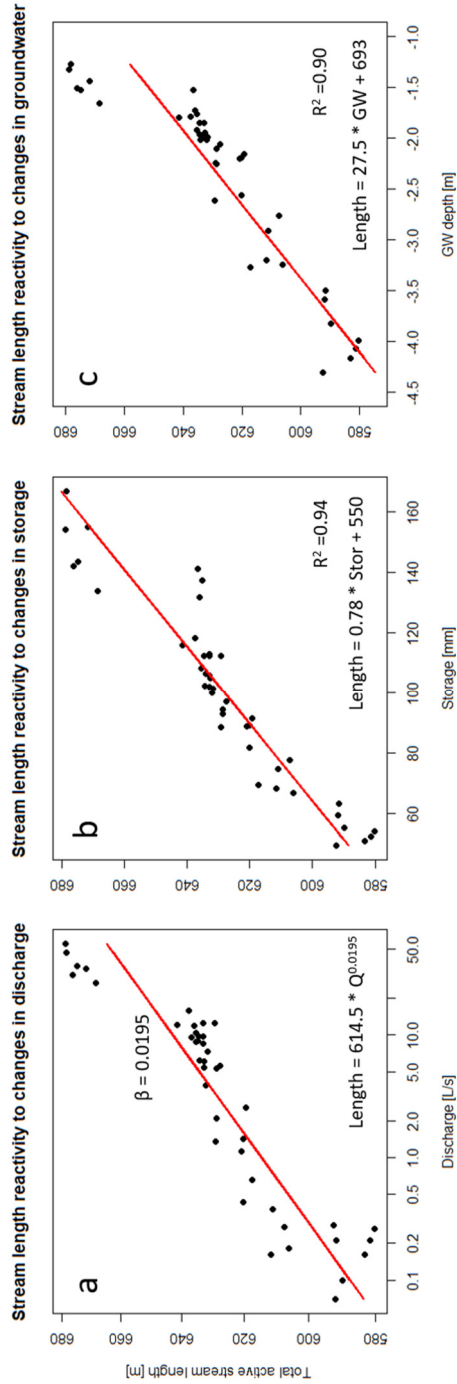


Figure 6.7: Relationships between stream length and catchment conditions. Shown are relations between total active stream length and discharge at the outlet (a – in log-log space), estimated catchment storage (b) and groundwater (GW) depth (c).

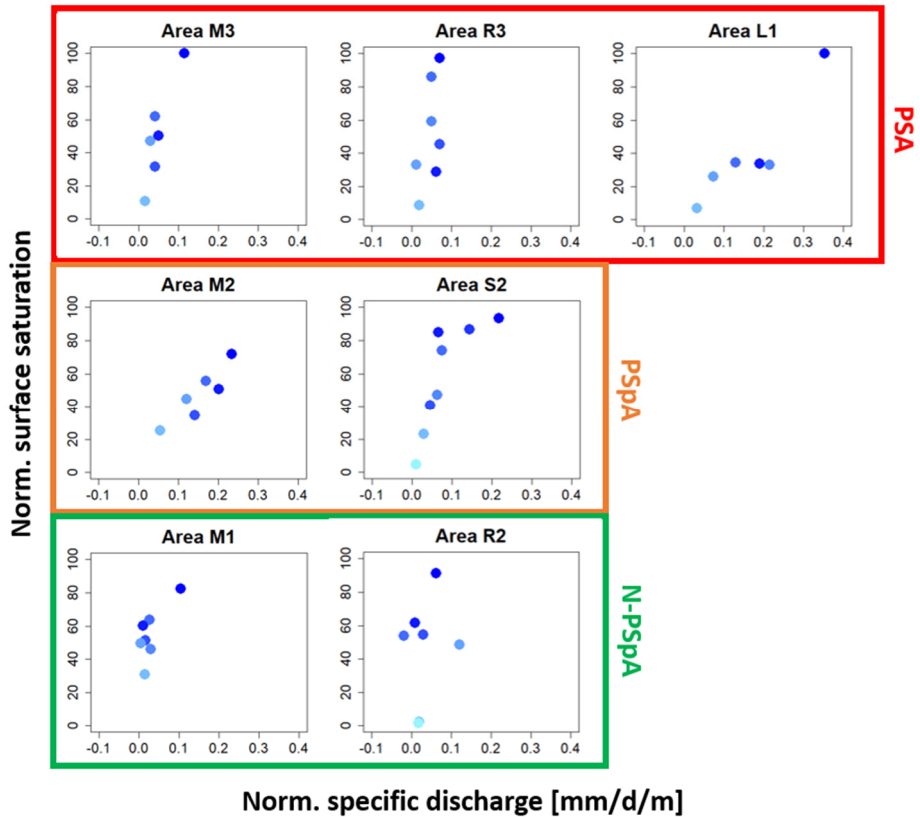


Figure 6.8: Relationship between normalized extent of surface saturation in the seven investigated riparian areas and normalised specific discharge contribution (mm/d/m) of the correspondent reach. Points' blue shades indicate observations during dryer (lighter blue shade) or wetter conditions (darker blue shades).

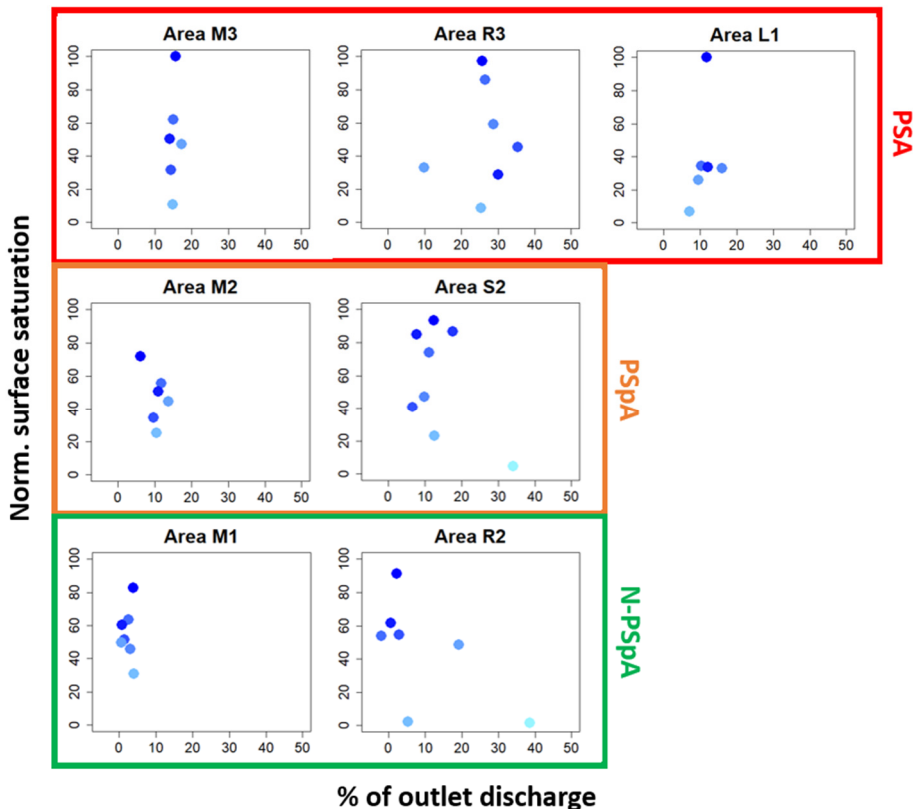


Figure 6.9: Relationship between normalized extent of surface saturation in the seven investigated riparian areas and net discharge (expressed as % of outlet discharge) of the correspondent reach. Points' blue shades indicate observations during dryer (lighter blue shade) or wetter conditions (darker blue shades).

6.4.3 Relationships between topography and streamflow contribution

A set of topographic characteristics have been initially considered in the multiple linear regression analyses for discharge and specific discharge of sub-catchments (Table 6.1) and reaches (Table 6.2). After having accounted for collinearity between the variables, only catchment area, riparian buffer, median elevation and percentage of steep slope were retained for the multiple linear regression analyses considering the sub-catchments. For the multiple linear regression analyses relative to the reaches, only percentage of riparian area was excluded. Similarly, employing backward selection, different combinations of topographic variables were retained as significant variable for the model when considering different discharge measurement dates.

Sub-catchment area and reaches' upslope catchment area significantly predicted discharge (l/s) (positive regression coefficient) in all the models (except for the 22/04/2016 reaches' model) (Table 6.3 – first two columns). Median sub-catchment elevation was also identified as a good predictor of sub-catchments' discharge (positive regression coefficient, except for the 26/11/2015 model), especially during dry and intermediate catchment wetness conditions. All models considering discharge as response variable where significant (p -value ≤ 0.05) and explained a good proportion of the discharge variance (i.e. 98-99% for sub-catchments' models; 44-94% for reaches' models).

The predictive power and significance of the models considering specific discharge (mm/d) as response variable was considerably lower (Table 6.3 – third column). For the sub-catchments, only 7 out of the 11 models were significant (p -value ≤ 0.05) and explained between 35 to 78% of specific discharge variance. In these cases, median sub-catchment elevation significantly predicted sub-catchments' specific discharge most of the times (positive regression coefficient). All the models considering reaches' specific discharge were found to be not significant.

Table 6.1: Sub-catchment topographic characteristics.

Sub-catch.	Area (m ²)	Riparian area (m ²)	% Riparian area	Riparian buffer	% Steep slope (>15°)	Median flowpath length (m)	Median elevation (m)
SW1	423438	5041	1.19	0.012	9.72	557	497
QS1	386880	4520	1.17	0.012	7.69	487	497
QS2	368549	4155	1.13	0.011	5.91	422	497
QS3	351816	3623	1.03	0.010	5.19	391	498
QS4	178668	1317	0.74	0.007	3.87	310	502
SW2	34757	153	0.44	0.005	0.00	122	500
SW3	94371	679	0.72	0.008	5.03	233	504
QM1	77164	491	0.63	0.006	3.84	197	504
QM2	63668	262	0.41	0.004	1.7	159	505
QR1	134182	1135	0.85	0.009	4.5	349	497
SW4	129339	480	0.37	0.004	3.9	268	497
QR2	113840	302	0.26	0.003	2.72	254	498

Table 6.2: Upslope catchment topographic characteristics for the portion of the catchment between the lowest and the highest discharge measurement location for every reach (i.e. upslope catchment).

Reach	Area (m ²)	Ripar. area (m ²)	% Ripar. area	Ripar. buffer	Median slope (°)	% Steep slope (>15°)	Median elevat. (m)	Reach length (m)
R-S0	16869	522	3.09	0.02	14.3	19.58	483	56
R-S1	21451	364	1.70	0.02	11.3	24.07	486	57
R-S2	16733	532	3.18	0.033	6.4	10.34	490	75
Confl. 1	38966	1170	3.00	0.03	6.1	3.50	489	100
Confl. 2	49540	153	0.44	0.01	4.5	0.12	500	87
R-L1	34757	153	0.44	0.005	4.5	0.00	500	18.36 (avg)
R-M1	17207	188	1.09	0.011	5.7	1.52	501	48
R-M2	13496	229	1.69	0.02	5.7	2.62	498	43
R-M3	63668	262	0.41	0.004	4.5	1.70	505	46.85 (avg)
R-R1	4843	656	13.54	0.16	12.6	8.01	485	91
R-R2	15499	178	1.15	0.012	5.7	4.22	493	53
R-R3	113840	302	0.26	0.003	4.5	2.72	498	41.69 (avg)

Reach length for the three headwater reaches is reported as an average.

Table 6.3: Multiple linear regression analyses output.

<i>Date</i>	<i>Sub-catch. Q [L/s]</i>	<i>Reaches Q [L/s]</i>	<i>Sub-catch. Specific Q [mm/d]</i>
26/11/2015	Area: 2.2×10^{-5} *** Elev: -8.6×10^{-2} *	Area: 2.8×10^{-5} *** Length: -1.9×10^{-2} *	Area: -3.0×10^{-6} **
15/12/2015	Area: 2.2×10^{-5} ***	Area: 1.7×10^{-5} ** Length: -2.3×10^{-2} ** Area rip: 1.3×10^{-3} *	Non-significant
25/01/2016	Area: 2.5×10^{-5} ***	Area: 2.0×10^{-5} **	Elev: 0.1 *
17/02/2016	Area: 5.8×10^{-5} ***	Area: 5.7×10^{-5} **	Non-significant
17/03/2016	Area: 3.0×10^{-5} ***	Area: 2.7×10^{-5} **	Elev: 0.1 *
22/04/2016	Area: 1.4×10^{-5} *** Elev: 1.0×10^{-1} *	Median slope: -0.7 *	Elev: 8.4×10^{-2} *
19/05/2016	Area: 5.5×10^{-6} *** Elev: 3.9×10^{-2} *	Few data	Elev: 0.03 ** Steep slope: 0.02 *
01/07/2016	Area: 8.6×10^{-6} ***	Area: 5.8×10^{-6} **	Elev: 0.03 **
23/08/2016	Few data	Few data	Few data
16/03/2017	Area: 3.0×10^{-5} ***	Area: 2.9×10^{-5} **	Non-significant
27/04/2017	Area: 3.4×10^{-6} *** Elev: 1.6×10^{-2} *	Area: 3.0×10^{-6} ***	Elev: 0.01 ** Steep slope: 0.01 *

Significant linear regression parameters are reported for the models run for the different dates taking into account sub-catchments' and reaches' discharge [L/s] – first two columns – and sub-catchments' specific discharge [mm/d] – third column. For each significant parameters the regression coefficient and the statistical significance (p-value < 0.001 ***; p-value < 0.01 **, p-value < 0.05 *) are shown.

6.5 Discussion

Until now, previous research carried out in the Weierbach catchment has led to considerable advancement in our level of understanding of how its hydrological response is generated. Through modelling and tracer based studies (Fenicia et al., 2014; Glaser et al., 2016; Klaus et al., 2015; Martínez-Carreras et al., 2016; Martínez Fernández et al., 2015; Schwab et al., 2018; Wrede et al., 2014) it has been possible to develop a solid perceptual model of the catchment, being able to explain its dual hydrological behaviour and related water sources. With the exception of the parallel modelling study by Glaser, Antonelli, Hopp, & Klaus (2019) on surface saturated areas, all the observations made until now have been based on the hydrological response of the catchment observed at its outlet. This response integrates, and perhaps smoothens possible intra-catchment heterogeneity, providing only a lumped view of the catchment functioning. To date, we still lack information on the possible heterogeneity of small-scale processes taking place in the Weierbach catchment such as surface saturation dynamics occurring at the riparian – stream interface. Krause et al. (2017) highlighted the importance of characterising catchments' eco-hydrological interfaces (e.g., the riparian zone) structuring mechanisms and processes in order to predict the occurrence and understand the importance of hydrological hotspots (or “control points”) on larger-scale processes. Here, we focused our attention on streamflow generation by separating the catchment into multiple – potentially – streamflow contributing portions. We aimed to better understand the spatial and temporal variability of streamflow within the catchment and how this information relates to the local dynamics of surface saturation.

Catchment area showed to be the dominant topographic control on sub-catchments' and reaches' discharge. The same relationship has been reported in several studies (e.g. Anderson and Burt, 1978; Bergstrom et al., 2016b; Jencso et al., 2009; Payn et al., 2012). During dry and intermediate catchment wetness conditions, catchment median elevation was an additional significant positive predictor for sub-catchments' discharge. This positive correlation is probably the result of the presence of losing sections of the stream within sub-catchments with overall lower median elevation (e.g. in reach SW1- QS2 and QR1- SW4 – cf. Figure 6.4 a). We observed quite homogeneous specific discharge contributions from the different sub-catchments (cf. Figure 6.4). Sub-catchments' specific discharge was well correlated with the hydrometric measurements of outlet discharge, GW levels and thus, estimated catchment storage. Consistent with observations by Seibert et al. (2003), we found that the correlation between sub-catchments' specific discharge and GW levels decreased with increasing distance of the wells from the stream (i.e. GW2 and GW3 generally better correlated with specific discharge than GW5 and GW6). In our case, this trend existed in particular for the most upstream sub-catchments, which were the catchments exhibiting the highest variability in specific discharge contributions – probably because their dynamics were not mitigated by catchments' area overlap (as noted by Kuraś et al., 2008) (cf. Figure 6.5 b).

When considering sub-catchments' and reaches' contributions as specific discharge, the significance of both topographic predictors and multiple linear regression models decreased dramatically, to the point that no significant models could be identified for the reaches. The only parameter that had a consistent significant positive predictive power on sub-catchments' specific discharge was

median elevation, once again mainly during dry conditions. These results suggest the presence of one/several important controlling factor/factors on specific discharge – especially when considering the different reaches – which has/have not been taken into account. As the high spatial and temporal variability observed in the reaches' normalised specific discharge (cf. Figure 6.4 and Figure 6.5 a) and their variable relationship with the different hydrometric measurements suggest, the specific discharge produced by each reach could be the result of very location-specific factors. For example, the presence of perennial springs in some of the reaches often resulted in generally higher normalised specific discharge (cf. Fig. 6.5 a). These reaches were the ones corresponding to PSA and PSpA locations observed via TIR imagery (described in our first contribution – Chapter 5). An exception was the reach “QR1-SW4”, which was identified as a losing reach during low flow and appeared to be quite active in terms of normalised specific discharge during higher flow. This is probably due to the activation of temporary springs in the streambed during wetter conditions. The activation of a temporary spring additionally to the perennial ones could be observed via TIR imagery in area S2, which also became very active during wetter conditions (cf. Figure 6.4 c). Spring location and the delivery of water from the hillslopes to the stream is likely substantially controlled by bedrock characteristics as schists/slate weathering degree, fractures' size and orientation within the catchment (Gourdol et al., 2018; Scaini et al., 2018), and/or presence of faults (Shaw, 2016; Whiting and Godsey, 2016). The aforementioned bedrock characteristics have been shown to be variable within the Weierbach catchment (Gourdol et al., 2018), representing a substantial source of variability that can be hardly disentangled.

The stream network was observed to be dynamic, but it was not very responsive to changes in catchment outlet discharge. Stream network dynamics in the three headwater locations showed to be well monotonically related to catchment outlet discharge (Fig. 6.6). However, the relationship between the total stream length and catchment outlet discharge suggested relatively small responsiveness of the stream network to changes in discharge (i.e. the low β value in the power law relationship). This is typical of catchments with stream heads “anchored” by perennial springs (cf. Fig. 6.6), as reported by Whiting and Godsey (2016) and Shaw et al. (2017). In accordance with the observations by Whiting and Godsey (2016), we detected a higher stability in reaches L1 and M3 compared to R3 (cf. Figure 6.6), which was the headwater location with the smaller accumulation area during higher flow (likely to be supported by longer, deeper and slower flowpaths) and a flatter topography. Even though stream network dynamics were found to not to be very responsive to changes in the outlet discharge, they were found to be very well correlated to estimated catchment storage and groundwater depth. This suggests the total active stream length to reflect subsurface processes variability rather than surface water dynamics at the outlet.

Riparian areas have their surface saturation positively correlated to normalised specific discharge from the correspondent reach. Antonelli et al. (Chapter 5) questioned if the small differences detected in the riparian surface saturation development and dynamics of the different riparian areas (PSA, PSpA and N-PSpA) reflected their degree of hydrological connectivity with the hillslopes. As previously observed, reaches corresponding to PSA and PSpA provided generally higher streamflow contributions than N-PSpA. Analysing how reaches' contribution varied in relation to riparian surface saturation variations (cf. Figure 6.8) we noticed that an increase in the amount of surface saturation in the riparian area corresponded to a

positive increase in normalised specific discharge, this being especially visible in PSA and PSpA. This could be related to the fact that both surface saturation and streamflow contributions from the hillslopes are influenced by groundwater fluctuations (Antonelli et al., 2019; Glaser et al., 2019, 2016; Martínez-Carreras et al., 2016; Wrede et al., 2014). The observed surface saturation vs. streamflow contribution relationships may mirror the level of connectivity of the different areas to the subsurface system as suggested in the perceptual model of Antonelli et al. (Chapter 5). Groundwater level fluctuations are likely to influence both the saturation in the riparian zone and the streambed in all the areas (Glaser et al., 2019). Eventually, water exchange between the riparian zone and the stream may contribute to the maintenance of a positive relationship between surface saturation and streamflow contribution. An example is represented by the activation of temporal springs in the riparian zone and the connectivity of the exfiltrated groundwater to the stream. This could be observed for area S2, where a clear increase in surface saturation and streamflow contribution is visible in moments of high flow (cf. Fig. 6.8 – area S2). This sharp increase is very likely to correspond to moments of activation of a temporal spring observed at the hillslope foot in this area. At a lesser extent, this was also observed in area M1 and L1. The effect of longitudinal connectivity (i.e. water contributions from upstream) was also reflected in the surface saturation vs. streamflow contribution relationship: in areas R2, this resulted in higher mapped surface saturation regardless whether the reach was gaining, losing or not contributing to streamflow (e.g. Figure 6.8 – area R2). It is difficult to understand if the extensive and stable surface saturation developing in PSA and PSpA is related to their high streamflow contribution. While this could be the case during rainfall events, in moments when the system is not affected by the occurrence of precipitations the level of surface saturation in one area and the streamflow generated by the correspondent reach seem not to really influence each other, but rather be influenced by a common factors as groundwater dynamics and springs locations. Note that since surface saturation has been quantified as percentage of saturated pixels and not as area, we could not quantify if areas with an absolute larger surface saturation provided more streamflow contribution than others.

The described positive relationship between surface saturation and streamflow contribution disappears when we consider the percentage contribution of a specific reach to the total catchment outlet discharge. We noticed that some areas contributed for very stable percentage of total discharge regardless of the general catchment wetness conditions and the level of surface saturation in the area (cf. Figure 6.9). A more stable percentage of contribution seemed to be associated to the reaches located in the middle and west part of the stream (i.e. reaches M3, M2; M1 and L1), in contrast to the reaches located in the east (R2 and R2) and lower part (S2) of the stream. As previously mentioned, the investigations of Gourdol et al. (2018) employing soil drilling and Electrical Resistivity Tomography (ERT) revealed some heterogeneities in the subsurface structure of the Weierbach catchment. In particular, they have shown that the northern and western part of the catchment is characterised by overall thinner solum (i.e. “true soil”, where pedogenic processes are dominant; cf. Gourdol et al., 2018) and shallower hard bedrock compared to the eastern portion of the catchment. This may determine differences in the way different sides of the catchment deliver water to the stream. However, the mechanism behind the consistency of the relative contribution of some specific reaches to the total catchment outlet discharge remains of difficult interpretation.

The key role of near-stream surface saturation in mediating hydrological connectivity between hillslopes and streams has been acknowledged across a range of landscapes and climate conditions, such as – just to mention a few – catchments in boreal and temperate environments (Birkel et al., 2010; Devito et al., 2005; Tetzlaff et al., 2007), Mediterranean (Lana-Renault et al., 2014; Latron and Gallart, 2007; Niedda and Pirastru, 2014) and alpine environments (Kirnbauer and Haas, 1998; von Freyberg et al., 2014). Similarly to what we observed in the Weierbach catchment, groundwater dynamics and local topography – and in some cases the presence of perennial groundwater springs – have been recognised as the main controls on surface saturation dynamics in the majority of the aforementioned studies. Thus, we believe our results to provide a good representation of the spatio-temporal dynamics of surface saturation and streamflow generation occurring in most headwater catchments.

Recent studies have reaffirmed the need for catchments' interfaces to be characterised for their own processes and fluxes in order to have a better perception of where and when connectivity may take place in a catchment (Blöschl et al., 2019; Wohl et al., 2019). Failure in assessing possible heterogeneities may lead to erroneous processes conceptualisation and discrepancies between processes observed at smaller scales and responses that may occur at larger scales (Krause et al., 2017; Ward and Packman, 2019). In this study – together with its accompanying manuscript – we go beyond the sole characterisation of the surface saturation vs. outlet baseflow discharge relationship of a catchment (Ambrose, 2016; Latron and Gallart, 2007). Our results suggest that a deeper understanding of the role played by riparian surface saturation in mediating hydrological connectivity along the HRS continuum (and how it translates into the total discharge volume observed at the outlet) is possible – probably only – if considering the riparian zone (and the multitude of its hydrological processes) as a complex feature of the system, rather than as a single homogeneous entity (as suggested by Ledesma et al. (2018)). Interfaces in hydrology have been traditionally considered as a boundary condition (Blöschl et al., 2019) where complexity is commonly reduced for the sake of simplicity in experimental and conceptual model designs (Krause et al., 2017). However, Blöschl et al. (2019) also recognise the need to start looking for more typical cases where this simplification can be applied or not. In our catchment, we observed that, although the seasonal dynamics of surface saturation in the different investigated areas seem to be synchronous (Chapter 5), this does not necessarily translate into similar hydrological behaviour in terms of streamflow contribution for all areas. This kind of variability is at the base of the difference between variable active and variable contributing areas (or periods) described by Ambrose (2004) and has important implications for investigating and modelling catchments' responses. This is fundamental in studies which focus on biogeochemical transformations occurring in the riparian zone (Blume and van Meerveld, 2015; Laudon et al., 2016; Ledesma et al., 2018). Indeed, variable dynamics of surface saturation could provide indications on potentially different buffer capacities of distinct riparian sections, both in terms of water quantity and quality.

6.6 Conclusion

In this contribution, we have explored the spatio-temporal variability of streamflow generation in the Weierbach catchment. We investigated possible links to the occurrence and dynamics of surface saturation and active stream length. We carried out our investigations at a finer scale compared to previous studies and showed that a considerable level of heterogeneity can be found within a small, homogeneous (e.g. vegetation coverage and pedological and geological characteristics) headwater catchment.

We found that the net discharge contribution variability between different sub-catchments and between different reaches could be explained by the contributing area. However, this was not the case when considering the area-specific discharge contribution of different sub-catchments and reaches. In this case, no clear topographic control was able to explain the variability in contribution, suggesting that very local factors may influence streamflow generation, such as bedrock characteristics or the presence of perennial springs. We related the surface saturation dynamics observed within the catchment to the streamflow dynamics. The stream network expansion and contraction dynamics reflected the general wetness state of the catchment (i.e. they were related to groundwater fluctuations and changes in the estimated catchment storage), but they were not very responsive to changes in outlet discharge (i.e. perennial springs would “anchor” the channel head in specific locations for most of the time). Finally, we showed that the surface saturation vs. streamflow contribution relationship in different riparian areas could mirror the degree of connectivity of the areas to the subsurface system.

Besides providing new information on sub-catchment scale processes in the Weierbach catchment, we have shown that a combination of a thorough investigation of surface saturated areas dynamics within the catchment through TIR imagery with sequential measurements of stream discharge can be used to improve our perception and understanding of the internal heterogeneity of catchments. Our approach is in line with the “Roadmap for Eco-hydrological Interface Research” proposed by Krause et al. (2017), since we applied a combination of approaches from different disciplines to investigate the complexity of the riparian – stream interface and identify hotspots of hydrological connectivity / streamflow generation. This information is also fundamental in studies which have their focus on nutrients and tracers transport and eco-hydrological processes in the riparian zone. Future research should focus on analysing and linking the observed catchment’s internal heterogeneities with reference to stream water isotopic and chemical signature or through simulation approaches.

Chapter 7

Synthesis

7.1 Main findings

The aim of this thesis was to improve our understanding of hydrological connectivity between different structural and functional elements of the hydrological system by looking at the spatial and temporal dynamics of surface water at different spatial scales. In order to achieve this objective, two innovative multidisciplinary approaches for tracing hydrological connectivity – namely terrestrial diatoms and ground-based thermal infrared imagery – were employed in the Attert River basin in Luxembourg. The five studies presented in the Chapters of this thesis contribute (i) to the development of the used techniques (Chapters 2, 3, and 4) and (ii) to the advancement of our comprehension of the different hydrological processes related to connectivity (Chapters 4, 5, and 6). The Chapters' main scientific and technical findings are summarised as follows:

- Understanding the physiographic controls on terrestrial diatom communities is fundamental for advancing their employment as tracer of hydrological connectivity at catchment-scale (Chapter 2). Species assemblages in terrestrial diatom communities are influenced by soil parameters such as soil pH, land use, total carbon and nitrogen content. Species assemblages are able to provide information on soil anthropic disturbance levels (i.e. different terrestrial diatom species showing different sensitivity to anthropic disturbance). However, we still lack information on the ecological behaviour and sensitivity to disturbance of many terrestrial diatom species abundant in our study area.
- Ground-based TIR imagery provides valuable information for rapid *in-situ* visualisation of water mixing and mixing dynamics at the confluence-scale represented in the study (Chapter 3). Cross-sectional variability in surface temperature observed through TIR imagery reflects the in-stream variability of temperature and chemistry. TIR imagery allows the identification of the mixing front position along the stream cross-sections and of the distance to complete mixing in both natural and urbanised stream confluences, especially when the TIR images are acquired under favourable conditions (i.e. good temperature contrast between tributaries and nearly total absence of surface roughness).

- Ground-based thermal infrared imagery is a very powerful method for mapping surface saturation in terms of practicability and spatial and temporal flexibility (Chapter 4). Thermal infrared imagery is applicable throughout the year and it can reveal spatially heterogeneous surface saturation dynamics (i.e. different surface saturation expansion and contraction dynamics in different riparian locations within the catchment) and distinct types of saturation patterns (i.e. parallel or perpendicular orientation of riparian surface saturation to the adjacent stream). Surface saturation patterns observed through ground-based thermal infrared imagery helped identifying different processes underlying the development of surface saturation (i.e. groundwater exfiltration points or stream expansion into the riparian zone) (Chapter 4).
- The repeated mapping of riparian surface saturation is fundamental to explore and characterise the similarities and dissimilarities of both the spatio-temporal dynamics of surface saturation in different riparian areas within the catchment and their relationship with streamflow generation (Chapter 5 and 6).
 - Storage thresholds may control the transition between low extents of riparian surface saturation and high extents of riparian surface saturation (Chapter 5).
 - Sources of intra-catchment heterogeneity are represented by the location of the riparian surface saturated areas along the stream network (i.e. their elevation), the local riparian morphology (i.e. width of the riparian area) and the presence or absence of groundwater exfiltration points in the areas. These features influence the development of surface saturation and the shape of the surface saturation – outlet baseflow relationship observed in different riparian areas (Chapter 5).
 - Streamflow generation in the catchment is influenced by very local bedrock characteristics (variable within the catchment) and the presence or absence of perennial groundwater exfiltration points. These perennial groundwater exfiltration points also cause the stream network not to be very responsive to changes of outlet discharge (Chapter 6).
 - The relationship between surface saturation in different areas and streamflow contribution of the corresponding reaches provides information on the degree of connectivity of the different areas to the subsurface system (i.e. activation of temporal springs), although the level of surface saturation in one area and the streamflow generated by the corresponding reach do not seem to influence each other (investigated during absence of precipitation) (Chapter 6).
 - Some of the investigated stream reaches generated a very stable percentage of the total outlet discharge, regardless of the wetness state of the catchment and the level of surface saturation observed in the corresponding riparian area (Chapter 6).

In summary, this thesis is an example of how multidisciplinary approaches and techniques can provide new information on hydrological processes related to connectivity across different spatial and temporal scales of investigation.

The terrestrial diatom approach can be adopted to investigate sub-catchment connectivity in any catchment where idoneous substrates (e.g. soils, rocks, lichen, litter, vegetation) and favourable environmental conditions (e.g. a certain level of moisture and light) for terrestrial diatom growth are present. This approach requires that different diatom species or assemblages can be assigned to different source areas. In catchments characterised by a variety of soil types (e.g. soil of different pH, carbon and nitrogen content) and land use, heterogeneous diatom assemblages may be expected within the catchment, similarly to what was observed in the Attert River basin (Chapter 2). Since different environmental parameters other than those observed in the Attert River basin can influence terrestrial diatom assemblages, a thorough characterisation of the communities occurring in the study area is still necessary.

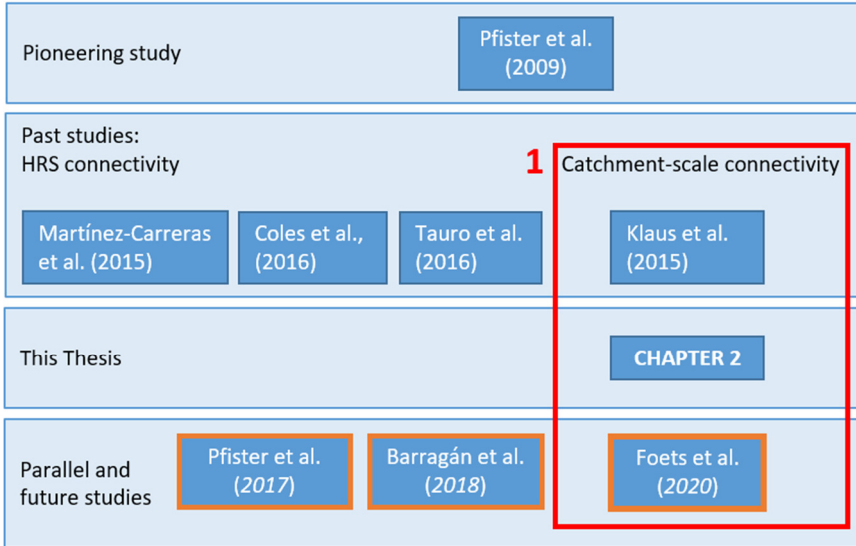
Thermal infrared imagery can be applied for mapping surface saturation in different environmental set-ups, provided that a good temperature contrast is present between the water and the surrounding environment and that the obstructions between the camera and the object are limited (e.g. surface saturated area) (Chapter 4). Similarly to what has been observed in the Weierbach catchment, groundwater dynamics and local topography have been identified as the main controls on surface saturation dynamics in many studies (e.g. Birkel et al., 2010; Devito et al., 2005; Kirnbauer and Haas, 1998; Lana-Renault et al., 2014; Latron and Gallart, 2007; Niedda and Pirastru, 2014; Tetzlaff et al., 2007; von Freyberg et al., 2014), carried out across different landscapes and climate conditions (e.g. boreal, temperate, Mediterranean and alpine environments). For this reason, the findings presented in chapters 5 and 6 may provide a good representation of the spatio-temporal dynamics of surface saturation and streamflow generation that can be occurring in most headwater catchments.

7.2 Contribution of this work to hydrological sciences

7.2.1 Local hydrology research

The work presented in this thesis is closely associated with a series of parallel and planned future studies in Luxembourg. Figure 7.1 resumes Figure 1.3 presented in the thesis introduction and shows the studies that have been carried out – or are currently under preparation – which include information from the work presented in this thesis (orange rectangles).

Terrestrial diatom studies



TIR studies

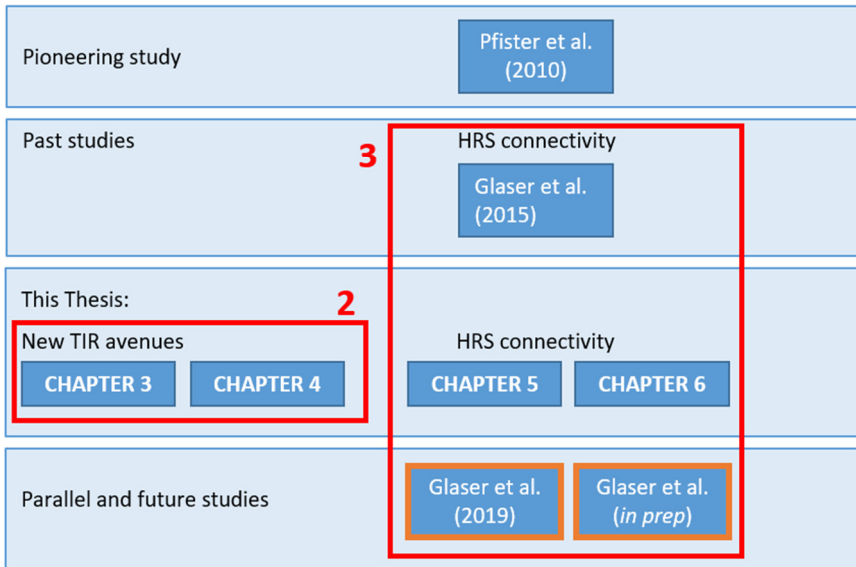


Figure 7.1: Thesis framework. Each chapter is assigned to a different broad research topic (indicated by the red boxes): 1) Terrestrial diatoms as a tracer of hydrological connectivity at the catchment scale (Chapter 2); 2) New avenues for thermal infrared (TIR) imagery as a tracer of hydrological connectivity (Chapters 3 and 4); 3) TIR imagery as a tracer of hydrological connectivity along the HRS continuum (Chapters 5 and 6). Studies that have been carried out or are currently under preparation and include information from the work presented in this thesis are indicated by orange rectangles.

Additional work on terrestrial diatom communities has continued focusing on the development of a rigorous terrestrial diatom sampling protocol (Barragán et al., 2018) and on the identification of environmental controls on terrestrial diatom communities (Foets et al., 2020). Surface saturation mapping through TIR imagery has been used by Glaser et al. (2019, n.d.) for the validation of a spatially distributed, physically-based, integrated hydrological model, with the aim of accurately reproducing and analysing the generation and development of riparian surface saturation.

7.2.2 International hydrology research

Scientific advancements

The development of innovative, multidisciplinary approaches and techniques for tracing hydrological connectivity is indispensable for generating new information on connectivity processes across multiple spatial and temporal scales (Abbott et al., 2016; Hannah et al., 2007; Smith et al., 2019; Tetzlaff et al., 2007; Wainwright et al., 2011). Thanks to the employment of novel techniques such as terrestrial diatoms and TIR imagery, some of the challenging aspects of investigating hydrological connectivity (described in the introduction of this thesis) have been further explored in this thesis. In particular:

- The development of new approaches for tracing hydrological connectivity at the catchment scale (Chapter 2).
Terrestrial diatom species have great potential to be used as a proxy of connectivity at the catchment scale. Once the abundance of specific terrestrial diatom species is associated to certain environmental conditions, the occurrence of these species in the stream network could provide an indication of the hydrological connection of specific areas within the catchment to the catchment outlet.
- The identification of intra-catchment homogeneous and heterogeneous landscape structures and connectivity pathways (Chapters 5 and 6) and the characterisation of the processes and water fluxes occurring around transition zones, or interfaces (Chapters 4, 5, and 6).
An improved understanding of the development and dynamics of riparian surface saturation and of its role in mediating hydrological connectivity along the hillslope-riparian-stream continuum (and how it translates into the total discharge volume observed at the outlet) is possible – probably only – if considering the riparian zone (and the multitude of hydrological processes taking place there) as a complex, possibly heterogeneous, feature of the system, rather than as a single homogeneous entity.

Technical advancements

The work presented in Chapter 3 and Chapter 4 provides detailed indications of how TIR imagery can be adopted in hydrological research for the investigation of water mixing at confluences and for mapping surface saturation

dynamics. Chapter 3 shows how the observation of surface water mixing at confluences through thermal infrared imagery can be translated into information on the mixing front position along the stream cross-sections and of the distance to complete mixing. Chapter 4 is a technical note which can be used by researchers as a handbook. It provides a complete review of all the necessary steps (from thermal infrared image acquisition to post-processing, and creation of surface saturation maps) to successfully apply thermal infrared imagery for surface saturation mapping.

7.3 Concluding remarks and future avenues

Due to the difficulties in employing geochemical and isotopic tracers at the catchment scale because of the extreme water mixing (Klaus et al., 2015; Klaus and McDonnell, 2013), working on the development of alternative, conservative tracers that can be used at large-scale is relevant for advancing hydrological connectivity research. Investigating environmental controls on terrestrial diatom communities is fundamental to advance the use of terrestrial diatoms as a tracer of catchment-scale connectivity (Chapter 2). To date, the terrestrial diatom approach is still qualitative (Pfister et al., 2017). In order to make this approach more quantitative, the next research step would be to relate the occurrence of specific terrestrial diatom species to the habitats characterising distinct source areas. In this way, once a limited number of target species have been identified, their behaviour in association to different hydrological processes (e.g. surface runoff) can be investigated. To considerably reduce the diatom sample processing time, which is labour-intensive, the target species could be traced in water using genetic analysis such as DNA barcoding. Nowadays, DNA barcoding applied to aquatic diatom species is used in different fields, such as river quality assessment (e.g. Mortágua et al., 2019) and forensic studies (e.g. Fang et al., 2019). Recently, an open-access, curated barcode library for diatoms has been created (Rimet et al., 2019 - https://www6.inra.fr/cartel-collection_eng/Barcoding-database).

The investigation of the spatial and temporal variability of the multitude of hydrological processes taking place at catchment interfaces is challenging. However, the characterisation of these processes is fundamental in order to better understand catchment hydrological and biochemical functioning (Grabs et al., 2012; Krause et al., 2017; Ledesma et al., 2018; Tetzlaff et al., 2008; Vidon and Hill, 2004). In this thesis, the TIR imagery approach has been employed to investigate two hydrological processes at interfaces: water mixing at stream confluences and surface saturation dynamics in the riparian zone.

Stream confluences represent important eco-hydrological hotspots, where water with potentially different physio-chemical characteristics mixes along an interface (Chapter 3). Understanding water mixing dynamics at confluences is fundamental to characterise the local dispersion dynamics of suspended sediments and dissolved substances (Best, 1987; Boyer et al., 2006), which eventually influence the habitat variability and stream biodiversity downstream of the confluence (Rice et al., 2008). Future work may focus on exploring how changing hydrological conditions at confluences affect downstream ecology by combining frequent *in-situ* thermal infrared observations of mixing dynamics with water sampling for qualitative and quantitative hydrological analyses.

A detailed characterisation of the expansion and contraction of surface saturation in riparian zones and its connectivity to the stream is fundamental to improve our understanding of the spatial and temporal variability of streamflow generation processes (Chapters 4, 5 and 6). Understanding where, when and how connectivity takes place at the hillslope-riparian-stream interface has important implications for investigating and modelling catchment responses. Moreover, it is fundamental in studies which focus on biogeochemical transformations occurring in the riparian zone (Blume and van Meerveld, 2015; Laudon et al., 2016; Ledesma et al., 2018). Indeed, variable dynamics of surface saturation could provide indications on potentially different buffer capacities of distinct riparian sections, both in terms of water quantity and quality.

Overall, the work presented in Chapters 5 and 6 has improved the perception and understanding of the internal heterogeneity of the catchment and how it affects hydrological connectivity and streamflow generation. This has generated new research questions that should be investigated in the future:

- Analysing and linking the observed intra-catchment heterogeneities with stream water isotopic and chemical signature (e.g. combining fixed *in-situ* TIR camera observations with water sampling) or through simulation approaches.
- Deepening the investigation of the geological and topographic controls of surface saturation (i.e. frequent surface saturation mapping should be carried out in catchments presenting different geological and physiographic characteristics).
- Further explore the effects of storage thresholds on the development of surface saturation (e.g. catchment storage and riparian soil capacity to store and release water – combining fixed *in-situ* thermal infrared camera observations and hydrometric measurements during periods of seasonal transition).
- Further investigate possible seasonal shifts in the dominant processes influencing surface saturation development and dynamics (and how this may affect the calculation of topographic wetness indices).

Did a multidisciplinary approach help investigating hydrological connectivity?

The multidisciplinary approach is a mainstay of this work. Some of the specific research hypotheses and questions proposed in this thesis could not be answered without the help of the employed approaches, especially for what concerns the TIR methodology.

In this thesis, the thermal infrared technology is confirmed as valid routine method for repeated mapping of surface saturation. The frequency at which riparian surface saturation was mapped was critical to characterise the similarities and dissimilarities in both the temporal dynamics of surface saturation in different areas and their connectivity to the stream. Thermal infrared imagery allowed the acquisition of surface saturation data at a frequency high enough to disclose the behaviour of riparian saturated areas and characterise their particular dynamics. Equally important, the repeated observation of a catchment through a thermal infrared camera eventually helps the researcher to gain a deeper empirical understanding of

the catchment. This eventually leads to a better perceptual understanding of the dominant hydrological processes in the studied area.

The use of terrestrial diatoms as a tracer of hydrological connectivity is still under development. Progress in this direction is hampered by the challenging aspects of collecting and analysing diatoms in practice. As stated by Pfister et al., (2017): “Any diatom-based tracer experiment requires expert knowledge. [...] Consequently, using diatoms as an environmental tracer is not accessible *per se*, but rather an approach that is still occupying a niche in disciplines such as hydrology or eco-hydrology”. This may discourage hydrologists from using this technique in the first place. Probably, it is also the reason why studies that could advance this method are still scarce and carried out in a limited number of research groups. However, recent efforts made by the diatom experts to create a curated barcode library for diatom species (Rimet et al., 2019), will eventually make diatoms more accessible to a broader scientific public. Eco-hydrologists should not abandon the idea of employing diatoms in hydrological investigation as the best, for this relatively new approach in eco-hydrology, may be yet to come.

Appendix

Appendix to Chapter 2

Table A2.1: raw values for the measured geochemical (a) and seasonal (b) environmental parameters. Legend for pedology abbreviations: MA: silty-clay soils from marls; SC: Silty-Stony soils from schists; RS: Silty-stony soils from red sandstone; AL: Recent soils from alluvial valleys; LS: Sandy and loamy soils derived from sandstone.

a

Sample	Month	Land use	Geology	Pedology	EC ($\mu\text{S}/\text{cm}$)	pH _{CaCl2}	C (%)	N (%)
1	August	Grassland	Alluvial	SC	252	6.5	5.6	0.5
2	August	Grassland	Alluvial	SC	211	5.1	5.4	0.6
3	August	Agriculture	Schists	SC	86.1	5.2	3.3	0.4
4	August	Forest	Schists	SC	182.4	5.3	6.4	0.7
5	August	Forest	Alluvial	AL	280	7.0	6.6	0.5
6	August	Grassland	Schists	SC	127.3	5.6	2.6	0.3
7	August	Grassland	Sandstone	LS	161.5	5.2	4.9	0.4
8	August	Forest	Sandstone	LS	237	7.3	3.1	0.1
9	August	Agriculture	Schists	SC	103.3	4.9	3.4	0.4
10	August	Forest	Schists	SC	79.7	5.2	3.7	0.3
11	August	Grassland	Schists	RS	327	5.1	6.6	0.6
12	August	Forest	Sandstone	RS	170.8	5.0	3.1	0.2
13	August	Agriculture	Alluvial	AL	91	5.5	1.3	0.2
14	August	Grassland	Sandstone	LS	214	6.6	2.1	0.2
15	August	Agriculture	Alluvial	MA	77.2	5.7	1.1	0.1
16	August	Grassland	Alluvial	AL	190.9	7.0	2.4	0.2
17	August	Grassland	Marls	MA	411	6.3	6.9	0.6
18	August	Agriculture	Marls	MA	120.3	6.2	1.7	0.2
19	August	Grassland	Alluvial	MA	513	7.3	3.2	0.3
20	August	Grassland	Alluvial	MA	361	6.6	17.9	1.2
21	August	Grassland	Alluvial	AL	96.5	6.9	1.3	0.2
22	August	Agriculture	Sandstone	LS	18.1	6.2	0.4	0.0
23	August	Agriculture	Alluvial	AL	69.5	5.7	1.3	0.1
24	August	Grassland	Alluvial	AL	107.2	5.2	2.7	0.3
25	August	Forest	Alluvial	RS	77.8	7.0	0.9	0.1
26	August	Forest	Alluvial	RS	159.4	7.4	2.3	0.1
27	August	Grassland	Alluvial	MA	401	7.1	10.3	0.8
28	August	Agriculture	Sandstone	AL	92.2	5.6	0.9	0.1

Appendix

29	August	Forest	Schists	SC	135.9	4.9	3.3	0.3
30	August	Forest	Schists	SC	393	4.6	2.4	0.2
31	August	Grassland	Marls	AL	123.8	6.8	2.5	0.5
32	August	Agriculture	Marls	AL	154.6	6.1	9.9	0.6
33	August	Grassland	Marls	AL	230	6.2	11.1	0.5
34	November	Grassland	Alluvial	SC	132.6	6.2	4.5	0.4
35	November	Grassland	Alluvial	SC	66.2	5.1	4.6	0.5
36	November	Agriculture	Schists	SC	48.2	5.4	2.7	0.4
37	November	Forest	Schists	SC	120	5.4	5.4	0.5
38	November	Forest	Alluvial	AL	89.9	4.7	5.6	0.4
39	November	Grassland	Schists	SC	49.5	4.9	3.1	0.4
40	November	Grassland	Sandstone	LS	79.5	5.7	2.1	0.2
41	November	Forest	Sandstone	LS	118.9	7.2	2.5	0.1
42	November	Agriculture	Schists	SC	46.8	4.9	2.9	0.4
43	November	Forest	Schists	SC	171.1	7.2	2.4	0.2
44	November	Grassland	Schists	RS	94.5	5.1	3.4	0.3
45	November	Forest	Sandstone	RS	101.3	5.4	8.6	0.5
46	November	Agriculture	Alluvial	AL	68.5	6.3	1.4	0.3
47	November	Grassland	Sandstone	LS	129	6.6	2.0	0.3
48	November	Agriculture	Alluvial	AL	151.6	7.4	2.5	0.3
49	November	Agriculture	Alluvial	MA	150.4	6.7	2.4	0.3
50	November	Grassland	Marls	MA	203	5.9	8.6	0.8
51	November	Agriculture	Marls	MA	80.3	6.6	1.4	0.2
52	November	Grassland	Alluvial	MA	188.3	7.3	1.2	0.1
53	November	Grassland	Alluvial	MA	344	6.9	23.2	1.5
54	November	Grassland	Alluvial	AL	61.2	6.4	1.5	0.2
55	November	Agriculture	Alluvial	AL	87.3	5.0	1.3	0.1
56	November	Grassland	Alluvial	AL	55.2	5.7	1.2	0.1
57	November	Forest	Alluvial	RS	106.1	6.9	1.5	0.1
58	November	Forest	Alluvial	RS	145.7	7.5	1.3	0.1
59	November	Agriculture	Sandstone	AL	77.8	6.2	0.8	0.1
60	November	Forest	Schists	SC	112.3	4.6	3.3	0.3
61	November	Forest	Schists	SC	56	4.7	1.7	0.2
62	November	Grassland	Marls	AL	124.4	7.1	3.4	0.2
63	November	Agriculture	Marls	AL	118	6.8	11.8	0.7
64	November	Grassland	Marls	AL	239	6.5	11.5	0.6
65	March	Grassland	Alluvial	SC	243	6.0	4.3	0.4
66	March	Grassland	Alluvial	SC	253	5.0	6.2	0.6
67	March	Forest	Schists	SC	274	5.2	6.4	0.6
68	March	Forest	Alluvial	AL	92	5.3	3.1	0.3
69	March	Grassland	Schists	SC	201	5.1	2.7	0.3
70	March	Grassland	Sandstone	LS	52.4	5.6	1.5	0.1
71	March	Forest	Sandstone	LS	99.5	7.2	1.6	0.1
72	March	Agriculture	Schists	SC	81	5.3	3.3	0.3

73	March	Forest	Schists	SC	210	7.3	2.1	0.1
74	March	Grassland	Schists	RS	110.6	5.3	3.4	0.3
75	March	Forest	Sandstone	RS	186.5	7.5	2.2	0.2
76	March	Agriculture	Alluvial	AL	131.7	6.4	1.4	0.2
77	March	Grassland	Sandstone	LS	142.8	7.0	1.5	0.2
78	March	Agriculture	Marls	MA	204	6.9	1.3	0.1
79	March	Grassland	Alluvial	MA	180.7	7.0	3.0	0.3
80	March	Grassland	Alluvial	MA	286	6.3	6.2	0.7
81	March	Grassland	Alluvial	AL	84.5	6.5	1.6	0.2
82	March	Grassland	Alluvial	AL	176.3	6.0	2.7	0.3
83	March	Grassland	Alluvial	MA	185.2	7.4	7.1	0.3
84	March	Agriculture	Sandstone	AL	65.5	6.0	1.1	0.2
85	March	Forest	Schists	SC	116.5	5.1	2.9	0.3
86	March	Forest	Schists	SC	61	5.0	2.8	0.3
87	March	Grassland	Marls	AL	175.3	7.0	6.0	0.6
88	March	Agriculture	Marls	AL	265	6.7	13.8	0.8
89	March	Grassland	Marls	AL	285	6.9	11.2	0.6

b

Month	Temp_day_ 10days average (°C)	Temp_night_ 10days average (°C)	Precip_cum_ 10days (mm)	Soil_temp_5cm daily average (°C)	Air humidity (%)
August	25.4 ± 5.7	14.3 ± 2.9	55.6	20.1 ± 1.6	85.8
November	8.8 ± 2.3	5.8 ± 1.9	15.2	9.0 ± 0.6	95.9
March	9.4 ± 5.6	2.4 ± 3.5	5.7	7.2 ± 1.2	85.1

Table A2.2: partial RDA model output.

Partitioning of variance:

	Inertia	Proportion
Total	0.7680	1.00000
Conditioned	0.0497	0.06472
Constrained	0.2025	0.26364
Unconstrained	0.5158	0.67165

Eigenvalues, and their contribution to the variance after removing the contribution of conditioning variables

Importance of components:

	RDA1	RDA2	RDA3	RDA4	RDA5	RDA6	RDA7
Eigenvalue	0.05738	0.04703	0.01943	0.01590	0.01269	0.009984	0.00868
Proportion Explained	0.07989	0.06547	0.02705	0.02214	0.01766	0.013900	0.01208
Cumulative Proportion	0.07989	0.14536	0.17241	0.19455	0.21221	0.226110	0.23819

	RDA8	RDA9	RDA10	RDA11	RDA12	RDA13
Eigenvalue	0.007027	0.006429	0.005743	0.004901	0.004418	0.002864
Proportion Explained	0.009780	0.008950	0.008000	0.006820	0.006150	0.003990
Cumulative Proportion	0.247970	0.256920	0.264920	0.271740	0.277890	0.281880

	PC1	PC2	PC3	PC4	PC5	PC6	PC7
Eigenvalue	0.04707	0.03237	0.03148	0.02430	0.02336	0.02294	0.02142
Proportion Explained	0.06553	0.04507	0.04383	0.03383	0.03252	0.03193	0.02981
Cumulative Proportion	0.34740	0.39247	0.43631	0.47014	0.50266	0.53459	0.56440

	PC8	PC9	PC10	PC11	PC12	PC13	PC14
Eigenvalue	0.01775	0.01719	0.01643	0.01604	0.01440	0.01398	0.01375
Proportion Explained	0.02471	0.02393	0.02287	0.02233	0.02004	0.01946	0.01914

Cumulative Proportion 0.58911 0.61304 0.63591 0.65824 0.67828 0.69773 0.71687

	PC15	PC16	PC17	PC18	PC19	PC20
Eigenvalue	0.01252	0.01144	0.01023	0.009757	0.009553	0.00927
Proportion Explained	0.01743	0.01592	0.01425	0.013580	0.013300	0.01291
Cumulative Proportion	0.73431	0.75023	0.76447	0.778060	0.791350	0.80426

Accumulated constrained eigenvalues

Importance of components:

	RDA1	RDA2	RDA3	RDA4	RDA5	RDA6	RDA7
Eigenvalue	0.05738	0.04703	0.01943	0.01590	0.01269	0.009984	0.00868
Proportion Explained	0.28340	0.23228	0.09596	0.07853	0.06265	0.049310	0.04287
Cumulative Proportion	0.28340	0.51568	0.61165	0.69018	0.75283	0.802140	0.84501

	RDA8	RDA9	RDA10	RDA11	RDA12	RDA13
Eigenvalue	0.007027	0.006429	0.005743	0.004901	0.004418	0.002864
Proportion Explained	0.034710	0.031750	0.028360	0.024210	0.021820	0.014140
Cumulative Proportion	0.879710	0.911470	0.939830	0.964040	0.985860	1.000000

Scaling 2 for species and site scores

- * Species are scaled proportional to eigenvalues
- * Sites are unscaled: weighted dispersion equal on all dimensions
- * General scaling constant of scores: 2.867241

Appendix to Chapter 5

Bibliography for the 30 studies considered for the review figure (Chapter 5 Figure 5.1):

Ali, G., Birkel, C., Tetzlaff, D., Soulsby, C., McDonnell, J. J., & Tarolli, P. (2013). A comparison of wetness indices for the prediction of observed connected saturated areas under contrasting conditions. *Earth Surface Processes and Landforms*, 39(3), 399–413. <https://doi.org/10.1002/esp.3506>

Ambrose, B. (2016). Variable water-saturated areas and streamflow generation in the small Ringelbach catchment (Vosges Mountains, France): the master recession curve as an equilibrium curve for interactions between atmosphere, surface and ground waters. *Hydrological Processes*, 30(20), 3560–3577. <https://doi.org/10.1002/hyp.10947>

Bari, M. A., Smettem, K. R. J., & Sivapalan, M. (2005). Understanding changes in annual runoff following land use changes: A systematic data-based approach. *Hydrological Processes*, 19(13), 2463–2479. <https://doi.org/10.1002/hyp.5679>

Birkel, C., Tetzlaff, D., Dunn, S. M., & Soulsby, C. (2010). Towards a simple dynamic process conceptualization in rainfall-runoff models using multi-criteria calibration and tracers in temperate, upland catchments. *Hydrological Processes*, n/a-n/a. <https://doi.org/10.1002/hyp.7478>

Blazkova, S., Beven, K. J., & Kulasova, A. (2002). On constraining TOPMODEL hydrograph simulations using partial saturated area information. *Hydrological Processes*, 16(2), 441–458. <https://doi.org/10.1002/hyp.331>

Brun, C., Bernard, R., Vidal-Madjar, D., Gascuel-Oudou, C., Merot, P., Duchesne, J., & Nicolas, H. (1990). Mapping Saturated Areas With a Helicopter-Borne C-Band Scatterometer. *Water Resources Research*, 26(5), 945–955. <https://doi.org/10.1029/89wr03627>

Buttle, J. M., & Sami, K. (1992). Testing the groundwater ridging hypothesis of streamflow generation during snowmelt in a forested catchment. *Journal of Hydrology*, 135(1–4), 53–72. [https://doi.org/10.1016/0022-1694\(92\)90080-F](https://doi.org/10.1016/0022-1694(92)90080-F)

Chabot, D., & Bird, D. M. (2014). Small unmanned aircraft: precise and convenient new tools for surveying wetlands. *Journal of Unmanned Vehicle Systems*, 01(01), 15–24. <https://doi.org/10.1139/juvs-2013-0014>

Coles, A. E., & McDonnell, J. J. (2018). Fill and spill drives runoff connectivity over frozen ground. *Journal of Hydrology*, 558, 115–128. <https://doi.org/10.1016/j.jhydrol.2018.01.016>

Creed, I. F., Sanford, S. E., Beall, F. D., Molot, L. A., & Dillon, P. J. (2003). Cryptic wetlands: Integrating hidden wetlands in regression models of the export of dissolved organic carbon from forested landscapes. *Hydrological Processes*, 17(18), 3629–3648. <https://doi.org/10.1002/hyp.1357>

de Alwis, D. a., Easton, Z. M., Dahlke, H. E., Philpot, W. D., & Steenhuis, T. S. (2007). Unsupervised classification of saturated areas using a time series of remotely sensed images. *Hydrology and Earth System Sciences*, 11(5), 1609–1620. <https://doi.org/10.5194/hess-11-1609-2007>

- Devito, K. J., Creed, I. F., & Fraser, C. J. D. (2005). Controls on runoff from a partially harvested aspen-forested headwater catchment, Boreal Plain, Canada. *Hydrological Processes*, 19(1), 3–25. <https://doi.org/10.1002/hyp.5776>
- Dunne, T., Moore, T. R., & Taylor, C. H. (1975). Recognition and prediction of runoff-producing zones in humid regions. *Hydrological Sciences Bulletin*, 20(3), 305–327. [https://doi.org/Cited By \(since 1996\) 102rExport Date 4 April 2012](https://doi.org/Cited%20By%20(since%201996)%20102rExport%20Date%204%20April%202012)
- Franks, S. W., Gineste, P., Beven, K. J., & Merot, P. (1998). On constraining the predictions of a distributed model: The incorporation of fuzzy estimates of saturated areas into the calibration process. *Water Resources Research*, 34(4), 787–797. <https://doi.org/10.1029/97WR03041>
- Gineste, P., Puech, C., & Mérot, P. (1998). Radar remote sensing of the source areas from the Coët-Dan catchment. *Hydrological Processes*, 12(2), 267–284. [https://doi.org/10.1002/\(SICI\)1099-1085\(199802\)12:2<267::AID-HYP576>3.0.CO;2-G](https://doi.org/10.1002/(SICI)1099-1085(199802)12:2<267::AID-HYP576>3.0.CO;2-G)
- Glaser, B., Klaus, J., Frei, S., Frentress, J., Pfister, L., & Hopp, L. (2016). On the value of surface saturated area dynamics mapped with thermal infrared imagery for modeling the hillslope-riparian-stream continuum. *Water Resources Research*, 52(10), 8317–8342. <https://doi.org/10.1002/2015WR018414>
- Grabs, T., Seibert, J., Bishop, K., & Laudon, H. (2009). Modeling spatial patterns of saturated areas: A comparison of the topographic wetness index and a dynamic distributed model. *Journal of Hydrology*, 373(1–2), 15–23. <https://doi.org/10.1016/j.jhydrol.2009.03.031>
- Güntner, A., Uhlenbrook, S., Seibert, J., & Leibundgut, C. (1999). Multi-criterial validation of TOPMODEL in a mountainous catchment. *Hydrological Processes*, 13(11), 1603–1620. [https://doi.org/10.1002/\(SICI\)1099-1085\(19990815\)13:11<1603::AID-HYP830>3.0.CO;2-K](https://doi.org/10.1002/(SICI)1099-1085(19990815)13:11<1603::AID-HYP830>3.0.CO;2-K)
- Güntner, Andreas, Seibert, J., & Uhlenbrook, S. (2004). Modeling spatial patterns of saturated areas: An evaluation of different terrain indices. *Water Resources Research*, 40(5), 1–19. <https://doi.org/10.1029/2003WR002864>
- Inamdar, S. P., & Mitchell, M. J. (2007). Contributions of riparian and hillslope waters to storm runoff across multiple catchments and storm events in a glaciated forested watershed. *Journal of Hydrology*, 341(1–2), 116–130. <https://doi.org/10.1016/j.jhydrol.2007.05.007>
- Kulasova, A., Beven, K. J., Blazkova, S. D., Rezacova, D., & Cajthaml, J. (2014). Comparison of saturated areas mapping methods in the Jizera Mountains, Czech Republic. *Journal of Hydrology & Hydromechanics*, 62(2), 160–168. <https://doi.org/10.2478/johh-2014-0002>
- Latron, J., & Gallart, F. (2007). Seasonal dynamics of runoff-contributing areas in a small mediterranean research catchment (Vallcebre, Eastern Pyrenees). *Journal of Hydrology*, 335(1–2), 194–206. <https://doi.org/10.1016/j.jhydrol.2006.11.012>
- McDonnell, J. J., & Taylor, C. H. (1987). Surface and subsurface water contributions during snowmelt in a small precambrian shield Watershed, Muskoka, Ontario. *Atmosphere - Ocean*, 25(3), 251–266. <https://doi.org/10.1080/07055900.1987.9649274>
- Mengistu, S. G., & Spence, C. (2016). Testing the ability of a semidistributed hydrological model to simulate contributing area. *Water Resources Research*, 52(6), 4399–4415. <https://doi.org/10.1002/2016WR018760>
- Pfister, L., McDonnell, J. J., Hissler, C., & Hoffmann, L. (2010). Ground-based thermal imagery as a simple, practical tool for mapping saturated area connectivity and dynamics. *Hydrological Processes*, 24(May), 3123–3132. <https://doi.org/10.1002/hyp.7840>

Phillips, R. W., Spence, C., & Pomeroy, J. W. (2011). Connectivity and runoff dynamics in heterogeneous basins. *Hydrological Processes*, 25(19), 3061–3075. <https://doi.org/10.1002/hyp.8123>

Rinderer, M., Kollegger, A., Fischer, B. M. C., Stähli, M., & Seibert, J. (2012). Sensing with boots and trousers - qualitative field observations of shallow soil moisture patterns. *Hydrological Processes*, 26(26), 4112–4120. <https://doi.org/10.1002/hyp.9531>

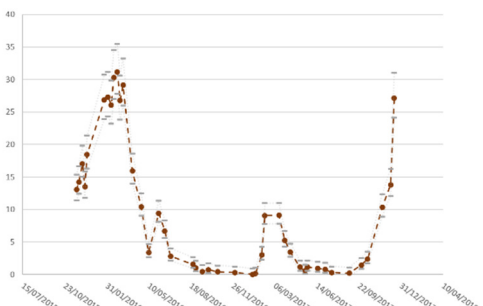
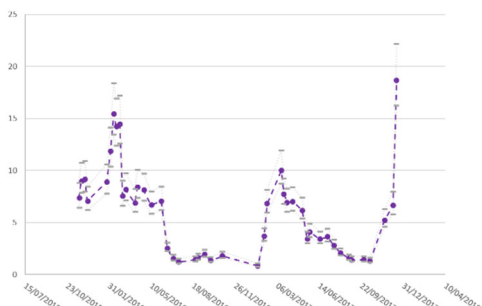
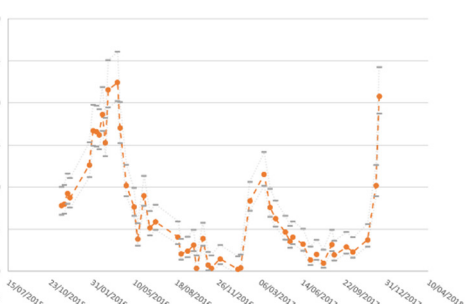
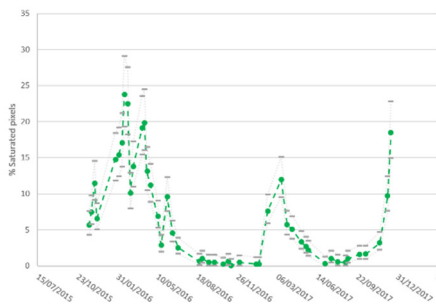
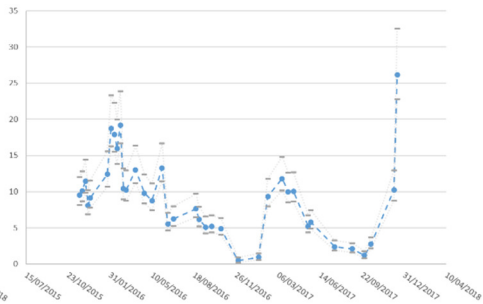
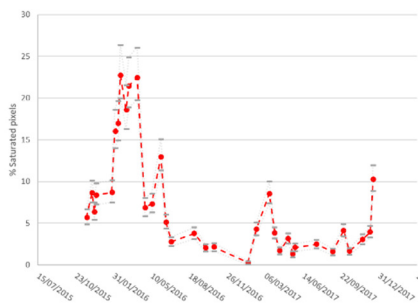
Roulet, N. T. (1990). Hydrology of a headwater basin wetland. *Hydrological Processes*, 4(April), 387–40

Silasari, R., Parajka, J., Ressler, C., Strauss, P., & Blöschl, G. (2017). Potential of time-lapse photography for identifying saturation area dynamics on agricultural hillslopes. *Hydrological Processes*, 31(21), 3610–3627. <https://doi.org/10.1002/hyp.11272>

Tanaka, T., Yasuhara, M., Sakai, H., & Marui, A. (1988). The Hachioji Experimental Basin Study - Storm runoff processes and the mechanism of its generation. *Journal of Hydrology*, 102(1–4), 139–164. [https://doi.org/10.1016/0022-1694\(88\)90095-9](https://doi.org/10.1016/0022-1694(88)90095-9)

Figure A5.1 (next page):

Range of possible outcomes for the estimation of the percentage of saturated pixels for areas L1 (red), M1 (blue), M2 (yellow), M3 (green), R2 (purple) and R3 (brown). Coloured points and dashed lines refer to the optimal estimated saturation (cf. manuscript Figure 7 and optimal solution definition in section 3.2). Grey dashes and dotted lines refer to the maximum and minimum estimated saturation (cf. manuscript Figure 7 and maximum and minimum estimated saturation definition in section 3.2). Linear interpolations between the different observation dates are displayed as dashed and dotted lines and are meant to show the overall time series trend and might not reflect the actual saturation.



Bibliography

- Abbott, B.W., Baranov, V., Mendoza-Lera, C., Nikolakopoulou, M., Harjung, A., Kolbe, T., Balasubramanian, M.N., Vaessen, T.N., Ciocca, F., Campeau, A., Wallin, M.B., Romeijn, P., Antonelli, M., Gonçalves, J., Datry, T., Laverman, A.M., de Dreuzy, J.R., Hannah, D.M., Krause, S., Oldham, C., Pinay, G., 2016. Using multi-tracer inference to move beyond single-catchment ecohydrology. *Earth-Science Rev.* 160, 19–42. <https://doi.org/10.1016/j.earscirev.2016.06.014>
- Ala-aho, P., Rossi, P.M., Isokangas, E., Kløve, B., 2015. Fully integrated surface–subsurface flow modelling of groundwater–lake interaction in an esker aquifer: Model verification with stable isotopes and airborne thermal imaging. *J. Hydrol.* 522, 391–406. <https://doi.org/10.1016/j.jhydrol.2014.12.054>
- Ali, G. a., Roy, A.G., 2009. Revisiting hydrologic sampling strategies for an accurate assessment of hydrologic connectivity in humid temperate systems. *Geogr. Compass* 3, 350–374. <https://doi.org/10.1111/j.1749-8198.2008.00180.x>
- Ali, G., Birkel, C., Tetzlaff, D., Soulsby, C., McDonnell, J.J., Tarolli, P., 2013a. A comparison of wetness indices for the prediction of observed connected saturated areas under contrasting conditions. *Earth Surf. Process. Landforms* 39, 399–413. <https://doi.org/10.1002/esp.3506>
- Ali, G., Birkel, C., Tetzlaff, D., Soulsby, C., McDonnell, J.J., Tarolli, P., 2013b. A comparison of wetness indices for the prediction of observed connected saturated areas under contrasting conditions. *Earth Surf. Process. Landforms* 39, 399–413. <https://doi.org/10.1002/esp.3506>
- Allen, R.G., Pereira, L.S., Raes, D., Smith, M., Ab, W., 1998. Crop evapotranspiration - Guidelines for computing crop water requirements. *Irrig. Drain. Pap. No. 56*, FAO 300. <https://doi.org/10.1016/j.eja.2010.12.001>
- Ambroise, B., 2016. Variable water-saturated areas and streamflow generation in the small Ringelbach catchment (Vosges Mountains, France): the master recession curve as an equilibrium curve for interactions between atmosphere, surface and ground waters. *Hydrol. Process.* 30, 3560–3577. <https://doi.org/10.1002/hyp.10947>
- Ambroise, B., 2004. Variable 'active' versus 'contributing' areas or periods: a necessary distinction. *Hydrol. Process.* 18, 1149–1155. <https://doi.org/10.1002/hyp.5536>
- Anderson, M.G., Burt, T.P., 1978. The role of topography in controlling. *Earth Surf. Process.* 3, 331–344.
- Antonelli, M., Glaser, B., Teuling, A.J., Klaus, J., Pfister, L., 2019. Saturated areas through the lens: 1. Spatio-temporal variability of surface saturation documented through Thermal Infrared imagery. Submitted.
- Antonelli, M., Klaus, J., Smettem, K., Teuling, A.J., Pfister, L., 2017. Exploring streamwater mixing dynamics via handheld thermal infrared imagery. *Water (Switzerland)* 9. <https://doi.org/10.3390/w9050358>

Bibliography

- Appels, W.M., Bogaart, P.W., van der Zee, S.E.A.T.M., 2016. Surface runoff in flat terrain: How field topography and runoff generating processes control hydrological connectivity. *J. Hydrol.* 534, 493–504. <https://doi.org/10.1016/j.jhydrol.2016.01.021>
- Aubry-Wake, C., Baraer, M., McKenzie, J.M., Mark, B.G., Wigmore, O., Hellström, R.Å., Lutz, L., Somers, L., 2015. Measuring glacier surface temperatures with ground-based thermal infrared imaging. *Geophys. Res. Lett.* 42, 8489–8497. <https://doi.org/10.1002/2015GL065321>
- Baker, M.E., Wiley, M.J., Seelbach, P.W., 2001. GIS-BASED HYDROLOGIC MODELING OF RIPARIAN AREAS: IMPLICATIONS FOR STREAM WATER QUALITY. *J. Am. Water Resour. Assoc.* 37.
- Banks, W.S.L., Paylor, R.L., Hughes, W.B., 1996. Using Thermal-Infrared Imagery to Delineate Ground-Water Discharge. *Ground Water* 34, 434–443.
- Barragán, C., Wetzel, C.E., Ector, L., 2018. A standard method for the routine sampling of terrestrial diatom communities for soil quality assessment. *J. Appl. Phycol.* 30, 1095–1113. <https://doi.org/10.1007/s10811-017-1336-7>
- Bastida, F., Zsolnay, a., Hernández, T., García, C., 2008. Past, present and future of soil quality indices: A biological perspective. *Geoderma* 147, 159–171. <https://doi.org/10.1016/j.geoderma.2008.08.007>
- Bate, N., Newall, P., 2002. Techniques for the use of diatoms in water quality assessment: how many valves?, in: John, J. (Ed.), *Proceedings of the 15th International Diatom Symposium*. A.R.G. Gantner Verlag K.G. Ruggell/Liechtenstein, Perth, Australia, pp. 153–160.
- Bérard, a., Rimet, F., Capowicz, Y., Leboulanger, C., 2004. Procedures for Determining the Pesticide Sensitivity of Indigenous Soil Algae: A Possible Bioindicator of Soil Contamination? *Arch. Environ. Contam. Toxicol.* 46, 24–31. <https://doi.org/10.1007/s00244-003-2147-1>
- Bergstrom, A., Jencso, K., McGlynn, B., 2016a. Spatiotemporal processes that contribute to hydrologic exchange between hillslopes, valley bottoms, and streams. *Water Resour. Res.* 52, 4628–4645. <https://doi.org/10.1002/2015WR017972>
- Bergstrom, A., McGlynn, B., Mallard, J., Covino, T., 2016b. Watershed structural influences on the distributions of stream network water and solute travel times under baseflow conditions. *Hydrol. Process.* 30, 2671–2685. <https://doi.org/10.1002/hyp.10792>
- Best, J.L., 1987. Flow dynamics at river channel confluences: Implications for sediment transport and bed morphology, in: Ethridge, F.G., Flores, R.M., Harvey, M.D. (Eds.), *Recent Developments in Fluvial Sedimentology*. Sepm Society for Sedimentary, Tulsa, OK, USA, pp. 27–35.
- Beven, K.J., Kirkby, M.J., 1979. A physically based, variable contributing area model of basin hydrology. *Hydrol. Sci. Bull.* 24, 43–69. <https://doi.org/10.1080/02626667909491834>
- Birkel, C., Tetzlaff, D., Dunn, S.M., Soulsby, C., 2010. Towards a simple dynamic process conceptualization in rainfall-runoff models using multi-criteria calibration and tracers in temperate, upland catchments. *Hydrol. Process.* n/a-n/a. <https://doi.org/10.1002/hyp.7478>
- Birkinshaw, S.J., Webb, B., 2010. Flow pathways in the Slapton Wood catchment using temperature as a tracer. *J. Hydrol.* 383, 269–279.

- <https://doi.org/10.1016/j.jhydrol.2009.12.042>
- Black, P.E., 1997. Watershed functions. *J. Am. Water Resour. Assoc.* 33.
- Blanco, S., 2014. Environmental factors controlling lake diatom communities: a meta-analysis of published data. *Biogeosciences Discuss.* 11, 15889–15909. <https://doi.org/10.5194/bgd-11-15889-2014>
- Blazkova, S., Beven, K.J., Kulasova, A., 2002. On constraining TOPMODEL hydrograph simulations using partial saturated area information. *Hydrol. Process.* 16, 441–458. <https://doi.org/10.1002/hyp.331>
- Blöschl, G., Bierkens, M.F.P., Chambel, A., Cudennec, C., Destouni, G., Fiori, A., Kirchner, J.W., McDonnell, J.J., Savenije, H.H.G., Sivapalan, M., Stumpp, C., Toth, E., Volpi, E., Carr, G., Lupton, C., Salinas, J., Széles, B., Viglione, A., Aksoy, H., Allen, S.T., Amin, A., Andréassian, V., Arheimer, B., Aryal, S.K., Baker, V., Bardsley, E., Barendrecht, M.H., Bartosova, A., Batelaan, O., Berghuijs, W.R., Beven, K., Blume, T., Bogaard, T., Borges de Amorim, P., Böttcher, M.E., Boulet, G., Breinl, K., Brilly, M., Brocca, L., Buytaert, W., Castellarin, A., Castelletti, A., Chen, X., Chen, Yangbo, Chen, Yuanfang, Chiffard, P., Claps, P., Clark, M.P., Collins, A.L., Croke, B., Dathe, A., David, P.C., de Barros, F.P.J., de Rooij, G., Di Baldassarre, G., Driscoll, J.M., Duethmann, D., Dwivedi, R., Eris, E., Farmer, W.H., Feiccabrino, J., Ferguson, G., Ferrari, E., Ferraris, S., Fersch, B., Finger, D., Foglia, L., Fowler, K., Gartsman, B., Gascoin, S., Gaume, E., Gelfan, A., Geris, J., Gharari, S., Gleeson, T., Glendell, M., Gonzalez Bevacqua, A., González-Dugo, M.P., Grimaldi, S., Gupta, A.B., Guse, B., Han, D., Hannah, D., Harpold, A., Haun, S., Heal, K., Helfricht, K., Herrnegger, M., Hipsey, M., Hlaváčiková, H., Hohmann, C., Holko, L., Hopkinson, C., Hrachowitz, M., Illangasekare, T.H., Inam, A., Innocente, C., Istanbuluoglu, E., Jarihani, B., Kalantari, Z., Kalvans, A., Khanal, S., Khatami, S., Kiesel, J., Kirkby, M., Knoben, W., Kochanek, K., Kohnová, S., Kolechkina, A., Krause, S., Kremer, D., Kreibich, H., Kunstmann, H., Lange, H., Liberato, M.L.R., Lindquist, E., Link, T., Liu, J., Loucks, D.P., Luce, C., Mahé, G., Makarieva, O., Malard, J., Mashtayeva, S., Maskey, S., Mas-Pla, J., Mavrova-Guirguinova, M., Mazzoleni, M., Mernild, S., Misstear, B.D., Montanari, A., Müller-Thomy, H., Nabizadeh, A., Nardi, F., Neale, C., Nesterova, N., Nurtaev, B., Odongo, V.O., Panda, S., Pande, S., Pang, Z., Papacharalampous, G., Perrin, C., Pfister, L., Pimentel, R., Polo, M.J., Post, D., Prieto Sierra, C., Ramos, M.H., Renner, M., Reynolds, J.E., Ridolfi, E., Rigon, R., Riva, M., Robertson, D.E., Rosso, R., Roy, T., Sá, J.H.M., Salvadori, G., Sandells, M., Schaeffli, B., Schumann, A., Scolobig, A., Seibert, J., Servat, E., Shafiei, M., Sharma, A., Sidibe, M., Sidle, R.C., Skaugen, T., Smith, H., Spiessl, S.M., Stein, L., Steinsland, I., Strasser, U., Su, B., Szolgay, J., Tarboton, D., Tauro, F., Thirel, G., Tian, F., Tong, R., Tussupova, K., Tyralis, H., Uijlenhoet, R., van Beek, R., van der Ent, R.J., van der Ploeg, M., Van Loon, A.F., van Meerveld, I., van Nooijen, R., van Oel, P.R., Vidal, J.P., von Freyberg, J., Vorogushyn, S., Wachniew, P., Wade, A.J., Ward, P., Westerberg, I.K., White, C., Wood, E.F., Woods, R., Xu, Z., Yilmaz, K.K., Zhang, Y., 2019. Twenty-three unsolved problems in hydrology (UPH)—a community perspective. *Hydrol. Sci. J.* 64, 1141–1158. <https://doi.org/10.1080/02626667.2019.1620507>
- Blume, T., van Meerveld, H.J.I., 2015. From hillslope to stream: methods to investigate subsurface connectivity. *Wiley Interdiscip. Rev. Water* 2, 177–198. <https://doi.org/10.1002/wat2.1071>
- Blumstock, M., Tetzlaff, D., Dick, J.J., Nuetzmann, G., Soulsby, C., 2016. Spatial organization of groundwater dynamics and streamflow response from different hydrogeological units in a montane catchment. *Hydrol. Process.* 30, 3735–3753. <https://doi.org/10.1002/hyp.10848>

Bibliography

- Bottin, M., Giraudel, J.-L., Lek, S., Tison-Rosebery, J., 2014. diatSOM : a R-package for diatom biotypology using self-organizing maps. *Diatom Res.* 29, 5–9. <https://doi.org/10.1080/0269249X.2013.804447>
- Boyer, C., Roy, A.G., Best, J.L., 2006. Dynamics of a river channel confluence with discordant beds: Flow turbulence, bed load sediment transport, and bed morphology. *J. Geophys. Res.* 111, F04007. <https://doi.org/10.1029/2005JF000458>
- Bracken, L.J., Croke, J., 2007. The concept of hydrological connectivity and its contribution to understanding runoff-dominated geomorphic systems. *Hydrol. Process.* 21, 1749–1763. <https://doi.org/10.1002/hyp.6313>
- Breiman, L., 2001. Random forests. *Mach. Learn.* 45, 5–32.
- Breiman, L., Friedman, J.H., Olshen, R.A., Stone, C.I., 1984. *Classification and Regression Trees*. Wadsworth Belmont, California.
- Briggs, M.A., Dawson, C.B., Holmquist-Johnson, C.L., Williams, K.H., Lane, J.W., 2019. Efficient hydrogeological characterization of remote stream corridors using drones. *Hydrol. Process.* 33, 316–319. <https://doi.org/10.1002/hyp.13332>
- Briggs, M.A., Hare, D.K., 2018. Explicit consideration of preferential groundwater discharges as surface water ecosystem control points. *Hydrol. Process.* 32, 2435–2440. <https://doi.org/10.1002/hyp.13178>
- Briggs, M.A., Hare, D.K., Boutt, D.F., Davenport, G., Lane, J.W., 2016. Thermal infrared video details multiscale groundwater discharge to surface water through macropores and peat pipes. *Hydrol. Process.* 30, 2510–2511. <https://doi.org/10.1002/hyp.10722>
- Burt, T.P., Gardiner, T., 1982. The permanence of stream networks in Britain: some further comments. *Earth Surf. Process. Landforms* 7, 327–332.
- Cammeraat, L.H., 2002. A review of two strongly contrasting geomorphological systems within the context of scale. *Earth Surf. Process. Landforms* 27, 1201–1222. <https://doi.org/10.1002/esp.421>
- Cardenas, M.B., Doering, M., Rivas, D.S., Galdeano, C., Neilson, B.T., Robinson, C.T., 2014. Analysis of the temperature dynamics of a proglacial river using time-lapse thermal imaging and energy balance modeling. *J. Hydrol.* 519, 1963–1973. <https://doi.org/10.1016/j.jhydrol.2014.09.079>
- Cardenas, M.B., Harvey, J.W., Packman, A.I., Scott, D.T., 2008. Ground-based thermography of fluvial systems at low and high discharge reveals potential complex thermal heterogeneity driven by flow variation and bioroughness. *Hydrol. Process.* 22, 980–986. <https://doi.org/10.1002/hyp.6932>
- Cardenas, M.B., Neale, C.M.U., Jaworowski, C., Heasler, H., 2011. High-resolution mapping of river-hydrothermal water mixing: Yellowstone National Park. *Int. J. Remote Sens.* 32, 2765–2777. <https://doi.org/10.1080/01431161003743215>
- Cemagref, 1982. *Etude des méthodes biologiques d'appréciation quantitative de la qualité des eaux*. Lyon.
- Chabot, D., Bird, D.M., 2014. Small unmanned aircraft: precise and convenient new tools for surveying wetlands. *J. Unmanned Veh. Syst.* 01, 15–24. <https://doi.org/10.1139/juvs-2013-0014>
- Cherkauer, K. a., Burges, S.J., Handcock, R.N., Kay, J.E., Kampf, S.K., Gillespie, a. R., 2005.

- Assessing Satellite-Based and Aircraft-Based Thermal Infrared Remote Sensing for Monitoring Pacific Northwest River Temperature. *J. Am. Water Resour. Assoc.* 41, 1149–1159. <https://doi.org/10.1111/j.1752-1688.2005.tb03790.x>
- Chini, M., Chiancone, A., Stramondo, S., 2014. Scale Object Selection (SOS) through a hierarchical segmentation by a multi-spectral per-pixel classification. *Pattern Recognit. Lett.* 49, 214–223. <https://doi.org/10.1016/j.patrec.2014.07.012>
- Chini, M., Hostache, R., Giustarini, L., Matgen, P., 2017. A hierarchical split-based approach for parametric thresholding of SAR images: Flood inundation as a test case. *IEEE Trans. Geosci. Remote Sens.* 55, 6975–6988. <https://doi.org/10.1109/TGRS.2017.2737664>
- Chini, M., Pacifici, F., Emery, W.J., Pierdicca, N., Del Frate, F., 2008. Comparing Statistical and Neural Network Methods Applied to Very High Resolution Satellite Images Showing Changes in Man-Made Structures at Rocky Flats. *IEEE Trans. Geosci. Remote Sens.* 46, 1812–1821. <https://doi.org/10.1109/TGRS.2008.916223>
- Chini, M., Pierdicca, N., Emery, W.J., 2009. Exploiting SAR and VHR Optical Images to Quantify Damage Caused by the 2003 Bam Earthquake. *IEEE Trans. Geosci. Remote Sens.* 47, 145–152. <https://doi.org/10.1109/TGRS.2008.2002695>
- Chow, V.T., 1959. *Open-Channel Hydraulics*. McGraw-Hill, New York, NY, USA.
- Coles, A.E., McDonnell, J.J., 2018. Fill and spill drives runoff connectivity over frozen ground. *J. Hydrol.* 558, 115–128. <https://doi.org/10.1016/j.jhydrol.2018.01.016>
- Coles, A.E., Wetzel, C.E., Martínez-Carreras, N., Ector, L., McDonnell, J.J., Frentress, J., Klaus, J., Hoffmann, L., Pfister, L., 2016. Diatoms as a tracer of hydrological connectivity: are they supply limited? *Ecohydrology* 9, 631–645. <https://doi.org/10.1002/eco.1662>
- Compton, J.E., Boone, R.D., 2000. Long-term impacts of agriculture on soil carbon and nitrogen in carbon and nitrogen in New England forests. *Ecology* 81, 2314–2330.
- Cooper, M., 2010. *Advanced Bash-Scripting Guide An in-depth exploration of the art of shell scripting Table of Contents*. Okt 2005 Abrufbar über <http://www.tldp.org/LDP/absabsguide.pdf> Zugriff 1112 2005 2274, 2267–2274. <https://doi.org/10.1002/hyp>
- Corripio, J.G., 2004. Snow surface albedo estimation using terrestrial photography. *Int. J. Remote Sens.* 25, 5705–5729. <https://doi.org/10.1080/01431160410001709002>
- Creed, I.F., Sanford, S.E., Beall, F.D., Molot, L.A., Dillon, P.J., 2003. Cryptic wetlands: Integrating hidden wetlands in regression models of the export of dissolved organic carbon from forested landscapes. *Hydrol. Process.* 17, 3629–3648. <https://doi.org/10.1002/hyp.1357>
- Cristea, N.C., Burges, S.J., 2009. Use of Thermal Infrared Imagery to Complement Monitoring and Modeling of Spatial Stream Temperatures. *J. Hydrol. Eng.* 14, 1080–1090. [https://doi.org/10.1061/\(ASCE\)HE.1943-5584.0000072](https://doi.org/10.1061/(ASCE)HE.1943-5584.0000072)
- Davidson, E.A., Ackerman, I.L., 1993. Changes in soil carbon inventories following cultivation of previously untilled soils. *Biogeochemistry* 20, 161–193. <https://doi.org/10.1007/BF00000786>
- Day, T.J., 1977. Observed mixing lengths in mountain streams. *J. Hydrol.* 35, 125–136. [https://doi.org/10.1016/0022-1694\(77\)90081-6](https://doi.org/10.1016/0022-1694(77)90081-6)
- Day, T.J., 1976. On the precision of salt dilution gauging. *J. Hydrol.* 31, 293–306.

- [https://doi.org/10.1016/0022-1694\(76\)90130-X](https://doi.org/10.1016/0022-1694(76)90130-X)
- De Alwis, D.A., Easton, Z.M., Dahlke, H.E., Philpot, W.D., Steenhuis, T.S., 2007. Unsupervised classification of saturated areas using a time series of remotely sensed images. *Hydrol. Earth Syst. Sci.* 11, 1609–1620. <https://doi.org/10.5194/hess-11-1609-2007>
- Deitchman, R.S., Loheide, S.P., 2009. Ground-based thermal imaging of groundwater flow processes at the seepage face. *Geophys. Res. Lett.* 36, 1–6. <https://doi.org/10.1029/2009GL038103>
- Devito, K.J., Creed, I.F., Fraser, C.J.D., 2005. Controls on runoff from a partially harvested aspen-forested headwater catchment, Boreal Plain, Canada. *Hydrol. Process.* 19, 3–25. <https://doi.org/10.1002/hyp.5776>
- Dick, J.J., Tetzlaff, D., Birkel, C., Soulsby, C., 2015. Modelling landscape controls on dissolved organic carbon sources and fluxes to streams. *Biogeochemistry* 122, 361–374. <https://doi.org/10.1007/s10533-014-0046-3>
- Do, H.T., Lo, S.-L., Chiueh, P.-T., Phan Thi, L.A., 2012. Design of sampling locations for mountainous river monitoring. *Environ. Model. Softw.* 27–28, 62–70. <https://doi.org/10.1016/j.envsoft.2011.09.007>
- Doppler, T., Honti, M., Zihlmann, U., Weisskopf, P., Stamm, C., 2014. Validating a spatially distributed hydrological model with soil morphology data. *Hydrol. Earth Syst. Sci.* 18, 3481–3498. <https://doi.org/10.5194/hess-18-3481-2014>
- Dreßler, M., Verweij, G., Kistenich, S., Kahler, M., Werner, P., 2015. Applied use of taxonomy: lessons learned from the first German intercalibration exercise for benthic diatoms. *Acta Bot. Croat.* 74, 211–232. <https://doi.org/10.1515/botcro-2015-0017>
- Dugdale, S.J., 2016. A practitioner's guide to thermal infrared remote sensing of rivers and streams: recent advances, precautions and considerations. *Wiley Interdiscip. Rev. Water* 3, 251–268. <https://doi.org/10.1002/wat2.1135>
- Dugdale, S.J., Bergeron, N.E., St-Hilaire, A., 2015. Spatial distribution of thermal refuges analysed in relation to riverscape hydromorphology using airborne thermal infrared imagery. *Remote Sens. Environ.* <https://doi.org/10.1016/j.rse.2014.12.021>
- Dugdale, S.J., Bergeron, N.E., St-Hilaire, A., 2013. Temporal variability of thermal refuges and water temperature patterns in an Atlantic salmon river. *Remote Sens. Environ.* 136, 358–373. <https://doi.org/10.1016/j.rse.2013.05.018>
- Dunne, T., Black, R.D., 1970a. An Experimental Investigation of Runoff Production in Permeable Soils. *Water Resour. Res.* 6, 478–490. <https://doi.org/10.1029/WR006i002p00478>
- Dunne, T., Black, R.D., 1970b. Partial Area Contributions to Storm Runoff in a Small New England Watershed. *Water Resour. Res.* 6, 1296–1311.
- Dunne, T., Moore, T.R., Taylor, C.H., 1975. Recognition and prediction of runoff-producing zones in humid regions. *Hydrol. Sci. Bull.* 20, 305–327. [https://doi.org/Cited By \(since 1996\) 102\Export Date 4 April 2012](https://doi.org/Cited%20By%20(since%201996)%20102%20Export%20Date%204%20April%202012)
- Ecology, S., Jun, N., 2016. Partialling out the Spatial Component of Ecological Variation Author (s): Daniel Borcard , Pierre Legendre and Pierre Drapeau Stable URL : <http://www.jstor.org/stable/1940179> REFERENCES Linked references are available on

JSTOR for this article : You may 73, 1045–1055.

- Eschbach, D., Piasny, G., Schmitt, L., Pfister, L., Grussenmeyer, P., Koehl, M., Skupinski, G., Serradj, A., 2017. Thermal-infrared remote sensing of surface water-groundwater exchanges in a restored anastomosing channel (Upper Rhine River, France). *Hydrol. Process.* 31, 1113–1124. <https://doi.org/10.1002/hyp.11100>
- Estes, J.E., 1966. Some Applications of Aerial Infrared Imagery. *Ann. Assoc. Am. Geogr.* 56, 673–682.
- European Committee for Standardization, 2003. Water Quality – Guidance Standard for the Routine Sampling and Pretreatment of Benthic Diatoms from Rivers. EN 13946:2003. Brussels.
- Fang, T., Liao, S., Chen, X., Zhao, Y., Zhu, Q., Cao, Y., Wang, Q., Zhang, S., Gao, Z., Yang, Y., Wang, Y., Zhang, J., 2019. Forensic drowning site inference employing mixed pyrosequencing profile of DNA barcode gene (rbcl). *Int. J. Legal Med.* 133, 1351–1360. <https://doi.org/10.1007/s00414-019-02075-4>
- Fenicia, F., Kavetski, D., Savenije, H.H.G., Clark, M.P., Schoups, G., Pfister, L., Freer, J., 2014. Catchment properties, function, and conceptual model representation: is there a correspondence? *Hydrol. Process.* 28, 2451–2467. <https://doi.org/10.1002/hyp.9726>
- FLIR Systems, 2010. *ThermaCAM Researcher User's Manual*. Billerica, MA, USA,.
- Floriantic, M.G., van Meerveld, I., Smoorenburg, M., Margreth, M., Naef, F., Kirchner, J.W., Molnar, P., 2018. Spatio-temporal variability in contributions to low flows in the high Alpine Poschiavino catchment. *Hydrol. Process.* 32, 3938–3953. <https://doi.org/10.1002/hyp.13302>
- Flower, R.J., 2005. A TAXONOMIC AND ECOLOGICAL STUDY OF DIATOMS FROM FRESHWATER HABITATS IN THE FALKLAND ISLANDS, SOUTH ATLANTIC. *Diatom Res.* 20, 23–96. <https://doi.org/10.1080/0269249X.2005.9705620>
- Foets, J., Wetzel, C.E., Teuling, A.J., Pfister, L., 2020. Temporal and spatial variability of terrestrial diatoms at the catchment scale: controls on communities. *PeerJ.* <https://doi.org/10.7717/peerj.8296>
- Frei, S., Lischeid, G., Fleckenstein, J.H., 2010. Effects of micro-topography on surface-subsurface exchange and runoff generation in a virtual riparian wetland - A modeling study. *Adv. Water Resour.* 33, 1388–1401. <https://doi.org/10.1016/j.advwatres.2010.07.006>
- Frey, M.P., Schneider, M.K., Dietzel, A., Reichert, P., Stamm, C., 2009. Predicting critical source areas for diffuse herbicide losses to surface waters: Role of connectivity and boundary conditions. *J. Hydrol.* 365, 23–36. <https://doi.org/10.1016/j.jhydrol.2008.11.015>
- Fullerton, A.H., Torgersen, C.E., Lawler, J.J., Faux, R.N., Steel, E.A., Beechie, T.J., Ebersole, J.L., Leibowitz, S.G., 2015. Rethinking the longitudinal stream temperature paradigm: region-wide comparison of thermal infrared imagery reveals unexpected complexity of river temperatures. *Hydrol. Process.* n/a-n/a. <https://doi.org/10.1002/hyp.10506>
- Gaudet, J.M., Roy, A.G., 1995. Effect of bed morphology on flow mixing length at river confluences. *Nature.* <https://doi.org/10.1038/373138a0>
- Gburek, W.J., Sharpley, A.N., 1998. Hydrologic Controls on Phosphorus Loss from Upland

Bibliography

- Agricultural Watersheds. *J. Environ. Qual.* 27, 267.
<https://doi.org/10.2134/jeq1998.00472425002700020005x>
- Genereux, D.P., Hemond, H.F., Mulholland, P.J., 1993. Spatial and temporal variability in streamflow generation on the West Fork of Walker Branch Watershed. *J. Hydrol.* 142, 137–166. [https://doi.org/10.1016/0022-1694\(93\)90009-X](https://doi.org/10.1016/0022-1694(93)90009-X)
- Gibson, J.A.E., Roberts, D., Van De Vijver, B., 2006. Salinity control of the distribution of diatoms in lakes of the Bunge Hills, East Antarctica. *Polar Biol.* 29, 694–704. <https://doi.org/10.1007/s00300-006-0107-8>
- Glaser, B., Antonelli, M., Chini, M., Pfister, L., Klaus, J., 2018. Technical note: Mapping surface-saturation dynamics with thermal infrared imagery. *Hydrol. Earth Syst. Sci.* 22, 5987–6003. <https://doi.org/10.5194/hess-22-5987-2018>
- Glaser, B., Antonelli, M., Hopp, L., Klaus, J., 2019. Intra-catchment variability of surface saturation – insights from long-term observations and simulations. *Hydrol. Earth Syst. Sci. Discuss.* 1–22. <https://doi.org/10.5194/hess-2019-203>
- Glaser, B., Klaus, J., Frei, S., Frentress, J., Pfister, L., Hopp, L., 2016. On the value of surface saturated area dynamics mapped with thermal infrared imagery for modeling the hillslope-riparian-stream continuum. *Water Resour. Res.* 52, 8317–8342. <https://doi.org/10.1002/2015WR018414>
- Glaser, B., Partington, D., Hopp, L., Brunner, P., Therrien, R., Klaus, J., n.d. Sources of surface water in space and time.
- Godsey, S.E., Kirchner, J.W., 2014. Dynamic, discontinuous stream networks: Hydrologically driven variations in active drainage density, flowing channels and stream order. *Hydrol. Process.* 28, 5791–5803. <https://doi.org/10.1002/hyp.10310>
- Gourdol, L., Clément, R., Juilleret, J., Pfister, L., Hissler, C., 2018. Large-scale ERT surveys for investigating shallow regolith properties and architecture. *Hydrol. Earth Syst. Sci. Discuss.* 1–39. <https://doi.org/10.5194/hess-2018-519>
- Grabs, T., Bishop, K., Laudon, H., Lyon, S.W., Seibert, J., 2012. Riparian zone hydrology and soil water total organic carbon (TOC): Implications for spatial variability and upscaling of lateral riparian TOC exports. *Biogeosciences* 9, 3901–3916. <https://doi.org/10.5194/bg-9-3901-2012>
- Grabs, T., Seibert, J., Bishop, K., Laudon, H., 2009. Modeling spatial patterns of saturated areas: A comparison of the topographic wetness index and a dynamic distributed model. *J. Hydrol.* 373, 15–23. <https://doi.org/10.1016/j.jhydrol.2009.03.031>
- Green, P.J., Silverman, B.W., 1994. *Nonparametric Regression and Generalized Linear Models: A Roughness Penalty Approach*, 1st editio. ed. Chapman and Hall, London, UK.
- Guiry, M.D., 2012. HOW MANY SPECIES OF ALGAE ARE THERE? *J. Phycol.* 48, 1057–1063. <https://doi.org/10.1111/j.1529-8817.2012.01222.x>
- Güntner, A., Seibert, J., Uhlenbrook, S., 2004. Modeling spatial patterns of saturated areas: An evaluation of different terrain indices. *Water Resour. Res.* 40, 1–19. <https://doi.org/10.1029/2003WR002864>
- Hahn, A., Neuhaus, W., 1997. Boden-diatomeen einer landwirtschaftlichennutzfläche bei potsdam, deutschland. *Nov. Hedwigia* 65, 285–298.

- Handcock, R.N., Gillespie, a. R., Cherkauer, K. a., Kay, J.E., Burges, S.J., Kampf, S.K., 2006. Accuracy and uncertainty of thermal-infrared remote sensing of stream temperatures at multiple spatial scales. *Remote Sens. Environ.* 100, 427–440. <https://doi.org/10.1016/j.rse.2005.07.007>
- Handcock, R.N., Torgersen, C.E., Cherkauer, K. a., Gillespie, A.R., Tockner, K., Faux, R.N., Tan, J., 2012. Thermal Infrared Remote Sensing of Water Temperature in Riverine Landscapes, in: *Fluvial Remote Sensing for Science and Management*. John Wiley & Sons, Ltd, Chichester, UK, pp. 85–113. <https://doi.org/10.1002/9781119940791.ch5>
- Hannah, D.M., Sadler, J.P., Wood, P.J., 2007. Hydroecology and ecohydrology: a potential route forward? *Hydrol. Process.* 21, 3385–3390. <https://doi.org/10.1002/hyp.6888>
- Hannah, D.M., Webb, B.W., Nobilis, F., 2008. River and stream temperature: dynamics, processes, models and implications. *Hydrol. Process.* 22, 899–901. <https://doi.org/10.1002/hyp.6997>
- Härer, S., Bernhardt, M., Corripio, J.G., Schulz, K., 2013. PRACTISE – Photo Rectification And ClassificaTion SoftwarE (V.1.0). *Geosci. Model Dev.* 6, 837–848. <https://doi.org/10.5194/gmd-6-837-2013>
- Heathwaite, A.L., Quinn, P.F., Hewett, C.J.M., 2005. Modelling and managing critical source areas of diffuse pollution from agricultural land using flow connectivity simulation. *J. Hydrol.* 304, 446–461. <https://doi.org/10.1016/j.jhydrol.2004.07.043>
- Heger, T.J., Straub, F., Mitchell, E. a D., 2012. Impact of farming practices on soil diatoms and testate amoebae: A pilot study in the DOK-trial at Therwil, Switzerland. *Eur. J. Soil Biol.* 49, 31–36. <https://doi.org/10.1016/j.ejsobi.2011.08.007>
- Hewlett, J.D., 1961. Soil moisture as a source of baseflow from steep mountain watersheds. *Southeast. For. Exp. Stn. Asheville, North Carolina*.
- Hewlett, J.D., Hibbert, A.R., 1967. Factors affecting the response of small watershed to precipitation in humid areas. *For. Hydrol.* 275–279.
- Hlúbiková, D., Novais, M.H., Dohet, A., Hoffmann, L., Ector, L., 2014. Effect of riparian vegetation on diatom assemblages in headwater streams under different land uses. *Sci. Total Environ.* 475, 234–47. <https://doi.org/10.1016/j.scitotenv.2013.06.004>
- Hongve, D., 1987. A revised procedure for discharge measurement by means of the salt dilution method. *Hydrol. Process.* 1, 267–270. <https://doi.org/10.1002/hyp.3360010305>
- Huff, D.D., O'Neill, R. V., Emanuel, W.R., Elwood, J.W., Newbold, J.D., 1982. Flow variability and hillslope hydrology. *Earth Surf. Process. Landforms* 7, 91–94. <https://doi.org/10.1002/esp.3290070112>
- International Organization for Standardization, 2005. *Soil quality – Determination of pH*. ISO 10390:2005. Geneva, Switzerland.
- International Organization for Standardization, 1994. *Soil quality – Determination of the specific electrical conductivity*. ISO 11265:1994. Geneva, Switzerland.
- Ishaq, R.M., Huff, D.D., 1974. Application of remote sensing to the location of hydrodynamically active (source) areas, in: *Proceedings of 9th International Symposium on Remote Sensing of the Environment*. Environmental Research Institute of Michigan, Ann Arbor, Michigan, pp. 653–666.
- Jencso, K.G., McGlynn, B.L., Gooseff, M.N., Wondzell, S.M., Bencala, K.E., Marshall, L. a.,

2009. Hydrologic connectivity between landscapes and streams: Transferring reach- and plot-scale understanding to the catchment scale. *Water Resour. Res.* 45, 1–16. <https://doi.org/10.1029/2008WR007225>
- Juilleret, J., Iffly, J.F., Pfister, L., Hissler, C., 2011. Remarkable Pleistocene periglacial slope deposits in Luxembourg (Oesling): pedological implication and geosite potential. *Bull. la Société des Nat. Luxemb.* 112, 125–130.
- Kahlert, M., Ács, É., Almeida, S.F.P., Blanco, S., Dreßler, M., Ector, L., Karjalainen, S.M., Liess, A., Mertens, A., van der Wal, J., Vilbaste, S., Werner, P., 2016. Quality assurance of diatom counts in Europe: towards harmonized datasets. *Hydrobiologia* 772, 1–14. <https://doi.org/10.1007/s10750-016-2651-8>
- Kahlert, M., Kelly, M., Albert, R.L., Almeida, S.F.P., Bešta, T., Blanco, S., Coste, M., Denys, L., Ector, L., Fránková, M., Hlúbíková, D., Ivanov, P., Kennedy, B., Marvan, P., Mertens, A., Miettinen, J., Picinska-Fałtynowicz, J., Rosebery, J., Tornés, E., Vilbaste, S., Vogel, A., 2012. Identification versus counting protocols as sources of uncertainty in diatom-based ecological status assessments. *Hydrobiologia* 695, 109–124. <https://doi.org/10.1007/s10750-012-1115-z>
- Keesstra, S., Nunes, J.P., Saco, P., Parsons, T., Poepl, R., Masselink, R., Cerdà, A., 2018. The way forward: Can connectivity be useful to design better measuring and modelling schemes for water and sediment dynamics? *Sci. Total Environ.* 644, 1557–1572. <https://doi.org/10.1016/j.scitotenv.2018.06.342>
- Kelcey, J., Lucieer, A., 2012. Sensor Correction of a 6-Band Multispectral Imaging Sensor for UAV Remote Sensing. *Remote Sens.* 1462–1493. <https://doi.org/10.3390/rs4051462>
- Kelly, M., Bennion, H., Burgess, A., Ellis, J., Juggins, S., Guthrie, R., Jamieson, J., Adriaenssens, V., Yallop, M., 2009. Uncertainty in ecological status assessments of lakes and rivers using diatoms. *Hydrobiologia* 633, 5–15. <https://doi.org/10.1007/s10750-009-9872-z>
- Kelly, M.G., Penny, C.J., Whitton, B. a., 1995. Comparative performance of benthic diatom indices used to assess river water quality. *Hydrobiologia* 302, 179–188. <https://doi.org/10.1007/BF00032108>
- Kelly, M.G., Whitton, B.A., 1995. The Trophic Diatom Index: a new index for monitoring eutrophication in rivers. *J. Appl. Phycol.* 7, 433–444. <https://doi.org/10.1007/BF00003802>
- Kemp, M.J., Dodds, W.K., 2001. Spatial and temporal patterns of nitrogen concentrations in pristine and agriculturally-influenced prairie streams. *Biogeochemistry* 53, 125–141. <https://doi.org/https://doi.org/10.1023/A:1010707632340>
- Keys, T. a., Jones, C.N., Scott, D.T., Chuquin, D., 2016. A cost-effective image processing approach for analyzing the ecohydrology of river corridors. *Limnol. Oceanogr. Methods* 14, 359–369. <https://doi.org/10.1002/lom3.10095>
- Kiffney, P.M., Greene, C.M., Hall, J.E., Davies, J.R., 2006. Tributary streams create spatial discontinuities in habitat, biological productivity, and diversity in mainstem rivers. *Can. J. Fish. Aquat. Sci.* 63, 2518–2530. <https://doi.org/10.1139/f06-138>
- Kirnbauer, R., Haas, P., 1998. Observations on runoff generation mechanism in small Alpine catchments. *Hydrol. Water Resour. Ecol. Headwaters* 248, 275–283.
- Klaus, J., McDonnell, J.J., 2013. Hydrograph separation using stable isotopes: Review and

- evaluation. *J. Hydrol.* 505, 47–64. <https://doi.org/10.1016/j.jhydrol.2013.09.006>
- Klaus, J., Wetzel, C.E., Martínez-Carreras, N., Ector, L., Pfister, L., 2015. A tracer to bridge the scales: on the value of diatoms for tracing fast flow path connectivity from headwaters to meso-scale catchments. *Hydrol. Process.* 29, 5275–5289. <https://doi.org/10.1002/hyp.10628>
- Kohonen, T., 1982. Self-organized formation of topologically correct feature maps. *Biol. Cybern.* 43, 59–69. <https://doi.org/10.1007/BF00337288>
- Krause, S., Lewandowski, J., Grimm, N.B., Hannah, D.M., Pinay, G., McDonald, K., Martí, E., Argerich, A., Pfister, L., Klaus, J., Battin, T., Larned, S.T., Schelker, J., Fleckenstein, J., Schmidt, C., Rivett, M.O., Watts, G., Sabater, F., Sorolla, A., Turk, V., 2017. Ecohydrological interfaces as hot spots of ecosystem processes. *Water Resour. Res.* 53, 6359–6376. <https://doi.org/10.1002/2016WR019516>
- Kulasova, A., Beven, K.J., Blazkova, S.D., Rezacova, D., Cajthaml, J., 2014a. Comparison of saturated areas mapping methods in the Jizera Mountains, Czech Republic. *J. Hydrology Hydromechanics* 62, 160–168. <https://doi.org/10.2478/johh-2014-0002>
- Kulasova, A., Blazkova, S., Beven, K., Rezacova, D., Cajthaml, J., 2014b. Vegetation pattern as an indicator of saturated areas in a Czech headwater catchment. *Hydrol. Process.* 28, 5297–5308. <https://doi.org/10.1002/hyp.10239>
- Kuraš, P.K., Weiler, M., Alila, Y., 2008. The spatiotemporal variability of runoff generation and groundwater dynamics in a snow-dominated catchment. *J. Hydrol.* 352, 50–66. <https://doi.org/10.1016/j.jhydrol.2007.12.021>
- Kwandrans, J., Eloranta, P., Kawecka, B., Wojtan, K., 1998. Use of benthic diatom communities to evaluate water quality in rivers of southern Poland. *J. Appl. Phycol.* 10, 193–201. <https://doi.org/10.1023/A:1008087114256>
- Lana-Renault, N., Regüés, D., Serrano, P., Latron, J., 2014. Spatial and temporal variability of groundwater dynamics in a sub-Mediterranean mountain catchment. *Hydrol. Process.* 28, 3288–3299. <https://doi.org/10.1002/hyp.9892>
- Latron, J., Gallart, F., 2007. Seasonal dynamics of runoff-contributing areas in a small mediterranean research catchment (Vallcebre, Eastern Pyrenees). *J. Hydrol.* 335, 194–206. <https://doi.org/10.1016/j.jhydrol.2006.11.012>
- Laudon, H., Kuglerová, L., Sponseller, R.A., Futter, M., Nordin, A., Bishop, K., Lundmark, T., Egnell, G., Ågren, A.M., 2016. The role of biogeochemical hotspots, landscape heterogeneity, and hydrological connectivity for minimizing forestry effects on water quality. *Ambio* 45, 152–162. <https://doi.org/10.1007/s13280-015-0751-8>
- Lavoie, I., Vincent, W.F., Pienitz, R., Painchaud, J., 2004. Benthic algae as bioindicators of agricultural pollution in the streams and rivers of southern Québec (Canada). *Aquat. Ecosyst. Health Manag.* 7, 43–58. <https://doi.org/10.1080/14634980490281236>
- Leach, J.A., Lidberg, W., Kuglerová, L., Peralta-Tapia, A., Ågren, A., Laudon, H., 2017. Evaluating topography-based predictions of shallow lateral groundwater discharge zones for a boreal lake-stream system. *Water Resour. Res.* 53, 5420–5437. <https://doi.org/10.1002/2016WR019804>
- Lecoite, C., Coste, M., Prygiel, J., 1993. Omnidia: software for taxonomy, calculation of diatom indices and inventories management. *Hydrobiologia* 269/270, 509–513.

- Ledesma, J.L.J., Futter, M.N., Blackburn, M., Lidman, F., Grabs, T., Sponseller, R.A., Laudon, H., Bishop, K.H., Köhler, S.J., 2018. Towards an Improved Conceptualization of Riparian Zones in Boreal Forest Headwaters. *Ecosystems* 21, 297–315. <https://doi.org/10.1007/s10021-017-0149-5>
- Legendre, P., Legendre, L., 1998. *Numerical Ecology.*, 2nd editio. ed. Elsevier Science, Amsterdam.
- Lenoir, A., Coste, M., 1996. Development of a practical diatom index of overall water quality applicable to the French Water Board network., in: Rott, E. (Ed. . (Ed.), *Proceedings of International Symposium Use of Algae for Monitoring Rivers II*. Institut Für Botanik, Universität Innsbruck. pp. 29–45.
- Lewis, Q.W., Rhoads, B.L., 2015. Rates and patterns of thermal mixing at a small stream confluence under variable incoming flow conditions. *Hydrol. Process.* 29, 4442–4456. <https://doi.org/10.1002/hyp.10496>
- Lewkowicz, A.G., 2008. Evaluation of miniature temperature-loggers to monitor snowpack evolution at mountain permafrost sites, northwestern Canada. *Permafr. Periglac. Process.* 19, 323–331. <https://doi.org/10.1002/ppp.625>
- Li, C.J., Ling, H., 2015. Synthetic aperture radar imaging using a small consumer drone, in: *2015 IEEE International Symposium on Antennas and Propagation & USNC/URSI National Radio Science Meeting*. IEEE, pp. 685–686. <https://doi.org/10.1109/APS.2015.7304729>
- Li, H.-C., Celik, T., Longbotham, N., Emery, W.J., 2015. Gabor Feature Based Unsupervised Change Detection of Multitemporal SAR Images Based on Two-Level Clustering. *IEEE Geosci. Remote Sens. Lett.* 12, 2458–2462. <https://doi.org/10.1109/LGRS.2015.2484220>
- Liu, S., Xie, G., Wang, L., Cottenie, K., Liu, D., Wang, B., 2016. Different roles of environmental variables and spatial factors in structuring stream benthic diatom and macroinvertebrate in Yangtze River Delta, China. *Ecol. Indic.* 61, 602–611. <https://doi.org/10.1016/j.ecolind.2015.10.011>
- Lobo, E.A., Heinrich, C.G., Schuch, M., Wetzel, C.E., Ector, L., 2016. Diatoms as Bioindicators in Rivers, in: *River Algae*. Springer International Publishing, Cham, pp. 245–271. https://doi.org/10.1007/978-3-319-31984-1_11
- Logez, M., Bady, P., Melcher, A., Pont, D., 2013. A continental-scale analysis of fish assemblage functional structure in European rivers. *Ecography (Cop.)*. 36, 80–91. <https://doi.org/10.1111/j.1600-0587.2012.07447.x>
- Loheide, S.P., Gorelick, S.M., 2006. Quantifying stream-aquifer interactions through the analysis of remotely sensed thermographic profiles and in situ temperature histories. *Environ. Sci. Technol.* 40, 3336–3341. <https://doi.org/10.1021/es0522074>
- Luscombe, D.J., Anderson, K., Gatis, N., Grand-Clement, E., Brazier, R.E., 2015. Using airborne thermal imaging data to measure near-surface hydrology in upland ecosystems. *Hydrol. Process.* 29, 1656–1668. <https://doi.org/10.1002/hyp.10285>
- Luzi, G., 2010. Ground Based SAR Interferometry: a Novel Tool for Geoscience, in: *Geoscience and Remote Sensing New Achievements*. InTech. <https://doi.org/10.5772/9090>
- Martínez-Carreras, N., Hissler, C., Gourdol, L., Klaus, J., Juilleret, J., Iffly, J.F., Pfister, L.,

2016. Storage controls on the generation of double peak hydrographs in a forested headwater catchment. *J. Hydrol.* 543, 255–269. <https://doi.org/10.1016/j.jhydrol.2016.10.004>
- Martínez-Carreras, N., Wetzel, C.E., Frentress, J., Ector, L., McDonnell, J.J., Hoffmann, L., Pfister, L., 2015a. Hydrological connectivity as indicated by transport of diatoms through the riparian–stream system. *Hydrol. Earth Syst. Sci. Discuss.* 12, 2391–2434. <https://doi.org/10.5194/hessd-12-2391-2015>
- Martínez-Carreras, N., Wetzel, C.E., Frentress, J., Ector, L., McDonnell, J.J., Hoffmann, L., Pfister, L., 2015b. Hydrological connectivity inferred from diatom transport through the riparian-stream system. *Hydrol. Earth Syst. Sci.* 19, 3133–3151. <https://doi.org/10.5194/hess-19-3133-2015>
- Martínez Fernández, J., Ceballos Barbancho, A., Hernández Santana, V., Casado Ledesma, S., Morán Tejada, C., 2015. Procesos hidrológicos en una cuenca forestal del Sistema Central : cuenca experimental de Rinconada. *Cuad. Investig. Geográfica* 31, 7. <https://doi.org/10.18172/cig.1171>
- Matgen, P., El Idrissi, a., Henry, J.B., Tholey, N., Hoffmann, L., de Fraipont, P., Pfister, L., 2006. Patterns of remotely sensed floodplain saturation and its use in runoff predictions. *Hydrol. Process.* 20, 1805–1825. <https://doi.org/10.1002/hyp.5963>
- McDonnell, J., 2003. Where does water go when it rains? Moving beyond the variable source area concept of rainfall-runoff response. *Hydrol. Process.* 17, 1869–1875. <https://doi.org/10.1002/hyp.5132>
- Mcdonnell, J.J., Owens, I.F., Stewart, M.K., 1991. A CASE STUDY OF SHALLOW FLOW PATHS IN AN STEEP ZERO-ORDER BASIN. *Water Resour. bulletin* 27, 679–685.
- McGlynn, B.L., 2003. Distributed assessment of contributing area and riparian buffering along stream networks. *Water Resour. Res.* 39, 1–7. <https://doi.org/10.1029/2002WR001521>
- McGlynn, B.L., McDonnell, J.J., 2003. Quantifying the relative contributions of riparian and hillslope zones to catchment runoff. *Water Resour. Res.* 39. <https://doi.org/10.1029/2003WR002091>
- McGlynn, B.L., McDonnell, J.J., Seibert, J., Kendall, C., 2004. Scale effects on headwater catchment runoff timing, flow sources, and groundwater-streamflow relations. *Water Resour. Res.* 40, 1–14. <https://doi.org/10.1029/2003WR002494>
- Mengistu, S.G., Spence, C., 2016. Testing the ability of a semidistributed hydrological model to simulate contributing area. *Water Resour. Res.* 52, 4399–4415. <https://doi.org/10.1002/2016WR018760>
- Miller, E.E., Miller, R.D., 1956. Physical Theory for Capillary Flow Phenomena. *J. Appl. Phys.* 27, 324–332. <https://doi.org/10.1063/1.1722370>
- Montgomery, D.R., Dietrich, W.E., 1989. Source Areas, Drainage Density, and Channel Initiation. *Water Resour. Res.* 25, 1907–1918.
- Moore, R.D., 2004. Introduction to salt dilution gauging for streamflow measurement Part 1. *Streamline Watershed Manag. Bull.* 7, 20–23. <https://doi.org/10.1592/phco.23.9.1S.32890>
- Moragues-Quiroga, C., Juilleret, J., Gourdol, L., Pelt, E., Perrone, T., Aubert, A., Morvan, G., Chabaux, F., Legout, A., Stille, P., Hissler, C., 2017. Genesis and evolution of regoliths:

- Evidence from trace and major elements and Sr-Nd-Pb-U isotopes. *Catena* 149, 185–198. <https://doi.org/https://doi.org/10.1016/j.catena.2016.09.015>
- Mortágua, A., Vasselon, V., Oliveira, R., Elias, C., Chardon, C., Bouchez, A., Rimet, F., João Feio, M., F.P. Almeida, S., 2019. Applicability of DNA metabarcoding approach in the bioassessment of Portuguese rivers using diatoms. *Ecol. Indic.* 106, 105470. <https://doi.org/10.1016/j.ecolind.2019.105470>
- Myrabø, S., 1997. Temporal and spatial scale of response area and groundwater variation in Till. *Hydrol. Process.* 11, 1861–1880. [https://doi.org/10.1002/\(sici\)1099-1085\(199711\)11:14<1861::aid-hyp535>3.0.co;2-p](https://doi.org/10.1002/(sici)1099-1085(199711)11:14<1861::aid-hyp535>3.0.co;2-p)
- Niedda, M., Pirastru, M., 2014. Field investigation and modelling of coupled stream discharge and shallow water-table dynamics in a small Mediterranean catchment (Sardinia). *Hydrol. Process.* 28, 5423–5435. <https://doi.org/10.1002/hyp.10016>
- Noga, T., Stanek-Tarkowska, J., Peszek, Ł., Pajączek, A., Kowalska, S., 2013. USE OF DIATOMS TO ASSES WATER QUALITY OF ANTHROPOGENICALLY MODIFIED MATYSÓWKA STREAM. *J. Ecol. Eng.* 14, 1–11. <https://doi.org/10.5604/2081139X.1043166>
- O'Loughlin, E.M., 1987. Prediction of surface saturation zones in natural catchments by topographic analysis. *Water Resour. Res.* 23, 1709–1709. <https://doi.org/10.1029/wr023i008p01709>
- Ocampo, C.J., Oldham, C.E., Sivapalan, M., Turner, J. V., 2006. Hydrological versus biogeochemical controls on catchment nitrate export: a test of the flushing mechanism. *Hydrol. Process.* 20, 4269–4286. <https://doi.org/10.1002/hyp.6311>
- Oksanen, J., Guillaume Blanchet, F., Kindt, R., Legendre, P., Minchin, P.R., O'Hara, R.B., Al., E., 2015. Community Ecology Package. R Package Version 2.
- Orillo, J.W., Bansil Jr., G., Bernardo, J.J., Dizon, C., Imperial, H., Macabenta, A.M., Palima Jr., R., 2017. Determination of Green Leaves Density Using Normalized Difference Vegetation Index via Image Processing of In-Field Drone-Captured Image. *J. Telecommun. Electron. Comput. Eng.* 9, 1–5.
- Pacifici, F., Chini, M., Emery, W.J., 2009. A neural network approach using multi-scale textural metrics from very high-resolution panchromatic imagery for urban land-use classification. *Remote Sens. Environ.* 113, 1276–1292. <https://doi.org/10.1016/j.rse.2009.02.014>
- Parsons, A.J., Bracken, L., Poepl, R.E., Wainwright, J., Keesstra, S.D., 2015. Introduction to special issue on connectivity in water and sediment dynamics. *Earth Surf. Process. Landforms* 40, 1275–1277. <https://doi.org/10.1002/esp.3714>
- Paton, E.N., Smetanová, A., Krueger, T., Parsons, A., 2019. Perspectives and ambitions of interdisciplinary connectivity researchers. *Hydrol. Earth Syst. Sci.* 23, 537–548. <https://doi.org/10.5194/hess-23-537-2019>
- Patra, S., Ghosh, S., Ghosh, A., 2011. Histogram thresholding for unsupervised change detection of remote sensing images. *Int. J. Remote Sens.* 32, 6071–6089. <https://doi.org/10.1080/01431161.2010.507793>
- Payn, R.A., Gooseff, M.N., McGlynn, B.L., Bencala, K.E., Wondzell, S.M., 2012. Exploring changes in the spatial distribution of stream baseflow generation during a seasonal recession. *Water Resour. Res.* 48, 1–15. <https://doi.org/10.1029/2011WR011552>

- Pedregosa, F., Grisel, O., Weiss, R., Passos, A., Brucher, M., 2011. Scikit-learn : Machine Learning in Python. *J. Mach. Learn. Res.* 12, 2825–2830. <https://doi.org/10.1007/s13398-014-0173-7.2>
- Pfister, L., Humbert, J., Hoffmann, L., 2000. Recent Trends in Rainfall-Runoff Characteristics in the Alzette River Basin, Luxembourg. *Clim. Change* 45, 323–337.
- Pfister, L., Iffly, J. François, Hoffmann, L., Humbert, J., 2002. Use of regionalized stormflow coefficients with a view to hydroclimatological hazard mapping. *Hydrol. Sci. J.* 47, 479–491. <https://doi.org/10.1080/02626660209492948>
- Pfister, L., McDonnell, J.J., Hissler, C., Hoffmann, L., 2010. Ground-based thermal imagery as a simple, practical tool for mapping saturated area connectivity and dynamics. *Hydrol. Process.* 24, 3123–3132. <https://doi.org/10.1002/hyp.7840>
- Pfister, L., McDonnell, J.J., Wrede, S., Hlúbiková, D., Matgen, P., Fencia, F., Ector, L., Hoffmann, L., 2009. The rivers are alive: on the potential for diatoms as a tracer of water source and hydrological connectivity. *Hydrol. Process.* 23, 2841–2845. <https://doi.org/10.1002/hyp.7426>
- Pfister, L., Wetzel, C.E., Klaus, J., Martínez-Carreras, N., Antonelli, M., Teuling, A.J., McDonnell, J.J., 2017. Terrestrial diatoms as tracers in catchment hydrology: a review. *Wiley Interdiscip. Rev. Water* 4, e1241. <https://doi.org/10.1002/wat2.1241>
- Phillips, R.W., Spence, C., Pomeroy, J.W., 2011. Connectivity and runoff dynamics in heterogeneous basins. *Hydrol. Process.* 25, 3061–3075. <https://doi.org/10.1002/hyp.8123>
- Pinay, G., 2005. Linking hydrology and biogeochemistry. *Prog. Phys. Geogr.* 3, 297–316.
- Pletterbauer, F., Melcher, A.H., Ferreira, T., Schmutz, S., 2015. Impact of climate change on the structure of fish assemblages in European rivers. *Hydrobiologia* 744, 235–254. <https://doi.org/10.1007/s10750-014-2079-y>
- Ploum, S.W., Leach, J.A., Kuglerová, L., Laudon, H., 2018. Thermal detection of discrete riparian inflow points (DRIPs) during contrasting hydrological events. *Hydrol. Process.* 32, 3049–3050. <https://doi.org/10.1002/hyp.13184>
- Pluhowski, E.J., 1972. Hydrologic interpretations based on infrared imagery of Long Island, New York, Contributions to the hydrology of the United States. <https://doi.org/10.3133/wsp2009B>
- Portmann, F.T., 1997. Hydrological runoff modelling by the use of remote sensing data with reference to the 1993–1994 and 1995 floods in the river Rhine catchment. *Hydrol. Process.* 11, 1377–1392.
- Power, M.E., Dietrich, W.E., 2002. Food webs in river networks. *Ecol. Res.* 17, 451–471. <https://doi.org/10.1046/j.1440-1703.2002.00503.x>
- Pringle, C.M., 2001. HYDROLOGIC CONNECTIVITY AND THE MANAGEMENT OF BIOLOGICAL RESERVES: A GLOBAL PERSPECTIVE. *Ecol. Appl.* 11, 981–998.
- Prygiel, J., Coste, M., 1993. The assessment of water quality in the Artois-Picardie water basin (France) by the use of diatom indices. *Hydrobiologia* 269–270, 343–349. <https://doi.org/10.1007/BF00028033>
- R Core Team, 2015. R: A Language and Environment for Statistical Computing.

Bibliography

- Rademacher, L.K., Clark, J.F., Clow, D.W., Hudson, G.B., 2005. Old groundwater influence on stream hydrochemistry and catchment response times in a small Sierra Nevada catchment: Sagehen Creek, California. *Water Resour. Res.* 41. <https://doi.org/10.1029/2003WR002805>
- Rakowska, B., Szczepocka, E., 2011. Demonstration of the Bzura River restoration using diatom indices. *Biologia (Bratisl.)* 66. <https://doi.org/10.2478/s11756-011-0032-3>
- Rao, C.R., 1995. A review of canonical coordinates and an alternative to correspondence analysis using Hellinger distance. *Qüestiió* 19, 23–63.
- Reginato, R.J., Idso, S.B., Vedder, J.F., Jackson, R.D., Blanchard, M.B., Goettelman, R., 1976. Soil water content and evaporation determined by thermal parameters obtained from ground-based and remote measurements. *J. Geophys. Res.* 81, 1617–1620. <https://doi.org/10.1029/JC081i009p01617>
- Rhoads, B.L., Kenworthy, S.T., 1998. Time-averaged flow structure in the central region of a stream confluence. *Earth Surf. Process. Landforms* 23, 171–191. [https://doi.org/10.1002/\(SICI\)1096-9837\(199802\)23:2<171::AID-ESP842>3.0.CO;2-T](https://doi.org/10.1002/(SICI)1096-9837(199802)23:2<171::AID-ESP842>3.0.CO;2-T)
- Rhoads, B.L., Sukhodolov, A.N., 2001. Field investigation of three-dimensional flow structure at stream confluences: 1. Thermal mixing and time-averaged velocities. *Water Resour. Res.* 37, 2393–2410. <https://doi.org/10.1029/2001WR000316>
- Rice, S.P., 2017. Tributary connectivity, confluence aggradation and network biodiversity. *Geomorphology* 277, 6–16. <https://doi.org/10.1016/j.geomorph.2016.03.027>
- Rice, S.P., Rhoads, B.L., Roy, A.G., 2008. Introduction: River Confluences, Tributaries and the Fluvial Network, in: *River Confluences, Tributaries and the Fluvial Network*. John Wiley & Sons, Ltd, Chichester, UK, pp. 1–9. <https://doi.org/10.1002/9780470760383.ch1>
- Rimet, F., Ector, L., Gauchie, H.M., Hoffmann, L., 2004. Regional distribution of diatom assemblages in the headwater streams of Luxembourg. *Hydrobiologia* 520, 105–117. <https://doi.org/10.1023/B:HYDR.0000027730.12964.8c>
- Rimet, F., Gusev, E., Kahlert, M., Kelly, M.G., Kulikovskiy, M., Maltsev, Y., Mann, D.G., Pfannkuchen, M., Trobajo, R., Vasselon, V., Zimmermann, J., Bouchez, A., 2019. Diat.barcode, an open-access curated barcode library for diatoms. *Sci. Rep.* 9, 15116. <https://doi.org/10.1038/s41598-019-51500-6>
- Rinderer, M., Kollegger, A., Fischer, B.M.C., Stähli, M., Seibert, J., 2012. Sensing with boots and trousers - qualitative field observations of shallow soil moisture patterns. *Hydrol. Process.* 26, 4112–4120. <https://doi.org/10.1002/hyp.9531>
- Rinderer, M., Meerveld, H.J., McGlynn, B.L., 2019. From Points to Patterns: Using Groundwater Time Series Clustering to Investigate Subsurface Hydrological Connectivity and Runoff Source Area Dynamics. *Water Resour. Res.* 5784–5806. <https://doi.org/10.1029/2018wr023886>
- Rodhe, A., Seibert, J., 1999. Wetland occurrence in relation to topography: A test of topographic indices as moisture indicators. *Agric. For. Meteorol.* 98–99, 325–340. [https://doi.org/10.1016/S0168-1923\(99\)00104-5](https://doi.org/10.1016/S0168-1923(99)00104-5)
- Rodriguez, N.B., Klaus, J., n.d. Catchment travel times from composite StorAge Selection functions representing the superposition of streamflow generation processes. *Water Resour. Res.*

- Röper, T., Greskowiak, J., Massmann, G., 2013. Detecting Small Groundwater Discharge Springs Using Handheld Thermal Infrared Imagery. *Groundwater* 52, 936–942. <https://doi.org/10.1111/gwat.12145>
- Rosin, P.L., 2002. Thresholding for Change Detection. *Comput. Vis. Image Underst.* 86, 79–95. <https://doi.org/10.1006/cviu.2002.0960>
- Roulet, N.T., 1990. Hydrology of a headwater basin wetland. *Hydrol. Process.* 4, 387–40.
- Round, F.E., Crawford, R.M., Mann, D.G., 1990. *Diatoms: Biology And Morphology Of The Genera*. Cambridge: Cambridge University Press.
- Sanders, T.G., 1982. Representative sampling location criterion for rivers. *Water SA* 8, 169–172.
- Sanders, T.G., Adrian, D.D., Joyce, J.M., 1977. Mixing Length for Representative Water Quality Sampling. *J. (Water Pollut. Control Fed.)* 49, 2467–2478.
- Scaini, A., Audebert, M., Hissler, C., Fenicia, F., Gourdol, L., Pfister, L., Beven, K.J., 2017. Velocity and celerity dynamics at plot scale inferred from artificial tracing experiments and time-lapse ERT. *J. Hydrol.* 546, 28–43. <https://doi.org/10.1016/j.jhydrol.2016.12.035>
- Scaini, A., Hissler, C., Fenicia, F., Juilleret, J., Iffly, J.F., Pfister, L., Beven, K., 2018. Hillslope response to sprinkling and natural rainfall using velocity and celerity estimates in a slate-bedrock catchment. *J. Hydrol.* 558, 366–379. <https://doi.org/10.1016/j.jhydrol.2017.12.011>
- Schmugge, T., 1978. Remote Sensing of Surface Soil Moisture. *J. Appl. Meteorol.* 17, 1549–1557. [https://doi.org/10.1175/1520-0450\(1978\)017<1549:RSOSSM>2.0.CO;2](https://doi.org/10.1175/1520-0450(1978)017<1549:RSOSSM>2.0.CO;2)
- Schuetz, T., Weiler, M., 2011. Quantification of localized groundwater inflow into streams using ground-based infrared thermography. *Geophys. Res. Lett.* 38, 1–5. <https://doi.org/10.1029/2010GL046198>
- Schuetz, T., Weiler, M., Lange, J., Stoelzle, M., 2012. Two-dimensional assessment of solute transport in shallow waters with thermal imaging and heated water. *Adv. Water Resour.* 43, 67–75. <https://doi.org/10.1016/j.advwatres.2012.03.013>
- Schwab, M.P., Klaus, J., Pfister, L., Weiler, M., 2018. Diel fluctuations of viscosity-driven riparian inflow affect streamflow DOC concentration. *Biogeosciences* 15, 2177–2188. <https://doi.org/10.5194/bg-15-2177-2018>
- Seibert, J., Bishop, K., Rodhe, A., McDonnell, J.J., 2003. Groundwater dynamics along a hillslope: A test of the steady state hypothesis. *Water Resour. Res.* 39, 1–9. <https://doi.org/10.1029/2002WR001404>
- Seibert, S.P., Jackisch, C., Ehret, U., Pfister, L., Zehe, E., 2017. Unravelling abiotic and biotic controls on the seasonal water balance using data-driven dimensionless diagnostics. *Hydrol. Earth Syst. Sci.* 21, 2817–2841. <https://doi.org/10.5194/hess-21-2817-2017>
- Selker, J., van de Giesen, N.C., Westhoff, M., Luxemburg, W., Parlange, M.B., 2006. Fiber optics opens window on stream dynamics. *Geophys. Res. Lett.* 33, 27–30. <https://doi.org/10.1029/2006GL027979>
- Selker, J.S., Thévenaz, L., Huwald, H., Mallet, A., Luxemburg, W., van de Giesen, N., Stejskal, M., Zeman, J., Westhoff, M., Parlange, M.B., 2006. Distributed fiber-optic temperature sensing for hydrologic systems. *Water Resour. Res.* 42.

- <https://doi.org/10.1029/2006WR005326>
- Shaw, S.B., 2016. Investigating the linkage between streamflow recession rates and channel network contraction in a mesoscale catchment in New York state. *Hydrol. Process.* 30, 479–492. <https://doi.org/10.1002/hyp.10626>
- Shaw, S.B., Bonville, D.B., Chandler, D.G., 2017. Combining observations of channel network contraction and spatial discharge variation to inform spatial controls on baseflow in Birch Creek, Catskill Mountains, USA. *J. Hydrol. Reg. Stud.* 12, 1–12. <https://doi.org/10.1016/j.ejrh.2017.03.003>
- Silasari, R., Parajka, J., Ressler, C., Strauss, P., Blöschl, G., 2017. Potential of time-lapse photography for identifying saturation area dynamics on agricultural hillslopes. *Hydrol. Process.* 31, 3610–3627. <https://doi.org/10.1002/hyp.11272>
- Smith, L.L., Jones, C.N., Nelson, N.G., 2019. Featured Collection Introduction: The Emerging Science of Aquatic System Connectivity II. *J. Am. Water Resour. Assoc.* 55, 526–528. <https://doi.org/10.1111/1752-1688.12760>
- Soininen, J., 2007. Environmental and spatial control of freshwater diatoms - A review. *Diatom Res.* 22, 473–490. <https://doi.org/10.1080/0269249X.2007.9705724>
- Soininen, J., Jamoneau, A., Rosebery, J., Passy, S.I., 2016. Global patterns and drivers of species and trait composition in diatoms. *Glob. Ecol. Biogeogr.* 25, 940–950. <https://doi.org/10.1111/geb.12452>
- Sougnéz, N., Vanacker, V., 2011. The topographic signature of Quaternary tectonic uplift in the Ardennes massif (Western Europe). *Hydrol. Earth Syst. Sci.* 15, 1095–1107. <https://doi.org/10.5194/hess-15-1095-2011>
- Soulsby, C., Birkel, C., Tetzlaff, D., 2016a. Modelling storage-driven connectivity between landscapes and riverscapes: towards a simple framework for long-term ecohydrological assessment. *Hydrol. Process.* 30, 2482–2497. <https://doi.org/10.1002/hyp.10862>
- Soulsby, C., Bradford, J., Dick, J., McNamara, J.P., Geris, J., Lessels, J., Blumstock, M., Tetzlaff, D., 2016b. Using geophysical surveys to test tracer-based storage estimates in headwater catchments. *Hydrol. Process.* 30, 4434–4445. <https://doi.org/10.1002/hyp.10889>
- Soulsby, C., Malcolm, I.A., Youngson, A.F., Tetzlaff, D., Gibbins, C.N., Hannah, D.M., 2005. Groundwater–surface water interactions in upland Scottish rivers: hydrological, hydrochemical and ecological implications. *Scottish J. Geol.* 41, 39–49. <https://doi.org/10.1144/sjg41010039>
- Spence, C., Mengistu, S., 2016. Deployment of an unmanned aerial system to assist in mapping an intermittent stream. *Hydrol. Process.* 30, 493–500. <https://doi.org/10.1002/hyp.10597>
- Stanek-Tarkowska, J., Noga, T., 2012. DIVERSITY OF DIATOMS (BACILLARIOPHYCEAE) IN THE SOIL UNDER TRADITIONAL TILLAGE AND REDUCED TILLAGE. *Inżynieria Ekol.* 30, 287–296.
- Stanek-Tarkowska, J., Noga, T., Kochman-kędziora, N., Peszek, Ł., Pajaczek, A., Kozak, E., 2015. The diversity of diatom assemblages developed on fallow soil in Pogórska Wola near Tarnów (southern Poland). *Acta Agrobot.* 33–42. <https://doi.org/10.5586/aa.2015.011>

- Stanek-tarkowska, J., Noga, T., Paj, A., 2013. The occurrence of *Sellaphora nana* (Hust .) Lange- Bert . Cavacini , Tagliaventi & Alfi nito , *Stauroneis borrichii* (J . B . Petersen) J . W . G . Lund , S . parathermicola Lange-Bert . and S . thermicola (J . B . Petersen) J . W . G . Lund on 142, 109–120. <https://doi.org/10.1127/1864-1318/2013/0114>
- Stieglitz, M., 2003. An approach to understanding hydrologic connectivity on the hillslope and the implications for nutrient transport. *Global Biogeochem. Cycles* 17, 1–15. <https://doi.org/10.1029/2003GB002041>
- Story, A., Moore, R.D., Macdonald, J.S., 2003. Stream temperatures in two shaded reaches below cutblocks and logging roads: downstream cooling linked to subsurface hydrology. *Can. J. For. Res.* 33, 1383–1396. <https://doi.org/10.1139/x03-087>
- Sutton, R.J., Deas, M.L., Tanaka, S.K., Soto, T., Corum, R.A., 2007. Salmonid observations at a Klamath River thermal refuge under various hydrological and meteorological conditions. *River Res. Appl.* 23, 775–785. <https://doi.org/10.1002/rra.1026>
- Tanaka, T., Yasuhara, M., Sakai, H., Marui, A., 1988. The Hachioji Experimental Basin Study - Storm runoff processes and the mechanism of its generation. *J. Hydrol.* 102, 139–164. [https://doi.org/10.1016/0022-1694\(88\)90095-9](https://doi.org/10.1016/0022-1694(88)90095-9)
- Tauro, F., Martínez-Carreras, N., Barnich, F., Juilleret, J., Wetzels, C.E., Ector, L., Hissler, C., Pfister, L., 2016. Diatom percolation through soils: a proof of concept laboratory experiment. *Ecohydrology* 9, 753–764. <https://doi.org/10.1002/eco.1671>
- Tetzlaff, D., Birkel, C., Dick, J., Geris, J., Soulsby, C., 2014. Storage dynamics in hydrogeological units control hillslope connectivity, runoff generation, and the evolution of catchment transit time distributions. *Water Resour. Res.* 50, 969–985. <https://doi.org/10.1002/2013WR014147>
- Tetzlaff, D., McDonnell, J.J., Uhlenbrook, S., McGuire, K.J., Bogaart, P.W., Naef, F., Baird, A.J., Dunn, S.M., Soulsby, C., 2008. Conceptualizing catchment processes: simply too complex? *Hydrol. Process.* 22, 1727–1730. <https://doi.org/10.1002/hyp.7069>
- Tetzlaff, D., Soulsby, C., Waldron, S., Malcolm, I.A., Bacon, P.J., Dunn, S.M., Lilly, A., Youngson, A.F., 2007. Conceptualization of runoff processes using a geographical information system and tracers in a nested mesoscale catchment. *Hydrol. Process.* 21, 1289–1307. <https://doi.org/10.1002/hyp.6309>
- The European Parliament and the Council of the European Union, 2000. Directive 2000/60/EC of the European Parliament and of the Council of 23 establishing a framework for Community action in the field of water policy.
- Torgersen, C.E., Faux, R.N., McIntosh, B. a., Poage, N.J., Norton, D.J., 2001. Airborne thermal remote sensing for water temperature assessment in rivers and streams. *Remote Sens. Environ.* 76, 386–398. [https://doi.org/10.1016/S0034-4257\(01\)00186-9](https://doi.org/10.1016/S0034-4257(01)00186-9)
- Turnbull, L., Hütt, M.T., Ioannides, A.A., Kininmonth, S., Poepl, R., Tockner, K., Bracken, L.J., Keesstra, S., Liu, L., Masselink, R., Parsons, A.J., 2018. Connectivity and complex systems: learning from a multi-disciplinary perspective. *Appl. Netw. Sci.* 3. <https://doi.org/10.1007/s41109-018-0067-2>
- Turnbull, L., Wainwright, J., Brazier, R.E., 2008. A conceptual framework for understanding semi-arid land degradation: ecohydrological interactions across multiple-space and time scales. *Ecohydrology* 1, 23–34. <https://doi.org/10.1002/eco.4>
- Turner, D., Lucieer, A., Malenovsky, Z., King, D., Robinson, S., 2014. Spatial Co-Registration

- of Ultra-High Resolution Visible, Multispectral and Thermal Images Acquired with a Micro-UAV over Antarctic Moss Beds. *Remote Sens.* 6, 4003–4024. <https://doi.org/10.3390/rs6054003>
- Vacht, P., Puusepp, L., Koff, T., Reitalu, T., 2014. Variability of riparian soil diatom communities and their potential as indicators of anthropogenic disturbances. *Est. J. Ecol.* 63, 168–184. <https://doi.org/10.3176/eco.2014.3.04>
- Van Dam, H., Mertens, A., Sinkeldam, J., 1994. A coded checklist and ecological indicator values of freshwater diatoms from The Netherlands. *Netherlands J. Aquat. Ecol.* 28, 117–133. <https://doi.org/10.1007/BF02334251>
- Van de Vijver & Beyens 1998 *Eur. J. Soil Biol.* 34 (3) 133-141 soil diatom assemblages Crozet Subantarctica.pdf, n.d.
- van Kerckvoorde, A., Trappeniers, K., Nijs, I., Beyens, L., 2000. Terrestrial soil diatom assemblages from different vegetation types in Zackenberg (Northeast Greenland). *Polar Biol.* 23, 392–400. <https://doi.org/10.1007/s0030000050460>
- van Meerveld, H.J., Seibert, J., Peters, N.E., 2015. Hillslope-riparian-stream connectivity and flow directions at the Panola Mountain Research Watershed. *Hydrol. Process.* 29, 3556–3574. <https://doi.org/10.1002/hyp.10508>
- Vereecken, H., Pachepsky, Y., Bogaen, H., Montzka, C., 2019. Upscaling Issues in Ecohydrological Observations 435–454. https://doi.org/10.1007/978-3-662-48297-1_14
- Verhoest, N.E.C., Troch, P.A., Paniconi, C., De Troch, F.P., 1998. Mapping basin scale variable source areas from multitemporal remotely sensed observations of soil moisture behavior. *Water Resour. Res.* 34, 3235–3244. <https://doi.org/10.1029/98WR02046>
- Vidon, P.G.F., Hill, A.R., 2004. Landscape controls on the hydrology of stream riparian zones. *J. Hydrol.* 292, 210–228. <https://doi.org/10.1016/j.jhydrol.2004.01.005>
- Vivoni, E.R., Rango, A., Anderson, C.A., Pierini, N.A., Schreiner-McGraw, A.P., Saripalli, S., Laliberte, A.S., 2014. Ecohydrology with unmanned aerial vehicles. *Ecosphere* 5, 130. <https://doi.org/10.1890/ES14-00217.1>
- von Freyberg, J., Radny, D., Gall, H.E., Schirmer, M., 2014. Implications of hydrologic connectivity between hillslopes and riparian zones on streamflow composition. *J. Contam. Hydrol.* 169, 62–74. <https://doi.org/10.1016/j.jconhyd.2014.07.005>
- Wahab, I., Hall, O., Jirström, M., 2018. Remote Sensing of Yields: Application of UAV Imagery-Derived NDVI for Estimating Maize Vigor and Yields in Complex Farming Systems in Sub-Saharan Africa. *Drones* 2, 28. <https://doi.org/10.3390/drones2030028>
- Wainwright, J., Turnbull, L., Ibrahim, T.G., Lexartza-Artza, I., Thornton, S.F., Brazier, R.E., 2011. Linking environmental régimes, space and time: Interpretations of structural and functional connectivity. *Geomorphology* 126, 387–404. <https://doi.org/10.1016/j.geomorph.2010.07.027>
- Ward, A.S., Packman, A.I., 2019. Advancing our predictive understanding of river corridor exchange. *Wiley Interdiscip. Rev. Water* 6, e1327. <https://doi.org/10.1002/wat2.1327>
- Ward, A.S., Schmadel, N.M., Wondzell, S.M., 2018. Simulation of dynamic expansion, contraction, and connectivity in a mountain stream network. *Adv. Water Resour.* 114, 64–82. <https://doi.org/10.1016/j.advwatres.2018.01.018>
- Webb, B.W., Hannah, D.M., Moore, R.D., Brown, L.E., Nobilis, F., 2008. Recent advances in

- stream and river temperature research. *Hydrol. Process.* 22, 902–918. <https://doi.org/10.1002/hyp.6994>
- Weber, I., Jenal, a., Kneer, C., Bongartz, J., 2015. Pantir - a Dual Camera Setup for Precise Georeferencing and Mosaicing of Thermal Aerial Images. *ISPRS - Int. Arch. Photogramm. Remote Sens. Spat. Inf. Sci.* XL-3/W2, 269–272. <https://doi.org/10.5194/isprsarchives-XL-3-W2-269-2015>
- Weill, S., Altissimo, M., Cassiani, G., Deiana, R., Marani, M., Putti, M., 2013. Saturated area dynamics and streamflow generation from coupled surface-subsurface simulations and field observations. *Adv. Water Resour.* 59, 196–208. <https://doi.org/10.1016/j.advwatres.2013.06.007>
- Western, A.W., Grayson, R.B., Blöschl, G., Willgoose, G.R., McMahon, T.A., 1999. Observed spatial organization of soil moisture and its relation to terrain indices. *Water Resour. Res.* 35, 797–810. <https://doi.org/10.1029/1998WR900065>
- Westhoff, M.C., Bogaard, T. a., Savenije, H.H.G., 2011. Quantifying spatial and temporal discharge dynamics of an event in a first order stream, using distributed temperature sensing. *Hydrol. Earth Syst. Sci.* 15, 1945–1957. <https://doi.org/10.5194/hess-15-1945-2011>
- Wetzel, C.E., Martínez-Carreras, N., Hlúbiková, D., Hoffmann, L., & L.P., Ector, L., 2013. New Combinations and Type Analysis of Chamaepinnularia Species (Bacillariophyceae) from Aerial Habitats. *Cryptogam. Algal.* 34, 149–168. <https://doi.org/10.7872/crya.v34.iss2.2013.149>
- Wetzel, C.E., Van de Vijver, B., Kopalová, K., Hoffmann, L., Pfister, L., Ector, L., 2014. Type analysis of the South American diatom *Achnanthes haynaldii* (Bacillariophyta) and description of *Planothidium amphibium* sp. nov., from aerial and aquatic environments in Oregon (USA). *Plant Ecol. Evol.* 147, 439–454. <https://doi.org/10.5091/pecevo.2014.1058>
- Whiting, J.A., Godsey, S.E., 2016. Discontinuous headwater stream networks with stable flowheads, Salmon River basin, Idaho. *Hydrol. Process.* 30, 2305–2316. <https://doi.org/10.1002/hyp.10790>
- Wohl, E., Brierley, G., Cadol, D., Coulthard, T.J., Covino, T., Fryirs, K.A., Grant, G., Hilton, R.G., Lane, S.N., Magilligan, F.J., Meitzen, K.M., Passalacqua, P., Poepl, R.E., Rathburn, S.L., Sklar, L.S., 2019. Connectivity as an emergent property of geomorphic systems. *Earth Surf. Process. Landforms* 44, 4–26. <https://doi.org/10.1002/esp.4434>
- Wrede, S., Fenicia, F., Martínez-Carreras, N., Juilleret, J., Hissler, C., Krein, A., Savenije, H.H.G., Uhlenbrook, S., Kavetski, D., Pfister, L., 2015. Towards more systematic perceptual model development: A case study using 3 Luxembourgish catchments. *Hydrol. Process.* 29, 2731–2750. <https://doi.org/10.1002/hyp.10393>
- Wrede, S., Fenicia, F., Martínez-Carreras, N., Juilleret, J., Hissler, C., Krein, A., Savenije, H.H.G., Uhlenbrook, S., Kavetski, D., Pfister, L., 2014. Towards more systematic perceptual model development: a case study using 3 Luxembourgish catchments. *Hydrol. Process.* n/a-n/a. <https://doi.org/10.1002/hyp.10393>
- Zancan, S., Trevisan, R., Paoletti, M.G., 2006. Soil algae composition under different agroecosystems in North-Eastern Italy. *Agric. Ecosyst. Environ.* 112, 1–12. <https://doi.org/10.1016/j.agee.2005.06.018>
- Zehe, E., Lee, H., Sivapalan, M., 2006. Dynamical process upscaling for deriving catchment

Bibliography

- scale state variables and constitutive relations for meso-scale process models. *Hydrol. Earth Syst. Sci.* 10, 981–996. <https://doi.org/10.5194/hess-10-981-2006>
- Zelinka, M., Marvan, P., 1961. Zur Präzisierung der biologischen Klassifikation der Reinheit fließender Gewässer. *Arch. Hydrobiol.* 57, 389–407.
- Zillgens, B., Merz, B., Kirnbauer, R., Tilch, N., 2007. Analysis of the runoff response of an alpine catchment at different scales. *Hydrol. Earth Syst. Sci.* 11, 1441–1454. <https://doi.org/10.5194/hess-11-1441-2007>
- Zuecco, G., Penna, D., Borga, M., 2018. Runoff generation in mountain catchments: long-term hydrological monitoring in the Rio Vauz Catchment, Italy. *Cuad. Investig. Geográfica* 44, 397. <https://doi.org/10.18172/cig.3327>

Summary

This thesis deals with the investigation of hydrological connectivity between different structural and functional elements of the hydrological system by studying the spatial and temporal dynamics of surface water, through innovative multidisciplinary approaches (terrestrial diatoms and thermal infrared imagery). This will eventually lead to an improved understanding of how streamflow is generated and open new possibilities for a better management of hydrological systems (and their ecological integrity), which are increasingly put under pressure by climate change and anthropogenic activities.

In Chapter 2, terrestrial diatoms' ecological behaviour and sensitivity to environmental factors are investigated. Understanding the physiographic controls on terrestrial diatom communities is fundamental for advancing their employment as tracer of hydrological connectivity at the catchment scale. As an extension to this exploratory work, we have tested the hypothesis that terrestrial diatom communities can be used as indicators of soil quality. We found an effect of seasonality on soil diatom communities, reflected by different diatom species' dominance and abundances in samples during three seasons. Soil pH and land use (which translates in a different amount of total carbon and nitrogen in soil) were identified as the variables having the largest impact in structuring the communities. They were also found to be among the most relevant features for defining the ecological status of the investigated sites (e.g. disturbed farmlands having higher pH and lower carbon and nitrogen content compared to forest and grassland). These results suggest that soil diatom communities are likely to contain information about soil ecological status and highlight the importance of a better characterisation of terrestrial diatom species for developing a quality index based on soil communities.

In Chapter 3, the potential for ground-based thermal infrared imagery to provide instantaneous mapping of stream water mixing patterns at or near the water surface is explored. Stream confluences are important hotspots of aquatic ecological processes. Water mixing dynamics at stream confluences influence physio-chemical characteristics of the stream as well as sediment mobilisation and pollutant dispersal. We show that the use of a portable TIR camera can enhance the visualisation of mixing dynamics taking place at stream confluences and help to identify the location of the mixing front between two different water sources and the degree of mixing. Interpretation of handheld TIR observations also provided information on how stream morphology and discharge can influence mixing dynamics in small streams. These results show that thermal infrared imagery is a valuable support tool for eco-hydrological investigation at small stream confluences.

Chapter 4 reports a technical study on the practicability of applying thermal infrared imagery for mapping surface-saturation dynamics. Surface saturation can have a critical impact on runoff generation and water quality. We show that the advantages

Summary

of thermal infrared imagery compared to other surface saturation mapping methods are its large spatial and temporal flexibility, its non-invasive character, and the fact that it allows for a rapid and intuitive visualization of surface saturated areas. In addition, we elaborate on image post-processing and test different methods for the generation of saturation maps from the thermal infrared images.

In Chapter 5, ground-based thermal infrared imagery is used for characterising the seasonal dynamics of the surface saturation of seven different riparian areas. We collected bi-weekly thermal panoramic images of the seven areas over a period of two years. We identified the degree of saturation in each collected panoramic image (i.e. the percentage of pixels corresponding to saturated surfaces in each riparian area) to generate time series of surface saturation. Riparian surface saturation in all areas was found to be seasonally variable and saturation dynamics were in accordance with lower hillslope groundwater level fluctuations. Surface saturation in the different areas was related to catchment outlet discharge through power law relationships. Differences in these relationships for different areas could be associated with the location of the areas along the stream network and to a possible influence of local riparian morphology on the development of surface saturation, suggesting a certain degree of intra-catchment heterogeneity.

In Chapter 6, we investigated the spatio-temporal variability of streamflow in different sub-catchments and for different reaches in the catchment, and explored the topographical controls on streamflow variability. We found heterogeneities in the streamflow contribution from different portions of the catchment. While the size of the contributing area could explain differences in sub-catchments' and reaches' net discharges, no clear topographic controls could be found when considering the area-normalised discharges. This suggests that some local conditions exert control on the variability of specific discharge (e.g. local bedrock characteristics and occurrence of perennial springs). The surface saturation dynamics (as investigated and presented in Chapter 5) were found to be in agreement with the level of streamflow contribution from the correspondent reach in some of the investigated riparian areas. These results suggest that the combination of different techniques can be used to characterise the internal heterogeneity of the catchment and thus improve our understanding of how hydrological connectivity is established and streamflow is generated.

The development of innovative, multidisciplinary approaches and techniques for tracing hydrological connectivity is indispensable for generating new information on connectivity processes across multiple spatial and temporal scales. Thanks to the employment of novel techniques such as terrestrial diatoms and thermal infrared imagery, some challenging aspects of investigating hydrological connectivity have been further explored in this thesis. This concerned in particular the development of new approaches for tracing hydrological connectivity at the catchment scale (through terrestrial diatom characterisation, Chapter 2), the identification of intra-catchment homogeneous and heterogeneous landscape structures and connectivity pathways (Chapters 5 and 6) and the characterisation of the processes and water fluxes occurring around transition zones, or interfaces (through ground-based thermal imagery, Chapters 4, 5, and 6).

Acknowledgments

Here, I would like to thank the people who made the completion of this work possible with their help and support.

Thank you to my supervisors Laurent Pfister, Ryan Teuling and Remko Uijlenhoet. Each of you contributed to the realisation of my PhD in different ways, all necessary for me to grow both professionally and personally. I am grateful to Laurent for having given me the opportunity to join his research group in Luxembourg. Thank you for having supported and encouraged me when I most needed it and for showing me that one shouldn't be afraid to be creative in research. Thank you Ryan for having done a great job as supervisor even from afar. You taught me that, to reach an objective, I just need to start and work toward it. Without this mind-set, I would have never been able to write and publish my last two papers in the timeframe of little more than one year. Thank you Remko, for allowing me to be part of your research group in Wageningen and for your support. I felt very welcomed every time I visited the group.

This experience wouldn't have been so nice and meaningful without the people of the Catchment and Ecohydrology group. Thanks to my office mates Barbara Glaser, Nicolas Rodriguez, Cristina Moragues-Quiroga, Michael Schwab, and Anna Scaini, for all the shared time (in and outside the office) and the fruitful discussions. A particular thank you to Barbara. I couldn't have hoped for a better person to share this journey and all the scientific discussions with. In the process of unravelling the mysteries of the Weierbach together, I gained a friendship that I am sure will last a lifetime. Thanks to the people who provided indispensable help with the field work, laboratory work and data analysis, François Barnich, Jean François Iffly, Oliver O' Nagy, Jérôme Juilleret, Luc Ector, Dario Torregrossa. A big thank you to Carlos Eduardo Wetzel, Núria Martínez-Carreras and Julian Klaus for their help and for always finding the time for meeting (and encouraging) me despite being super busy!

Thank you to the PhDs, Post-docs and supervisors of the Interfaces project. It has been a pleasure to get to know you all, and share the funniest time with you during our project meetings. I hope to meet you all again in future.

Thanks to my friends in Italy and in Luxembourg for never forgetting to ask me how my work was going and for always supporting me.

Thank you to my parents, because without their trust, guidance and support (also financial), all this wouldn't have been possible. Grazie Mona e Pone per avermi sempre sostenuto e per aver creduto nelle mie scelte. Vi voglio bene! Thanks to my boyfriend Marco, because he was the one that encouraged me to start a PhD. Thanks for your patience, support and for not allowing me to get discouraged. Most importantly, thank you for believing in my future as a researcher... I really hope it is what the future has in store for me.

List of publications

First author manuscripts in peer-reviewed journals:

- Antonelli, M., Wetzel, C.E., Ector, L., Teuling, A.J., Pfister, L. 2017. On the potential for terrestrial diatom communities and diatom indices to identify anthropogenic disturbance in soils. *Ecol. Indic.*, 75:73 – 81. <https://doi.org/10.1016/j.ecolind.2016.12.003>.
- Antonelli, M., Klaus, J., Smettem, K.R.J., Teuling, A.J., Pfister, L. 2017. Inferring Streamwater Mixing Dynamics from Thermal Infrared Imagery. *Water*, 9 – 358. <https://doi.org/10.3390/w9050358>.
- Antonelli, M., Glaser, B., Teuling, A.J., Klaus, J., Pfister, L. 2020. Saturated areas through the lens: 1. Spatio-temporal variability of surface saturation documented through thermal infrared imagery. *Hydrological Processes*, 34: 1310– 1332. <https://doi.org/10.1002/hyp.13698>.
- Antonelli, M., Glaser, B., Teuling, A.J., Klaus, J., Pfister, L. 2020. Saturated areas through the lens: 2. Spatio-temporal variability of streamflow generation and its relationship with surface saturation. *Hydrological Processes*, 34: 1333– 1349. <https://doi.org/10.1002/hyp.13607>.

Co-authored manuscripts in peer-reviewed journals:

- Abbott, B.W., Baranov, V., Mendoza-Lera, C., Nikolakopoulou, M., Harjung, A., Kolbe, T., Balasubramanian, M.N., Vaessen, T.N., Ciocca, F., Campeau, A., Wallin, M.B., Romeijn, P., Antonelli, M., Gonçalves, J., Detry, T., Laverman, A.M., de Dreuzy, J.R., Hannah, D.M., Krause, S., Oldham, C., Pinay, G. 2016. Using multi-tracer inference to move beyond single-catchment ecohydrology, *Earth-Science Reviews*, 160, 19 – 42, <https://dx.doi.org/10.1016/j.earscirev.2016.06.014>.
- Pfister, L., Wetzel, C.E., Klaus, J., Martínez-Carreras, N., Antonelli, M., Teuling, A.J., McDonnell, J.J. 2017. Terrestrial diatoms as tracers in catchment hydrology: a review. *WIREs Water*, 4: e1241. <https://doi.org/10.1002/wat2.1241>.

List of publications

- Glaser, B., Antonelli, M., Chini, M., Pfister, L., Klaus, J. 2018. Technical note: Mapping surface-saturation dynamics with thermal infrared imagery, *Hydrol. Earth Syst. Sci.*, 22, 5987-6003. <https://doi.org/10.5194/hess-22-5987-2018>.
- Glaser, B., Antonelli, M., Hopp, L., and Klaus, J. 2020. Intra-catchment variability of surface saturation – insights from physically based simulations in comparison with biweekly thermal infrared image observations, *Hydrol. Earth Syst. Sci.*, 24, 1393–1413, <https://doi.org/10.5194/hess-24-1393-2020>.



*Netherlands Research School for the
Socio-Economic and Natural Sciences of the Environment*

D I P L O M A

for specialised PhD training

The Netherlands research school for the
Socio-Economic and Natural Sciences of the Environment
(SENSE) declares that

Marta Antonelli

born on 24 March 1988 in Sezze, Italy

has successfully fulfilled all requirements of the
educational PhD programme of SENSE.

Wageningen, 25 May 2020

Chair of the SENSE board

Prof. dr. Martin Wassen

The SENSE Director

Prof. dr. Philipp Pattberg

The SENSE Research School has been accredited by the Royal Netherlands Academy of Arts and Sciences (KNAW)



K O N I N K L I J K E N E D E R L A N D S E
A K A D E M I E V A N W E T E N S C H A P P E N



The SENSE Research School declares that **Marta Antonelli** has successfully fulfilled all requirements of the educational PhD programme of SENSE with a work load of 38.0 EC, including the following activities:

SENSE PhD Courses

- o Environmental research in context (2015)
- o Research in context activity: 'Designing and producing accessible video presentation of research on "Tracing hydrological connectivity in the riparian zone via Thermal Infrared imagery"' (2020)

Other PhD and Advanced MSc Courses

- o Interfaces Summer School, IGB Berlin (2014)
- o Interfaces ATC2: 'Advanced distributed sensing', CRP-GL (now LIST) (2014)
- o Interfaces ATC3 – ATC5 – ATC7: 'Smart tracing techniques', 'High-resolution fluorescence absorption spectrophotometry' and 'Principles of bioengineering', University of Barcelona, CEAB-CSIC and Naturalea (2015)
- o Aberdeen Catchment Science Summer School, University of Aberdeen (2015)
- o Interfaces ATC6: 'Qualitative and quantitative molecular techniques', NIB and Biosistemika (2015)
- o Joint field experiment: 'Integrated multi-method framework', Centre National de la Recherche Scientifique (2016)
- o 'Water lecture series' – Catchment and Ecohydrology group, Luxembourg Institute of Science and Technology (2017)
- o Project Management, Fond National de la Recherche Luxembourg (2015)
- o Boost your energy, Luxembourg Institute of Science and Technology (2017)

Other, external training

- o Safety driving, Centre de Formation pour Conducteurs S.A., (2017)
- o Web Video Hackathon 2019, Fond National de la Recherche Luxembourg (2019)

Management and Didactic Skills Training

- o LIST PhD representative - design and implementation of the PhD area of LIST's new intranet (2016-2017).

Oral Presentations

- o *Diatoms as a tracer of hydrological connectivity: the Oak Creek case study*. EGU General Assembly, 12-17 May 2015, Vienna, Austria
- o *Runoff generation processes inferred from surface water network dynamics*. 6th International Multidisciplinary Conference on Hydrology and Ecology, 18-23 June 2017, Birmingham, United Kingdom

SENSE coordinator PhD education

Dr. ir. Peter Vermeulen

The research described in this thesis was financially supported by the European Union's Seventh Framework Program for research, technological development and demonstration under grant agreement No. 607150 (FP7-PEOPLE-2013-ITN—INTERFACES—Ecohydrological interfaces as critical hotspots for transformations of ecosystem exchange fluxes and bio-geochemical cycling).

Financial support from Wageningen University for printing this thesis is gratefully acknowledged.

Cover design by Marta Antonelli. Photo by Steve Meyers.

Printed by Digiforce – ProefschriftMaken, Wageningen, NL

